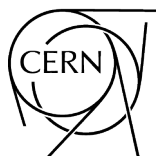


Proceedings of the Injector MD Days 2017

Geneva, Switzerland
23 – 24 March 2017

Editors: H. Bartosik
G. Rumolo



CERN Proceedings

Published by CERN, CH-1211 Geneva 23, Switzerland

ISBN 978-92-9083-474-8 (paperback)

ISBN 978-92-9083-475-5 (PDF)


ISSN 2078-8835 (Print)

ISSN 2518-315X (Online)

DOI <https://doi.org/10.23727/CERN-Proceedings-2017-002>

Available online at <http://publishing.cern.ch/> and <http://cds.cern.ch/>

Copyright © the Authors, 2017

 Creative Commons Attribution 4.0

Knowledge transfer is an integral part of CERN's mission.

CERN publishes this volume Open Access under the Creative Commons Attribution 4.0 license (<http://creativecommons.org/licenses/by/4.0/>) in order to permit its wide dissemination and use. The submission of a contribution to CERN Proceedings shall be deemed to constitute the contributor's agreement to this copyright and license statement. Contributors are requested to obtain any clearances that may be necessary for this purpose.

This volume is indexed in: CERN Document Server (CDS), INSPIRE.

This volume should be cited as:

Proceedings of the iNJECTOR md dAYS 2017, Geneva, Switzerland, 22 – 25 August 2016, edited by H. Bartosik and G. Rumolo, CERN Proceedings, Vol. 2/2017, CERN-Proceedings-2017-002 (CERN, Geneva, 2017), <https://doi.org/10.23727/CERN-Proceedings-2017-002>

A contribution in this volume should be cited as:

[Author name(s)], in Proceedings of the Injector MD Days 2017, Geneva, Switzerland, 23 – 24 March 2017, edited by H. Bartosik and G. Rumolo, CERN Proceedings, Vol. 2/2017, CERN-Proceedings-2017-002 (CERN, Geneva, 2017), pp. [first page]–[last page], <https://doi.org/10.23727/CERN-Proceedings-2017-002>. [first page]

Abstract

The Injector Machine Development (MD) days 2017 were held on 23-24 March, 2017, at CERN with the following main goals:

- Give a chance to the MD users to present their results and show the relevant progress made in 2016 on several fronts.
- Provide the MD users and the Operation (OP) crews with a general overview on the outcome and the impact of all ongoing MD activities.
- Identify the open questions and consequently define - with priorities - a list of machine studies in the injectors for 2017 (covering the operational beams, LHC Injectors Upgrade, High Luminosity LHC, Physics Beyond Colliders, other projects).
- Create the opportunity to collect and document the highlights of the 2016 MDs and define the perspectives for 2017.
- Discuss how to make best use of the MD time, in particular let the main MD user express their wishes and see whether/how OP teams can contribute to their fulfilment.

Contents

Introduction and welcome

INJECTOR MACHINE DEVELOPMENT DAYS 2017 <i>H. Bartosik, G. Rumolo</i>	1
---	---

PSB

MACHINE DEVELOPMENT STUDIES FOR PSB EXTRACTION 160 MEV AND PSB TO PS BEAM TRANSFER <i>V. Forte et al.</i>	5
--	---

PSB LLRF: NEW FEATURES FOR MACHINE STUDIES AND OPERATION IN THE PSB 2016 RUN <i>M. E. Angoletta</i>	17
--	----

LONGITUDINAL EMITTANCE BLOW-UP AND PRODUCTION OF FUTURE LHC BEAMS <i>S. Albright, E. Shaposhnikova, D. Quartullo</i>	23
---	----

HOLLOW BUNCHES PRODUCTION <i>S. Hancock, A. Oeftiger</i>	27
---	----

PSB-to-PS transfer and PS

SPACE CHARGE STUDIES IN THE PS <i>F. Asvesta et al.</i>	37
--	----

THE (7,7) OPTICS AT CERN PS <i>M. Serluca et al.</i>	43
---	----

PS ans PS-to-SPS transfer

INJECTION SEPTA POSITION AND ANGLE OPTIMISATION IN VIEW OF THE 2 GEV LIU UPGRADE OF THE CERN PS <i>M. Serluca et al.</i>	51
---	----

LONGITUDINAL COUPLED-BUNCH INSTABILITY STUDIES IN THE PS <i>H. Damerou, L. Ventura</i>	59
---	----

PS-to-SPS transfer and SPS

LOSSES ON SPS FLAT BOTTOM AND BEAM LOADING WITH LHC BEAMS <i>H. Bartosik et al.</i>	63
--	----

BEAM MEASUREMENTS OF THE SPS LONGITUDINAL IMPEDANCE <i>A. Lasheen, E. Shaposhnikova</i>	73
--	----

FIXED TARGET BEAMS <i>V. Kain et al.</i>	81
---	----

SLOW EXTRACTION AT THE SPS: EXTRACTION EFFICIENCY AND LOSS REDUCTION STUDIES	
<i>M.A. Fraser et al.</i>	87
WIDEBAND FEEDBACK SYSTEM PROTOTYPE VALIDATION	
<i>K. Li et al.</i>	95
SPS	
SPS BATCH SPACING OPTIMISATION	
<i>F.M. Velotti et al.</i>	103
EMITTANCE GROWTH IN COAST IN THE SPS	
<i>A. Alekou et al.</i>	107
Ions (source, Linac3, LEIR)	
SOURCE AND LINAC3 STUDIES	
<i>G. Bellodi</i>	113
SPACE CHARGE AND WORKING POINT STUDIES IN THE CERN LOW ENERGY ION RING	
<i>A. Huschauer et al.</i>	117
LEIR LONGITUDINAL STUDIES	
<i>S. Albright, S. Hancock, M. E. Angoletta</i>	123
LEIR IMPEDANCE MODEL AND COHERENT BEAM INSTABILITY OBSERVATIONS	
<i>N. Biancacci et al.</i>	129
100MS INJECTION INTO LEIR	
<i>R. Scrivens et al.</i>	133
Ions (PS, SPS)	
YASP FOR LEIR TO PS INJECTION	
<i>V. Kain et al.</i>	137
BATCH COMPRESSION TO 50 NS SPACING AT PS FLAT-TOP	
<i>H. Damerou</i>	139
TRANSVERSE STUDIES WITH IONS AT SPS FLAT BOTTOM	
<i>F. Antoniou et al.</i>	145
PB-IONS IN HARMONIC NUMBER 4653 AT SPS FLAT BOTTOM	
<i>H. Bartosik et al.</i>	151
SMOOTH B-TRAIN	
<i>T. Bohl, A. Pashnin</i>	155

INJECTOR MACHINE DEVELOPMENT DAYS 2017

H. Bartosik and G. Rumolo*, CERN, Geneva, Switzerland

Abstract

Following the important progress made in 2016 in the Machine Development (MD) activities that took place in all the accelerators of the LHC injector chain, the days 23-24 March, 2017, have been devoted to summarise the main outcome from the MDs and lay out the plans for the next steps. The event was also triggered by the following motivations and goals:

- Give a chance to the MD users to present their results;
- Provide a platform in which MD users, MD coordinators and operations crews meet and discuss openly the optimisation of the MD time and procedures, taking into account of the different perspectives;
- Provide an overview of all the ongoing activities to better frame their impact in the broader picture of the CERN short and long term projects;
- Identify the open questions, define and prioritise machine studies in the injectors for 2017;
- Create the opportunity to obtain and document written reports from MD users.

Within this contribution, we just summarise the context and the main points discussed at the event, which should be retained in an effort to improve the MD logistics and organisation. Concerning the individual MD activities and results, these are described in detail in the other papers of these Proceedings.

THE CONTEXT

The MD organising web tool

Since 2015, in the CERN accelerator complex the MD requests are made via the web interface [1] (see Fig. 1), which has significantly simplified the procedures of MD requesting for the users and planning for the coordinators. Starting from the web interface, generic MD requests can be made through the tab “New MD Request” (second from left). Once the MD request is created, time slots for parallel MDs can be directly requested by the MD users on a weekly basis, by simply editing the existing MD request and providing the number of the requested shifts as well as the user’s availability for the coming week. One cycle in the supercycle is always reserved for parallel MDs in all machines (PSB, PS, SPS) every working day during the working hours – but also during nights and weekends, if MD users are available. On the other hand, dedicated MDs are selected and assigned by the MD coordinators (among the received requests) on the days with 10 hours of dedicated injector MDs (usually on

Wednesdays). To facilitate coordination and avoid overloading the OP crews with requests, dedicated injector MDs do not take place on the weeks of LHC MDs. During the weeks of LHC Technical Stop (TS), however, dedicated injector MD blocks are allocated, giving priority to those SPS MD users which are incompatible with injection into LHC (e.g. the COLDEX runs). Low intensity MDs (e.g. those using a single bunch in coasting mode in the SPS) also usually take place in the shadow of the machine cool-down over the 24 hours preceding an injector TS (leaving the last three hours without beam for complete cool-down). When dedicated MDs take place in PSB or PS, disrupting physics in these machines more than on days of simple SPS dedicated MDs, special announcements are made at Facility Operation Meetings (FOMs) to warn specifically physics users.

Every week, all requests for parallel MDs for the following week are collected by Friday and the MD program, generated through a visually intuitive editing mode of the “Schedule” tab, is then published late on Fridays. Since 2016, also LEIR is included in the MD planning and the requests for LEIR MDs can be made through the same interface as for the other machines. While in previous years, the dedicated Wednesday blocks were not scheduled during the LHC ion run, since 2016 they are preserved also in this period mainly to allow for dedicated SPS MDs with ions to take place in the framework of the LHC Injectors Upgrade (LIU) [2] study program.

The Injector MD program in 2016

Although there were important limitations in the SPS due to a vacuum leak in the main internal dump block (TIDVG), many machine studies could be performed in 2016, which have led to:

- Improved performance of the currently operational beams, with both a better beam quality for (proton and ion) LHC and FT physics and an important loss reduction in all the machines (and reduced machine activation);
- A better understanding of the performance limitations of future beams (e.g., within the LIU project) and study of mitigation techniques for the expected bottlenecks.

In 2016, the ion program could greatly benefit from the early start of the ion injector chain. This gave time to study intensity limitations in the pre-injectors and notably resulted in the delivery of ion beams to the LHC that are already compliant with the final LIU/HL-LHC request in terms of single bunch parameters [3]. Unfortunately, due to then aforementioned problem with the SPS dump, all the SPS MDs requiring acceleration of bunch trains could not be performed in 2016 and will have to be postponed to 2017. This includes for example all the MDs on longitudinal coupled

* Giovanni.Rumolo@cern.ch

Injector MDs

Parallel MDs in all machines take place every weekday during working hours (8:00–18:00). There is always one available MD cycle in PSB, PS and SPS.

During dedicated MDs, usually on Wednesdays (8:00–18:00), MD users have priority over physics users. When LHC is operating, dedicated MDs take place in parallel to LHC operation and may have to be stopped when LHC needs to refill. No physics is guaranteed during the MD time, but beam will be provided to PSB/PS physics users on a best effort basis.

The latest Injector schedule can be found [here](#)

Contact
Giovanni Rumolo (MD Coordinator)
Hannes Bartosik (MD Coordinator)

LHC MDs

MD1 to take place on 25-29 July 2016, MD requests accepted until 21 June.

Next LSWG on 28 June

[All LSWG meetings](#)

[Run II MD Notes](#)

[Instructions and examples for MD procedures and MD notes publication](#)

Contact
Rogelio Tomas Garcia (MD Coordinator)
Jan Uythoven (MD Coordinator)
Giulia Papotti (Scientific Secretary)

Figure 1: Snapshot of the application (web tool) for the CERN MD management.

bunch instabilities along the ramp and at flat top, absolutely instrumental for the LIU program.

The available MD time was anyway fully used in 2016 and at least the same level of MD time should be allocated in 2017 to progress on the various fronts and accommodate additional requests from the different projects. These include e.g. all the LIU MDs that could not be carried out in 2016, the HL-LHC MDs on crab cavities preparation and the new studies on the limitations of the Fixed Target beams in all machines, relevant for the Physics Beyond Collider program.

SOME POINTS OF DISCUSSION

At the Injector MD days 2017, two types of presentations were requested (and provided). Basically at the opening of each session, representatives of the OP crews for the different machines made an attempt to address the questions whether the present setting of MD coordination and execution works, and what remains to be improved for the general satisfaction and efficiency. Then, there were the talks from the MD users, which were required to cover

- Context and goals of each MD
- Results, lesson learnt and outlook for 2017
- Comments on number of MD hours used vs. requested, efficiency of the MD time, level of satisfaction, main issues encountered (e.g. in terms of beam preparation, machine support or required instrumentation).

The following points emerged during the discussions and have been retained for future action:

- The new tool for MD scheduling and viewing has been widely appreciated, however there is room for improvement both in its function and in the way it is used.

- The option to associate a beam to an MD is not sufficiently used. In many cases, the beam for the planned MD is either not declared or just declared in terms of LSA cycle (probably also not matching the actual beam parameter request). The absent, or erroneous, beam declaration makes it difficult for the OP crews to prepare the MD in advance and may generate frustration in the first part of the MD, when the beam has to be set up in the middle of several other concurrent activities.
- The generation of LSA cycles for MDs seems to be quite wild, with possibly multiple LSA cycles generated for the same MD at different times of the year. While at the beginning of the 2015 run a naming convention had been encouraged when generating an LSA cycle for an MD (i.e. MD_MDIIdentifier_BeamType), the applied naming conventions turn out in practice to be neither respected nor intuitive. This not only creates a plethora of useless cycles that nobody can easily identify, but also makes it difficult, at the clean-up time, to assess whether the various “orphan” cycles should be kept or deleted.
- More reminders of MD program and beam requirements should be sent out other than the Friday email announcing the next week’s program. For instance, a reminder on Tuesdays before the dedicated MD would be welcome.
- It is desirable to relax the MD program during the time of beam set up and commissioning, to avoid unnecessarily increasing the workload on the OP crews at an already busy time. In particular, parallel MDs could be limited in these weeks, while “exotic” MDs should be avoided at all. In 2017, it could be advisable to move all the scheduled dedicated MD blocks of the first three weeks to a certain point later on in the year. when

e.g. a dedicated high intensity run in the SPS could be organised.

- On many fronts, the communication between MD users and OP crews could be also improved. For example, MD users who give up their slots although they are in the official planning should notify the operators that their MD is not taking place. MD users should also notify the operators when their MD ends and the console can be cleaned up. They should also leave instructions for night time MDs, when they want some acquisition to keep on running.
- On the side of the MD users, no complaint was raised concerning MD request tool, allocated (and available) MD time and execution of the MD (e.g., beam preparation, instrumentation, support). Conversely, it was noted that at PSB and PS the main problem is not the available but rather the availability of resources to carry out MDs on a certain subject.
- Clear follow up plans for 2017 were presented in most of the MD specific presentations. Given the high number, it seems that dedicated MD requests in SPS will be challenging to accommodate in 2017. Besides, in collaboration with the restricted Machine Protection Panel (rMPP), some of the MDs in SPS will need to be assessed in terms of safety and machine protection.
- The MDs that took place in 2016 can mostly be classified in: MDs of preparation, modeling and understanding; MDs for (or in view of) future modes of operation; and finally, the great majority, performance improving MDs. Concerning this last category, the importance was recognised to assess as quickly as possible the performance improving potential of certain MDs and use it in operation. In the future, to better close the loop between performance improving MD outcome and operational deployment, a path can be set, based on a relatively fast Machine Study Working Group (MSWG)

recommendation, followed by LHC Injector and Experimental Facilities Committee (IEFC) presentation and approval in the case of changes with hardware implications.

- Many good results appeared to be obtained in the last phases of the MD execution or run, which sometimes is normal due to the fact that MD requests and ideas naturally evolve during the year steered by the obtained MD results. However, it is important to work on mitigating the usual MD rush at the end of the year, especially in view on the critical 2018 end-of-run, by proposing a strong prioritisation of the MDs at beginning of run and a check-point in the middle of the run.

ACKNOWLEDGMENTS

The authors would like to thank G. Arduini and R. Steerenberg for the support of the Injector MD days 2017 and for their active participation in the event and in the various discussions. Besides, we are also grateful to the OP crew members who were present throughout the event to both learn about the goals of the MDs and offer their input on how to improve the organisational part. In particular we would like to thank J-F. Comblin, D. Cotte and V. Kain for presenting briefly and efficiently the OP point of view of the MDs.

REFERENCES

- [1] CERN Machine Development Coordination, <https://md-coord.web.cern.ch/app/#/>
- [2] “LIU Technical Design Report – Volume I: Protons” and “LIU Technical Design Report – Volume II: Ions”, edited by J. Coupard *et al.*, CERN-ACC-2014-0337 (2015) and CERN-ACC-2016-0041 (2016)
- [3] H. Bartosik *et al.*, TUPVA020 in Proc. of IPAC’17, Copenhagen, 14-19 May, 2017

MACHINE DEVELOPMENT STUDIES FOR PSB EXTRACTION AT 160 MEV AND PSB TO PS BEAM TRANSFER

V. Forte*, M.A. Fraser, S. Albright, W. Bartmann, J. Borburgh, L.M. Coralejo Feliciano, H. Damerau, A. Ferrero Colomo, D. Gamba, G. P. Di Giovanni, B. Mikulec, A. Guerrero Ollacarizqueta, M. Serluca, L. Sermeus, G. Sterbini, CERN, Geneva, Switzerland

Abstract

This paper collects the machine development (MD) activities for the beam transfer studies in 2016 concerning the PSB extraction and the PSB-to-PS transfer. Many topics are covered: from the 160 MeV extraction from the PSB, useful for the future commissioning activities after the connection with Linac4, to new methodologies for measuring the magnetic waveforms of kickers and dispersion reduction schemes at PS injection, which are of great interest for the LHC Injectors Upgrade (LIU) [1] project.

INTRODUCTION

Several MDs have been performed for the PSB-to-PS transfer and PSB extraction in 2016. The outcome of the studies has provided useful input for the hardware and beam study activities related to the LIU project. An exhaustive list is reported in Tab. 1:

Table 1: List of 2016 MDs

MD number	Description	Duration
88	PSB extraction at 160 MeV	2 days
1366	Recombination kickers waveforms measurements	>70 hours
1939	PS injection kicker (KFA45) waveform measurements	1 week
1904	PSB-BTi-BT-BTP-PS dispersion measurements	few slots
1829, 1893	LHC "long bunches" transfer and emittance evaluation	3 days
1928	Sanity tests of sem-grids after PS injection	5 hours
1769	Automatic alignment in the BTi-BT-BTP at PS injection	2 days
1740	Septum SMH42 new position and angle	0.5 days

MD88: PSB EXTRACTION AT 160 MEV

The extraction of the beam at 160 MeV is foreseen during the commissioning activities after the connection with Linac4. The intent is to inject and extract the beam to the dump in the beam transfer measurement (BTM) line and to avoid losing it all in the PSB during the commissioning phases. This possibility will facilitate initial injection checks and procedures at low energy, before the energy ramping phase [2]. For this reason it was important to prove the feasibility of such an extraction.

The MD was executed in 2 non-consecutive days in dedicated mode, as the power supplies of extraction septum and quadrupoles in the transfer lines cannot switch between 160 MeV and 1.4 GeV operations. The MD required coordination of experts between different groups, in order to relax the hardware and software interlock settings to operate the extraction at 160 MeV.

Initial setup and beam preparation

Initial optics simulations have been performed by W. Bartmann [3]. The cycle at 160 MeV up to extraction was prepared in advance and is shown in Fig. 1. The radio-frequency (RF) settings from LHC25 on PSB Ring 3 were used.

* vincenzo.forte@cern.ch

Many experts were involved and coordinated to perform modifications in the transfer line for the 160 MeV extraction (~ 27 % of the nominal magnetic beam rigidity at 1.4 GeV). In particular, they had to: modify the tolerances in the power supply, modify tolerances on the controls side and reduce limits for the extraction kicker (to 7 kV) and of the extraction bumpers (to +100 A), go locally to modify the limit for the extraction bumpers and change the interlock level for the extraction kicker (7 kV). The beam position monitors

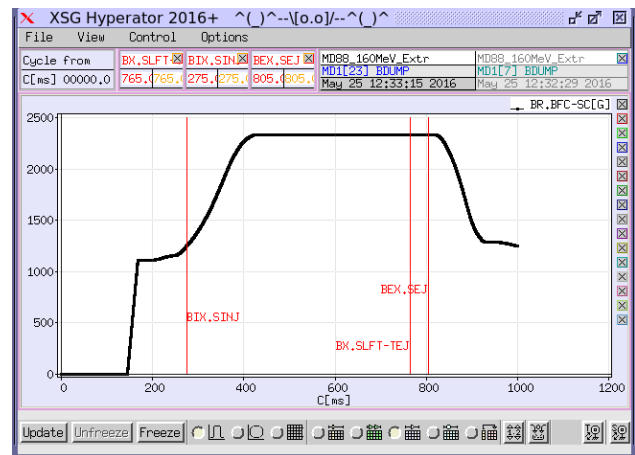


Figure 1: The PSB magnetic cycle at 160 MeV up to extraction (time marker “BEX.SEJ”, at ~ 805 ms).

sum signals along the beam transfer (BT-BTM) line to the dump (sketched in Fig. 2) were used to monitor step-by-step the beam threading in the line, while the evaluation of the transmission efficiency was performed through beam current transformers (BCTs) in the PSB ring (just before extraction) and at the end of the line (BTM.BCT10).

Conclusions of the MD

The final configuration was obtained by extending orbit correction functions to extraction, rescaling angle/position correctors, extraction bumpers (to 140 A, only in local mode), kicker (12 kV) and septum (1862 A), and by re-steering the line through the trajectory corrections. A transmission efficiency of ~ 80% to the dump was finally reached with a bunch of 60×10^{10} p, $(\delta p/p)_{rms} = 1.6 \times 10^{-3}$ and 474 ns total bunch length, as shown in Fig. 3.

The longitudinal beam profiles, trajectories and losses through beam loss monitors (BLMs) along the extraction line are shown in Fig. 4. Some issues remain to be investigated, like observed jitter on the synchronisation between the extraction kicker and beam, leading occasionally the beam to be extracted in two turns, and the losses in transfer line, probably related to limited acceptance and non-optimal trajectories (especially at higher intensities). These issues

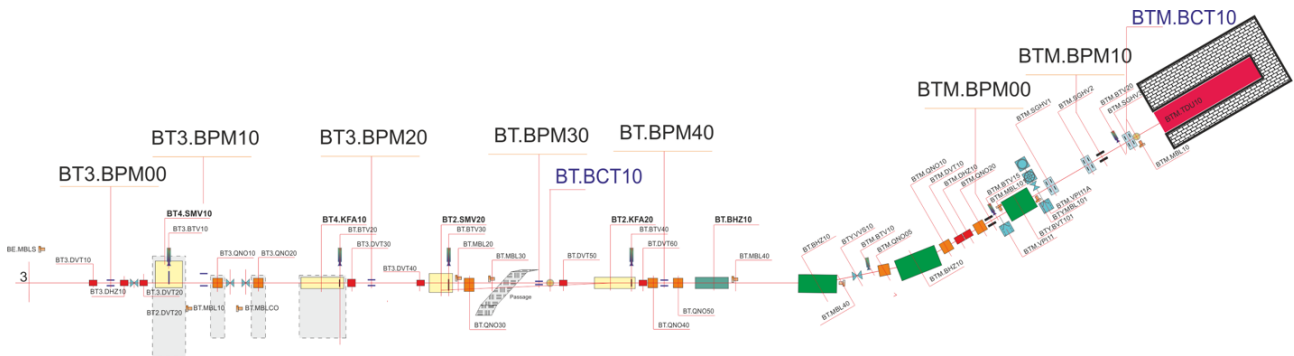


Figure 2: The transfer line (BT-BTM) from the PSB Ring 3 to the beam dump. The BPMs and BCTs are labelled with larger fonts (edited from [4]).

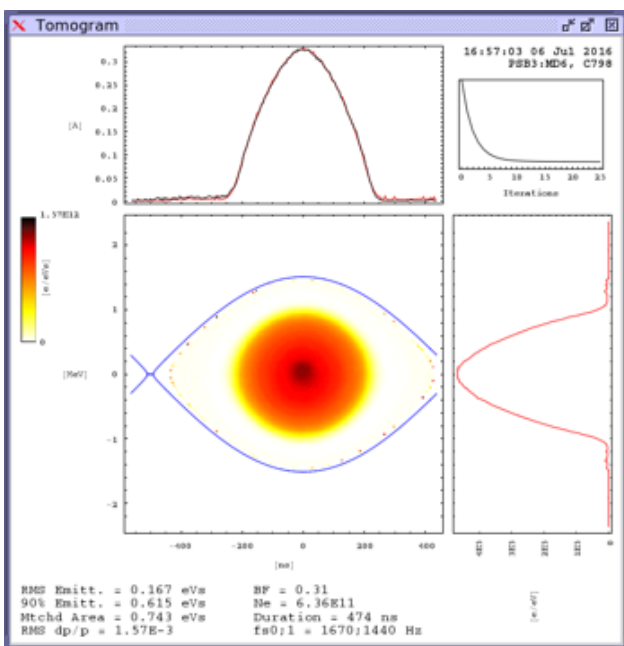


Figure 3: The tomographic reconstruction of the longitudinal phase space for the extracted bunch at 160 MeV.

should deserve more attention in order to try and achieve more than 80% transmission efficiency. However, the limited commissioning phase of extraction at 160 MeV foreseen during the PSB-Linac4 connection has steered the repetition of this dedicated MD in 2017 toward a lower priority.

MD1366: NEW BEAM-BASED MEASUREMENTS OF PSB-TO-PS VERTICAL RECOMBINATION KICKERS [5]

The increased bunch length demanded by the LIU project to mitigate emittance growth from space-charge on the PS injection plateau puts strong constraints on the rise-times of the recombination kickers in the transfer lines between the CERN Proton Synchrotron Booster (PSB) and the Proton Synchrotron (PS). A beam-based technique has been developed to validate the waveforms of the recombination kickers. High-resolution measurements are presented by extracting the intra-bunch deflection along bunches with lengths comparable to or longer than the rise-time of the kicker being

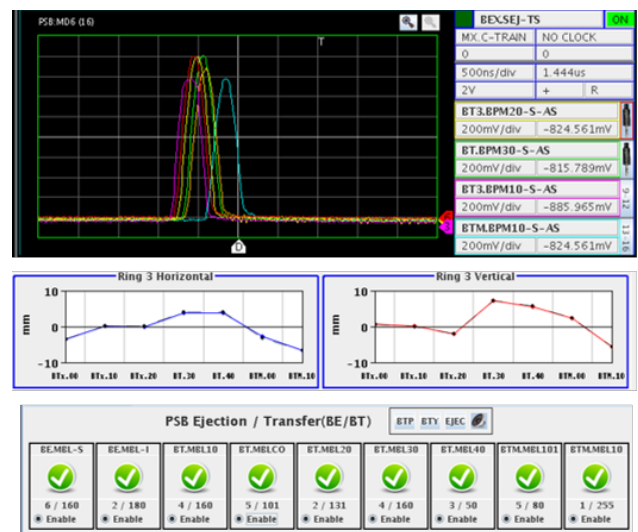


Figure 4: Longitudinal beam profiles (top), ejection trajectories (centre) and BLM levels (bottom).

probed. The methodology has been successfully applied to the three vertical recombination kickers named BT1.KFA10, BT4.KFA10 and BT2.KFA20, and benchmarked with direct measurements of the kicker field made using a magnetic field probe. This paper describes the beam-based technique, summarises the main characteristics of the measured waveforms, such as rise-time and flat-top ripple, and estimates their impact on beam brightness.

The BT1.KFA10, BT4.KFA10 and BT2.KFA20 kicker magnets are used to recombine the bunches coming from the four vertically-stacked rings of the PSB. The batch, constituted by several bunches, can then be directed to the dump at the end of the beam transfer measurement (BTM) line, or to the ISOLDE experiment, or to the PS through the BTP line. The single bunches going to the PS for the LHC (Standard production) are of interest for this paper. To preserve the brightness of the LHC bunches it is very important that the recombination does not disturb the vertical distribution of particles of the bunches.

The present LHC baseline (standard production) is constituted by 180 ns long bunches, spaced by 327 ns, at 1.4 GeV. The bunches, coming from different PSB rings, are labeled as "Rx", where x is the PSB ring number from which they are ejected. The LHC injections into the PS are performed with two batches separated by 1.2 s. i.e. the PSB basic period. In

the first PS injection four bunches are extracted from each ring in the following sequence: R3 → R4 → R2 → R1. The second injection is composed of two bunches: R3 → R4.

BT4.KFA10 recombines R3 (un-kicked) and R4 (kicked), BT1.KFA10 recombines R2 (un-kicked) and R1 (kicked), and finally, BT2.KFA20 recombines R3-R4 (un-kicked) and R2-R1 (kicked), as shown in Fig. 5.

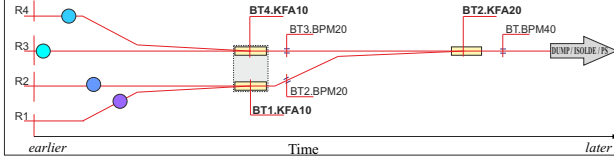


Figure 5: A simplified sketch (edited from [4]) of the recombination kickers in the BT-BTP line (lateral view) and the sequence of PSB bunches before being recombined.

The recombination kickers are triggered in the time between two adjacent bunches. A relatively short rise-time is important to avoid that the transient of the magnetic field perturbs the tail of the first bunch and/or the head of the second one. In order to obtain a clean transfer for the longer 220 ns LIU bunches, the specification [6] requires the 2-98% rise-time ≤ 105 ns.

The flat-top ripple of the kicker waveforms must be controlled to avoid the detrimental effects of vertical intra-bunch motion that will result in vertical emittance growth and filamentation in the PS. The specification requires ≤ 2% flat-top ripple for each recombination kicker.

These limits have to be considered without any further margin and are directly related to the emittance blow-up, which is expected from simulations [7] to be in the order of 2%.

Measurement set-up

The reconstruction of the kicker waveform was obtained from the measured displacement of the beam after it is kicked. In fact, the displacement δ at any beam position monitor (BPM) is directly proportional to the integrated magnetic field seen by the beam, such that the deflection angle θ at the kicker can be written as shown in Eq. 2:

$$\delta_{x,y} \propto \theta_{x,y} = \frac{e}{p} \int_0^L B_{y,x} dz \quad (1)$$

where p is the momentum, e is the electric charge, B is the magnetic field, L is the magnetic length and x , y , z are the horizontal, vertical and longitudinal coordinates respectively.

The first downstream BPM after each kicker was used to retrieve the beam displacement information in time, by taking the ratio between the vertical difference (Δ_y) and the sum (Σ) signals in a defined gating time window around the peak current location of the bunch. The BPM signals were monitored on an OASIS scope [8] in the control room and recorded as a function of the delay imposed on the kicker trigger.

Figure 6 shows an example of the sum and difference signals of BT.BPM40, which is the first downstream of BT2.KFA20. It is possible to distinguish different cases in the figure where (left) the first bunch (R4) is partially affected by the kick and R2 is fully kicked. the nominal case

(centre) where R4 is un-kicked and R2 is fully kicked and (right) the case where the second bunch (R2) is partially kicked and R4 stays un-kicked.

Figure 6 also shows the magnet input current signal of the BT2.KFA20 kicker on OASIS. It should be stressed that this last signal represents the input current for the magnet and is not representative of the magnetic waveform of the kicker. Moreover the current signal appears low-pass filtered due to the attenuation in its transmission to the OASIS scope and thus is only useful to determine and verify the delay applied to the trigger of the kicker.

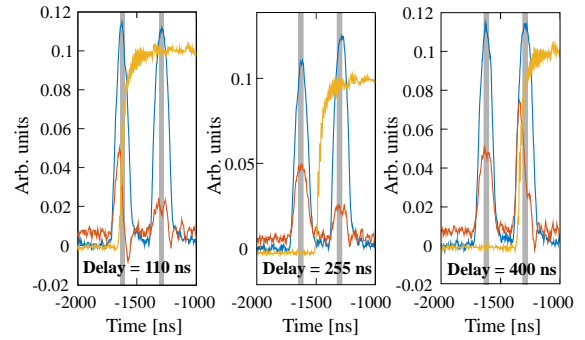


Figure 6: The BPM Δ_y (orange) and Σ (blue) signals, together with the current signal (yellow) for three different values of the BT2.KFA20 delay. The grey error-band is the chosen gating window around the peak current.

Measurement procedure

Calibration It is important to perform a beam-based calibration of the BPM with respect to the kicker voltage at the beginning of every measurement, as shown in Fig. 7. The calibration has to be performed in a nominal regime, i.e. with the first bunch completely un-kicked and the second one fully kicked, as in Fig. 6 (centre). Due to trajectory differences in the transfer line, the BPM signals of the two bunches have to be vertically shifted by an offset in order to be both aligned to the same reference. As shown in Fig. 6 (centre), the offset corresponds, for the fully kicked bunch, to the constant term of the linear regression of the measured deflection per kicker voltage, and, for the un-kicked bunch, to the average value.

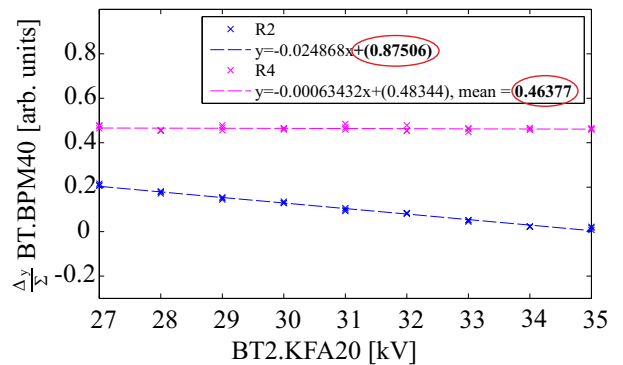


Figure 7: The calibration plot for the BT2.KFA20 kicker vs BT.BPM40 (the offsets are in the red ellipses).

Reconstruction The measurement was performed by scanning the fine delay of the recombination kicker and acquiring BPMs signals of the two consecutive bunches. The measured signal is shown in Fig. 8 (left). The reconstruction was then completed through the vertical shift of the two waveforms determined in the aforementioned calibration process. After further statistical processing the waveform is shown in Fig. 3 (right) plotted with 1 standard deviation (SD) significance bounds. As the BPM responses are more

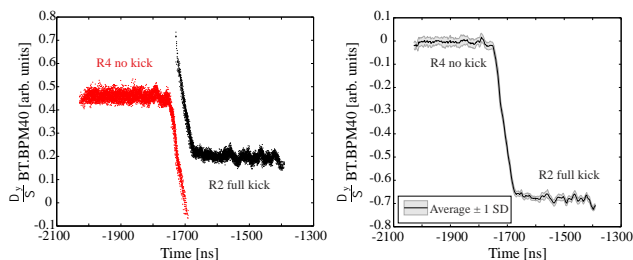


Figure 8: The magnetic waveform reconstruction process.

precise at high currents [7], the bunch population at the exit of the PSB was chosen at $\sim 200 \times 10^{10}$ protons and, owing to the length of the bunches (180 or 220 ns), multiple intra-bunch measurement samples could be taken within individual bunches. This allowed high granularity in the measurements.

The characteristics of the waveform were only measured at the relevant locations where the bunches sit, very close to, and either side of, the rising edge. For the BT1(4).KFA10 the flat-top ripple is relevant during only the first 220 ns before and after the rising edge as single bunches are recombined. For BT2.KFA20 up to ~ 550 ns (from one 220 ns bunch length plus 327 ns bunch spacing) is important, as it recombines doublets (R3-R4 and R2-R1).

The beam-based reconstructions were performed at the present operational voltages for an extraction energy of 1.4 GeV from the PSB, corresponding to: 43 kV for BT1(4).KFA10 and 27 kV for BT2.KFA20. At the future 2 GeV extraction energy (+30% magnetic rigidity) the kickers will require 56 kV for BT1(4).KFA10 and 35 kV for BT2.KFA20.

The magnetic field measurements using a magnetic measurement coil for the KFA20 kickers were performed at 27 kV on the magnets installed in the machine during a technical stop, while the others were done at 50 kV for BT1.KFA10 (in the machine) and 56 kV for BT4.KFA10 (in the lab). These measurements were then scaled-up to be compared with the beam-based measurements. This comparison is valid in the assumption of an ideal "linear" response of the kicker system, which was demonstrated in dedicated beam-based measurements [7].

Measurement results

The raw measurement data was filtered using a (low-pass) median filter with a time window of 10 ns. This choice was made to smooth the signal whilst at the same time keeping a large enough bandwidth to observe any significant frequency components. The beam-based measurements could be compared with the magnetic measurements from fast magnetic measurement coils, in the machine and/or in the lab.

BT1.KFA10 The beam based measurements, shown in Fig. 9, indicate the presence of ripple and an initial overshoot that is filtered by the field measurement probe whose characteristics are unknown. The measurement results from the probe appear low-pass filtered and do not present the initial overshoot.

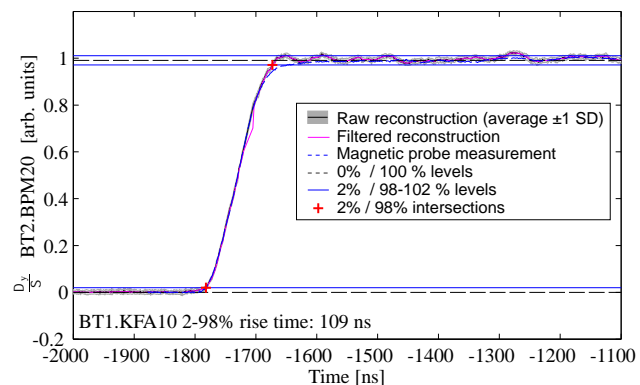


Figure 9: BT1.KFA10 waveform vs. probe in the machine.

BT4.KFA10 The comparison between the beam-based and lab-based measurements are shown in Fig. 10. A slight disagreement is visible in the amplitude of the flat-top ripple and might be induced by the fact that only one of the two modules of the kicker was probed and the system was not exactly equal to the one installed in the machine.

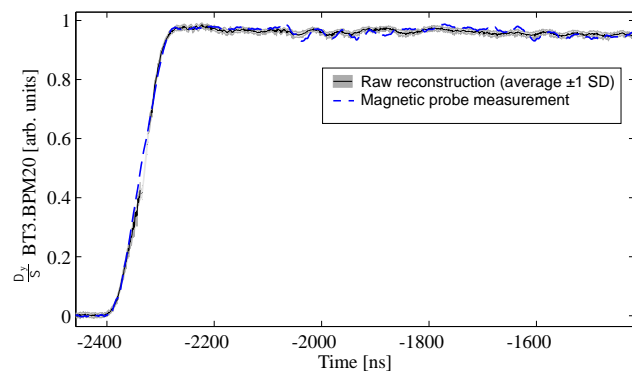


Figure 10: BT4.KFA10 waveform vs. probe in lab.

BT2.KFA20 The beam-based measurements were compared with the measurements from a fast and more reliable magnetic field probe, which was inserted directly inside the magnet in the machine. The results, in Fig. 11, show an excellent agreement. The flat-top peak ripple is confined inside $\pm 2\%$, except for a reflection inside the black dashed ellipse. The ripple induced from this reflection creates some undesired vertical emittance blow-up, and the KFA20 system will be recabled into the same configuration as KFA10 as part of the LIU project to remove this reflection.

Rise-times, flat-top ripples, frequency responses The rise-time and flat-top ripples estimated from the beam-based measurements, which are summarised in Tab. 3, are just in specification.

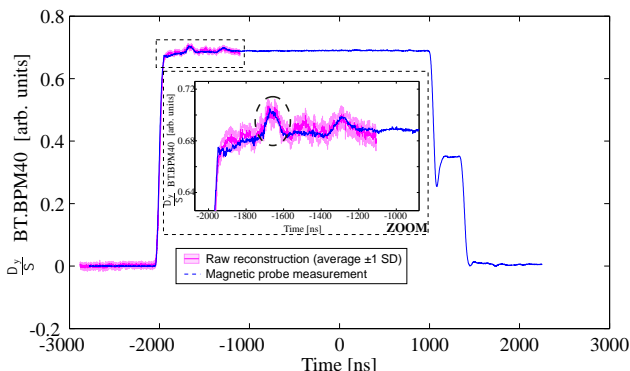


Figure 11: The BT2.KFA20 beam-based magnetic waveform.

After considering all the error sources such as the BPM sensitivity to current, the calibration technique, the beam reproducibility, the jitter of the firing trigger of the kicker, etc., the tolerance on the final rise-time measurements was conservatively set to ± 10 ns and the lab-based field measurements validated.

Table 2: The rise-times and flat-top ripples

	2-98% rise-time [± 10 ns]	Flat-top ripple \hat{B}/\bar{B} [%]
BT1.KFA10	109	2
BT4.KFA10	104	2
BT2.KFA20	105	2

In order to have high resolution needed for a fast Fourier transform (FFT), a detailed flat-top measurement was necessary. From the measurements in Fig. 12 the frequency components that need correction by the PS transverse feedback could be assessed: there is no significant component measured over 20 MHz (-3 dB bandwidth of the feedback). Moreover, the applied median filtering reproduced well the main frequency components of the raw signal.

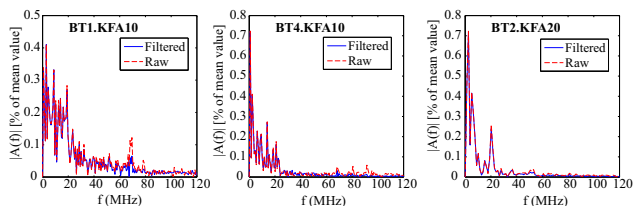


Figure 12: The measured frequency spectra of the flat-top ripple for BT1.KFA10 (left), BT4.KFA10 (centre) and BT2.KFA20 (right).

Conclusions of the MD

A new method to measure the magnetic waveform of the recombination kickers BT1(4).KFA10 and BT2.KFA20 was introduced. This method is valid for measurements in transfer lines where the waveform transients are comparable to the bunch length of the beam being used as a probe. The waveforms have been benchmarked with direct magnetic probe measurements, showing excellent agreement for all the kickers measured. The measured rise-times and flat-top ripples appear just within specification. The frequency components of the kickers are within the PS transverse feedback -3 dB bandwidth specification. Simulations of the incurred

emittance growth using the measured waveforms show a blow-up per ring up to 2.3% (summing in quadrature the contribution of each kicker) for 220 ns bunch lengths and 327 ns bunch spacing at 1.4 GeV [7]. Hardware modifications are on-going inside the framework of the LIU project to reduce the BT2.KFA20 ripple and increase the operational voltage margin at 2 GeV by recabling it as the KFA10.

MD1939: BEAM-BASED WAVEFORM MEASUREMENTS OF THE CERN PS INJECTION KICKER [9]

The KFA45 is the horizontal PS injection kicker used to transfer bunches from the BTP transfer line into the PS ring. During a PS cycle for the LHC, the kicker is fired at two instances in time spaced by 1.2 s, in order to fill the machine with a double-batch injection at 1.4 GeV from the PSB.

The four kicker modules have two modes of operation, linked with the termination impedance: terminated mode (TM), i.e. with a matched non-zero load impedance, and short-circuit mode (SC). Before 2017, the kicker was usually operated in TM and the SC mode was used only to compensate the missing current in case of module failures. The SC allows the doubling of the current going through the magnet and thus providing twice the kick. Since 2017 the KFA45 has been permanently configured in SC. In order to guarantee a clean transfer to the PS, the 2-98% rise and fall times and the 2% flat-top ripple of the KFA45 waveform must respect the specification [6], i.e. ≤ 105 ns and $\leq 2\%$ respectively.

Beam-based measurements of the KFA45 waveform are necessary because they represent the only way to retrieve the magnetic waveform of the installed system, required to confirm the kicker performance for LIU. A direct measurement with a field probe is very complicated to perform as it would require the movement of two main bending units in the PS.

Experimental method

The reconstruction of the kicker waveform is obtained from the displacement δ of the beam once it is kicked. In fact, δ at any subsequent beam position monitor (BPM) is directly proportional to the integrated magnetic field seen by the beam and to the deflection angle θ imposed by the kicker, as shown in Eq. 2:

$$\delta_{x,y} \propto \theta_{x,y} = \frac{e}{p} \int_0^L B_{y,x} dz \quad (2)$$

where p is the momentum, e is the electric charge, B is the magnetic field, L is the magnetic length and x , y , z are the horizontal, vertical and longitudinal coordinates respectively. A fast BPM, in section 02 (BPM02) [10], was used to retrieve the beam displacement information, by taking the ratio between the difference and the sum signal at the peak current location of the bunch. The kicker and the BPM signals were monitored and recorded from an OASIS scope [8].

The waveform measurements were made using the second instance of the kicker (~ 1 μ s pulse length), which was delayed from the injection plateau to the extraction flat-top at 26 GeV. The increased rigidity of the circulating beam permitted measurements to be made and the beam extracted to an external dump without significant beam losses.

The measurement method is based on the observation of the beam's displacement at a given time after it fires. A large number of cycles (occurrences) containing a single bunch were analysed to probe the entire waveform by shifting the delay between the circulating beam and kicker trigger, covering the whole revolution period in the PS.

A challenging issue was the asynchronous triggering of the kicker with respect to the circulating beam at flat-top energy; the injection kicker timing is only designed to be synchronous with the beam at injection energy. The asynchronous triggering induced a pseudo-randomisation of the shift in time of the beam with respect to the kicker delay. Figure 13 (left) shows the large amount of cycle occurrences that were required in order to cover uniformly the $2.1 \mu\text{s}$ revolution period in the PS. By imposing an initial shift on the KFA45 trigger of 5 ns/occurrence, and repeated at finer steps of 2 ns/occurrence, inside a span of 340 ns, the beam jittered with respect to the KFA45 trigger, which led to an uncontrollable granularity of the occurrences for a defined sampling time. The kicker trigger reference was also oscillating in the absolute reference of the OASIS scope: the jittering of the magnet input current signals with a defined signal threshold for every occurrence is shown in Fig. 13 (right).

The synchronisation issue is being solved for future measurements by adding another timing from which the injection kicker can be triggered synchronously with the beam at all energies.

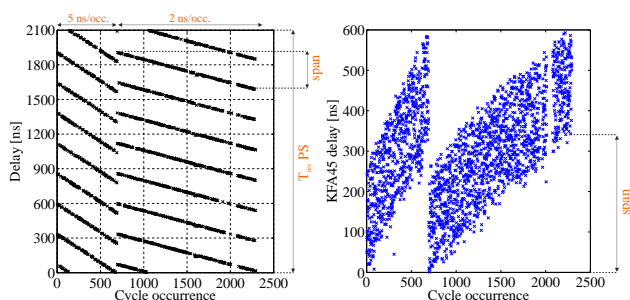


Figure 13: Beam (left) and KFA45 (right) delays.

Experimental results

A nominal single LHC bunch ($\sim 10 \times 10^{10}$ p) was used as a probe for the measurement, because it represented a good compromise between signal readability (for the BPM) and reduced losses at extraction.

Measurements were performed for TM and SC modes. The kicker total voltage was set equivalent to 270 kV. In TM all the four modules of the kicker were on, sharing the voltage, while in SC modules 1 and 2 were switched off, leaving modules 3 and 4 to work in short-circuit in order to compensate the missing current.

For every cycle, the closed orbit (CO) was approximated through a sinusoidal fit of the turn-by-turn position before the kick (through Eq. 3) and used to correct the baseline from the raw signal, as shown in Fig. 14. The residual signal from this difference was then considered for the reconstruction.

$$CO_{fit}(t) = A_0 + |A_1| \sin(2\pi f t + \phi_0) \quad (3)$$

The following parameters, shown in red in Eq. 3, are the free ones of the fit: A_0 is the measurement offset. A_1 is the

closed orbit amplitude, f is the horizontal frequency of the beam correlated to the horizontal betatron tune and ϕ_0 is the initial phase in the constant gating window around the kicker trigger. Systematic changes are observed in Fig. 15 where changes to the cycling of the machine during the long measurement campaign of many hours are evident and cannot be attributed to random errors. The signal recon-

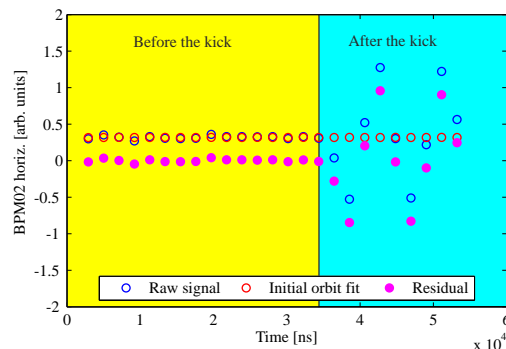


Figure 14: The BPM reading in time before and after the kick.

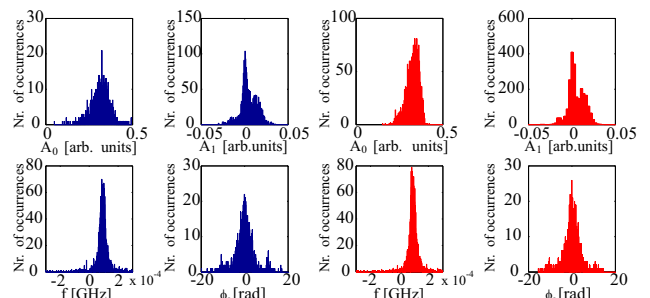


Figure 15: The distribution of the free fitting parameters for the measured occurrences in SC (blue) and TM (red).

struction, obtained by combining the occurrences, produces a waveform whose amplitude oscillates for nine times in the observation window at the horizontal betatron frequency of the machine, as shown in Fig. 16. The following analysis is

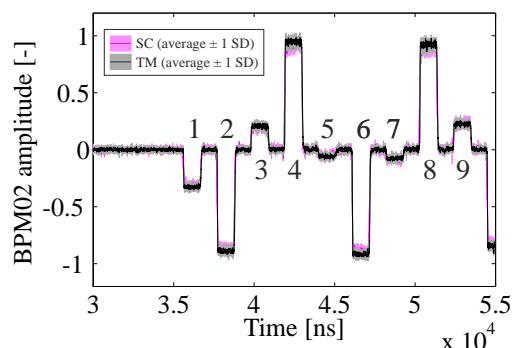


Figure 16: The numbered oscillations of the kicker waveform.

performed on the oscillation No. 2, as it presents the highest signal-to-noise ratio. The non-linearity of the BPM is being investigated, and the initial offset in the BPM before the kick appears to make oscillation No. 4 quite noisy.

Low-pass filtering and comparison with current measurements One can distinguish the measurements performed in TM and SC modes, as shown in Fig. 17. The signal has been low-pass filtered to smooth the measurement noise. Filtering was needed due to the poor granularity of the measurements. A moving average filter was applied with window sizes of 10 ns and 25 ns.

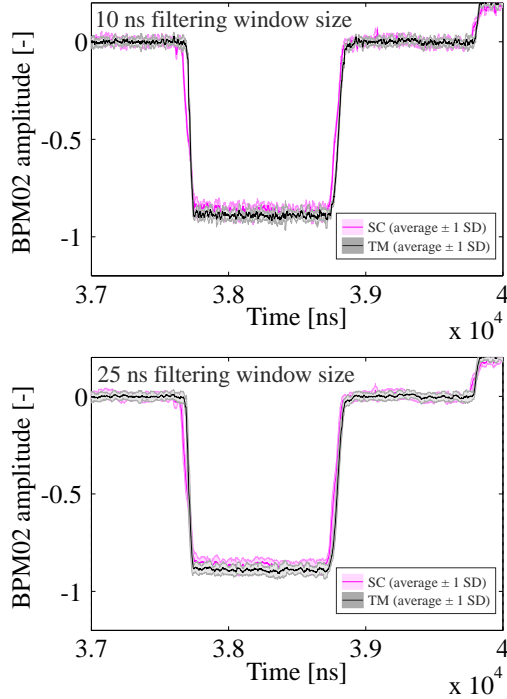


Figure 17: The (low-pass filtered) reconstructed waveforms.

Figure 18 shows the sum of the currents of modules 3 and 4, compared with the measured magnetic field waveforms.

The integrated magnetic field has a low-pass behaviour (both in SC and TM modes), not showing the ~ 20 MHz damped ripples shown in the current, related to the overshoot at the end of the rise time and to the reflection after ~ 600 ns of flat-top.

In SC mode the current rise and fall times are sharper than the measured magnetic field because of the the location of the current measurement point at the short circuit node downstream the magnet [11]. The rising and falling edges of the measured magnetic waveforms show an inflection: faster at the beginning of the rise and slower at the end. This phenomenon is related to the filling time of the magnet, which, in SC mode, is typically almost doubled due to the reflection of the current [11].

In TM mode, the excellent agreement between the current and beam-based magnetic measurements for both time constants confirms a good choice of the filtering.

Rise and fall times, flat-top ripple The evaluations of rise and falling times and flat-top ripple are shown in Fig. 19. 2-98% levels were computed with 25 ns time window filtering for TM, while, due to the more noisy data, a smaller interval, precisely 2.7-97.3%, has been considered for the SC. The values of rise and falling times correspond to the distances between two consecutive intersections at the bottom (top) and the top (bottom) edges of the waveform. The

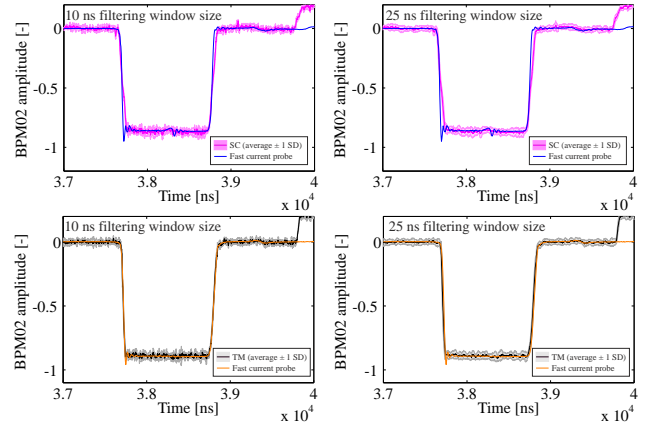


Figure 18: Reconstructed waveforms vs. currents.

values of flat-top ripple correspond to the maximum deflection, all along the flat-top, with respect to the flat-top average amplitude. Due to the filtering process and to the precision

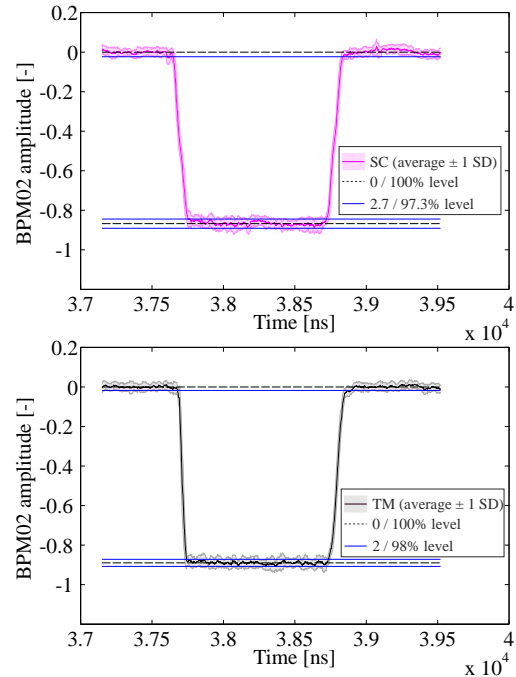


Figure 19: The rise and falling times evaluations.

level of the measurements, a ± 10 ns tolerance is considered on top of the reported values, as an educated guess. The results are summarised in Tab. 3.

Table 3: The rise and fall times and the flat-top ripple values for filter window sizes of 10 ns (and 25 ns in round brackets). Some values could not be determined (n.d.). *2.7-97.3% evaluation

KFA45 mode	Rise time [± 10 ns]		Fall time [± 10 ns]		Flat-top ripple (%)
	5-95%	2-98%	95-5%	98-2%	
SC	89 (92)	n.d. (104*)	93 (98)	n.d. (110*)	4.6 (2.7)
TM	46 (53)	n.d. (63)	96 (102)	n.d. (134)	3.3 (2.1)

Conclusions of the MD

An extensive MD campaign has been carried out to perform beam-based measurements of the magnetic waveform

of the PS injection kicker KFA45. These measurements were necessary to assess today's performance and that required by LIU in the future, and represent the only way to by LIU and present to date, the only way to probe the waveform of the magnet without moving other PS elements.

Measurements have been performed both in terminated (TM) and in short-circuit (SC) modes, which is the baseline configuration from 2017. The measurements in bunched mode showed rise times just consistent with specifications for SC mode. More measurements are, nevertheless, needed to investigate the flat-top ripple and improve precision. For this purpose, a new beam synchronous trigger will be used to improve the sampling. These new measurements will be performed in MD 2017, profiting from the hardware improvements [12].

MD1904: PSB-BT-BTP-PS DISPERSION MEASUREMENTS AND RE-MATCHING

One of the main priorities of the transfer between PSB and PS for the LIU project is to have a matched optics in order to preserve the brightness between the PSB extraction and PS injection. In particular, the dispersion mismatch at PS injection is important. Analytical calculations [13] show that the dispersion mismatch can cause for standard (long) LHC bunches an horizontal emittance blow-up up to 10 (30)% for LHC25 and 20 (65)% for BCMS beams. The betatron mismatch is up to 5%.

A matched optics from the 4 PSB rings is foreseen after LS2 with the installation of a new quadrupole in the BTP line: this will allow to obtain a negligible horizontal blow-up due to dispersion mismatch, while the vertical blow-up will be up to 15% for long BCMS bunches. In the future the betatron mismatch is supposed to be negligible.

The dispersion was measured in the PSB ring, in the extraction line and in the PS ring (1st turn).

As an example of in the PSB Ring 3, a dispersion measurement is shown in Fig. 20 (other measurements in the PSB rings can be found in [14]). The dispersion at the PSB horizontal wirescanner measurements showed a value of -1.38 m, i.e. 5% less than the operational value of -1.46 m. This is an important indication for measurements on beams like BCMS, where the dispersive component on the emittance is particularly relevant.

The dispersion in the extraction lines showed an excellent agreement with the model [16] for the PSB outer rings (1 and 4), while for the inner ones (2 and 3) a difference up to 0.5 m was present, as shown in Fig. 21.

Present measurements of emittance growth at PS injection [15] show more than 20% emittance growth for BCMS beams. A new optics was calculated using MadX [17] in order to reduce the dispersive mismatch at PS injection and disentangle the contribution of the horizontal dispersion on the emittance growth at PS injection from other possible causes (e.g. space charge). The re-matching was performed by using the quadrupoles in the BT line, as they can be changed for every PSB user in parallel operation. The strengths for the present and re-matched optics are represented in Tab. 4. The new optics was tried in operation at the 1st turn in the PS ring.

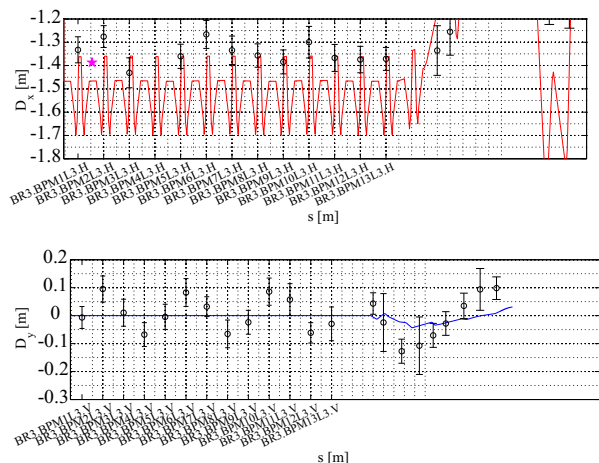


Figure 20: PSB Ring 3 dispersion in the horizontal (top) and vertical (bottom) planes (measurements - circle marker, model - solid lines). The measured horizontal wirescanner dispersion is represented by a magenta star on top.

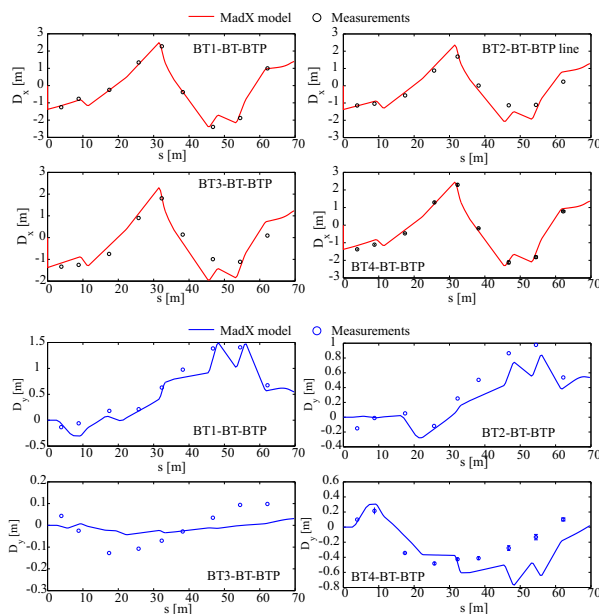


Figure 21: Dispersion in the BT i -BT-BTP lines (i represents the related PSB ring): measurements (circles) vs. MadX model (solid line) for the horizontal (top) and vertical (bottom) planes.

Conclusions of the MD

The PS first-turn horizontal dispersion was reduced from 5 m to ~ 2.5 m peak-to-peak, as shown in Fig. 22. This improvement, to date, did not affect the measured horizontal emittance at PS injection. Further efforts are on-going to better match the optics model of PSB-BT-BTP-PS with the measurements and validate its operational deployment for the 4 PSB rings, starting from ring 3.

MD1829 AND MD1893: TRANSFER OF LONG BUNCHES AND EMITTANCE EVALUATION

LHC "long" bunches (220 ns total bunch length, $(\delta v/v)_{rms} = 1.9 \times 10^{-3}$ and 3 eVs longitudinal emittance)

Table 4: Strengths of BT quadrupoles (operational and re-matched optics)

BT quadrupole	Operational strength [m ⁻²]	Scaling factor for re-matching
kBTQNO10	-0.66749	0.98
kBTQNO20	0.63160	1.02
kBTQNO30	-0.28709	0.94
kBTQNO40	0.92347	1.08
kBTQNO50	-0.73445	1.05

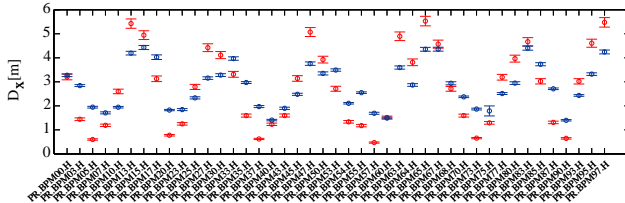


Figure 22: The measured horizontal dispersion (PS 1st turn from PSB ring 3) before (red) and after (blue) the correction.

were produced in the PSB and extracted to the PS [18]. The advantage of these bunches, with respect to the nominal 180 ns LHC bunches, is the increment of longitudinal emittance which leads to a 10% higher bunching factor at injection in the PS and, thus, a reduced transverse space charge tune spread.

The purpose of the MDs was to evaluate the transmission from PSB extraction to PS injection (MD1829) and the emittance growth at PS injection (MD1893).

The length of the bunches required a fine tuning of the recombination kickers fine delays, as the time margins were drastically reduced because of the new bunch lengths and same bunch spacings with respect to the 180 ns bunches [7].

The transmission, shown in Fig. 23, was optimised. Slow losses are still present along the flat-bottom, probably due to interaction with magnetic resonances.

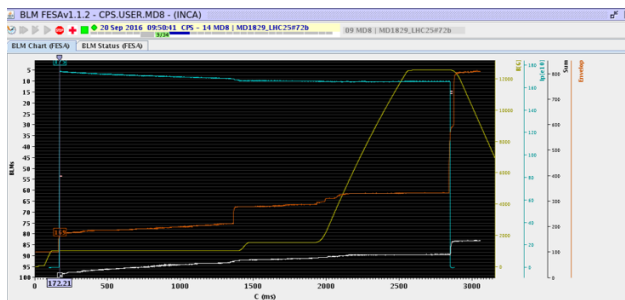


Figure 23: Single “long” bunch transmission in the PS.

The emittance evaluation was performed, in the horizontal plane, with the two wire scanners 65H and 54H. Unfortunately, probably due to the large momentum spread, the two instruments gave completely different values, as shown in Fig. 24. For this reason the topic needs further investigations in 2017.

During this MD, a peak line density increase was identified and correlated to a transverse space charge tune spread enhancement and consecutive vertical emittance growth during the transition from flat-bottom to intermediate flat-bottom (at around 1380 ms). Figure 25 shows the identified increase.

This finding was fundamental to improve the RF program and reduced the vertical emittance growth at flat-bottom of around 15% [15].

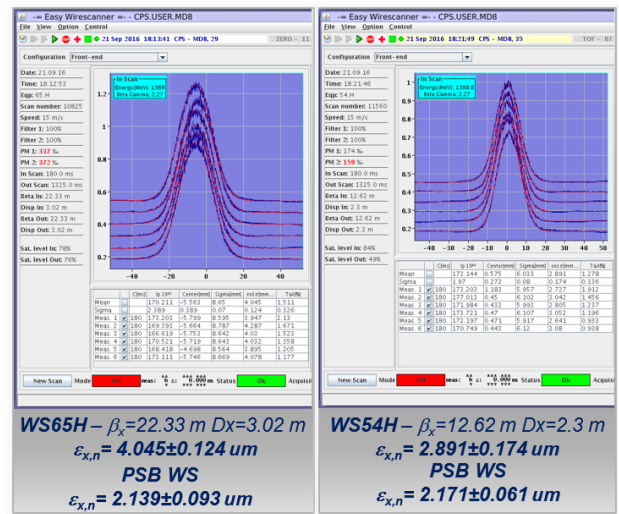


Figure 24: Different horizontal emittance evaluations from two PS wire scanners.

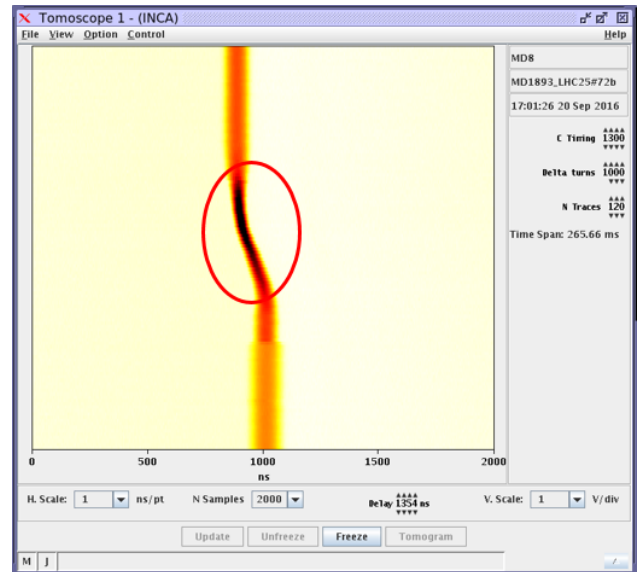


Figure 25: Longitudinal waterfall plot around the peak line density increase (in the red ellipse). Longitudinal density color-code: yellow - low particle density; black - high particle density.

Conclusions of the MD

The transfer of “long” bunches for LHC Standard production was performed successfully. Slow losses at PS flat-bottom energy have to be further investigated.

The emittance growth evaluation was stopped by the observation of different measurements from two horizontal PS wire scanners which also require further investigations.

A very important finding was the identification of the peak line density increase during the passage from flat-bottom to intermediate flat-bottom, which led to a 15% vertical emittance growth reduction for LHC beams.

MD1928: PS SEM-GRIDS AFTER INJECTION

The three SEM-grids in the PS sections 48, 52, 54 are named, respectively, PI.BSF48, PI.BSF52 and PI.BSF54. They are located after PS injection and represent important instruments in order to verify the LHC beams optics matching. These SEM-grids were unused for many years, so first purpose of the MD was their revival and functionality checks. A low intensity beam (LHCINDIV) was used.

The SEM-grids were used during a dedicated MD time. Parallel operation is not possible as they are moved by slow motors and need to work together with a device, called “ralentisseur”, which grants the single-passage of the beam, stopping it after it crosses the three SEM-grids. Multi-passage could, in fact, cause grid damage, especially for high intensity beams.

The SEM-grids have been verified and working. Dispersion measurements were performed. Further measurements will follow in 2017 in order to verify the transfer line with the 3-screens method [19].

MD1769: Automatic bunch alignment at PS injection

The 4 bunches coming from the PSB to the PS must be aligned in order to enter in the PS with the same trajectory. This process is usually performed by the operators in control room through the YASP program [20] and empirical approach.

An automatic tool developed by D. Gamba, called “linear feedback” [21], was adapted to try and align the 4 bunches to the beam dump in a semi-automatic way. The tool is capable of calculating on-line the response matrix and impose, in feedback, the right correction to the steerers in order to minimise the error in the alignment. The tool showed impressive potential, being capable of aligning the 4 bunches in the order of 0.5 mm. Further investigations switching the beam toward the PS are necessary in 2017.

MD1740: Septum SMH42 position and angle upgrade for LIU

This important MD was performed in order to verify if the new position and angle of the injection septum proposed to reduce injection losses of high intensity beams to the PS are feasible and do not disturb operation. The results were successful. More details are presented in [22].

CONCLUSIONS AND OUTLOOK

Many MD studies were carried out in 2016 for the beam transfer from the PSB to the PS, covering a wide amount of topics. The main ones concerned the PSB extraction at 160 MeV, the introduction of new methodologies for magnetic waveform measurements of kickers, dispersion measurement and re-matching between the PSB and the PS, transmission of long bunches and identification of a peak line density increase during the PS cycle, which was directly connected to a vertical emittance blow-up due to the transverse space charge tune shift enhancement.

Further investigations are planned for 2017. In particular:

- Improve re-matching of BT line optics (for Ring 3) in order to provide a matched optics and assess the impact of dispersion mismatch on emittance growth;

- evaluation of PS injection oscillations and injection bump non-closure with the aim to understand the shot-by-shot stability;
- quantification of the betatron mismatch at PS injection and analyse impact on emittance growth;
- repetition of KFA45 waveform measurements with the new hardware;
- improvement of the automatic steering technique to the PS;
- turn-by-turn SEM-grid measurements (when fast electronics is ready) in order to disentangle optics-related effects (faster) and space charge effects (slower) in emittance growth.

ACKNOWLEDGEMENTS

The authors would like to thank the PSB and PS OP teams for the important support.

REFERENCES

- [1] The LIU project: <https://espace.cern.ch/liu-project/default.aspx>
- [2] V. Forte *et al.*, Requirements and timeline for beam commissioning activities to operational beam, Linac4-PSB 160 MeV connection readiness review, 30/08/2016, <https://indico.cern.ch/event/548092/timetable>
- [3] W. Bartmann, PSB extraction at 160 MeV, LIU-PSB Meeting No. 56 (presented by B. Mikulec), <https://indico.cern.ch/event/160787>
- [4] F. Chapuis, “Booster Layout Drawings”, CERN EDMS: 492340
- [5] V. Forte, W. Bartmann, J.C.C.M. Borburgh, M.A. Fraser, L. Sermeus, “Beam-Based Kicker Waveform Measurements Using Long Bunches”, IPAC17 proceedings, Copenhagen, Denmark, MOPIK042
- [6] W. Bartmann *et al.*, “Specification for Kicker Systems For 2.0 GeV PSB to PS Beam Transfer”, CERN EDMS: PS-MKKIK-ES-0001
- [7] V. Forte, M. A. Fraser, W. Bartmann, J. Borburgh, L. Sermeus, “New beam-based and direct magnetic waveform measurements of the BTx.KFA10(20) vertical recombination kickers and induced emittance blow-up simulations at 1.4 and 2 GeV”, CERN-ATS-NOTE-2017
- [8] S. Deghaye *et al.*, “OASIS: A New System To Acquire And Display The Analog Signals For LHC”, Proceedings of ICALPCS2003
- [9] V. Forte, W. Bartmann, J.C.C.M. Borburgh, L.M.C. Feliciano, A. Ferrero Colomo, M.A. Fraser, T. Kramer, L. Sermeus, “Beam-Based Waveform Measurements of the CERN PS Injection Kicker”, IPAC17 proceedings, Copenhagen, Denmark, MOPIK043
- [10] J. Belleman, <http://jeroen.web.cern.ch/jeroen/tfpu/>
- [11] K.-D. Metzmacher, L. Sermeus, The PS Injection Kicker KFA45 Performance for LHC, PS/PO/Note 2002-015 (Tech.)
- [12] T. Kramer, Upgrade of the PS Injection Kicker KFA-45 for Operation with 2.0 GeV LIU Beams, CERN EDMS: PS-MKKFA-EC-0001 v.0.1

- [13] W. Bartmann, V. Forte, M.A. Fraser, "Emittance Growth at PS According to Model", CERN MSWG Meeting No. 15, 2016.
<https://indico.cern.ch/event/578789/>
- [14] G.P. Di Giovanni, V. Forte, G. Guidoboni, "Status of the PSB-to-PS transfer of long bunches preparation studies: BTM line SEM grid measurements", , CERN MSWG Meeting No. 15, 2016.
<https://indico.cern.ch/event/578789/>
- [15] H. Bartosik, "Emittance growth", CERN Injector MD Days 2017,
<https://indico.cern.ch/event/609486/>
- [16] PSB to PS optics:
<http://project-ps-optics.web.cern.ch/project-PS-optics/cps/TransLines/PSB-PS>
- [17] The MadX code: cern.ch/mad
- [18] S. Albright, "Longitudinal emittance blow up and production of future LHC beams", CERN Injector MD Days 2017,
<https://indico.cern.ch/event/609486/>
- [19] G. Arduini, M. Giovannozzi, D. Manglunki, M. Martini, "Measurement of the Optical Parameters of a Transfer Line Using Mutli-Profile Analysis", CERN PS (CA) 98-032 (1998).
- [20] The YASP steering program:
<https://jwenning.web.cern.ch/jwenning/documents/YASP/YAS1user-guide.pdf>
- [21] D. Gamba, F. Tecker, "Emittance Optimisation In The Drive Beam Recombination Complex at CTF3", Proceedings of IPAC14, Dresden, Germany, TUPRI080
- [22] M. Serluca, W. Bartmann, V. Forte, M. Fraser, G. Sterbini, "Injection Septa Position and Angle Optimisation in View of the 2 GeV LIU Upgrade of the CERN PS", *these proceedings*

PSB LLRF: NEW FEATURES FOR MACHINE STUDIES AND OPERATION IN THE PSB 2016 RUN

M. E. Angoletta[†], CERN, Geneva, Switzerland

Abstract

A new digital Low-Level RF (LLRF) system has been successfully deployed on the four PS Booster (PSB) rings in June 2014, after the Long-Shutdown 1 (LS1). Although only recently deployed, several new features for machine studies and operation have already been required and implemented. This note provides an overview of the main features deployed for the 2016 PSB run and of their results.

SYSTEM OVERVIEW

Introduction

A new digital PSB LLRF system has been successfully deployed in June 2014 in the four PSB Booster rings. The system represents the new standard foreseen for many machines in CERN's Meyrin site and it has already been deployed in CERN's Low Energy Ion Ring (LEIR) and Extra Low ENergy Antiproton Ring (ELENA) machines. It is also operational in the medical machine MedAustron [1].

Four separate LLRF systems control respectively PSB Rings 1 to 4. A fifth LLRF system, called "Ring 0" LLRF, allows to control the beam of the physical PSB Ring 4 in PPM with its operational LLRF system. The Ring 0 LLRF system is dedicated to machine studies and in particular it controls the Finemet-based High-Level RF (HLRF) system installed for test purposes in PSB Ring 0. To do this it includes additional hardware and software with respect to the operational rings.

Figure 1 shows the four operational LLRF systems for the PSB rings together with the "Ring 0" LLRF system.

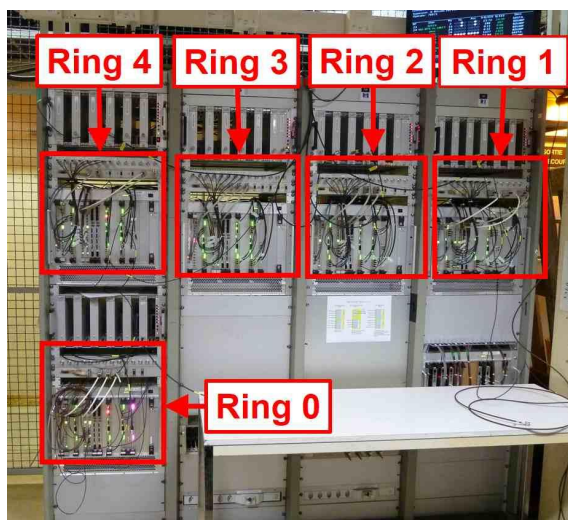


Figure 1: The PSB LLRF systems.

The total PSB downtime due to LLRF faults in the 39 week long 2016 run was of 34 minutes, thus proving the high reliability of the LLRF system and its positive impact on the machine operation. The system provides additional diagnostics as well as PPM controls with respect to previous PSB LLRF systems, in particular for the synchronisation at extraction process. Last but not least, the system is very powerful and flexible, and can be upgraded to new features often with a reasonable effort. More on this last point is detailed in the next section.

New Features

The PSB LLRF systems are under exploitation, fully operational and satisfied the current PSB operational needs. However, new features have been required in the past and are required to:

- Study and understand old problems. An example of this is the effect of the extraction bump on the synchronisation process, observed since 2008 in PSB Ring 4 by using a first generation LLRF system [2], at that time deployed operationally in LEIR.
- Implement new capabilities and allow studies for future beams/operational modes. An example of this are the features required for generating hollow bunches: this was done sporadically in the past but it was much more complex than with the new, powerful LLRF. Another example is the novel scheme of beam blowup at $h=1$ that will be studied within the framework of the PSB LIU project. Finally, interfacing with the new, white-rabbit based B-train distribution scheme will have to be validated.
- Validate implementations and prepare for the HLRF renovation which will take place after the injectors' Long Shutdown 2 (LS2). In particular, suitable schemes to control the Finemet voltage on several (10 or more) harmonics per HLRF system, to split the voltage at a certain harmonic amongst different cavities and to align these components over the PSB cycle will be devised and if possible partially validated. Furthermore, features required for future beams, such as the phase noise at harmonic $h = 1$, should be validated for Finemet operation, too. Finally, inputs for simulations will be provided, and simulation results will be validated against beam and system measurements.

As a summary, after LS2 the PSB will restart with substantial changes, such as: new HLRF, adapted LLRF, new B-train system, new injection scheme and new extraction energy. To have a smooth (or at least not too complex) restart after LS2, it is therefore essential to profit from the beam on the two last proton runs, in 2017 and in 2018, for schemes/approaches development and validation.

[†] maria.elena.angoletta@cern.ch

NEW FEATURES DEPLOYED IN THE 2016 RUN

This section details new PSB LLRF features partially commissioned or deployed in the 2016 run. They are the following:

- a) Improved extraction synchronisation process.
- b) Improved longitudinal beam blowup with the C16 HLRF system.
- c) B-train and frequency program studies.
- d) Operation with Linac4.
- e) Finemet operation.

Improved extraction synchronisation process

The synchronisation process is a very delicate and crucial RF gymnastic. Its aim is to modify the frequency and phase of the bunch(es) to be extracted in order to match an external reference, whose frequency and phase might vary during the extraction process itself. Jitters in the position of the extracted bunch(es) are present if the extraction synchronisation process does not perform well. If the process is too violent or fast, a beam carefully crafted with the RF gymnastics carried out during the cycle will be ruined.

The synchronisation algorithm implemented by the new PSB LLRF system has been from the very beginning much more performant than what was previously available. All control parameters such as gain, loop correctors transfer function, beating frequency etc. can be changed as PPM, thus allowing to adapt the extraction process to the beam characteristics. More diagnostics signals are available, such as the beam-to-extraction reference phase which has allowed to spot the effect of the extraction bump described below. These diagnostic signals are visible remotely on a standard Oasis Virtual Scope and can be saved for reference.

This section describes further improvements to the extraction synchronisation process carried out and deployed during the 2016 PSB run.

Optimised extraction synchronisation algorithm

The synchronisation process has been upgraded in November 2015 [3] to a new algorithm which minimises beam shaking and its potential blowup. The upgraded process was then deployed on all users in 2016.

Figure 2 shows the beam-to-extraction reference phase for the optimised (blue trace, Ring 4) and non-optimised (pink trace, Ring 3) algorithms, after reaching a beating relation.

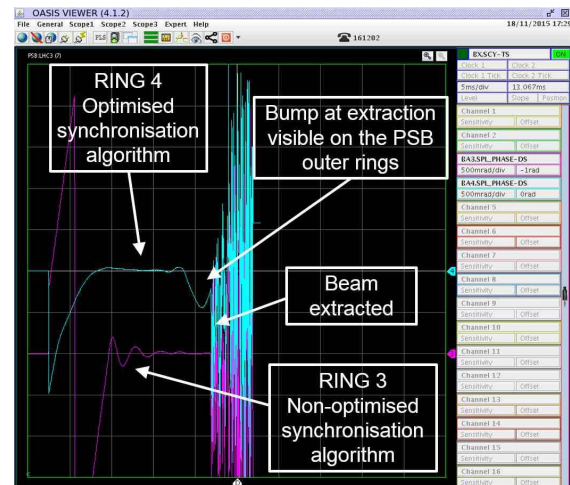


Figure 2: Beam-to-extraction reference phase signals during the extraction synchronisation phase loop. Violet trace: non-optimised algorithm in Ring 3. Blue trace: optimised algorithm in Ring 4. The perturbation on the Ring 4 phase signal is also visible.

Figure 3 shows the waterfall plot of the beam during the extraction synchronisation process, before (left picture) and after (right picture) the algorithm optimisation. The perturbation on the beam given by the non-optimised algorithm on the left hand-side is visible.

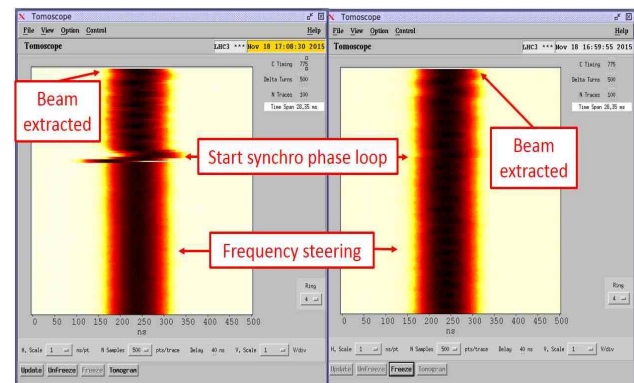


Figure 3: Waterfall plot of the beam during the extraction synchronisation process, before (left picture) and after (right picture) the algorithm optimisation.

Study of extraction bump effect on the synchronisation process

The measurement of beam-to-extraction reference phase showed a perturbation of the extraction process linked to the extraction bump fired during the last 5 ms of each cycle. The perturbation affected only the PSB outer rings. This bump was visible also in measurements carried out in 2008 with the prototype LLRF system on PSB Ring 4, as showed in Figure 4 and detailed elsewhere [2].

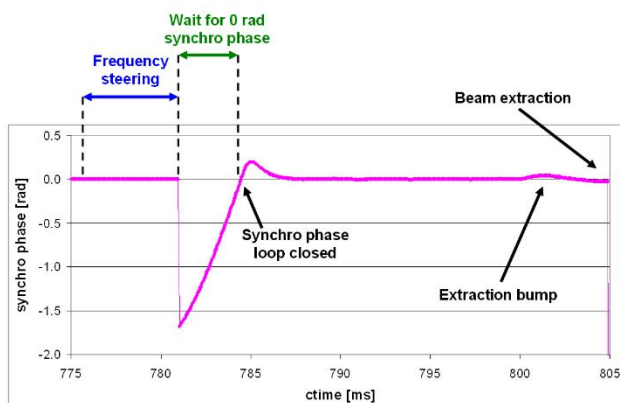


Figure 4: Plot of the beam-to-extraction reference signal phase measured in 2008 by the prototype LLRF system on PSB Ring 4 [2].

The improvements gained with the optimised algorithm described in the previous section were partially lost on the outer rings owing to the extraction bump-related perturbation. As shown in Figure 3, the perturbation shifted the beam radially; moreover, the amount of this shift varied from shot to shot, thus the beam was deposited at different radial positions at extraction.

Several debug features were then added to the LLRF in order to understand the source of the problem.

A measurement & logging of the beam-to-extraction reference phase synchro phase at a user-selectable time (snapshot feature) was deployed in April 2016 [4]. Figure 5 shows the operational knob used to enable the measurement, to decide its ctime and to read the measured phase.

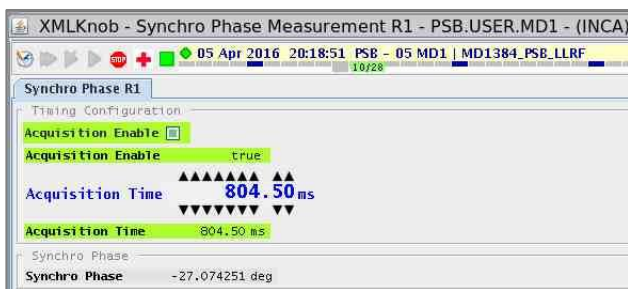


Figure 5: Operational knob allowing to measure and log the extraction reference-to-beam phase during the extraction synchronisation loop.

The capability to freeze the synchronisation loop operation or to end/freeze the phase & radial loops was also implemented [5].

The capability to use in PPM the LLRF input normally dedicated to the injection synchronisation reference for acquiring the signal from a second phase pick-up was deployed in March 2016. This feature was used later on in the year to operate the phase loop with the spare pick-ups located in sections 5L1 and 8L1, which are located far from the BSW. It was observed that the synchronisation response was not perturbed when these phase pick-ups. This prompted the installation of magnetic shielding plates in Ring 1 around the operational phase PU, which cured the

problem for that ring. The same shielding will be installed on the Ring4 phase pick-up during the 2017 run.

Improved longitudinal blowup by using the C16 HLRF system

Several improvements were devised, implemented and deployed in the 2016 PSB run.

First, a lack of phase lock between the C16 and the C02 HLRF drive signals was identified and a fix was deployed [6] in April 2016.

An improved version of the C16 blowup firmware was then deployed on all rings in June 2016 [7]. This not only definitely fixed the lock between the C16 and the C02 HLRF systems, but also insured a reproducible (although still harmonic-dependent) phase in the C16 HLRF system after the harmonic change ramp.

Finally, in September 2016 a new firmware was deployed in the Ring 0 LLRF system for tests and validation [8]. This included an automatic delay compensation after the harmonic change ramp, thus allowing changing the operational harmonics (as required for instance for the hollow-bunches operation) whilst obtaining the same phase at the end of the process. This firmware required a re-setup of the blowup parameters on all users and was not deployed on operational rings owing to the pressure to deliver the beams after the technical stop.

It should be underlined that most of the work invested on the C16 blowup improvement was addressed to cope with the C16 operational frequency range limitations, namely the need to change operational harmonics during the cycle. Whilst this is essential for the pre-LS2 operation, it will not profit the future (post-LS2) operation as the new Finemet-based HLRF system does not present the same frequency limitations.

B-train and frequency program studies

Two kinds of studies related to the B-train and to the generation of the frequency program have been carried out in 2016. More studies are planned for the 2017 run.

New transition method from fixed to B-train derived frequency

A new transition method from fixed injection frequency to B-train has been implemented in May 2016 [9]. The new algorithm, provided by S. Hancock, minimises the beam phase oscillations due to the transition, thus avoiding keeping an artificially high phase loop gain. Figure 6 shows the frequency program behaviour before (left picture) and after (right picture) the deployment of the new transition method. The phase loop contribution measured in Hertz is also shown for the two cases.

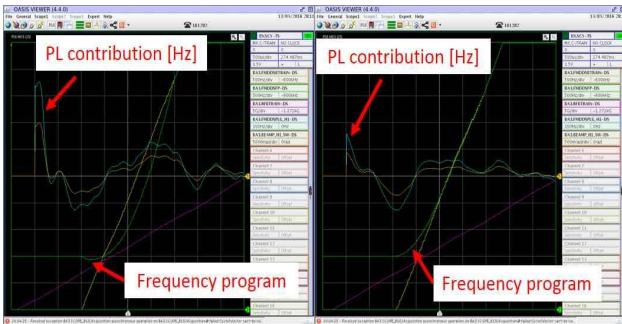


Figure 6: Transition from fixed injection frequency to B-train with the old (left picture) and with the new (right picture) transition methods. The contribution of the beam phase loop measured in Hz is also shown.

Programmable delay to simulate the effects of new B-train distribution scheme

After LS2 the B-train information will be generated and distributed digitally. This will present several advantages but will include an additional delay with respect to the current implementation. A programmable delay to the B-train value received by the LLRF was then added to evaluate the effect of this delay on the beam and how the LLRF would correct for it with its beam-related loops.

Initial tests [10] carried out in May 2016 have shown that the radial loop still manages to compensate for the incorrect frequency program generated from a strongly delayed B-train. Figure 7 shows the comparison in the radial loop contribution for an operational cycle and for a cycle where the B-train information is delayed by 100 μ s. The maximum contribution of the radial loop is increased by 450 Hz and no substantial beam losses were observed, although no specific observation on the longitudinal plane were done.

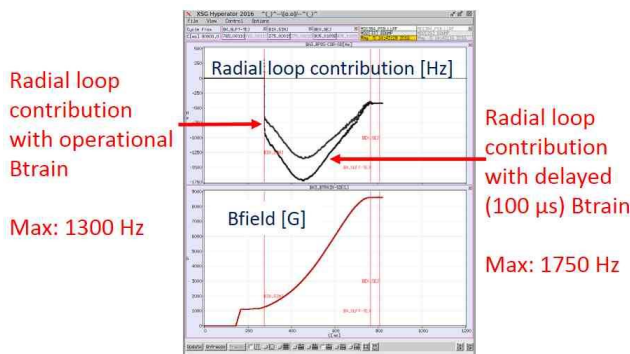


Figure 7: Upper window: radial loop contributions for operation with the operational B-train and with a B-train delayed by 100 μ s. Lower window: PSB measured magnetic field.

Operation with Linac4

Upgrades are needed in the PSB LLRF system to receive beam from Linac4. In particular, three tasks have to be deployed and commissioned. First, all rings must be synchronised in frequency and phase to an external injection reference shared with Linac4. Second, the RF interlock system must be commissioned with the PSB LLRF systems. Fi-

nally, the longitudinal painting scheme must be overall finalised, which represents a common effort of the ABP, OP and RF groups.

Good progress was made in 2016 on all these tasks, which are however not yet completed. The plan is to have the rings synchronisation commissioned and validated in 2017, as well as the RF interlock system operation with the LLRF. An application is needed to control the RF interlock system, and discussions on its specifications and development steps are under way.

Finemet operation

The month of September 2016 was devoted to restart the Finemet operation in view of the reliability run (6 to 29 September [11]). During this time the Ring 0 LLRF code was upgraded to the various improvements deployed on other rings in 2016. Once done that however the DSP code had to be optimised to allow a reliable operation with beam. In fact, the additional processing time required to deal with the fourth HLRF system (Finemet-based) in PSB Ring 4 was too long and did not allow to complete the synchronisation process.

An additional feature added in September 2016 to the Ring 0 LLRF system was the possibility to control in voltage and phase the third harmonic of the Finemet system [12], rather than simply servoing it to zero voltage to counteract the effects of the beam loading. This capability was required to contribute to future longitudinal painting and allows operation with harmonics $h=1+2+3$ [13].

PLANS FOR THE 2017 RUN

This sections gives an overview of the upgrades planned for the PSB LLRF in 2017. The new features should be deployed before the PSB spring startup if possible. Unfortunately, the PSB restart has been very demanding owing to several hardware- and cables-related problems originated by works around the rings, and in particular the switchboard installation. Figure 8 shows some of the hardware damages suffered by the PSB LLRF systems, which took a sizeable amount of time to be discovered.

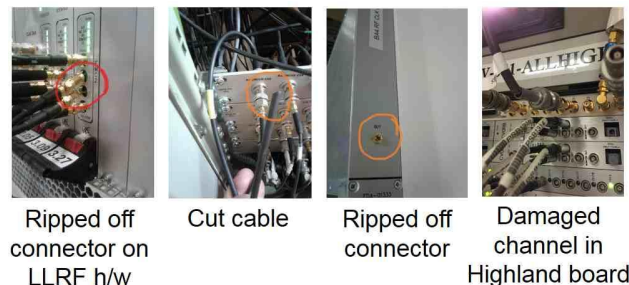


Figure 8: Some hardware damages collateral to the switchboard installation.

The main features to be deployed in the operational rings are the following:

- a) To deploy on all rings the firmware for improved beam blowup with the C16 HLRF system.
- b) To develop, deploy and commission the noise generation at the $h=1$ harmonic. This noise will be inserted in

the phase loop as well as in the C02 HLRF drive in order to study the replacement of the C16 blowup at a much lower frequency. An initial scheme will be deployed and additional improvements might be needed.

- c) To finalise and validate the tasks needed for injection from Linac4 and described by the “Operation with Linac4” section of this note.
- d) To prepare for tests with the White Rabbit-based distribution of the B-train values. If possible the tests will be carried out in late 2017. Upgrades of the firmware as well as of the DSP code and FESA classes are needed to acquire the B-train value from the new distribution medium. Comparison with the performance of the current B-train distribution scheme should be done, thus expanding the tests shown in the “Programmable delay to simulate the effects of new B-train distribution scheme” section of this document. The experience gained with the ELENA LLRF and machine, where the LLRF already received the B-train value via White Rabbit, will therefore be extremely useful.
- e) To upgrade a certain number of FESA classes to the FESA3 version.

The main features to be deployed in the Ring 0 LLRF are the following:

- a) To develop, deploy and commission the noise generation at the $h=1$ harmonic. This noise will be inserted in the phase loop as well as in the Finemet HLRF servoloop at $h=1$. Further improvements of this scheme might be needed, depending on the experimental results obtained.
- b) To upgrade the whole Ring 0 LLRF from the current sweeping to a fixed-frequency clock operation. This operational mode is already deployed in ELENA and will be the operational one for all CERN machines equipped with the same LLRF after LS2. From a beam performance viewpoint this upgrade will be transparent, i.e. it will bring no new capabilities apart from a better signal-to-noise ratio. It will be however an important step allowing the beam validation of existing features with the new scheme.
- c) To provide the “Beams and RF Studies” section of the RF group with data on LLRF and HLRF behaviours for studies. An example is the phase measurement of the Finemet HLRF when the LLRF servoloops are active.

CONCLUSION

The PSB LLRF systems are fully operational, provide a higher performance than ever before as well as a very high reliability. New features are however required for beam studies and to prepare for operating the future PSB HLRF and with injection from Linac4.

After LS2 the PSB will restart as a very different machine, equipped with a new, H- injection scheme, HLRF, LLRF, extraction energy, B-train system. Moreover, some key people in the LLRF, HLRF and studies sections will likely have retired by then.

It is therefore essential that we profit as much as possible from the beam before LS2 to validate new approaches and to define the future LLRF system.

ACKNOWLEDGEMENTS

The author wishes to acknowledge the whole RF team. Many thanks to:

A. Findlay, M. Jaussi, J. Molendijk, J. Sanchez-Quesada as members of the LLRF team;

S. Albright, S. Hancock, D. Quartullo as members of the beam studies team;

M. Haase, M. Paoluzzi as members of the HLRF team.

All these colleagues of mine were instrumental in the development of the features described in this note as well as for the results obtained.

REFERENCES

- [1] www.medastron.at/
- [2] M. E. Angoletta, A. Blas, A. Butterworth, A. Findlay, F. Pedersen, “PSB LLRF Renovation: Initial Beam Tests of the New Digital Beam Control System”, CERN-BE-Note-2009-021.
- [3] <http://elogbook.cern.ch/eLogbook/eLogbook.jsp?shiftId=1071156>
- [4] http://elogbook.cern.ch/eLogbook/event_viewer.jsp?eventId=2085991
- [5] http://elogbook.cern.ch/eLogbook/event_viewer.jsp?eventId=2091799
- [6] http://elogbook.cern.ch/eLogbook/event_viewer.jsp?eventId=2091396
- [7] <http://elogbook.cern.ch/eLogbook/eLogbook.jsp?shiftId=1075694>
- [8] http://elogbook.cern.ch/eLogbook/event_viewer.jsp?eventId=2171366
- [9] http://elogbook.cern.ch/eLogbook/event_viewer.jsp?eventId=2110775
- [10] http://elogbook.cern.ch/eLogbook/event_viewer.jsp?eventId=2106061
- [11] http://elogbook.cern.ch/eLogbook/event_viewer.jsp?eventId=2187100
- [12] http://elogbook.cern.ch/eLogbook/event_viewer.jsp?eventId=2187003
- [13] S. Albright, E. Benedetto, M. E. Angoletta, M. Paoluzzi, M. Jaussi, “RF Capture in a Triple Harmonic Bucket”, paper under preparation.

LONGITUDINAL EMITTANCE BLOW-UP AND PRODUCTION OF FUTURE LHC BEAMS

S. Albright, E. Shaposhnikova, D. Quartullo, CERN, Geneva, Switzerland

Abstract

During Long Shutdown 2 the RF systems of the PSB will be replaced with broadband Finemet systems, there will also be an energy increase and many other modifications. This note summarises studies that were done to investigate how to meet the emittance requirements for the LIU-PSB baseline and a possible use of the broadband cavities to improve the capture process.

The LIU-PSB baseline requires longitudinal emittance blow-up to 3 eVs with 205 ns bunch length at extraction. The current ferrite RF systems were used, with phase modulation of a high harmonic, to produce 2.8 eVs bunches with 220 ns bunch length, as this is the largest that can currently be transferred to the PS. Larger emittances were possible, demonstrating the ability to reach the LIU-PSB baseline in the future, which is confirmed in simulation.

The broadband impedance of the Finemet was exploited to allow RF voltage to be supplied on three harmonics ($h=1, h=2, h=3$), as opposed to the usual 2. For high intensity beams this lead to an improved capture efficiency for the same total voltage, and future studies are planned to demonstrate if there is an effect on extracted transverse emittance.

INTRODUCTION

This paper describes two sets of MDs, the first is dedicated to the production of high emittance bunches for the LIU-PSB [1] program, the second is an investigation into the use of three harmonics at capture to produce longer and flatter bunches than otherwise possible.

At current extraction kinetic energy of 1.4 GeV the longest bunch that can be delivered from the PSB to the PS is 220 ns. On the flat top with both C02 ($h=1$) and C04 ($h=2$) operating at 8 kV in bunch shortening mode this gives a longitudinal emittance of 2.8 eVs.

Losses early in the cycle are partially due to the large transverse tune spread at low energies. Since the transverse tune spread is proportional to the longitudinal line density it follows that a reduction in the line density will reduce the losses. The new HLRF Finemet systems that will be installed over LS2 allow the possibility to arbitrarily divide voltage across multiple harmonics, therefore allowing three harmonics to be used during capture, rather than two as used in current operations [2, 3].

2016 MDS

This section summarises the two MDs carried out during 2016, the first related to production of large emittance bunches, the second to demonstration of triple harmonic capture using the Finemet test cavity in ring 4.

Longitudinal Emittance Blowup

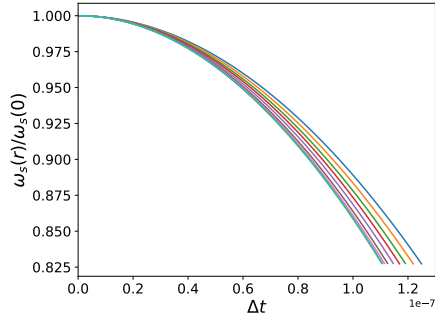
The objective of these MDs was to demonstrate the potential for a more optimised application of operational emittance blow-up to reach the LIU-PSB baseline of 2.8 eVs with nominal LHC intensities. Phase modulation of a high harmonic is used operationally in the PSB for either emittance blow-up, as in nominal LHC cycles, or longitudinal shaving, as in LHCINDIV type cycles. Phase modulation works by producing resonances between the high harmonic and the synchrotron motion of particles within the bunch. The induced resonances cause particles to move towards larger synchrotron amplitudes, therefore increasing the emittance of the bunch.

The ratio of synchrotron frequency distribution within the bunch (ω_s) and the modulation frequency of the high harmonic (Ω) determines the strength and position of resonances. Since there is no flat portion in the PSB cycle the emittance blowup is done on the fly, leading to a constant change in ω_s . Under these conditions relating the small amplitude synchrotron frequency (ω_{s0}) to Ω through a constant multiplier (M) is beneficial, and the condition $\Omega = M\omega_{s0}$ is imposed.

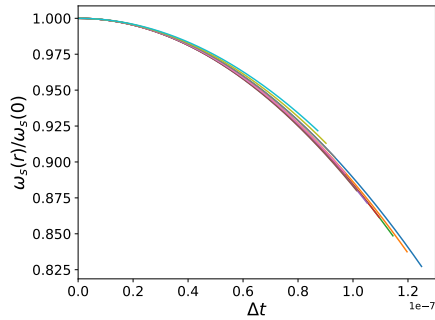
For a fixed voltage in the PSB the bucket area continually grows during acceleration, therefore the relative spread of synchrotron frequencies is reduced, as shown in figure 1a. Under these conditions the number of resonances for a given M will decrease during acceleration. For these MDs the constant voltage was replaced with a constant bucket area during emittance blowup. By applying a constant bucket area the relative spread $\frac{\omega_{s0}}{\omega_s}$ is maintained (figure 1b), therefore induced resonances will persist allowing more effective blowup.

Due to the presently available voltage in the machine the bucket area does not become sufficient to contain 2.8 eVs until near the end of the cycle. Therefore for these studies blowup was performed in three steps, with bucket areas set to 3 eVs, 4 eVs and 5 eVs, giving both time and sufficient acceptance for blowup.

Figure 2 shows the voltage functions used for the three RF systems (C02, C04 and C16) during emittance blowup and up to extraction. The 1st harmonic (C02) shows three sections where the voltage is reduced through time, these are the fixed bucket area sections. The 2nd harmonic (C04) is ramped down during blowup to remove the effect it has on ω_s , before being ramped up in bunch shortening mode for extraction. The high harmonic (C16) is maintained at a fixed multiple of the C02 voltage during blowup, before being ramped up afterwards to help improve filamentation of the bunch.



(a) Fixed voltage



(b) Fixed bucket area

Figure 1: Relative synchrotron frequency distribution ($\frac{\omega_s}{\omega_{s0}}$) with constant 8 kV vs constant bucket area during acceleration.

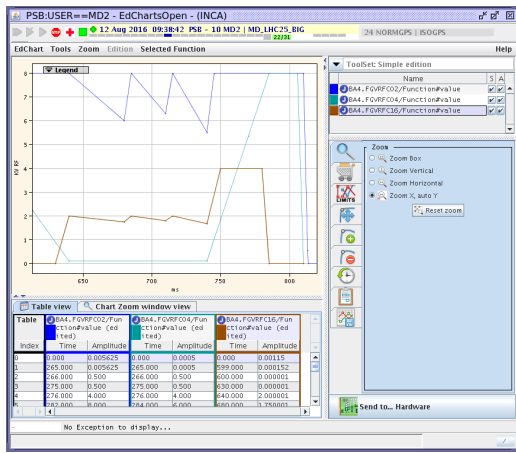


Figure 2: Voltage functions used for the three RF systems during and after longitudinal emittance blowup.

As all three fixed bucket area sections are independent from each other the modulation frequency and amplitude is different for all three. Due to the current LLRF operational conditions the optimum value of M in each section cannot be pre-calculated, instead an empirical scan was used to achieve desired effects.

The blowup was set up in each ring in a series of MDs, demonstrating the efficacy of the principle and the ability to achieve required similarity between the rings. Figure 3 shows the tomographic reconstruction of phase space prior

to extraction in ring 1. The other rings were similar in both appearance and numbers, however further work is needed to achieve uniform characteristics.

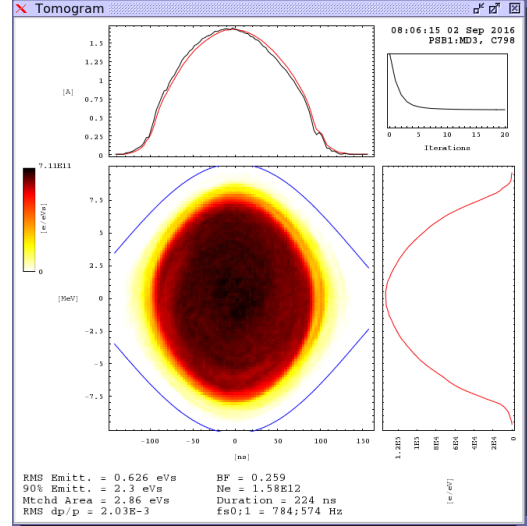
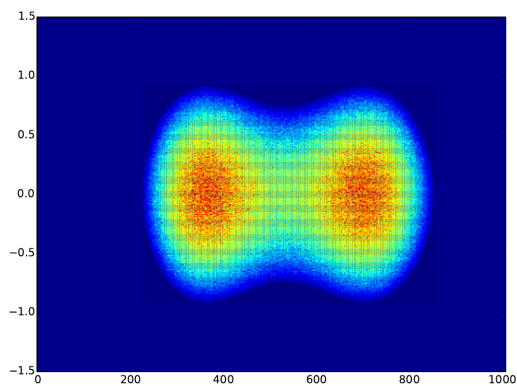


Figure 3: Phase space at extraction of the 2.8 eVs bunch in ring 1.

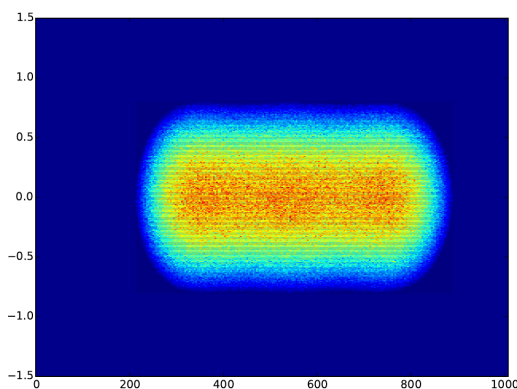
Triple Harmonic Capture

Due to a hardware fault the MD described in this section was limited to approximately 1 hour in length. However, it demonstrated the ability to use three harmonics during capture with minimal difficulty, and also showed that it may enable reduced losses in the early part of the PSB cycle. Large transverse space charge forces in the first tens of ms of the ramp lead to significant tune spreads, and correspondingly large losses. To reduce this effect the longitudinal line density can be reduced, increasing the bunching factor and decreasing the tune spread. For high intensity bunches the current operational condition is to use the 1st and 2nd harmonic in bunch lengthening mode, with 8 kV on both harmonics. The voltages and phases used provide maximum bucket area, and also reduce the line density of the beam. From simulations it was seen that maintaining the 16 kV total voltage, but including a third harmonic could reduce the line density by approximately 20% as shown in figure 4.

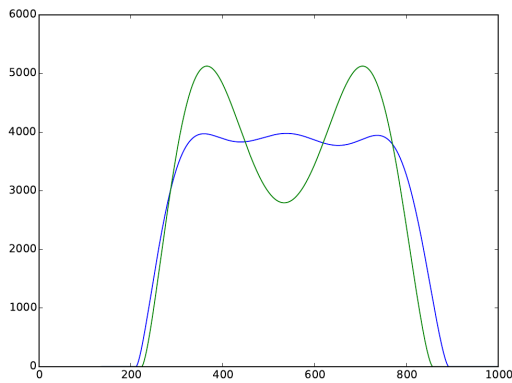
Using the ring 0 LLRF beam control, which controls the ring 4 HLRF systems, the beam was captured first with the standard 8 kV + 8 kV on C02 and C04, after which the Finemet system was enabled and the voltage was redistributed to 6.4 kV + 6.4 kV + 3.2 kV on C02, C04 and Finemet $h=3$ respectively. After carefully aligning the phases to give the standard profile with two harmonics and the flattest bunches possible with three harmonics the tomoscope waterfall plots shown in figure 5 were obtained. Figure 5a shows the standard double peaked structure associated with a phase space distribution like that in figure 4a, whereas figure 5b shows a significantly flatter profile, as would be caused by the distribution in figure 4b.



(a) Double harmonic



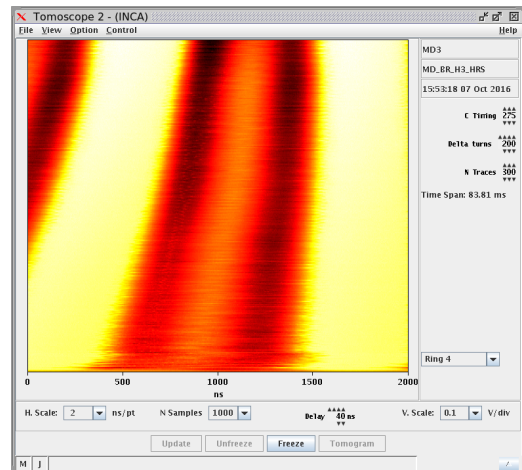
(b) Triple harmonic



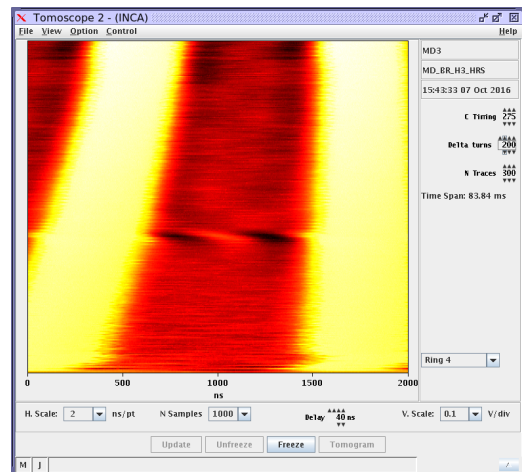
(c) Line densities

Figure 4: Simulated phase space with two harmonics, three harmonics, and corresponding line densities.

After setting up the voltages and phases correctly in each case the BCT traces for a series of shots were recorded. Figure 6 shows the recorded intensities with two (red) and three (blue) harmonics. As can be seen the use of three harmonics enabled reliably higher intensities with approximately 10% difference on average. Whilst the difference here is small it should be stressed that approximately one hour of beam time was used, and further improvements are expected to be possible.



(a) Double harmonic



(b) Triple harmonic

Figure 5: Waterfall plots of capture and the early part of the cycle with 2 and 3 harmonics.

PLANS FOR 2017

Both the longitudinal emittance blow-up and triple harmonic studies discussed have significant room for further research. This section discusses some of the work that is intended to be carried out during the 2017 run.

Longitudinal Emittance Blowup

In most current operational cycles blow-up is performed with voltage on both $h=1$ and $h=2$, as well as the high harmonic, with $h=2$ in bunch lengthening mode. The disadvantage of using $h=2$ in bunch lengthening mode is that both ω_s and ω_{s0} are extremely sensitive to small changes in relative phase. However, if bunch shortening mode is used the sensitivity is greatly reduced, and is concentrated at large synchrotron amplitudes. Repeating the 2016 studies but with $h=2$ in bunch shortening mode is therefore planned for 2017, it is hoped that this will allow blowup to happen faster than with only $h=1$.

An alternative to phase modulation of a high harmonic is to use phase noise. Band limited white noise injected onto

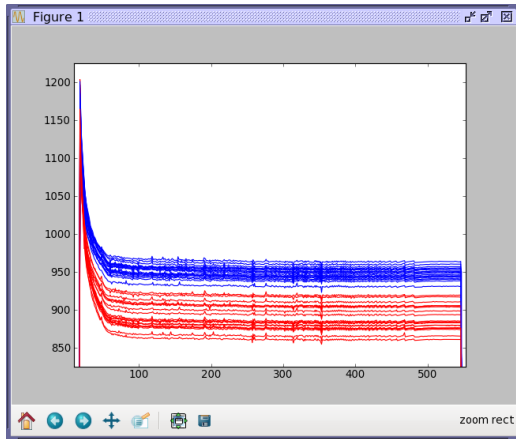


Figure 6: Recorded BCT traces for capture with two harmonics (red) and three harmonics (blue).

the main harmonic is currently used in both the SPS and LHC for emittance blowup to great effect [4]. The hardware capability exists to do this in the PSB, but it has not yet been tested. Simulations show that it should be effective after LS2, but machine measurements are needed for validation [5].

Triple Harmonic Capture

As a continuation of the first validation of triple harmonic capture further studies are intended to quantify the effect on the tune spread in two ways. First the transverse emittance can be measured at the end of the cycle, since the emittance growth appears to be driven by space charge effects lower values are expected. Alternatively the working point can be moved towards resonances that are known to be damaging, it would be expected that incoherent losses will be reduced with triple harmonics compared to double harmonics as the footprint should be smaller.

These tests should be performed with a variety of combinations of voltages on the three harmonics. Equal bucket area and equal total voltage between $V_{h1} = V_{h2}$, $V_{h1} = 2V_{h2}$ and $V_{h1} = V_{h2} = 2V_{h3}$, which will allow comparison between the standard double lobed structure used in operation now, a flat double harmonic profile and the flattened triple harmonic profile.

CONCLUSION

Two sets of MDs from 2016 have been discussed. Longitudinal emittance blowup studies have demonstrated an optimisation of operational norms, which demonstrated the ability to reach the LIU-PSB baseline for the first time. The blow-up was applied in all four rings to confirm efficacy and reproducibility, and whilst improvements are still possible the system was shown to be effective. Secondly the use of three harmonics, rather than the standard two, during capture and early in the cycle was shown. Using three harmonics allows longer and flatter bunches than otherwise possible, and it was shown that this can give better transmission than otherwise possible.

ACKNOWLEDGEMENTS

The authors would like to thank A. Findlay, M. E. Angoletta, M. M. Paoluzzi and M. Haase and all those involved with PSB operation, without whom this work could not have happened.

REFERENCES

- [1] LHC Injectors Upgrade TDR-Volume 1: Protons Chapter 3, Editors: J. Coupard et al, *CERN-ACC-2014-0337*
- [2] Design of the PSB Wideband RF System, M. M. Paoluzzi, *CERN-ACC-NOTE-2013-0030*
- [3] Control and Operation of a Wideband RF System in CERN's PS Booster, M. E. Angoletta et al, *IPAC2017 THPAB141*
- [4] Studies on Controlled RF Noise for the LHC, H. Timko et al, *HB2014, THO4LR03*
- [5] Controlled Longitudinal emittance Blow-Up Using Band-Limited Phase Noise in CERN PSB, D. Quartullo et al, *IPAC2017, THPVA024*

HOLLOW BUNCHES PRODUCTION

S. Hancock, A. Oeftiger

Abstract

Hollow bunches address the issue of high-brightness beams suffering from transverse emittance growth in a strong space charge regime. During the Proton Synchrotron (PS) injection plateau, the negative space charge tune shift can push the beam onto the $Q_y = 6$ integer resonance. Modifying the longitudinal bunch profile in order to reduce the peak line charge density alleviates the detrimental impact of space charge. To this end we first produce longitudinally hollow phase space distributions in the PS Booster by exciting a parametric resonance with the phase loop feedback system. These inherently flat bunches are then transferred to the PS, where the beam becomes less prone to the emittance growth caused by the integer resonance.

During the late 2016 machine development sessions in the PS Booster we profited from solved issues from 2015 and managed to reliably extract hollow bunches of 1.3 eV s matched longitudinal area. Furthermore, first results to create hollow bunches with larger longitudinal emittances towards the LHC Injector Upgrade project goals proved successful. Here, we present the ingredients to the established hollow bunch procedure, showing the few involved changes to the PS Booster cycle for nominal LHC beam production. We also discuss challenges related to the competing phase loop and radial loop feedback systems: their mutual responses can effectively inhibit the excitation of the parametric resonance which should deplete the core of the initially parabolic bunches.

INTRODUCTION

The impact of transverse space charge can be mitigated by flattening the usually parabolic longitudinal bunch profile. Consequently, the peak beam self-field around the longitudinal peak line density decreases. The direct space charge tune spread for bunched beams can thus be reduced, which helps to find good machine tunes minimising the interaction with betatron resonances. The latter can result in transverse emittance growth as well as beam losses, which is detrimental to beam quality. The most common approach to achieve a flat bunch profile is to use a second RF system in bunch lengthening mode.

In view of the LHC Injectors Upgrade (LIU), the intensity of the nominal Large Hadron Collider (LHC) beams is to be increased twice while keeping the same transverse emittances [1]. These high-brightness beams are expected to encounter a strong space charge regime during the Proton Synchrotron (PS) injection plateau. Transverse space charge inflicts a negative tune shift on the beam, which in the case of the PS can shift the beam into the vertical integer betatron resonance stop-band $Q_y = 6$. At the same time, the PS structure resonance $8Q_y = 50$ puts an upper limit to the bare machine tune in this tune diagram quadrant: peri-

odic trapping of halo particles [2] leads to intolerable beam losses [3]. Thus, the machine tune should remain slightly below $Q_y = 6.25$ while emittance growth due to the integer stop-band needs to be minimised. Hollow Bunches provide a solution to this problem by shrinking the overall space charge tune spread at PS injection.

This paper summarises the current status of MDs 210 and 211. Section I explains the theoretical considerations behind hollow bunches. In section II we outline the 2015 proof of concept experiments: (i.) production of $\epsilon_{z,100\%} \approx 1.3$ eV s hollow bunches in the PS Booster with a minimalistic set of changes to the presently operational nominal LHC beam production scheme and (ii.) first experimental quantification of the improved emittance preservation in the PS. Section III then reports on the 2016 advances on the study with improved reproducibility of the delivered hollow bunches in terms of longitudinal parameters, since some machine issues found in 2015 have been resolved in the meantime. First results to produce larger hollow bunches towards the $\epsilon_{z,100\%} = 3$ eV s LIU goal are reviewed. Section IV finally discusses the necessary ingredients to reach this goal, in particular how to avoid beam-induced voltage in the high frequency RF cavities as well as the mutual response of the radial and phase loop feedback systems which may affect the longitudinal parametric resonance excitation to create hollow bunches.

I. THEORETICAL CONSIDERATIONS

The transverse incoherent space charge tune spread along a transversely Gaussian distributed bunch reads

$$\Delta Q_u^{\text{SC}}(z) = -\frac{r_p \hat{\lambda}(z)}{2\pi \beta^2 \gamma^3} \oint ds \frac{\beta_u(s)}{\sigma_u(s) (\sigma_x(s) + \sigma_y(s))} \quad (1)$$

with $u = x$ for the horizontal and $u = y$ for the vertical plane. z denotes the longitudinal position with respect to the RF bucket centre, r_p the classic proton radius, q the elementary charge, $\hat{\lambda}(z)$ the line density in m^{-1} , β the beam speed in units of c , γ the relativistic Lorentz factor, s the position around the accelerator, $\beta_{x,y}(s)$ the local betatron functions, and $\sigma_{x,y}(s)$ the local transverse root mean square (RMS) beam sizes. In presence of dispersion $D_x(s) \neq 0$, the momentum distribution contributes to the horizontal beam size,

$$\sigma_x = \sqrt{\beta_x \epsilon_x / (\beta \gamma) + D_x^2 \delta_{\text{RMS}}^2} \quad , \quad (2)$$

where $\epsilon_{x,y}$ denotes the normalised transverse RMS emittances and $\delta_{\text{RMS}} \doteq \langle (p - p_0) / p_0 \rangle$ the RMS momentum deviation.

Since $\Delta Q_{x,y}^{\text{SC}} \propto 1/(\beta \gamma^2)$, it is foreseen to step up the PS injection energy from $E_{\text{kin}} = 1.4$ GeV to 2 GeV as the major measure to mitigate space charge. The total bunch length B ,

already exploits the time window given by the rise time of the PS Booster recombination kicker magnet and cannot be further increased to reduce $\hat{\lambda}_{\max}$. Bunch reshaping is hence a good option to support the raise in injection energy to decrease $\Delta Q_{x,y}^{\text{SC}}$ while fixing $\epsilon_{x,y}$, B_L and intensity N . This is where the concept of hollow bunches comes in, offering a few advantages over usual double-harmonic flattening:

1. By producing an inherently flat longitudinal phase space distribution upstream in the PS Booster, the PS can profit directly starting from injection instead of first having to adiabatically ramp up the double harmonic in bunch lengthening mode. Double-harmonic shaped bunches can in principle also be transferred directly. However, this requires precise relative phase alignments of the additional RF systems in both PS Booster and PS to avoid longitudinal mismatch. In contrast, hollow bunches can be transferred in a single-harmonic RF bucket between the machines without further adaptation.
2. The unused second harmonic voltage is available for bunch shortening instead which hence allows for larger longitudinal emittances at the same B_L . NB: the LIU goal is to reach a matched 100 % emittance of $\epsilon_{z,100\%} = 3 \text{ eV s}$ (the present LHC beams feature 1.3 eV s at PS injection).
3. In addition to reducing $\hat{\lambda}_{\max}$, hollow bunches feature a larger momentum spread δ_{RMS} . Due to Eq. (2) the horizontal beam size enlarges which provides another knob to reduce $\Delta Q_{x,y}^{\text{SC}}$.

Starting from 2015, MD 210 has set up hollow bunch production in the PS Booster and MD 211 has demonstrated the subsequent benefit in terms of transverse emittance preservation throughout the PS injection plateau. The present approach to create hollow phase space distributions goes back to an idea of Ref. [4]. The idea is to deliberately excite a longitudinal *dipolar parametric resonance*. For this purpose the phase loop feedback system can be used, which aligns the RF reference phase ϕ_{RF} with the longitudinal centre-of-gravity of the bunch. The dipole mode of the longitudinal parametric resonance can be excited by phase modulation [5]. The initially parabolic bunch has its centre depleted as the core particles are excited to higher synchrotron amplitudes during a few synchrotron periods. We modulate the phase loop offset around the synchronous phase ϕ_s :

$$\phi_{\text{RF}}(t) = \phi_s + \hat{\phi}_{\text{drive}} \sin(2\pi f_{\text{drive}} t) \quad . \quad (3)$$

To excite the beam core, the driving frequency needs to satisfy the resonance condition

$$mf_{\text{drive}} \approx nf_{s,0} \quad (4)$$

with $f_{s,0}$ denoting the linear synchrotron frequency. In reality, longitudinal space charge will reduce the RF phase focusing below transition. The synchrotron motion in the

RF bucket centre slows down correspondingly, which translates to lower resonant driving frequencies around $f_{\text{drive}} \lesssim 0.95f_{s,0}$ in our case. The integer numbers m and n characterise the $m : n$ parametric resonance, where for us $m = 1, n = 1$ proves to be most useful as only a single filament is excited. This bunchlet wraps around the emptied centre and would filament for a too long time before it effectively forms a smooth ring in phase space, given the time to extraction. The filamentation process can be enhanced by smoothing by high frequency phase modulation to achieve a stationary distribution within the PS Booster cycle, which features the aforementioned lower $\hat{\lambda}_{\max}$ and larger δ_{RMS} . In contrast to many other hollow bunch creation techniques (cf. chapter 5 in Ref. [6] for an overview), our approach can be implemented during the acceleration ramp rendering it a versatile tool to mitigate the impact of transverse space charge.

II. PROOF OF CONCEPT IN 2015

Production of Hollow Bunches

In August 2015, the radial loop feedback system has been used in a first attempt to drive a dipolar longitudinal parametric resonance [7]. The new digital low-level RF (LLRF) system of the PS Booster allowed to program a sinusoidal offset vector in the radial feedback. At this point the phase loop steering system only supported a fixed register value for the phase offset, i.e. exciting the resonance directly with the phase loop was not yet feasible. Nonetheless, one may control the longitudinal phase indirectly via the radial position: in order for the radial loop to steer the radial beam position, the feedback corrects the RF frequency programme. Non-adiabatic changes of the RF frequency affect the beam phase. Therefore, a sinusoidal radial steering at about the synchrotron frequency translates to a sinusoidal phase steering. We used this mechanism to excite the dipolar longitudinal parametric resonance as the waterfall plot in Fig. 1 shows. The bunch centre indeed depleted within a few synchrotron periods, hence demonstrating the conceptual feasibility of producing hollow phase space distributions in this manner.

However, the indirect approach via the radial loop proved to be rather ineffective: the phase loop acted against the excitation and limited the finally reached full longitudinal emittances (the ‘‘matched area’’ in tomoscope terms). For further details on the experiment results with the radial loop we refer the interested reader to Ref. [7]. The close link of radial and phase loop feedback systems and their mutually damping effect should play a role again at a later stage in 2016, as explained below and in section IV.

Later, the phase loop control system was extended to support offset vectors as well. This enabled us to directly program a sinusoidal beam phase steering in order to excite the resonance. In October and November 2015, a procedure was established to create hollow bunches via the dipolar resonance in the PS Booster [6, appendix A]. The goal was to involve a minimalistic set of changes to the conventional LHC nominal beam production scheme in the PS Booster

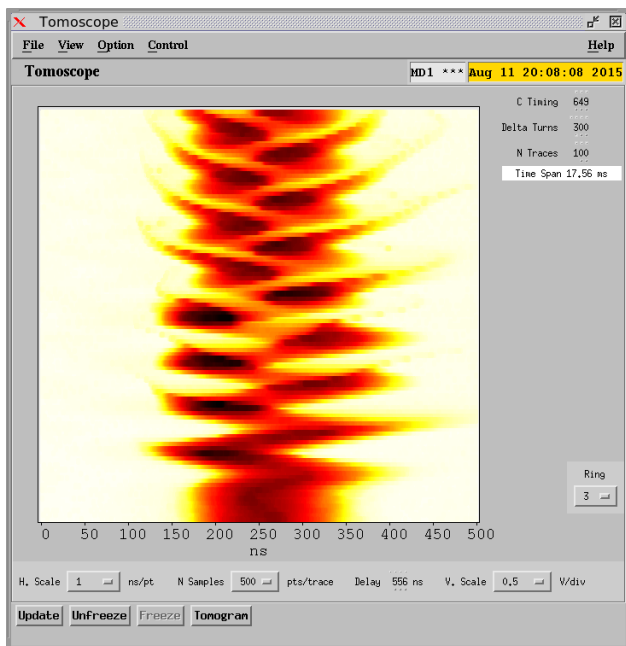


Figure 1: Waterfall view showing the profile evolution of an excited longitudinal phase space distribution. Turns increase towards the top and the colour range from black via red to white indicates decreasing line charge density. The initially parabolic profile in the lower part is excited during four synchrotron periods and then begins to filament in the upper half of the plot (to eventually become a hollow bunch).

in order to ease possible operational implementation. The following changes enabled a continuous delivery of hollow bunches to the PS:

1. adiabatic powering down of the second harmonic RF system C04 to provide single-harmonic parabolic bunches at c-time C575 (the double-harmonic RF bucket is required to reduce transverse space charge impact during the first part of the PS Booster cycle);
2. sinusoidal beam phase steering during 6 synchrotron periods (i.e. 9 ms) to excite bunch core particles to higher synchrotron amplitudes during the dipolar parametric resonance, thus depleting the RF bucket centre;
3. low phase loop gain during the resonance excitation and high gain afterwards; and
4. two further subsequent phases of high frequency phase modulation with the C16 RF systems at $h = 9$ in order to smooth the filamenting phase space distribution.

In contrast to the previous experiment with the radial loop, the phase loop approach provided highly reproducible results at a fixed time instant directly after the parametric resonance. Consecutive shots exhibited the same filamenting phase space distribution at c-time C591. Furthermore, the measured tomograms closely resembled simulations for the exact same time span including the resonance excitation and subsequent filamentation [8, Fig. 3d vs. Fig. 5b].

However, the outcome of the smoothing process varied on a shot-to-shot basis due to the fluctuating effectiveness of the high frequency C16 RF systems (problem 1). Later, during 2016 it has been found that the initial phase of the C16 wave has been randomly distributed for subsequent pulses [9–11]. Varying this initial phase changes the resonance conditions for the phase modulation [12]. Thus, the extracted hollow bunches in 2015 had fluctuating longitudinal parameters in terms of the matched 100 % emittance as well as the RMS emittance (as the finally achieved thickness of the hollow phase space ring varied).

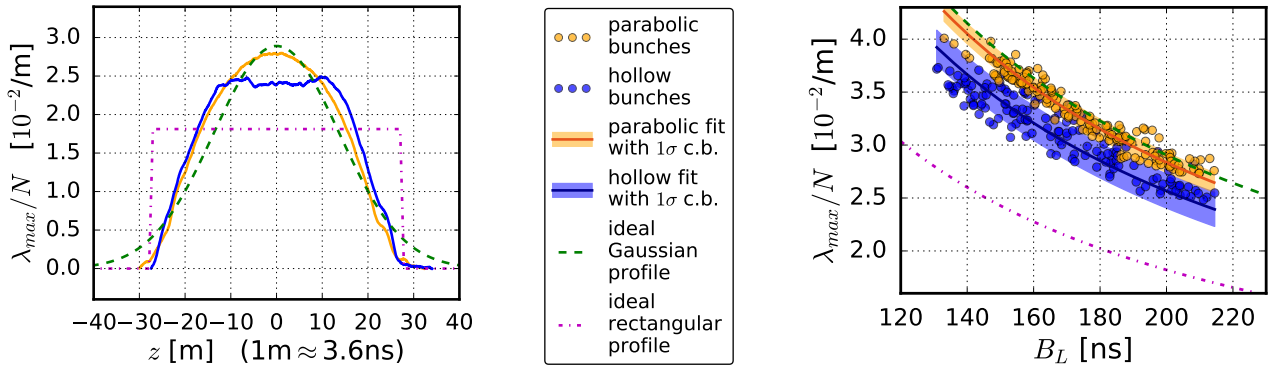
Moreover, hollow bunches proved to be more sensitive to the extraction synchronisation loop action. The synchronisation loop settings (including its gain) at the time have had quite a strong impact on the beam (problem 2). In particular, the sudden RF phase synchronisation disrupted the longitudinal phase space distribution: the centre-of-gravity was relocated, which is much more visible in a hollow distribution than compared to a usual parabolic distribution (although both are affected in the same way). Consequently the filamenting phase space density in the bucket centre increased resulting in non-flat-topped bunch shapes. Weaker synchronisation loop gain (as a first remedy) and a lower phase loop gain improved the situation in 2015 for the time being.

Space Charge Mitigation

Towards the end of beam time in 2015 we injected into the PS hollow bunches created as described above with moderately stable longitudinal parameters. The goal of the experiment was to assess how much hollow bunches improve the transmitted beam quality through the 1.2 s long PS injection plateau of the nominal LHC beam production scheme. We compared the transverse emittance growth of standard parabolic bunches to hollow bunches for given injected $\epsilon_{x,y}$, N and B_L . The results have been thoroughly discussed in Ref. [6, chapter 5] and presented in Refs. [8, 13]. Here we shall briefly outline relevant outcomes of the experiment.

Two measured examples of these bunch shapes are presented in Fig. 2a. A Gaussian and a rectangular bunch profile are plotted as ideal upper and lower limits of the peak line density. A rectangular profile of $4\sigma_z$ length correspondingly allows for a factor $\sqrt{2\pi}/4 \approx 0.63$ smaller $\hat{\lambda}_{\max}$ than the Gaussian profile. NB: a rectangular profile is an extreme case which can only be implemented in a double-harmonic bucket in bunch lengthening mode. In a single-harmonic bucket geometry one necessarily ends up with a finitely inclined flank of the profile. Here, the goal is to receive single-harmonic bunches in the PS, which is why the effective lower limit in the peak line density lies above the rectangular factor 0.63.

In order to vary the space charge strength, we compressed the injected bunches to bunch lengths between $130 \text{ ns} \leq B_L \leq 220 \text{ ns}$. Fig. 2b plots the measured peak line densities of the prepared parabolic and hollow bunches. The 1σ confidence band of the hyperbolic fit of the hollow bunch peak line densities is about twice as wide as in the parabolic case, which comes from the shot-to-shot fluctuating efficiency of



(a) Bunch shape comparison for equal B_L : measured examples and ideal limit cases.

(b) Measured peak line densities over total bunch length (with 1σ confidence bands and limit cases).

Figure 2: Comparison between peak line densities of parabolic and hollow bunches.

the high frequency phase modulation (cf. problem 1). The fits indicate 10 % lower peak line densities for the flat-topped bunches compared to the parabolic ones.

The essential goal is to compare the impact of space charge for both beam types. The vertical space charge detuning is stronger due to the smaller beam size (as $D_y = 0$ while the transverse emittances are the same), which explains why the vertical (and not the horizontal) integer resonance stop-band is the limiting factor. In order to assess the expected improvement of the eventually transmitted transverse emittances, we can refer to the maximal tune spread via Eq. (1) which unifies the initial B_L , N and $\epsilon_{x,y}$ in one quantity. B_L remained constant during the injection plateau and there were only marginal losses (constant N) but $\epsilon_{x,y}$ would grow due to the integer stop-band. To evaluate the reference Gaussian tune spread $\Delta Q_y^{\text{SC}}|_{\text{max,Gauss}}$, we fixed a peak line density of

$$\hat{\lambda}_{\text{max}} = \frac{N}{\sqrt{2\pi}B_L/4} \quad . \quad (5)$$

In reality, the direct space charge tune spread of the hollow bunches is around $0.88 \Delta Q_y^{\text{SC}}|_{\text{max,Gauss}}$ due to the larger momentum spread δ_{RMS} and the lower peak line density λ_{max} . On the contrary, the parabolic bunches are represented quite well by the Gaussian formula with a factor 0.97 lower real tune spread. The Gaussian tune spread therefore serves as a reference to evaluate how much transmission improves by using hollow bunches instead of parabolic bunches.

The measured final vertical emittances at the end of the injection plateau are presented in Fig. 3 along with empirical fits and their 1σ confidence bands. We concluded that for the same injected intensity, transverse emittances and (compressed) bunch length, hollow bunches indeed lead to lower final vertical emittances than parabolic bunches. Thus, hollow bunches provide a viable means to mitigate bunch core emittance growth coming from the integer resonance stop-band.

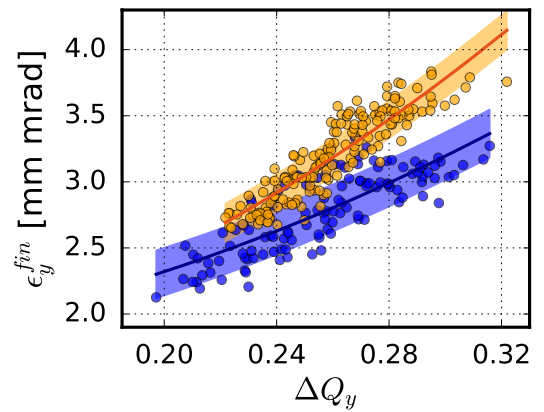


Figure 3: Transmitted vertical emittance at the end of the injection plateau over reference Gaussian space charge tune spread via Eqs. (1), (5) (for the legend cf. Fig. 2).

III. RELIABLE PRODUCTION IN 2016

During the first half of 2016, problem 1 and 2 as described in section II have been solved by the RF team:

1. The phase of the C16 RF systems can be reset to the same value at the start of each pulse (even for changing harmonics, this has been implemented with a new firmware upgrade on June 7), which renders the high frequency phase modulation reproducible.
2. The extraction synchronisation loop (in particular the phase synchronisation) has been optimised to avoid disruption of the longitudinal phase distribution.

This enabled us to reliably extract well-defined longitudinal parameters from the PS Booster: implementing the settings of the previous year stably produced hollow bunches at $\epsilon_{z,100\%} = 1.3 \text{ eV s}$ equivalent to nominal LHC-type beams.

In the following subsection we list the exact changes to the operational LHC1A cycle (at the end of 2016) to obtain these hollow bunches. We continue using ring 3 (implementing

HOLLOW BUNCHES PRODUCTION

the concept on all four rings should be straightforward). In a next step we present the $\epsilon_{z,100\%} = 2 \text{ eV s}$ approach.

Optimal Settings for $\epsilon_{z,100\%} = 1.3 \text{ eV s}$

The last beam modification during nominal LHC beam production in the PS Booster cycle is the longitudinal blow-up at c-time C500 by high frequency phase modulation. To this end, the C16 RF systems pulse during 50 ms at a voltage of $V_{C16} = 1.3 \text{ kV}$ at harmonic $h = 9$. The phase modulation uses $\hat{\phi} = 180^\circ$ modulation depth. Furthermore, the modulation frequency follows the decreasing linear synchrotron frequency by $1.75f_{s,0}$ (taking into account only the fundamental voltage of the C02 RF systems).

The starting point for the hollowing is again a single-harmonic RF bucket, i.e., after the longitudinal blow-up at c-time C550 we adiabatically ramp down the C04 RF systems to 0.5 kV during 20 ms. The fundamental C02 RF systems remain at 8 kV throughout the cycle. The initial longitudinal phase space distribution should exhibit as large a central black patch of constant phase space density as possible in the tomogram at c-time C573 directly before the parametric resonance (cf. Fig. 5a). This ensures a well-defined ring in longitudinal phase space afterwards, making the flanks of the flat-topped bunch profile as steep as possible. The above blow-up settings yield a parabolic bunch of $\epsilon_{z,100\%} = 1.1 \text{ eV s}$. At c-time C575, when the resonance excitation starts, the available RF bucket area is 1.8 eV s.

The ingredients to turn the parabolic bunch into a hollow one comprise [14]:

- phase loop gain at 0.4 throughout the cycle;
- 6 synchrotron periods of phase loop excitation starting at c-time C575 and ending 8.7 ms later (cf. Fig. 4) with
 - modulation depth of around $\hat{\phi}_{\text{drive}} \approx 17^\circ$,
 - modulation frequency of $f_{\text{drive}} = 690 \text{ Hz}$,
 - phase loop gain of 0.2 during the excitation; and
- smoothing of the filament with a second 50 ms long C16 pulse of high frequency modulation at c-time C600 with
 - voltage of 1 kV,
 - modulation depth of $\hat{\phi} = 180^\circ$, and
 - modulation frequency of $0.65f_{s,0}$ ($1.35f_{s,0}$ also works).

Fig. 5 presents tomographic reconstructions of the longitudinal phase space at important points during the cycle. The lower right sub-plot (obtained with the “specialist” tomography setting) shows the synchrotron amplitude projection for the phase space distribution in Figs. 5b and 5c. Towards the bucket centre, the phase space density clearly decreases. Especially for the non-stationary filament in Fig. 5b, the synchrotron amplitude projection provides a good tool to optimise for the resulting hollow bunches at the end of the cycle. The final bunch profile in Fig. 5c should feature steep

flanks and a steady flat top. The thickness of the excited filament and the minimal amount of particles left in the bucket centre have to be carefully adjusted to obtain an optimal bunch shape.

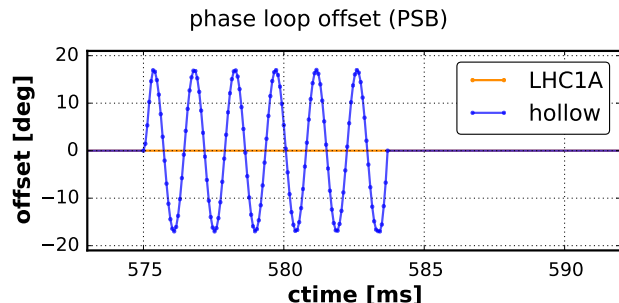


Figure 4: 6 synchrotron periods of phase modulation.

The third smoothing C16 pulse (at C700) from the 2015 set-up is not needed any more, as the blow-up works more reliably now due to the fixed initial relative phase of the C16 to C02. In general we found that, the more concise and well-defined the smoothing, the less the resulting longitudinal parameters seem to fluctuate. Fig. 5d shows an example of a hollow bunch with $\epsilon_{z,100\%} = 1.3 \text{ eV s}$ at c-time C795 10 ms before extraction [15].

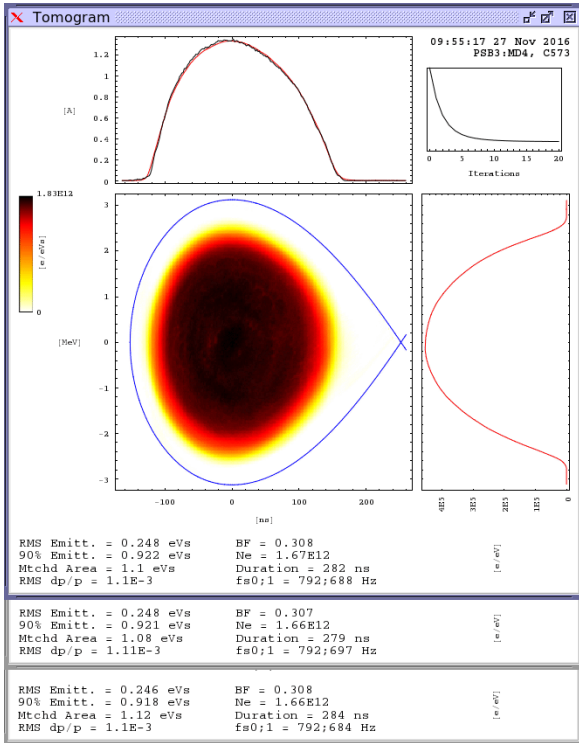
Settings for $\epsilon_{z,100\%} = 2 \text{ eV s}$

The energy acceptance $(\Delta E/E_0)_{\text{max}}$ in an accelerating single-harmonic RF bucket is given by [16, Eq. (65)]:

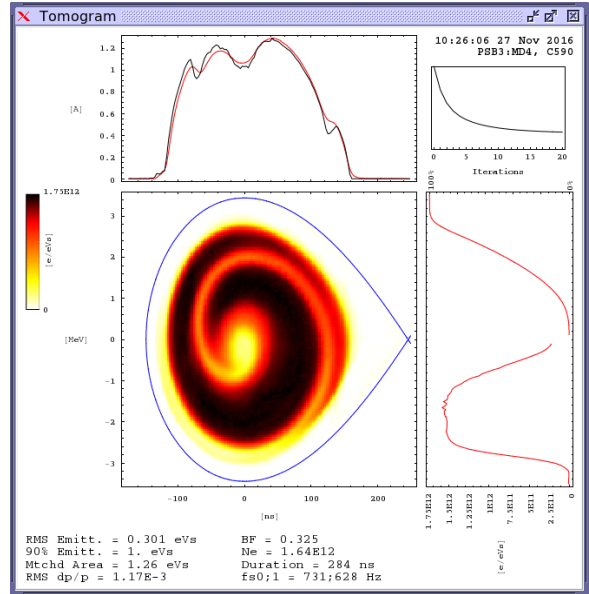
$$\left(\frac{\Delta E}{E_0}\right)_{\text{max}} = \pm \beta \sqrt{-\frac{eV}{\pi h \eta E_0}} \times \sqrt{2 \cos(\phi_s) + (2\phi_s - \pi) \sin(\phi_s)}, \quad (6)$$

where $\eta = \gamma_t^{-2} - \gamma^{-2}$ denotes the slippage factor with the transition energy γ_t and $E_0 = \gamma m_p c^2$ the total beam energy. For a fixed synchronous phase ϕ_s , the energy acceptance hence monotonically increases on the interval $1 \leq \gamma < \gamma_t$. This entails that the RF bucket area grows towards the end of the PS Booster cycle while, at the same time, the already blown-up longitudinal emittance remains constant. Therefore, the larger available RF bucket area at later c-times offers more space for the dipolar parametric resonance to excite the filament to larger synchrotron amplitudes. The achieved hollow bunches after smoothing should thus reach larger longitudinal emittances if the excitation is shifted towards the end of the PS Booster cycle.

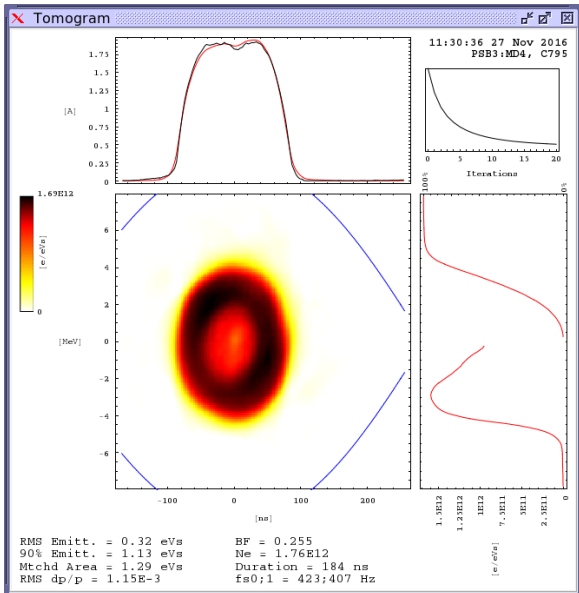
The parametric resonance should be followed by 50 ms of high frequency modulation for smoothing. The latter should finish before the radial loop may move the beam from the fixed radial position at 0 mm to the final -2 mm during some 20 ms before the synchronisation loop sets in. The first step of the synchronisation loop, the frequency steering, starts at c-time C775. Just as a remark, the second step is the phase alignment to the PS, which happens 7 ms to 10 ms after the revolution frequency of the PS Booster has been adapted to



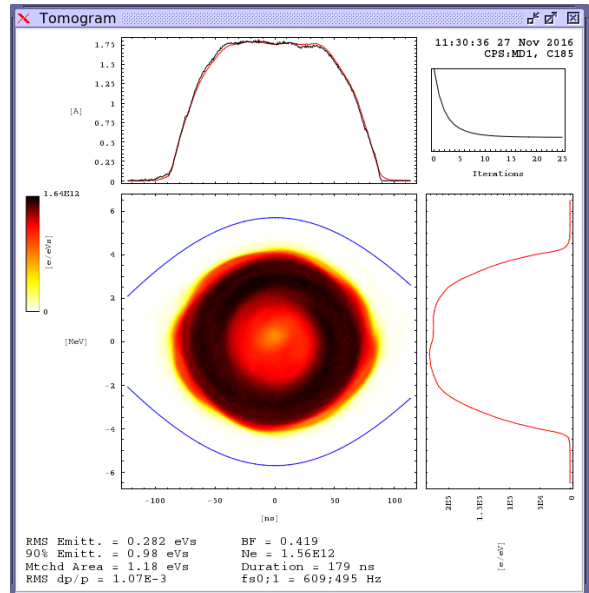
(a) The initial parabolic phase space distribution in a single-harmonic RF bucket at C573.



(b) The filamenting phase space distribution at C590 after 6 synchrotron periods of parametric resonance excitation.



(c) The smoothed final hollow phase space distribution at C795 after subsequent C16 pulses (10 ms to extraction).



(d) The received hollow bunch in the PS at C185 (15 ms after injection).

Figure 5: Snapshots of the longitudinal phase space distribution during creation of hollow bunches with the 2016 set-up.

the PS. Subtracting the 20 ms radial steering and the 50 ms C16 pulse from c-time C775 hence requires the parametric resonance excitation to finish at the latest at c-time C705. To extract larger longitudinal emittance, we also need to set up the second harmonic in bunch shortening mode at the end of the cycle in order to avoid beam loss of too long bunches interfering with the recombination kicker rise time window.

Following the same set-up (canonical blow-up, single-harmonic RF bucket) as for the excitation starting at c-time C575, we have achieved first good results starting at C675: the synchrotron frequency in the single-harmonic RF bucket with $V_{h=1} = 8$ kV amounts to $f_0 = 504$ Hz at this point. It is crucial to remove the interference of the radial loop feedback system (see section IV) to avoid complete suppression of the dipolar resonance excitation. A scan to determine the window of resonant frequencies f_{drive} reveals sharp edges (clearly defined to 1 Hz [17]):

$$408 \text{ Hz} < f_{\text{drive}} < 440 \text{ Hz} \quad . \quad (7)$$

Promising and reproducible first results from the excitation at this late point of the cycle have been achieved with $f_{\text{drive}} = 420$ Hz, $\hat{\phi}_{\text{drive}} = 45$ deg and 5 synchrotron periods duration (i.e. 12 ms) [18]. At the end of the 2016 run we were hence in a position to produce excited filaments at 0.5 eV s RMS longitudinal emittance (twice the nominal LHC beam-type value), while the matched 100 % longitudinal emittance reached 2 eV s. Fig. 6 demonstrates an example tomogram with the reconstructed longitudinal phase space. The effective blow-up due to the hollowing from the initial 1.1 eV s to 2 eV s is a step towards the LIU goal of injecting 3 eV s bunches into the PS.

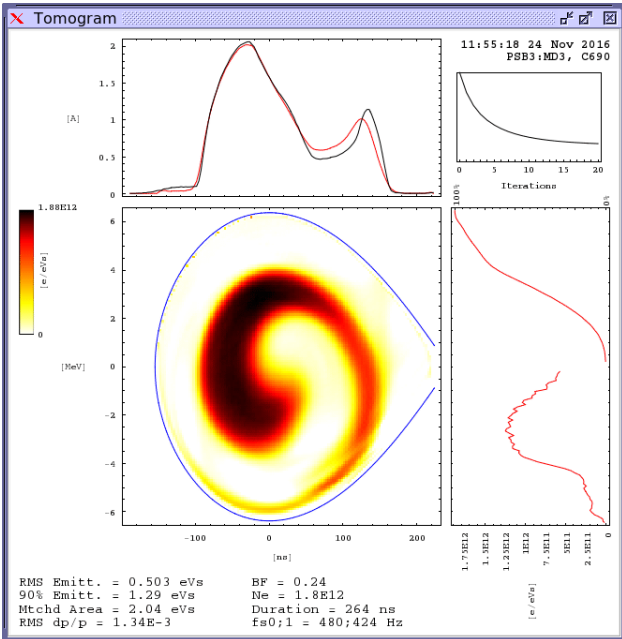


Figure 6: Longitudinal phase space after late resonance excitation starting at C675, showing a large excited filament (matched 100 % emittance of 2 eV s).

IV. LESSONS LEARNED

C16 Induced Voltage and its Harmonic Setting

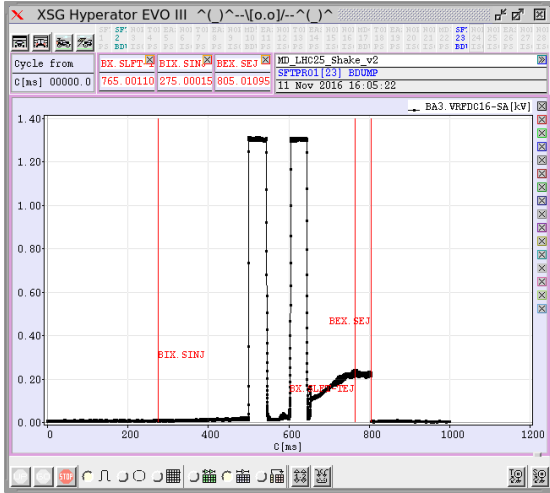
The C16 RF systems are used to smooth the excited bunch filament in a second pulse (the first one provides the canonical longitudinal blow-up for LHC beam production). It is important to control the high frequency modulation well in order to obtain well-defined longitudinal bunch parameters (RMS and 100 % emittances as well as momentum spread). We have noted a significant impact on reproducibility if the C16 cavities are left in a resonant state from the first blow-up onwards, i.e. when the programmed harmonic is an integer of the revolution frequency (which is the presently employed setting in operation). Fig. 7a shows the measured beam induced voltage in the C16 RF systems rising up to some 0.2 kV after the second pulse when the harmonic is left on $h = 9$.

Tuning the C16 to some non-integer multiple of the revolution frequency makes the cavities transparent to the beam. Unwanted further resonance effects distorting the longitudinal distribution can thus be suppressed. The higher the non-integer harmonic, the better the suppression seems to work. However, the C16 high frequency RF systems naturally have an upper limit: we find significant induced voltage by the beam passage when the frequency programme exceeds a certain frequency at around 17 MHz when programming $h = 10.5$. We achieved the best results at $h = 9.5$ in between the two first C16 pulses and again after the second one as shown in Figs. 7b and 7c.

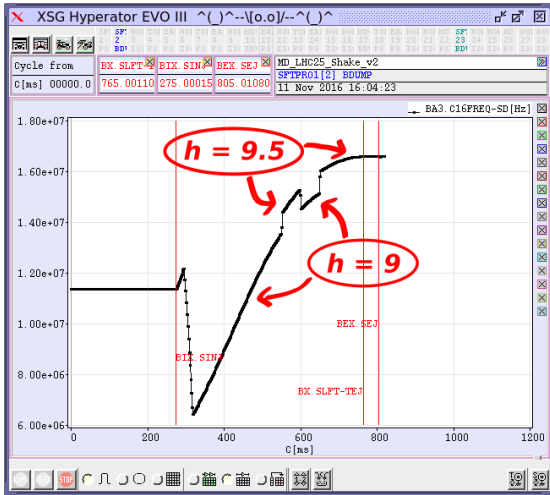
Cross-dependency of Radial and Phase Loop Feedback

The action-reaction coupling between the phase loop and radial loop feedback systems becomes more and more pronounced towards the end of the cycle. While the damping reaction of the radial loop to the excitation of the parametric resonance is present but limited around c-time C575, it effectively inhibits the resonance driving at later c-times around C675. The excitation works fine if we switch off the radial loop altogether, however, switching it back on afterwards may result in beam losses.

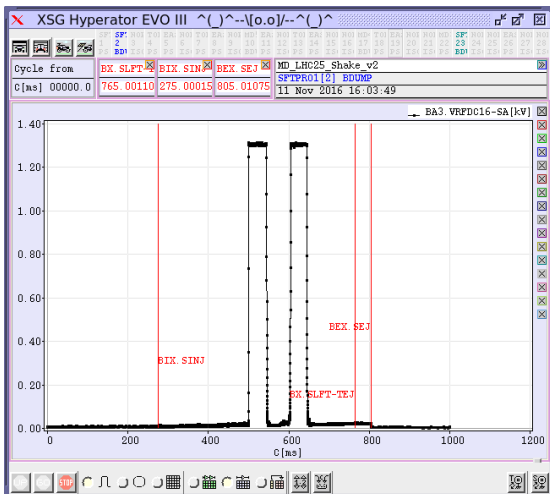
Simply reducing the radial loop gain directly (up to 2 orders of magnitude) unfortunately did not suffice to avoid the damping. Instead, we found that the radial loop biquad corrector has a strong influence on the immediate reaction of the radial loop. By reducing the biquad corrector gain (from the previous setting of 2.2 to 0.15), the coupling between the two feedback systems could finally be significantly reduced. Together with a half of the radial loop gain (1.5 instead of the canonical 3), this eventually enabled the excitation of the parametric resonance to deplete the phase space distribution [18]. At the same time, the radial loop steering behaved much smoother with less fluctuations across the entire cycle than before, which suggests that the radial loop in the canonical setting for LHC beam production acts overly strong.



(a) Measured C16 voltage while remaining on $h = 9$ after second smoothing pulse, clear sign of induced voltage after C650.



(b) Frequency programme avoiding induced voltage by setting a non-resonant $h = 9.5$ after C650.



(c) Measured C16 voltage without induced voltage after C650.

Figure 7: How to minimise induced voltage in the high frequency RF system.

Fig. 8 shows the feedback loops’ final steering on the scope for the optimal gain settings found to produce the large emittance hollow bunches (cf. Fig. 6).

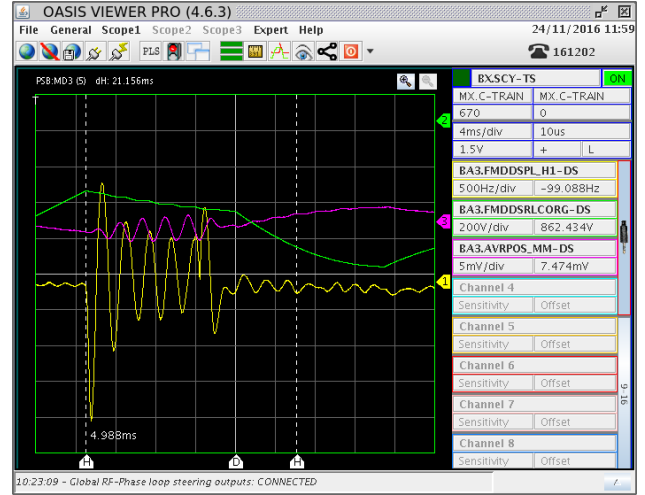


Figure 8: The final steering inputs for the phase loop (yellow) and the radial loop (green) along with the measured radial beam position (magenta) during the parametric resonance excitation around c-time C675.

The yellow curve for the phase loop clearly exhibits the 5 synchrotron periods long sinusoidal offset to drive the parametric resonance. At the sudden end of the excitation, the phase loop’s own feedback input makes it recapture the oscillating bunch, resulting in the last 180° shifted oscillation before it fluctuates around the programmed default phase offset of zero. The magenta curve marks the measured radial position of the beam, which shows the sinusoidal radial offset due to the RF frequency change caused by the phase loop steering. Note the 90° shift between the radial position and the phase loop curves: the phase loop provides the external driving and we expect the actual bunch phase to be shifted by 90° in case of resonant beam reaction to the driving frequency. This translates to the radial position oscillation in phase with the longitudinal bunch centre-of-gravity. The green curve represents the radial loop steering with negligible reaction to the phase loop’s oscillating steering. Our weak corrector gain settings indeed work as the radial loop does not inhibit the excitation process any more.

CONCLUSION

During MD 210, hollow bunches have been successfully produced in the PS Booster by means of exciting a longitudinal dipolar parametric resonance with the aid of the phase loop feedback system. We have presented the minimalistic set of changes to the LHC1A cycle for nominal LHC beam production which allows to extract hollow bunches with a matched longitudinal emittance of $\epsilon_{z,100\%} = 1.3 \text{ eV s}$. The space charge mitigating effect of hollow bunches during the PS injection plateau has been demonstrated in the context of MD 211. We have outlined a strategy to produce larger

HOLLOW BUNCHES PRODUCTION

longitudinal emittances with first results featuring a matched area of 2 eV s.

Crucial ingredients for the larger longitudinal emittances is to remove the response of the radial loop to the sinusoidal phase loop steering. The corresponding lower radial biquad corrector gain also led to a much smoother action of the phase loop compared to the fluctuating reaction under the strong setting of the nominal LHC1A cycle. Furthermore, the C16 needs to be set to a non-integer harmonic during the later part of the cycle to avoid a back reaction on the beam.

Next steps include implementing the smoothing of the large emittance hollow bunches. To this end, the second harmonic in bunch shortening mode might already be used during the resonance excitation: the correspondingly larger synchrotron frequency gradient across RF bucket should provide quicker filamentation. Furthermore, exciting the bunch core by a frequency band of phase loop noise instead of a single frequency might provide a more smooth hollowing procedure, which could avoid the radial loop interference as the bunch centre-of-gravity would not be as strongly affected.

ACKNOWLEDGEMENT

We would like to express our sincere gratitude for fruitful discussions as well as help with setting up the PS Booster LLRF to Maria-Elena Angoletta, Alan Findlay, Michael Jaussi, Elena Shaposhnikova and Guido Sterbini. In particular, we thank the PS Booster and the PS operation teams for the continuous support making these MDs a success.

REFERENCES

- [1] G. Apollinari et al. *High-Luminosity Large Hadron Collider (HL-LHC): Preliminary Design Report*. CERN Yellow Reports: Monographs. Geneva: CERN, 2015.
- [2] G. Franchetti et al. “Space charge and octupole driven resonance trapping observed at the CERN proton synchrotron.” In: *Phys. Rev. Spec. Top. Accel. Beams* 6.12 (2003), p. 124201.
- [3] R. Wasef et al. “Space Charge Effects and Limitations in the CERN Proton Synchrotron.” In: CERN-ACC-2013-0176 (May 2013), 3 p.
- [4] R. Cappi et al. “Measurement and Reduction of Transverse Emittance Blow-up Induced by Space Charge Effects.” In: *IEEE Particle Accelerator Conference (PAC 1993)*. IEEE, May 1993, pp. 3570–3572.
- [5] S. Lee. *Accelerator Physics*. World Scientific, 2004.
- [6] A. Oeftiger. “Space Charge Effects and Advanced Modelling for CERN Low Energy Machines.” Presented 28 Sep 2016. PhD thesis. École Polytechnique Fédérale de Lausanne, Aug. 2016.
- [7] A. Oeftiger et al. “MD210 Note: Creation of Hollow Bunches in the PSB.” In: *CERN ACC NOTE 2016-0045* (June 2016).
- [8] A. Oeftiger, S. Hancock, and G. Rumolo. “Space Charge Mitigation with Longitudinally Hollow Bunches.” In: *ICFA Advanced Beam Dynamics Workshop on High-Intensity and High-Brightness Hadron Beams (HB 2016)*. 2016, MOPR026.
- [9] CERN RF PSB Logbook. 23.03.2016. <https://op-webtools.web.cern.ch/eLogbook/index.php?shiftID=1081814>.
- [10] CERN PSB Logbook. 08.04.2016. http://eLogbook.cern.ch/eLogbook/event_viewer.jsp?eventId=2087751.
- [11] CERN PSB Logbook. 14.04.2016. http://eLogbook.cern.ch/eLogbook/event_viewer.jsp?eventId=2091396.
- [12] R. Cappi, E. Shaposhnikova, and R. Garoby. “Experimental Study of Controlled Longitudinal Blow-up.” In: *CERN PS 92-40-RF* (1992).
- [13] A. Oeftiger et al. “Flat Bunches with a Hollow Distribution for Space Charge Mitigation.” In: *International Particle Accelerator Conference (IPAC 2016)*. May 2016, MOPOR023.
- [14] CERN PSMD Logbook. 27.11.2016. <https://op-webtools.web.cern.ch/eLogbook/index.php?shiftID=1082236>.
- [15] CERN PSBMD Logbook. 16.11.2016. http://eLogbook.cern.ch/eLogbook/event_viewer.jsp?eventId=2080056.
- [16] F. Tecker. “Longitudinal beam dynamics.” In: arXiv:1601.04901 (2014). 21 pages, contribution to the CAS - CERN Accelerator School: Advanced Accelerator Physics Course, Trondheim, Norway, 18-29 Aug 2013, 1–22. 21 p.
- [17] CERN PSBMD Logbook. 22.11.2016. <https://op-webtools.web.cern.ch/eLogbook/index.php?shiftID=1082051>.
- [18] CERN PSBMD Logbook. 24.11.2016. <https://op-webtools.web.cern.ch/eLogbook/index.php?shiftID=1082139>.

SPACE CHARGE STUDIES IN THE PS

F. Asvesta*, H. Bartosik, H. Damerou, A. Huschauer, Y. Papaphilippou, M. Serluca, G. Sterbini, P. Zisopoulos

Abstract

In this paper the results of Machine Development (MD) studies conducted at the CERN Proton Sychrotron (PS) are presented. The main focus was the investigation of new working points in an effort to characterize and potentially improve the brightness for LHC-type beams in view of the LHC Injectors Upgrade (LIU). Various working points were compared in terms of losses and emittance evolution. Since space charge and the resonances it excites are the main cause for emittance blow-up and losses, tunes close to excited resonances were carefully studied. Mitigation techniques, such as bunch flattening using a double harmonic RF system, were also tested.

INTRODUCTION

Space charge is a dominant effect for low energy, high brightness accelerators. It creates an incoherent tune shift that depends on the line density of the longitudinal beam profile and the transverse beam size. For Gaussian beam distributions it yields [1]

$$\Delta Q_{h,v} = -\frac{r_0 \lambda}{2\pi e \beta^2 \gamma^3} \oint \frac{\beta_{h,v}(s)}{\sigma_{h,v}(s)(\sigma_h(s) + \sigma_v(s))} ds, \quad (1)$$

where r_0 is the classical particle radius, λ the line density, e the elementary charge, $\beta\gamma$ the relativistic factors, $\beta_{h,v}$, $\sigma_{h,v}$ the transverse β -functions and beam sizes, respectively. In the PS, at low energy, the space charge tune spread is significant. For the operational LHC25 beam [2] the incoherent space charge tune spread at PS injection, with maximum values $\Delta Q_h \approx -0.20$ and $\Delta Q_v \approx -0.26$, is shown in Fig. 1. The tune spread for the BCMS operational beam [2] is slightly smaller with maximum values $\Delta Q_h \approx -0.18$ and $\Delta Q_v \approx -0.24$. However, the space charge induced tune spread is sensitive to certain parameters, i.e. bunch intensity, bunching factor, transverse emittances and $\Delta p/p$, which may vary from shot to shot.

The main focus of the MDs presented here was the investigation of new working points in an effort to characterize and potentially improve the brightness for LHC-type beams in view of the LIU goals for protons [3]. In 2016, significant blow-up of the horizontal emittance was observed for LHC beams at PS injection [4], which was subject of MDs focused on the beam transfer from the PS-Booster (PSB) to the PS [5]. In this context, tune scans were performed in order to assess the emittance growth of the beam core due to the integer resonances, which might contribute to the observed blow-up. Furthermore, the excitation of other resonances was studied, in particular the space charge driven $Q_v = 6.25$ 8th order

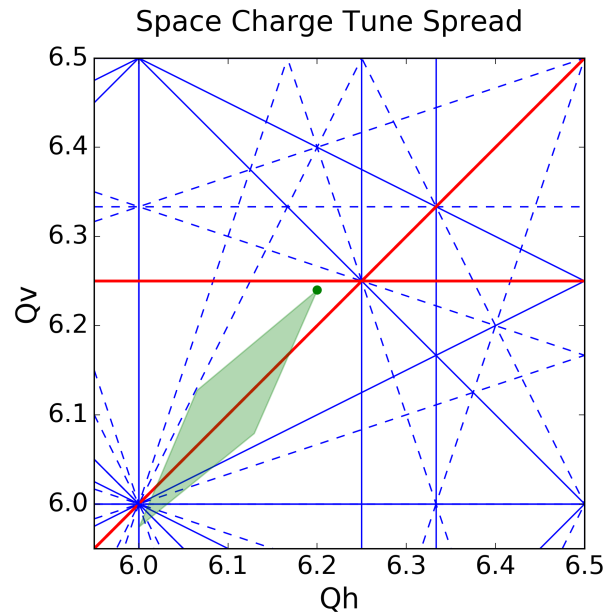


Figure 1: Sketch of the tune footprint for $Q_h = 6.20$, $Q_v = 6.24$ in the PS for the beam parameters of the operational LHC25 beam. Resonance lines up to 4th order marked in blue, the coupling resonance is plotted in red. The red lines at $Q_v = 6.25$ and $Q_h = 6.25$, correspond to 8th order structural resonances.

structural resonance [6], which presently limits the achievable beam brightness in the PS. The chromaticity remained uncorrected during the described MDs.

Since the space charge tune spread is proportional to the longitudinal line density, a smaller tune footprint can be achieved by flattening the bunch profile using additional RF harmonics. This was tested by introducing a second harmonic on the flat bottom of a LHC25 type cycle, i.e. a combination of $h = 7$ and $h = 14$ was used.

TUNE SCANS

Single bunches from PSB Ring 3 were used for the tune scans presented here. The machine cycles in the PS were clones of the LHC25 and the BCMS operational beams. For each working point the beam was injected at the corresponding tunes, which remained constant during the entire flat bottom. The evolution of intensity was monitored for both beam types, in order to deduce losses. The horizontal and vertical emittances were evaluated twice during the cycle: Profiles were taken 15 ms after injection at 185 ms, to avoid any secondary effects such as the injection bump [7], and at the end of the flat bottom at 1285 ms, where the second injection would take place. The emittance is calculated from

* foteini.asvesta@cern.ch

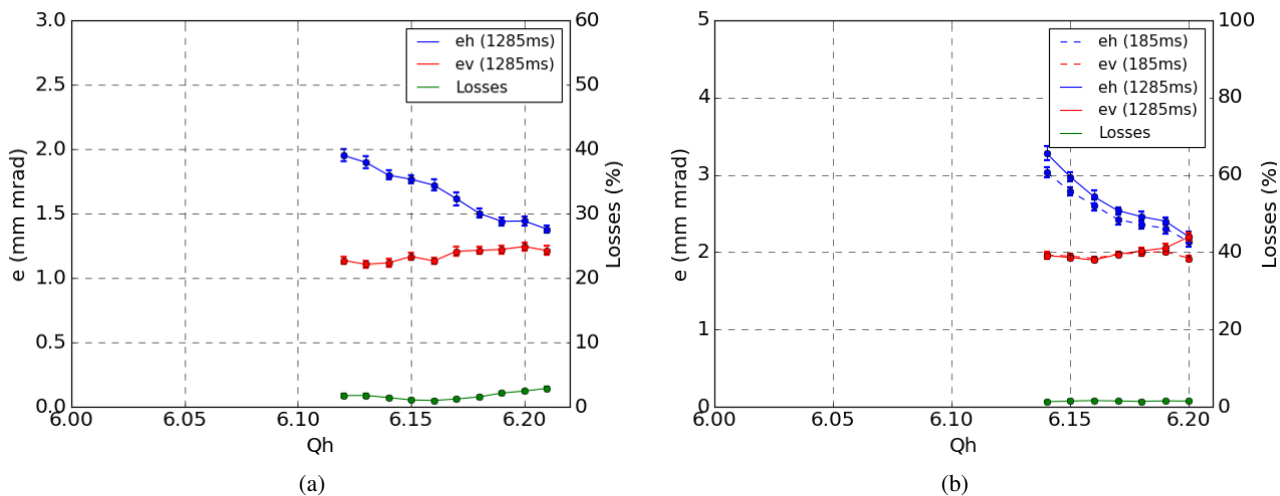


Figure 2: Horizontal tune scans using BCMS (a) and LHC25 (b) beams. Horizontal (blue) and vertical (red) emittances at injection (dashed) and at the end of the flat bottom (solid) as a function of the horizontal tune.

the transverse beam profiles using β -functions from the PS MADX-model, the measured dispersion and $\Delta p/p$ as measured with the tomoscope [8].

Horizontal tune scan

BCMS In order to study the effect of the horizontal integer resonance, the horizontal tune was varied while the vertical tune was fixed at $Q_v = 6.26$. The dependence of the transverse emittances and the losses on the tune is shown in Fig. 2a. Although the initial emittances were not systematically measured for this scan, there is no blow-up observed between injection and at the end of flat bottom for the nominal tune $Q_h = 6.20$. However, when the tune is set below $Q_h = 6.19$ horizontal emittance blow-up is observed. As expected from a blow-up of the beam core at the horizontal integer resonance, the vertical emittance and the bunch intensity are clearly unaffected.

LHC25 In Fig. 2b the emittance and losses evolution as function of the horizontal tune are plotted. For these measurements the vertical tune was fixed at $Q_v = 6.24$. The horizontal emittance growth due to the integer resonance is observed for tunes below $Q_h \approx 6.20$, already at the injection measurement. This blow-up is therefore very fast. Comparing the two beams, one can deduce that they behave similarly in terms of losses. However, the emittance blow-up seems to be larger for the LHC25 beam.

Vertical tune scan

BCMS Now the vertical tune is varied, while the horizontal is kept constant. The measurements were split in two parts. For tunes $Q_v < 6.23$, $Q_h = 6.22$, whereas for $Q_v \geq 6.23$, $Q_h = 6.20$. The resulting emittance and losses are shown in Fig. 3a.

As the tune approaches the integer resonance, a large emittance blow-up is observed even for the measurements at

injection. The emittance blow-up is also observed for tunes $Q_v \approx 6.23$, but only for the measurements at the end of the flat bottom. The effect disappears when $Q_v = 6.25$. For these working points the losses are negligible.

The study of tunes above $Q_v = 6.25$ clearly shows excitation of the 8th order structural resonance $8Q_v = 50$, as losses and emittance reduction are observed. The highest losses of about 14% are observed at $Q_v = 6.30$. The behaviour is improved for tunes $Q_v > 6.30$, where the losses drop and the emittance approaches the initial values. However, for tunes $Q_v > 6.33$ the emittances don't behave as expected.

The acquired vertical beam profiles, Figs. 4a and 4b appear asymmetric both at injection and at the end of flat bottom. This could be due to space charge effects or an instrumental effect of the wire scanner [9]. Nevertheless, for tunes $Q_v \approx 6.33$ there are indications for tail formation. This coincides with the reduction of losses and the increase of emittance. Less tail formation is observed for $Q_v = 6.35$.

LHC25 In Fig. 3b the dependence of the transverse emittances and losses on the working point is shown. The horizontal tune was fixed at $Q_h = 6.20$ throughout the scan.

The vertical integer resonance causes blow-up for tunes $Q_v \approx 6.10$. The effect is strong enough to be observed even with the measurements right after injection. Contrary, if the tune is set to $Q_v \approx 6.25$, the blow-up is only observed at the end of flat bottom.

Crossing the structural resonance, notable losses occur even when the tune is set to $Q_v = 6.25$. As the tune is further increased significant losses, almost 25% at $Q_v \approx 6.30$, cause a reduction in the transverse emittances of both planes. The fact that the losses remain significant for tunes $Q_v > 6.31$ could be an indication of a different resonance crossing close to $Q_v = 6.33$ [10].

Thorough examination of the vertical bunch profiles in Figs. 4c and 4d. provides important information for the beam

SPACE CHARGE STUDIES IN THE PS

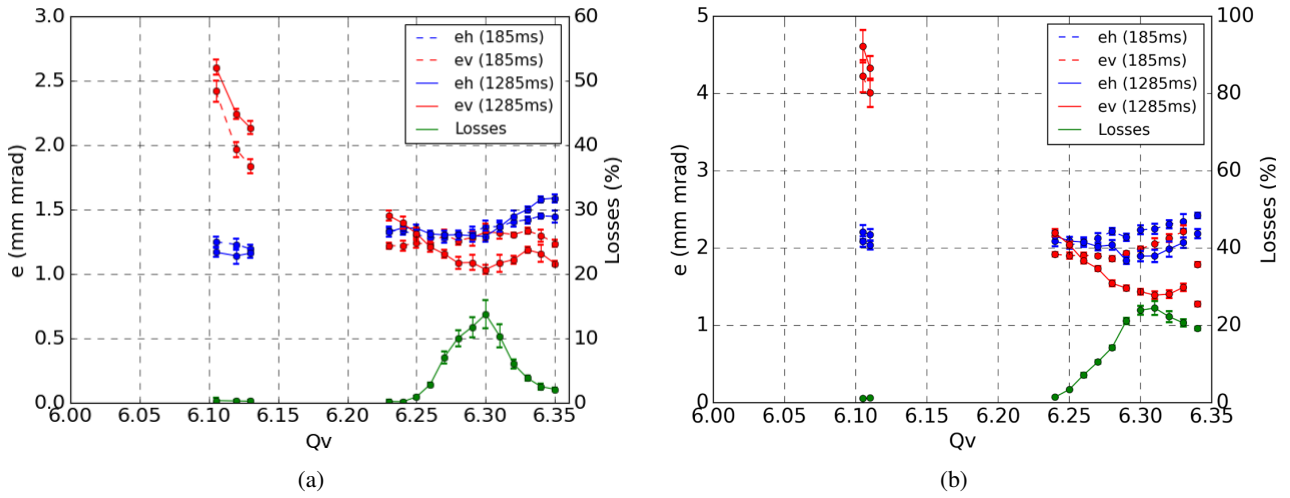


Figure 3: Vertical tune scans using BCMS (a) and LHC25 (b) beams. Horizontal (blue) and vertical (red) emittances at injection (dashed) and at the end of the flat bottom (solid) as a function of the horizontal tune. Losses (green) are shown using a second axis.

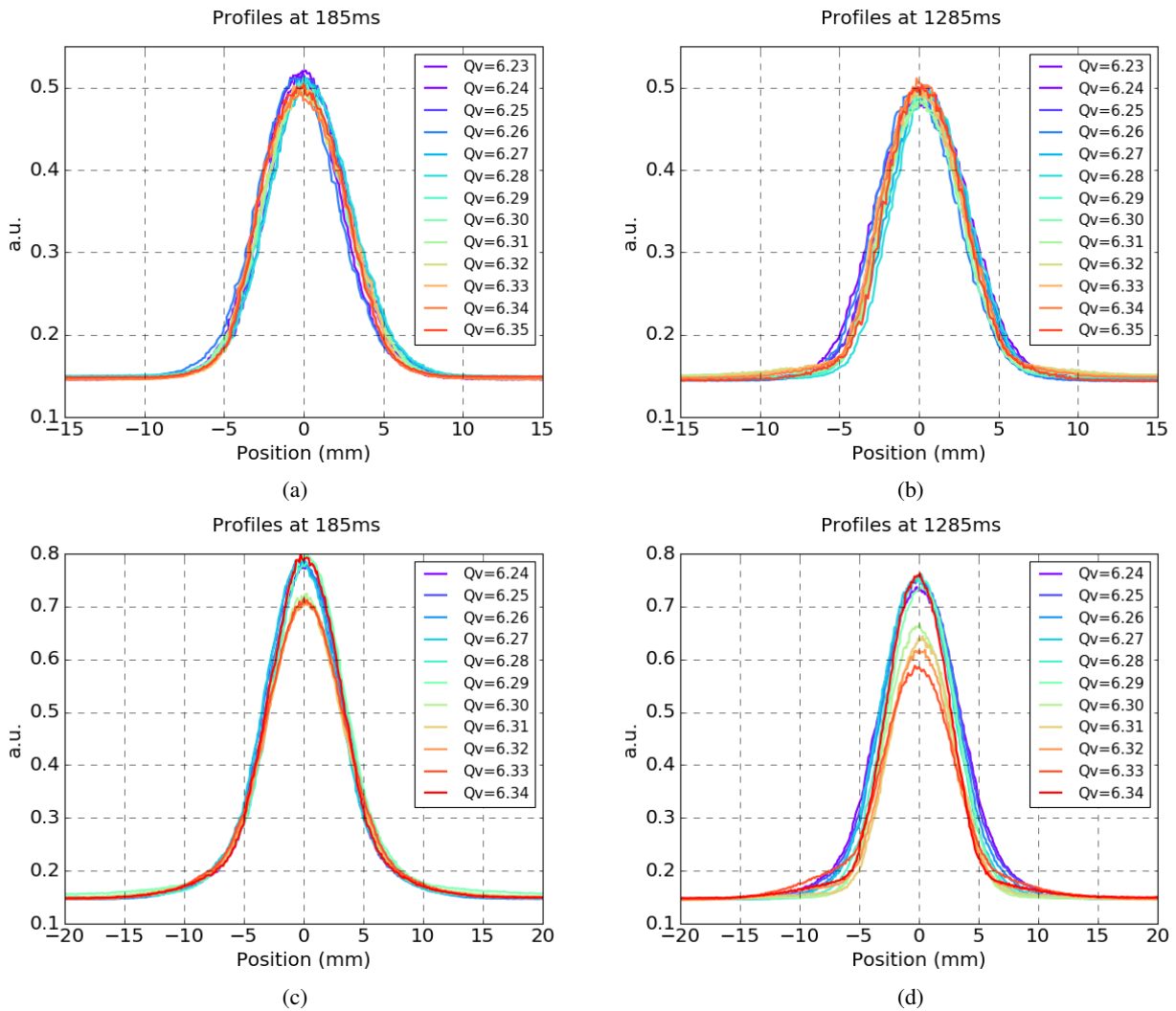


Figure 4: Vertical beam profiles at injection (a,c) and at the end of flat bottom (b,d) for BCMS (a,b) and LHC25 (c,d) beams.

quality, as well as a better understanding of the observables. Regarding the beam quality shortly after injection at 185 ms, the profiles deviate from a Gaussian as tails are observed. These tails, which appear regardless of the tune, could be a result of the strong space charge force, some injection phenomena or already generated in the PSB. The bunch is more Gaussian-like at the end of the flat bottom for tunes $Q_v \approx 6.25$, since large amplitude particles are lost. Excitation of the structural resonance modifies the bunch profiles as the amplitude of the signal is reduced, due to losses, and additional tails are formed. The halo formation dominates when the losses start to drop, implying that the particles affected by the resonance are closer to the beam core. The tails at the end of the flat bottom are reduced when $Q_v = 6.34$.

Both beams suffered transverse stability issues for tunes towards the integer resonance and for $Q_v > 6.33$, since the stabilizing effect from the linear coupling resonance was reduced. The consequences of resonance crossing appear stronger for the LHC25 beam, more losses and tail formation. A potential explanation for this could be the difference between the beam sizes. Scans with both beams encourage the study of higher tunes in the future, since the beam quality is observed to improve.

SPACE CHARGE MITIGATION

The incoherent space charge tune spread can be moderated by reducing the peak line density of the longitudinal profile. This may be accomplished by introducing a double harmonic RF voltage. In the case of the LHC25 beam tested here, the RF harmonics were $h = 7$ and $h = 14$ respectively. The voltage in the cavity at the principal harmonic was kept constant at 25 kV while the one in the cavity at twice that harmonic was varied in steps of 6 kV. The voltage in the double harmonic cavity was ramped up at 170 ms and ramped down at 1250 ms. The duration of the ramp was 20 ms, corresponding to several synchrotron oscillation periods. The working point chosen was $Q_h = 6.20$, $Q_v = 6.23$ to enhance the effect of the integer resonance. Throughout the MD the radial loop and the phase loop had to be turned off, as the spectrum of the bunches in the double-harmonic RF unfavorably influence the loops. The modification of the line density profile as function of the RF voltage measured at 190 ms is shown in Fig. 5.

The vertical emittance measurements for these machine settings are shown in Fig. 6. The emittance at injection was only measured once but the initial emittance should not change, as the parameters in the PSB remained constant. The emittance at the end of the flat bottom shows a clear dependence on the voltage of the cavity and hence the line density. The blow-up for the flatter longitudinal profile is reduced by approximately 50%, demonstrating a potential reduction of the incoherent space charge tune spread as the beam is less affected by the integer resonance.

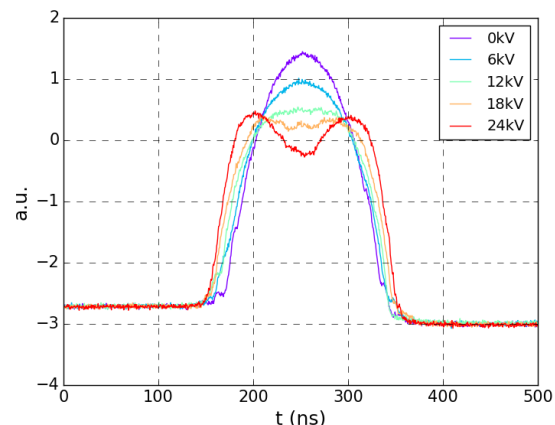


Figure 5: Longitudinal profiles acquired at 190 ms using a double harmonic cavity.

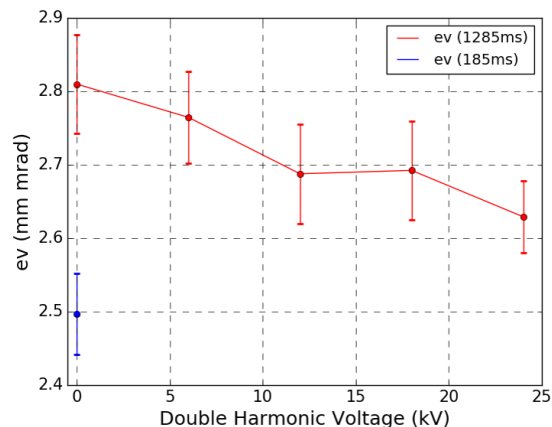


Figure 6: Vertical emittance at injection (blue) and at the end of flat bottom (red) as a function of the voltage in the double harmonic cavity.

CONCLUSION

Thorough tune scans in both planes towards the corresponding integer resonances have shown the expected blow-up of the emittances. Vertical tune scans for the two LHC beam types, LHC25 and BCMS, show clear excitation of the $Q_v = 6.25$ structural resonance. For the BCMS case the effect manifests only when the coherent tune is set above it. Thus, the best beam performance in terms of brightness is obtained when the working point is $Q_h = 6.20$, $Q_v = 6.25$. Tunes above $Q_v \approx 6.34$ should be studied in future MDs to check whether larger space charge tune spreads can be accommodated. This might require a compensation of the 3rd order resonance at $Q_v = 6.33$ as successfully demonstrated in the past [11]. The beam stability issues encountered for these tunes need to be cured with the transverse feedback system [12]. In the future the impact of chromaticity correction should be studied, as it might reduce the detrimental effects of the structural resonance.

SPACE CHARGE STUDIES IN THE PS

The use of a double harmonic RF system for space charge mitigation seems promising. The issues encountered with the beam phase and radial loops should be further studied so that it can operate throughout the cycle. The BCMS beam could also be tested once the settings of the timing tree and the functions for the harmonic numbers are modified.

ACKNOWLEDGEMENT

The authors would like to thank the PSB and PS OP teams for their help.

REFERENCES

- [1] K.Schindl, "Space Charge", *CERN/PS 99-012(DI)*, 1999.
- [2] R.Steerenberg *et al.*, "Beams from Injectors in 2016", *LHC Performance Workshop*, 2016.
- [3] G.Rumolo *et al.*, "LIU baseline for protons", *LHC Performance Workshop*, 2017.
- [4] H.Bartosik *et al.*, "PS emittance blow-up", *Injector MD days 2017*, CERN, 2017.
- [5] V.Forte *et al.*, "PSB-to-PS transfer studies", *Injector MD days 2017*, CERN, 2017.
- [6] R.Wasef *et al.*, "Space Charge effects and limitations in the CERN Proton Synchrotron", *IPAC'13*, Shanghai, China, 2013.
- [7] M.Serluca *et al.*, "Injection Bump Synchronization Study for the CERN PS", *CERN-ACC-NOTE-2016-0006*, CERN, 2016.
- [8] S. Hancock *et al.*, "Longitudinal Phase Space Tomography with Space Charge", *Proc. of EPAC'00*, Vienna, Austria, 2000.
- [9] M.Cieslak-Kowalska *et al.*, "Interpretation of Wire-Scanner asymmetric profiles in a Low-Energy ring", *CERN-ACC-2016-0109*, CERN, 2016.
- [10] A.Huschauer *et al.*, "Working Point and resonance studies at the CERN PS", *IPAC'13*, Shanghai, China, 2013.
- [11] A. Huschauer *et al.*, "Identification and compensation of resonances in the CERN Proton Synchrotron", *Space Charge Workshop*, CERN, 2013.
- [12] G.Sterbini *et al.*, "Beam-based Performance of the CERN PS Transverse Feedback", *54th ICFA Advanced Beam Dynamics Workshop*, 2015.

THE (7,7) OPTICS AT CERN PS

M. Serluca*, S. Aumon, I. Efthymiopoulos, F. Sperati,
G. Sterbini, F. Tecker, P. Zisopoulos CERN, Geneva, Switzerland

Abstract

The PS lattice is composed by one hundred combined function magnets, which set the bare tune of the machine to $(Q_h, Q_v) = (6.25, 6.28)$. Low energy quadrupoles are used at injection to move the tune in a limited working point area. In particular the vertical tune is moved below 6.25 to avoid the structural resonance $8 Q_v = 50$ coupled with space charge, which leads to strong losses. In view of the high demands in terms of beam brightness for LIU and HL-LHC projects, the interest of exploring different integer tune working area started during last years. During 2016, for the first time, it has been possible to explore the (7,7) tune working area at injection using the auxiliary circuits of the combined function magnets. A finite-element magnetic model, under development, has been used to predict the required currents in order to get the desired optical parameters. In this paper we present the results and issues encountered during the Machine Development (MD) studies about the injection in the (7,7) area along with optics and beam parameters measurements.

INTRODUCTION

The CERN PS has been working reliably for the past 60 years, during its long history it has been upgraded several times to cope with the increasing demands of the downstream accelerators and experiments. In view of LIU and HL-LHC projects, the injection kinetic energy of the PS will be increased from 1.4 to 2 GeV to mitigate the space charge tune spread of the increased brightness beams. The combined function magnet unit is composed of a focusing and a defocusing half-unit. So called "Pole Face Windings" (PFW) are placed on the pole faces and "Figure of eight Loop" (F8L) are mounted around each half unit. PFWs are used at high field level to compensate the quadrupolar saturation and leakage field, whereas F8L increases the quadrupolar field in one half-unit, while decreasing it on the other half without affecting the integrated bending field. The bare tunes of the machine are $(Q_h, Q_v) = (6.25, 6.28)$. At injection Low Energy Quadrupoles (LEQ) are used to set the tunes in a small area around the bare tune.

A structural resonance coupled with space charge limits the vertical exploitable area between 6.25 and the integer resonance 6 [1]. Injecting the beam above 6.25 lead to strong losses while pushing the tune close to the integer leads to emittance blow-up. In the effort of studying alternative scenario to exploit the full potential of the accelerator, the possibility of changing the integer tune was considered. While it is relatively simple to move the tunes in the (5,7) and (7,5) area using the F8L, which has almost a linear effect, it is

much more difficult to move the tunes in the (7,7) area using the non-linear PFWs. Indeed, in normal operation the working point is programmed by relative variations because the relationship between absolute value of the working point and currents in the auxiliary circuits is not known. The last point has also stimulated the collaboration with the magnet group at CERN to continue the development of the magnetic model of the PS in order to predict tunes and chromaticities for a given set of auxiliary currents. In the following section we present details of the PS main magnet and the magnetic cycle of LHC-type beams. Then we introduce the PS injection scheme and the experimental results of the MD1905 for the (7,7) optics.

THE CERN PS MAIN MAGNET

The PS ring is made by one hundred combined function magnets. A picture of the magnet is presented in Fig. 1 and the cross-section of the PFW plate with auxiliary circuits is illustrated in Fig. 2. Each magnet unit is divided into a focusing and a defocusing half unit, half units are composed of five consecutive blocks. The PFWs are divided into four independent circuits, named DN, DW, FN, FW. "F" and "D" represent the focusing and defocusing part where they are mounted, "N" and "W" stand for narrow and wide type of circuit. Wide circuits cover the whole magnetic pole whereas the narrow circuits only cover the part where the iron gap is narrow (smaller aperture). F8L is a winding describing a figure of eight around the focusing and defocusing poles of the magnet. The possibility to power the circuits independently gives control on the tunes, linear chromaticities and one additional parameter, usually Q''_h or Q''_v . An effective model is constructed with the measurements of the variation of betatron parameters in response of the PFWs and F8L currents at different momentum of the beam.



Figure 1: Picture of the PS combined function magnet unit.

* maurizio.serluca@cern.ch

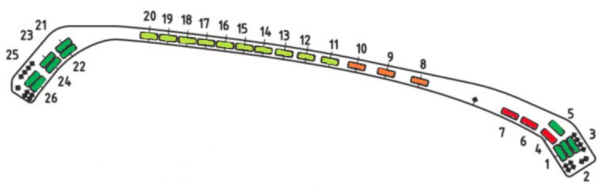


Figure 2: Cross-section of pole-face windings plate. Narrow circuits pole conductors are from 11 to 20 (light green) with return conductors 1-4 and 21-26 (green). Wide circuits are from 8 to 10 (orange) with return conductors 5-7 (red). The small black points are passive circuits that correct the eddy current effects.

Magnetic cycle of LHC-type beams in the PS

The role of the PS in the LHC injection chain (in addition to the acceleration) is to preserve the brightness of the beam and generate the final longitudinal structure of LHC-type beams. The beams are injected at 1.4 GeV kinetic energy and accelerated up to a momentum of 26 GeV/c. The magnetic cycle for the double batch injection scheme for LHC-type beam is presented in Fig. 3, the entire cycle is composed of three basic periods (1.2 s per period), the first batch is injected at 170 ms and the second batch at 1370 ms. After the injection of the two batches, the beam is accelerated on a second plateau for RF splitting. During the second acceleration the PS beam crosses the transition energy around 6 GeV and at top energy the beam is manipulated longitudinally to get the desired bunch spacing before extraction.

LHC-type beams can be produced using the classic scheme of double batch injection (4+2 bunches) in harmonic 7 (h7) followed by triple splitting on the intermediate energy plateau at 2.5 GeV and a double-double splitting at top energy to get the final 72 bunches with 25 ns bunch spacing. An alternative method is the Bunch Compression and Merging Scheme (BCMS) which is characterized by (4+4) bunches injected in h9, the bunches merge in four on the second plateau before triple splitting and a final double-double splitting at top energy to get 48 final bunches.

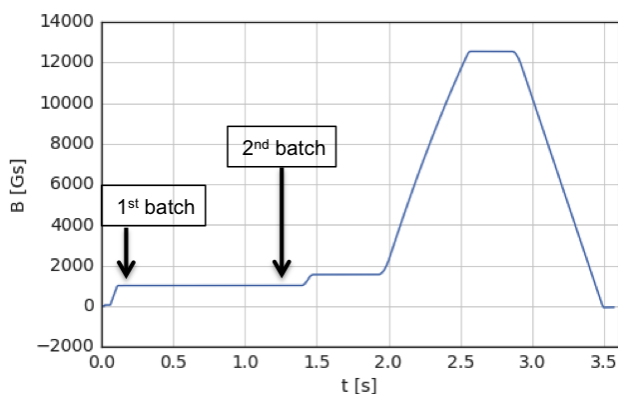


Figure 3: Magnetic cycle of CERN with double batch injection scheme for LHC-type beams.

WORKING POINT OF THE PS

The combined function magnets of the PS set the bare tune to $(Q_h, Q_v) = (6.25, 6.28)$ and natural chromaticities to $(\xi_h, \xi_v) = (-0.8, -1)$. Figure 4 shows the frequency space of the PS, the bare tune is represented by a black point. The blue area around the bare tune is the reachable area of LEQs with currents within ± 10 A. The plot also shows first (full black lines) and second (dashed blue lines) order resonances. The 8th order structural resonances are shown in red and can be written as $aQ_h + bQ_v = 50$ with $a + b = 8$. Several MDs have been performed during last years to characterise the resonances [2, 3], in particular the $8Q_v = 50$ is one of the limiting factor to increase the beam brightness. The outcome of the studies has shown that the structural resonance is coupled with space charge, i.e. intensity dependent, and it leads to strong losses during the long flat bottom if the beam is injected above $Q_v = 6.25$. This resonance limits the exploitable tune area to accommodate the expected Laslett tune spread of about -0.31 or more for LIU and HL-LHC. Figure 4 shows that the (7,7) area is free from structural resonances and, in principle, the area between the integer 7 and the third order resonance $Q_v = 7.33$ could be fully exploitable to place the high brightness LHC-type beam and keep the emittance growth and losses within LIU budget. F8L is linear circuit and can be used to move the tunes in the (5,7) or (7,5) area [1]. These particular cases are not discussed in this paper. PFWs are non-linear elements and not used at injection for regular operation. A basic approach to move the working point would be to ramp the PFWs currents along the flat bottom while measuring the tune in order to approach the working point space towards the (7,7) area. Unfortunately the beam does not survive to several resonances that are present in the machine and are excited by the ramping fields of the PFWs. In particular the resonance $Q_v = 6.75$ leads to a complete loss of the beam.

A finite-element magnetic model has been prepared in OPERA during last years to predict the required currents in the auxiliary circuits [4]. The model successfully reproduce the tune of the bare machine within 1% and chromaticity within 30%. When PFW currents are added to the model, the errors in tune and chromaticity increase. This magnetic model has some limitations: it uses a straight magnet (the real is bent), there is a clear dependence of the multipolar fields on the radius of expansion and therefore the conversion of the integrated fields to multipoles in MADX.

INJECTION IN THE (7,7) WORKING POINT AREA

The PS injection scheme for proton (Fig. 5) is performed with a four bumpers scheme to control the orbit displacement and the slope of the bumped orbit. The septum bends the beam from BT-BTP line by 55 mrad (nominal value) and then it goes through the bumper 43 and 44, a kicker in SS45 operated in terminated mode gives the final 4.3 mrad kick to place the beam on the closed orbit. For a given position and angle of the injected beam at the septum flange the bumpers

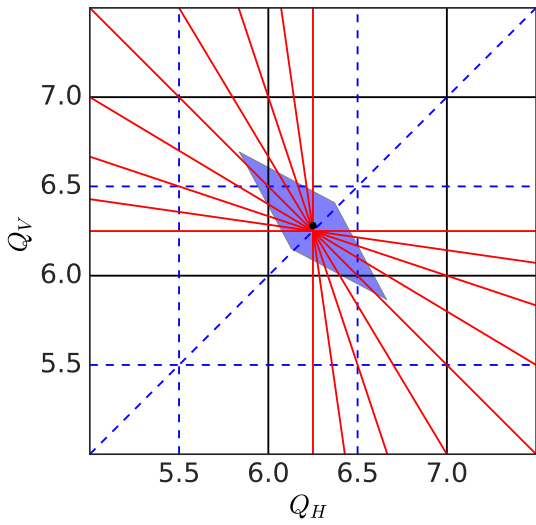


Figure 4: Tune area of the CERN PS. The black point represents the bare tunes of the machine $(Q_h, Q_v) = (6.25, 6.28)$, resonances: integers (black lines), second order (blue dashed lines), 8th order structural (red lines). The blue area around the bare tune represents the reachable area of the low energy quadrupoles at 1.4 GeV.

43, 44 are matched to steer the injected beam with zero horizontal orbit displacement and -4.3 mrad angle in the kicker 45. The bumpers 40 and 42 are then matched to close the bump for the circulating beam. Operationally the strength of the septum, kicker and bumpers are optimized for each different beam to minimize losses and close the bump. An injection steering program is used in operation to minimize injection oscillations and, as consequence, the emittance blow-up due to errors. SEM grids are also used in dedicated MDs to check the betatron and dispersion mismatches of the incoming beam with respect to the periodic optics solutions of the ring at the exit of the septum flange.

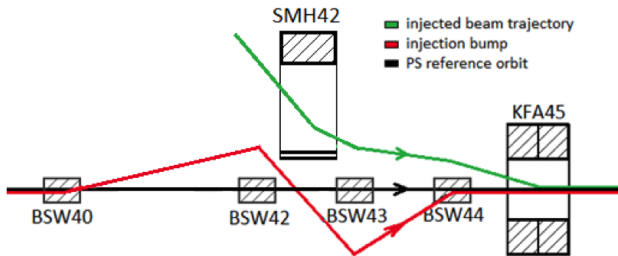


Figure 5: Injection scheme of the CERN PS at 1.4 GeV with bumpers, septum and kicker (not to scale). The injected beam trajectory from the transfer line in green and the bumped orbit in red.

The (7,7) optics changes the phase advances in the machine elements and it is not possible to use, in the standard way, the control room tools to adjust injection and orbit.

During 2015 several tests were performed to inject the beam using different settings of the PFWs currents calculated with the magnetic model. In most of the cases the beam did not survive injection, for one set with about 70 A in the wide circuits and 20 A in the narrow circuits of the PFWs, it was possible to observe part of the beam going through injection and survive for few ms ($\sim 1k$ turns). Figure 6 shows the magnetic cycle of LHC-type beam and the intensity of the injected beam. The beam used for this experiment is a clone of the BCMS operational beam, using a single bunch from ring 3 of the Booster with low intensity ($25 \cdot 10^{10}$ ppb).

The intensity of the beam at injection, presented in Fig. 6, shows that half of the beam is lost at injection and the remaining half is lost after few ms. The orbits, measured in 43 BPMs per plane, are presented in Fig. 7. Each line in the plot is an average over 200 turns after the end of the bump. It was not possible to measure the tunes in a clean way but it is possible to have an indirect measure of the integer part of the tune by counting the number of orbit oscillations around the machine in Fig. 7. This indirect measurement indicates that the tune is close to seven but it is not possible to get the fractional part of it or to understand if it is below or above seven.

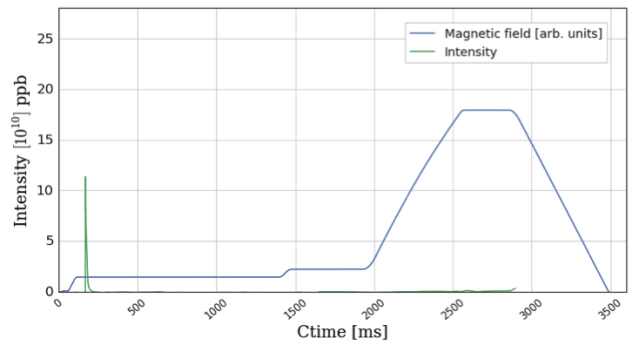


Figure 6: LHC-type beam magnetic cycle (blue line) and intensity evolution of the beam in green. The bunch intensity from the Booster is $25 \cdot 10^{10}$ ppb indicating that half of the beam is lost at injection. The beam survives for few ms ($\sim 1k$ turns).

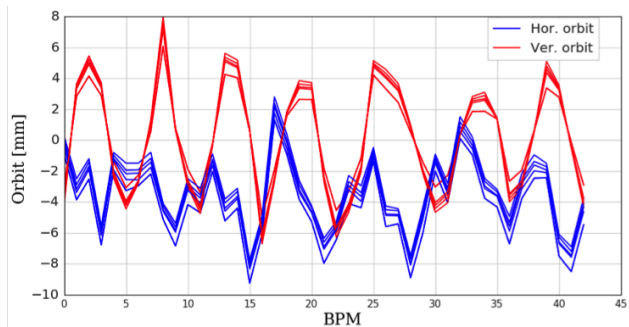


Figure 7: Vertical and horizontal orbit of the beam after injection. Each line is an average over 200 turns after the end of the injection bump which lasts about 500 turns.

In 2016 we continued the MD trying to improve the injection and measuring the optics and beam parameters. The orbits and the signals in the BPMs clearly show that the bump is not closed and the orbit needs to be corrected. As first attempt to correct the injection and orbit of the beam, we measured the response matrices of all injection elements: bumpers, kicker and septum, and the matrices from all orbit correctors in both planes. After applying the calculated corrections we did not observe any improvement in the behaviour of the beam. Several tests on other possible sources of the problem were not successful until we switched off the radial loop of the B-TRAIN, which measures the integrated bending field, seen by the beam. Even with strong losses, part of the beam was surviving along the injection plateau. This effect indicated that the use of the B-TRAIN for this configuration needed to be reconsidered. A further check on the timing of the PFWs currents led us to discover that the fields generated by the PFWs were changing the reading of the magnetic marker (around 60 ms ctime) used to set the B-TRAIN field. Delaying the start time of the PFWs after the magnetic marker solved the problem.

After optimizing the currents in the injection elements and correctors, we were able to inject properly the beam in the PS. An example of intensity along the injection flat bottom for the corrected case is presented in Fig. 8. The beam is dumped on the internal dump at the end of the flat bottom since the ramp and the extraction was not commissioned. The intensity in this case shows that almost no losses occur at injection, the $25 \cdot 10^{10}$ ppb from the PSB are transmitted to the PS, some losses are still observed during the injection plateau. The corresponding orbits of the beam are presented in Fig. 9, the plot clearly shows a strong reduction of the peak-to-peak orbit distortion with an oscillation amplitude similar to what is measured with the operational beams in the (6,6) tune area. The setting of the injection elements and PFWs used in the (6,6) operational area and in the new (7,7) area are reported in Table 1.

It is important to note that the maximum PFWs current is limited to 250 A. This means that the beam cannot be accelerated while keeping the PFWs proportional to energy, same argument regards the RMS currents during the cycle (80 A over the supercycle). The highest energy achievable in this condition is about 9 GeV. Even if it is not possible to extract the beam at top energy, the studies of the new working tune area are interesting because they improve our knowledge of the magnetic model and non-linear fields generated by the PFWs. We have also gained experience with the injection optics and the related tools in control room in view of the commissioning of the new injection at 2 GeV.

TUNE AND CHROMATICITY MEASUREMENTS

The measurement of the fractional part of the tune is based on an excitation of the beam and consecutive measurement of the beam response in a fast pick-up over a finite number of turns. The O-meter software tool in the control room

Table 1: PFWs, septum (SMH42), bumpers (BSW) and kicker (KFA45) settings at injection for the (6,6) and (7,7) WP area.

Element	I [A] ((6,6) area)	I [A] ((7,7) area)
FW	0.0	70.0
DW	0.0	70.0
FN	0.0	19.0
DN	0.0	15.0
BSW40	1030.2	1196.1
BSW42	3773.4	3780.8
BSW43	3090.7	3027.7
BSW44	1142.1	1124.85
KFA45	337.1 [KV]	356.6 [KV]
SMH42	31272.9	31739.2

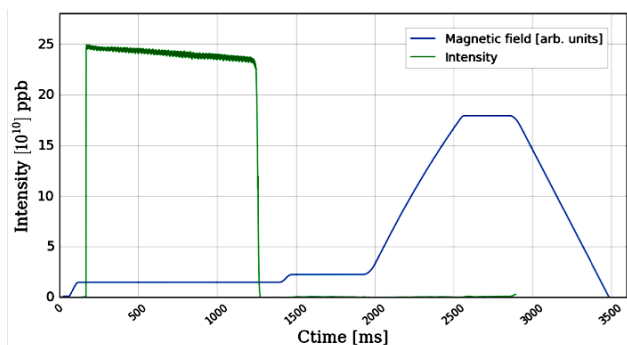


Figure 8: LHC-type beam magnetic cycle (blue line) and intensity evolution of the beam in green. The bunch intensity from the Booster is $25 \cdot 10^{10}$ ppb indicating that no losses occur at injection. The beam is dumped on the internal dump at the end of the injection plateau to avoid irradiation of the full ring.

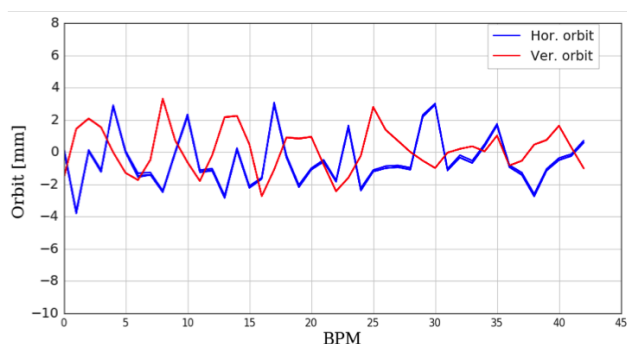


Figure 9: Vertical and horizontal orbit of the beam after injection. Each line is an average over 200 turns after the end of the injection bump which lasts about 500 turns.

calculates the fractional part of the tunes by Fourier analysis of the data. Using the PFW settings in Table1, the Q-meter calculates $(q_h, q_v) = (0.27, 0.16)$. For the following MDs we moved the fractional part of the tunes with LEQs to $(q_h, q_v) = (0.24, 0.22)$. To measure also the integer part of the tune and compare the results of the O-meter, an advanced

method based on multiple BPM data analysis with Numerical Analysis of Fundamental Frequencies (NAFF) algorithm was applied to the transverse data [5, 6]. The method does not need to excite the beam, it is very fast and allows to get turn-by-turn tune measurements with also the integer part. The orbit data during the injection bump are chosen due to the largest betatron oscillations. An example of tune measurement with this technique is presented in Fig. 10. The upper plot shows the turn-by-turn evolution of the tunes while the plot below shows the relative errors. In about 40 turns the measurements converge to the values obtained by the Q-meter with a perfect agreement in the horizontal plane and a small deviation of 0.02 in the vertical tune.

A chromaticity measurement was also performed to evaluate the effects of the non-linear PFWs. Indeed the measurements in Fig. 11 show that the horizontal chromaticity has a parabolic shape, the effect is less strong on the vertical plane. The linear chromaticities are comparable to the values measured in the (6,6) area. It should be noted that the Q-meter in the control room does not measure the integer part of the tune and the reported values by the software GUI in Fig. 11 are with the integer 6 by default.

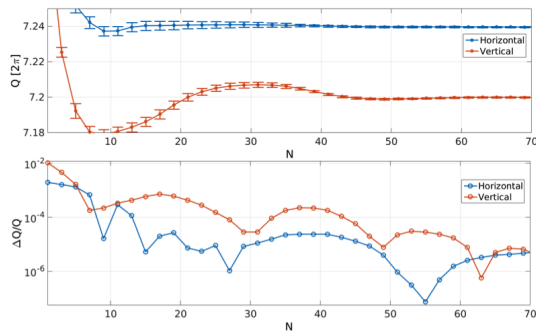


Figure 10: Tunes measurement with advanced multiple BPMs data and NAFF algorithm during the firsts 70 turns.

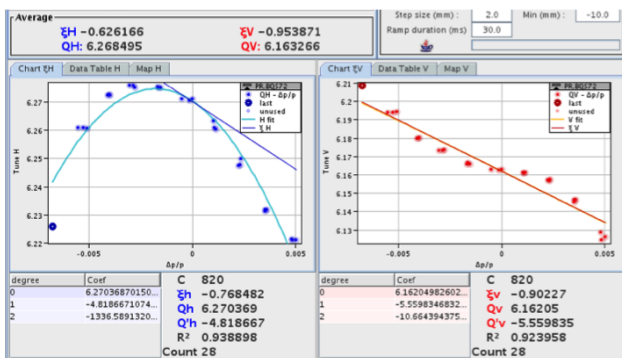


Figure 11: Chromaticity measurement snapshot using the Q-meter in the control room. Note that the tool does not measure the integer tune so it displays 6 by default.

DISPERSION MEASUREMENTS AND INJECTION STEERING PROGRAM

To continue the characterisation of the new optics we measured the dispersion, presented in Fig. 12. We continued our studies using LHCINDIV beam ($\sim 12^{10}$ ppb) to reduce irradiation due to the heavy use of the internal dump. The measured points in the plot are in a reasonable agreement with the MADX model at (7,7) (blue line in the plot). The MADX optics model was implemented in the injection steering tool of the PS, named YASP [7], to correct the injection orbit and minimize the oscillations. Apart from some issues uploading the model in YASP due to different naming convention in the element database, the implementation was successful and led to orbit correction at the very first try. The output of YASP showing the orbits in both planes for the first and second turn after correction are presented in Fig. 13, the superposition of the two orbits indicates that the injection steering program works correctly.

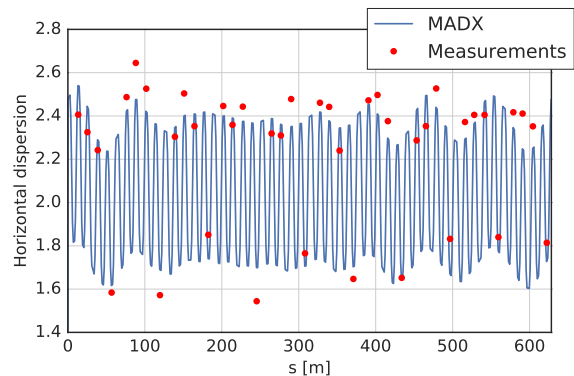


Figure 12: Dispersion measurement in the horizontal plane shows a good agreement with the MADX model.

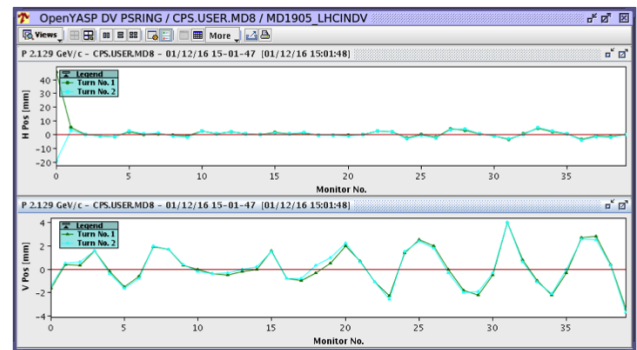


Figure 13: First and second turn orbit from the injection steering program YASP shows an excellent injection oscillation correction.

EMITTANCE MEASUREMENTS AND EFFECT OF THE $Q_v = 7.25$ LINE ON THE BEAM

To complete the beam characterisation with the new working point in the (7,7) area we measured the emittances at PSB extraction and PS injection to get some indications about the beam mismatch with the new optics. The transfer line is not fully PPM and the only way to inject without mismatch would have been to perform dedicated MDs. Given the complexity of the operation and few MD slots left at the end of last year operation, we decided to leave the transfer line mismatched. The results of the emittance measurements in the horizontal and vertical plane are reported in Fig. 14 and 15, respectively. The vertical axis represents the measurements at PSB extraction while the horizontal one represents measurements at PS injection; the colour scale indicates the bunch intensity. The results indicate a blow-up in the horizontal plane of about 10% and 40% in the vertical. Given the low intensity of the beam, the observed blow-ups are assumed to be mainly from the betatron and dispersion mismatches at injection.

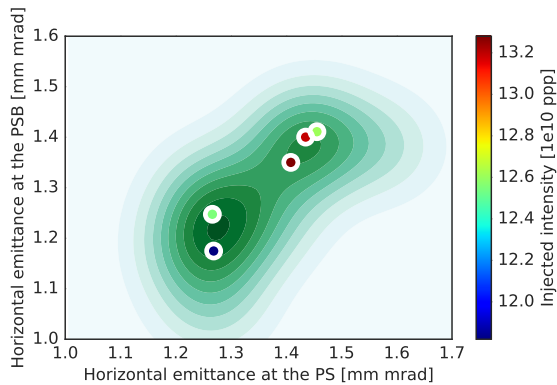


Figure 14: Horizontal emittance measurements at PSB extraction and PS injection. The colour scale indicates the bunch intensity.

An interesting study carried out is the effect of the line $Q_v = 7.25$. Frequency Map Analysis (FMA) do not show any 8th order resonance but the 4th order with the formation of the 4 islands in the transverse space [8]. To analyse the line we moved the vertical tune just below and above 7.25 ($Q_v = 7.245$ and 7.255) while measuring the losses between injection and the end of the flat bottom. The results are presented in Fig. 16, for each set of data it is clear a correlation between intensity of the beam and observed losses. In addition the result for $Q_v = 7.255$ indicates that losses increase above 7.25. Most likely the new observed resonance is a lattice resonance excited by the PFWs currents. A possible way to study the real nature of the $Q_v = 7.25$ resonance would be to move the tune in the (5,7) area using the linear F8L, and repeat the study for working points above and below 7.25.

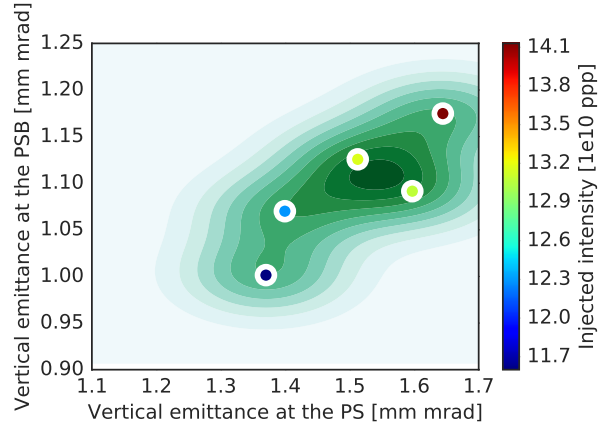


Figure 15: Vertical emittance measurements at PSB extraction and PS injection. The colour scale indicates the bunch intensity.

To complete the study we measured the response matrices of the system. A scan of the tune and chromaticity, adding 2 A on each PFW circuit to the nominal value listed in Table 1, has been performed. The results presented in Fig. 17 show that increasing the current in the defocusing circuits the tunes approach a common value, while the chromaticity has almost the same values for the wide circuit and inverted values for the narrow circuit. The effects of focusing circuits on the tunes are the opposite; the tunes diverge while the effect on chromaticity is similar, almost same value for wide circuit and inverted values for the narrow one. From these results it is possible to construct a matrix to move tunes and chromaticities in the (7,7) tune area.

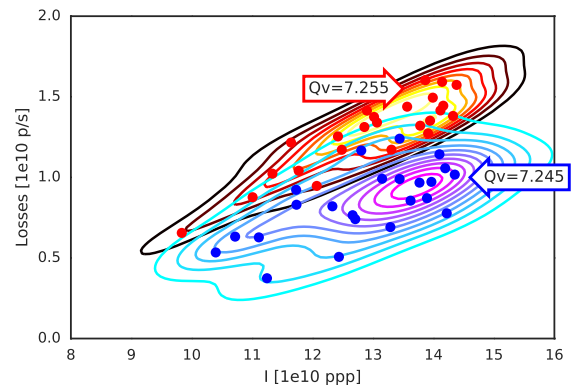


Figure 16: Losses as function of injected intensity for working point above and below $Q_v = 7.25$.

CONCLUSION

For the first time the injection of LHC-type beam in the (7,7) tune area of the PS has been achieved. The injection issues encountered during the MDs have been useful to understand the procedures to follow in case of operation with the auxiliary circuits at injection. Even if it is not possible to accelerate the beam at top energy, the exploration of

THE (7,7) OPTICS AT CERN PS

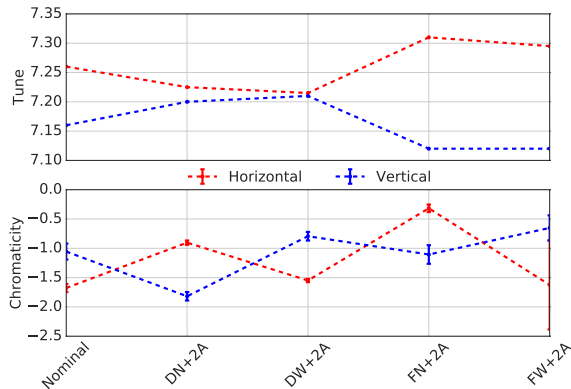


Figure 17: Tune and chromaticity scan adding (individually) 2 A on each PFW circuit to the nominal value listed in Table 1.

the new tune area gives us the opportunity to improve the non-linear model of the PS and the possibility to test the magnetic model over a wide range of currents in the auxiliary circuits. The line $Q_v = 7.25$ is probably a new lattice resonance excited by PFW fields, further studies using the F8L in the (5,7) area could confirm this result.

ACKNOWLEDGEMENT

The authors would like to thanks the OP team for the support during the MDs, the SWAN team for the development of online Python notebooks used for data analysis, Heiko Damerau for the useful discussions during the MDs and Foteini Asvesta for the FMA in the (7,7) area.

REFERENCES

- [1] R. Wasef, “Space Charge in the PS”, *MSWG Meeting*, CERN, July 2015.
- [2] H. Bartosik *et al.*, “PS emittance blow-up”, *Injector MD days 2017*, CERN, 2017.
- [3] F. Asvesta *et al.*, “Space Charge Studies in the PS”, *Injector MD days 2017*, CERN, 2017.
- [4] F. Sperati *et al.*, “New Working Point for CERN Proton Synchrotron”, in *International Particle Accelerator Conference (IPAC16)*, Busan, Korea, March 2016, paper THPOR050, pp. 3905–3907.
- [5] J. Laskar, “Frequency analysis for multi-dimensional systems. Global dynamics and diffusion”, *Physica D*, vol. 67, pp. 257–281, 1993.
- [6] P. Zisopoulos *et al.*, “Transverse tune determination from mixed BPM data”, in *International Particle Accelerator Conference (IPAC15)*, Richmond VA, USA, May 2015, paper TUPJE042, pp. 1709–1712.
- [7] J. Wenninger, “YASP: Yet Another Steering Program User Guide”, 2005.
- [8] F. Asvesta *et al.*, “Space Charge Studies at the PS”, *Space Charge meeting*, CERN, December 2016.

INJECTION SEPTA POSITION AND ANGLE OPTIMISATION IN VIEW OF THE 2 GEV LIU UPGRADE OF THE CERN PS

M. Serluca*, W. Bartmann, V. Forte, M. Fraser, G. Sterbini CERN, Geneva, Switzerland

Abstract

In the framework of the LHC Injector Upgrade (LIU) project the CERN PS injection kinetic energy will be upgraded from 1.4 to 2 GeV. The injection equipment, which is already operating close to its limit, is being redesigned to cope with 30% increase in the beam rigidity. In this paper we present the experimental results from Machine Development (MD) studies on the present septum to explore its operational hardware limits with respect to aperture restrictions, beam losses and kick strengths in view of the LIU upgrade.

INTRODUCTION

As part of the LIU project the injection kinetic energy of the CERN PS will be upgraded from 1.4 to 2 GeV to double the beams brightness. The BT-BTP transfer line and the PS injection scheme have been redesigned to have more flexibility and allow the injection at 2 GeV. Nevertheless PPM compatibility with beams at 1.4 GeV has to be ensured. The present layout of the injection region is presented in Fig. 1 which shows the bumper 42 and the septum between the main unit 41 and 42. The main features of the new injection system are: a five bumpers scheme, instead of the present four bumpers scheme, which gives a better control on the beam displacement in the injection area, and a low beta insertion for High Intensity (HI) beams with quadrupoles installed in SS33 and 49 to reduce the beam envelopes in the injection region and hence losses and hardware irradiation. The duration of the bump will be also halved from 2 to 1 ms. A new eddy current septum has been designed [1] and it will be installed in SS42, the physical length of new septum is 940 mm whereas the present septum is 620 mm. The bumper 42 will be a septum-like magnet and it will be hosted in the same vacuum vessel due to reduced longitudinal space availability. The new layout of the straight section 42 is presented in Fig. 2. Optics simulations on the beam envelopes of 2 GeV HI beams during injection [2] have shown that to minimise losses on the septum blade for the injected and circulating beams the optimal position of the future septum is 1 cm closer to the ring orbit with respect to the actual position (from 64 to 54 cm). These results triggered the interest to study the performance of the present septum position and angle and their relation with the observed losses due to the injection area aperture restrictions for HI beams and to verify that the LIU septum position is compatible with the more stringent requirements of HI beams at 1.4 GeV.

PS INJECTION BUMP AT 1.4 GEV

The PS injection scheme for proton (Fig. 3) is performed with a four bumpers scheme to control the orbit displacement

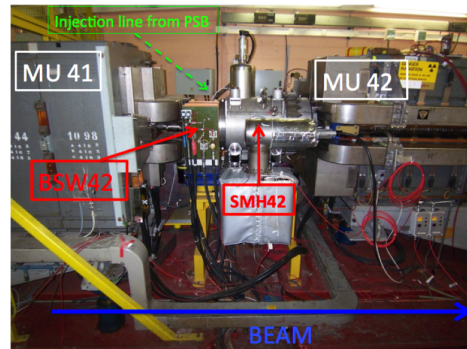


Figure 1: Present layout of SS42. From left to right: the MU41, the bumper 42, the septum 42 and the MU42.

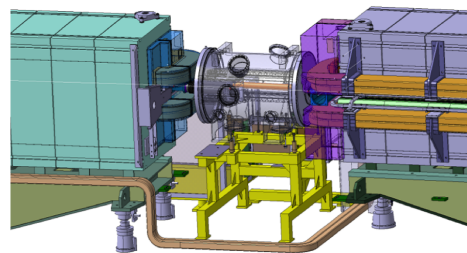


Figure 2: Layout of the SS 42 for the 2 GeV injection, the new eddy current septum in the centre and the main magnet unit 41 (on the left) and 42 (on the right).

and the slope of the bumped orbit. The septum bends the beam from BT-BTP line by 55 mrad (nominal value) and then it goes through the bumper 43 and 44, a kicker in SS45 operated in terminated mode gives the final 4.3 mrad kick to place the beam on the closed orbit. For a given position and angle of the injected beam at the septum flange the bumpers 43, 44 are matched to steer the injected beam with zero horizontal orbit displacement in the kicker 45. The bumpers 40 and 42 are then matched to close the bump for the circulating beam. Operationally the strength of the septum, kicker and bumpers are optimised for each different beam to minimise losses, injection oscillations and the bump closure. The present injection septum design has operated reliably since last PS injection energy upgrade from 1 to 1.4 GeV in 1999. The designed position of the septum was 56 mm from the ring closed orbit but it was moved to 64 mm in the following years to reduce losses during injection of HI beams [3]. For the experiment we used a TOF beam with currents and kick angles of the injection bumpers reported in Table 1.

* maurizio.serluca@cern.ch

Table 1: Currents and relative kick angles of the bumpers for TOF beam.

Element	BSW40)	BSW42	BSW43	BSW44
I [A]	846.52	3500.9	3131.75	1384.69
Θ [mrad]	3.32	13.72	12.27	5.43

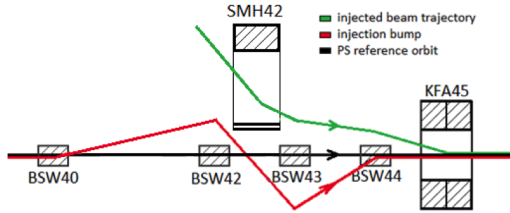


Figure 3: A schematic of the four bumpers injection at 1.4 GeV with $\pi/2$ phase advance between BSW40 and BWS44 [not to scale]. The injected beam trajectory from the transfer line in green and the bumped orbit in red.

THE MD: SETUP AND MEASUREMENTS

To study the effect of the septum position and angle on the beam passage through the injection apertures a dedicated MD has been performed on July 13th 2016. A TOF beam with an intensity of $800 \cdot 10^{10}$ ppb was chosen to explore the highest emittances and intensity which impose the most stringent requirements regarding aperture restrictions. The intensity evolution during the magnetic cycle is shown in Fig. 4 where the cyan line represents the intensity. The initial slope of the curve represents the injection losses, about 5% for HI beams. The measurements of the longitudinal phase space with the tomoscope and the horizontal emittance with the wirescanner are presented in Fig. 5 and 6, respectively. The longitudinal emittance is 2.75 eV s and the horizontal emittance is 17.4 mm mrad. The MD strategy has been to move the septum position and angle while adjusting the injection bump and recording the losses measured by the BLM42 due to the transverse beam tails scraped by the septum blade. A fast diamond BLM installed on the main unit 42 was also connected to an OASIS channel to record the fast losses generated by the injected beam on the inside part of the septum blade. The position of the fast BLM on the main unit 42 is shown in Fig. 7. An optimisation of the strength of the septum and kicker 45 was done by using the YASP injection steering tool in order to minimise the amplitude oscillation in the BPMs and, hence, to improve the bump closure. An example of orbit acquisition of the BPMs during injection after optimisation is shown in Fig. 8. The large oscillation signal is due to a malfunctioning pickup whereas the green line starting from -30 mm is the pickup signal in the SS43, which shows the amplitude-varving bump.

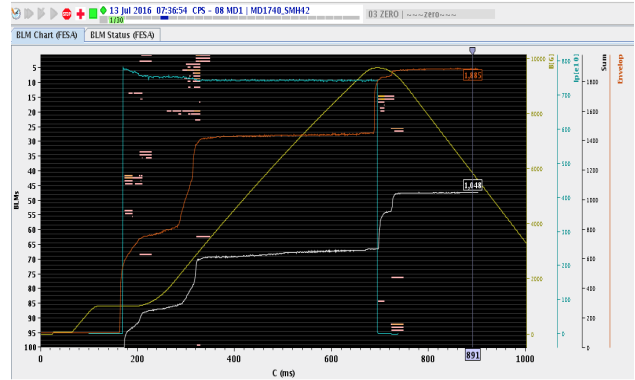


Figure 4: Intensity evolution (cyan line) during the magnetic cycle (yellow line) for TOF beam.

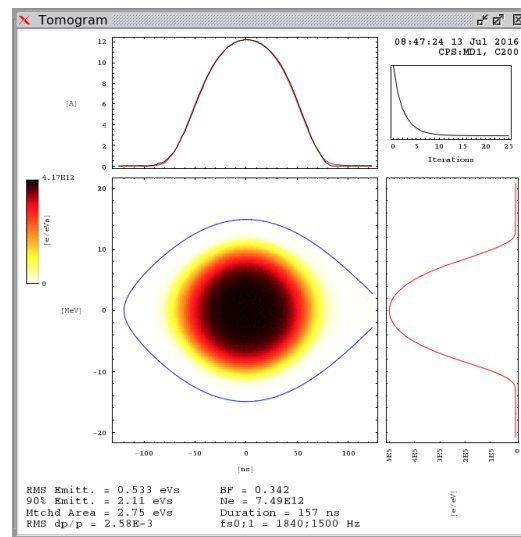


Figure 5: Longitudinal phase space for TOF beam as reconstructed by the tomoscope. The longitudinal emittance is 2.75 eV s.

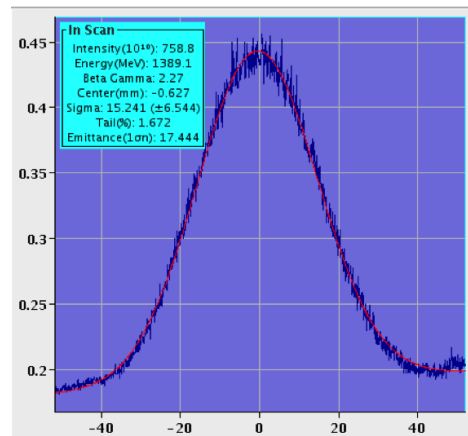


Figure 6: Wirescanner emittance measurement for TOF beam. The horizontal emittance is 17.44 mm mrad.

RATIONALE, PROCEDURE AND MEASUREMENT RESULTS

The rationale of the MD was to produce a map of losses



Figure 7: The white arrow in the picture indicates the position of the fast BLM on the top of main unit 42.

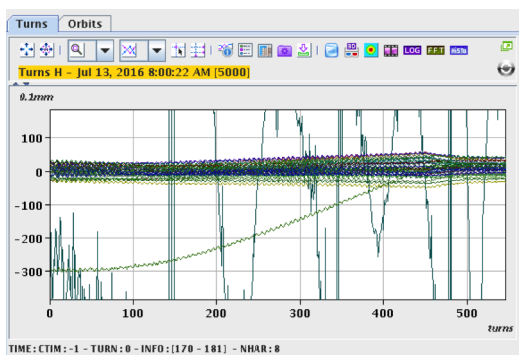


Figure 8: Example of horizontal turn-by-turn trajectory acquisition for TOF beam. Each line represents the acquisition of different pickups along the ring. The large oscillation signal is due to a malfunctioning pickup whereas the green line starting from -30 mm is the pickup signal in the SS43, which shows the amplitude-varying bump.

timization of the injection. The procedure was to move the septum from the original horizontal position of 64 mm towards the minimal value of 53 mm from the beam axis while recording the BLMs signal along the ring and the fast diamond BLM42 connected to an OASIS channel (e.g. Fig. 9). Then the trajectory of the injected beam was optimised with the septum and kicker to minimise losses. At the same time we lowered the bump height to reduce losses of the circulating beam. The measured scanned position and angle of the septum during the MD are presented in Fig. 10, the currents in the bumpers, kicker and septum in Fig. 11 and the recorded signal in the BLMs in Fig. 12. A total of about 3 thousand acquisitions were recorded in the 5 hours MD. The acquisitions are divided in 9 areas: (1) The first tens of acquisitions were done for the nominal setting of 64 mm and 10 mrad position and angle of the septum. The average signal in the BLM 42 was 23 ADC bits. (2) The angle of the septum was moved to its minimum value of 1 mrad, higher losses were recorded while decreasing the angle indicating that the beam was scraped on the inside part of the septum blade. (3) After that the angle was set to 13 mrad and the position was reduced to 54 mm with 1 mm step. During

the scan the BLM42 signal reduced down to 10 ADC bits and then it increased again at a position of 54 mm and an angle of 10 mrad. (4) At this point the fast diamond BLM was connected to the OASIS channel and we tested it by using the PS internal dump to disentangle the losses from the injected beam. (5) The acquisitions with the internal dump can be identified in Fig. 12 as the places where the BLM42 signal goes to zero and the signal from BLM 47 increases. An example of the OASIS signal acquisition is shown in Fig. 9, where the green line indicates the fast diamond BLM signal whereas the yellow line indicates the BLM 42 signal. (6) At 9:30 we reduced the bump height by lowering the strength of the bumpers and optimising the septum and kicker 45 currents. The bumper strength was reduced by 25% and the septum strength was increased by 4.2% while the kicker 45 was increased by 10%. The reduction of losses in the BLM42 is visible around 10:30 indeed for an angle of 10 mrad and the position varied from 54 to 60 mm the BLM42 indicates a constant value of 8 ADC bits. (7) For position higher than 60 mm the BLM42 signal starts to increase up to 40 ADC bits. (8) Acquisitions between 10:50 and 11:50 were done to see the effects on the BLM42 with the optimised bumpers, kicker and septum strengths. (9) We performed an automatized scan on septum position and angle. In Fig. 13 we present the results of the scan using the entire range of the BLM42. It shows that positions between 55 and 60 mm give the lowest BLM values. The same results with the data filtered to values below 8 ADC bits are presented in Fig. 14. The plot indicates that for positions between 57 and 59 mm and angles between 8 and 11 mrad we get the lowest BLM read of about 6 ADC bits. The same analysis has been done with the fast diamond BLM and the integrated signal in OASIS. The results shown in Fig. 15 and 16 confirm that losses are reduced for a lower position of the septum.

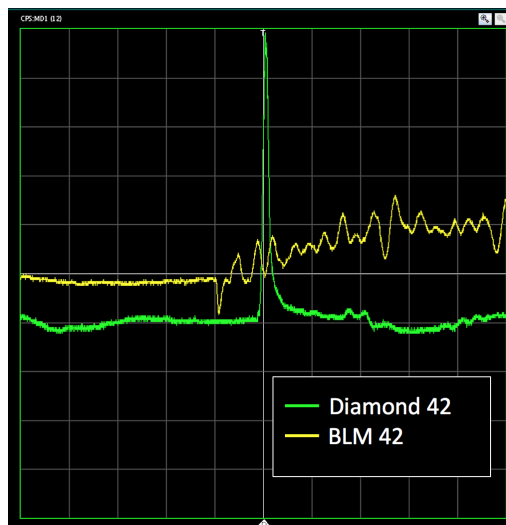


Figure 9: Acquisition example of Oasis slow BLM42 signal (yellow line) and diamond fast BLM42 (green line).

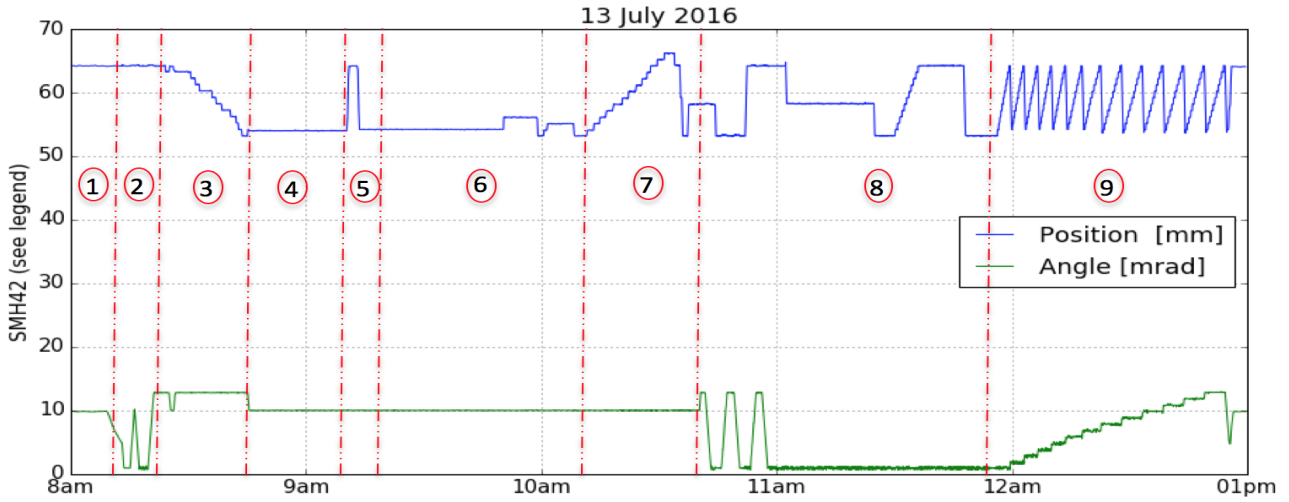


Figure 10: Acquisition of the septum position and angle variations during the MD for TOF beam.

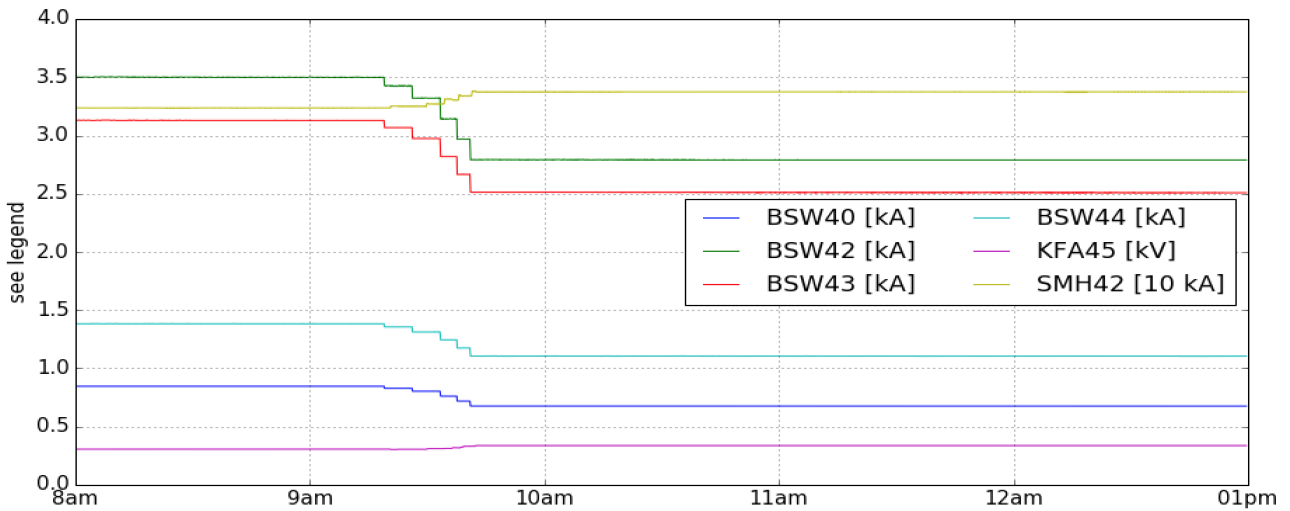


Figure 11: Bumpers, kicker and septum currents during the MD for TOF beam.

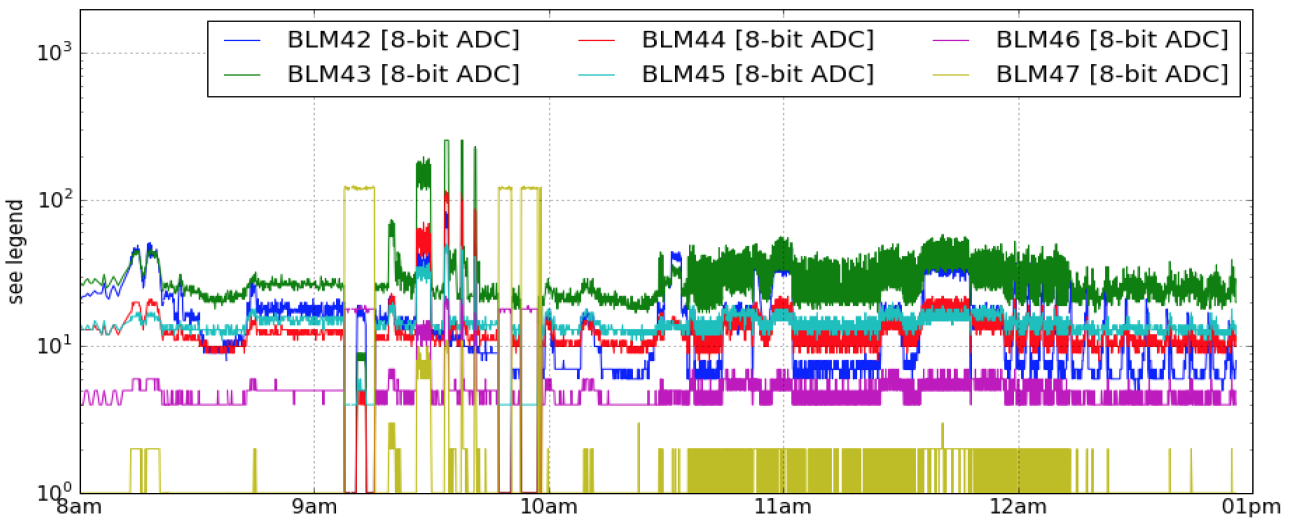


Figure 12: Measured losses in the BLMs downstream the injection section 42 for TOF beam.

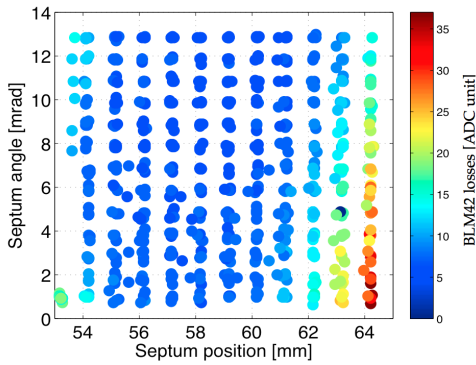


Figure 13: Results of the scan in position and angle for TOF beam. The colour scale is the BLM42 signal.

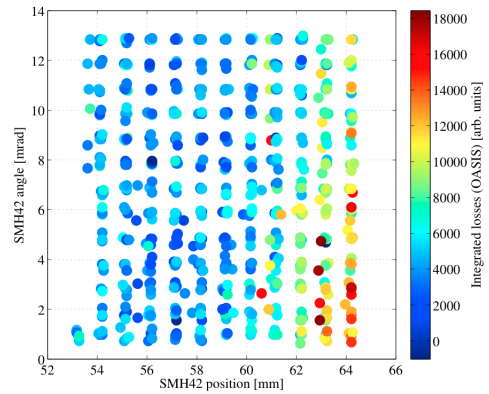


Figure 16: Results of the scan in position and angle for TOF beam. The colour scale is the integrated losses in OASIS.

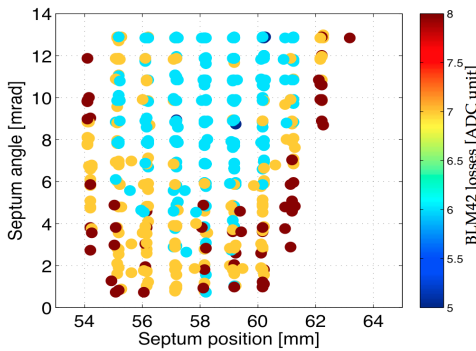


Figure 14: Results of the scan in position and angle for TOF beam. The colour scale is the BLM42 signal. The data have been filtered between 5 and 8 ADC bits.

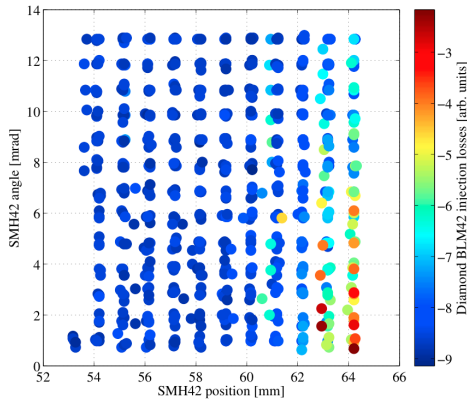


Figure 15: Results of the scan in position and angle for TOF beam. The colour scale is the Diamond BLM42 signal.

EFFECTS ON OTHER BEAMS IN THE PS: SFTPRO AND AD TYPE BEAMS

During the dedicated MD we decided to keep all the production beams in the cycle and measure the beam losses due to the septum position and angle. The septum, kicker and bumpers strengths were not optimised for these beams. The scanned positions and angles, the injection elements strength and the BLM readings for SFTPRO beam are presented in Fig. 19, 20 and 21, respectively. The colour map scan is

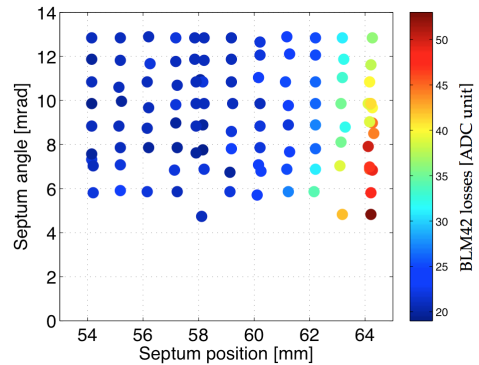


Figure 17: Results of the scan in position and angle for SFTPRO beam. The colour scale is the BLM42 signal.

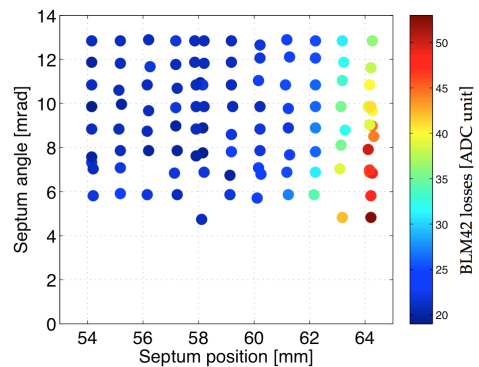


Figure 18: Results of the scan in position and angle for SFTPRO beam. The colour scale is the BLM42 signal. The data have been filtered between 19 and 25 ADC bits.

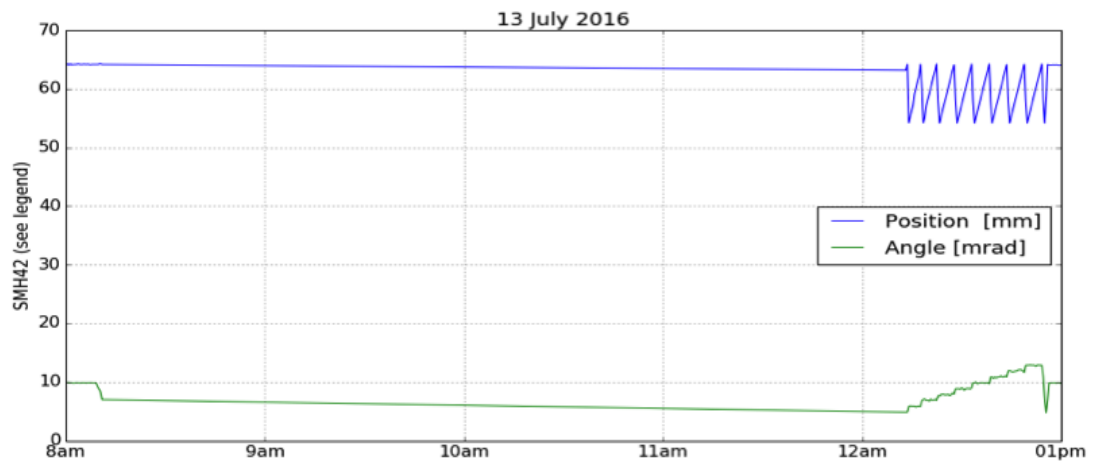


Figure 19: Acquisition of the septum position and angle variations during the MD for SFTPRO beam.

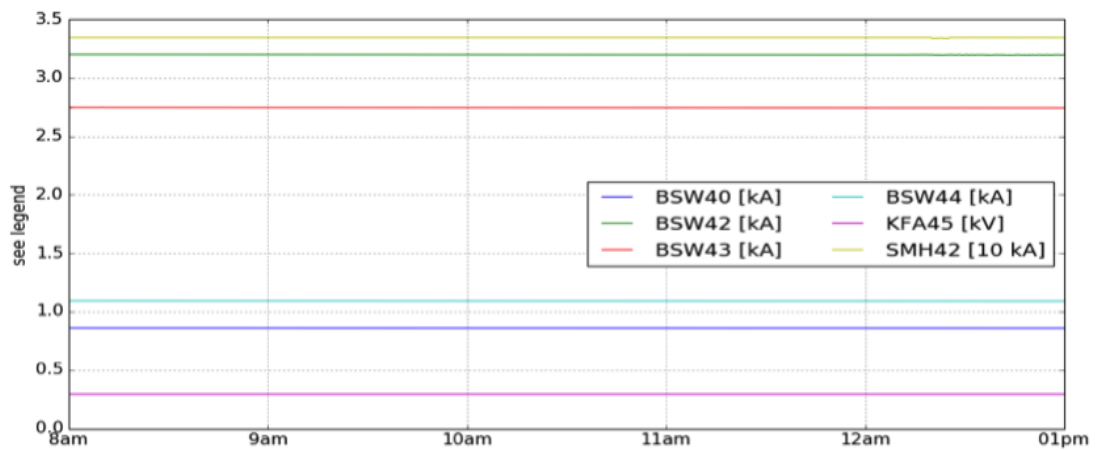


Figure 20: Bumpers, kicker and septum currents during the MD for SFTPRO beam.

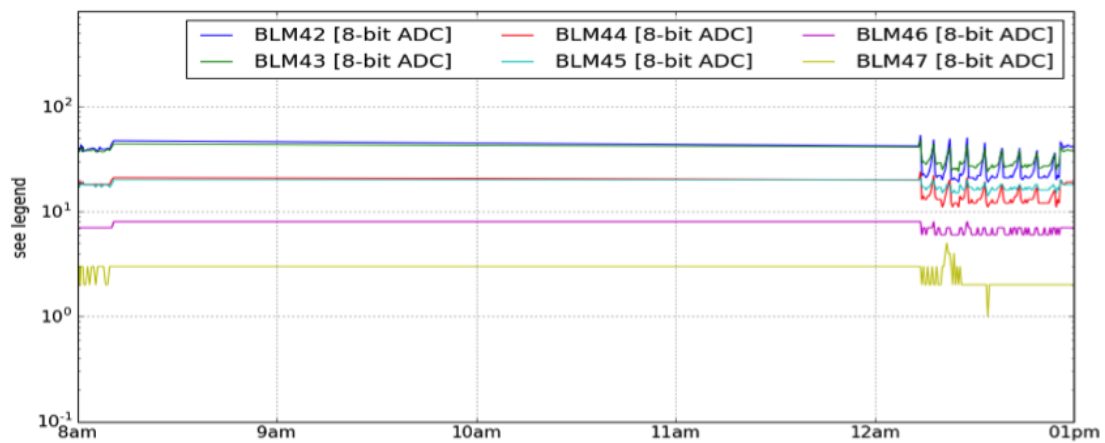


Figure 21: Measured losses in the BLMs downstream the injection section 42 for SFTPRO beam.

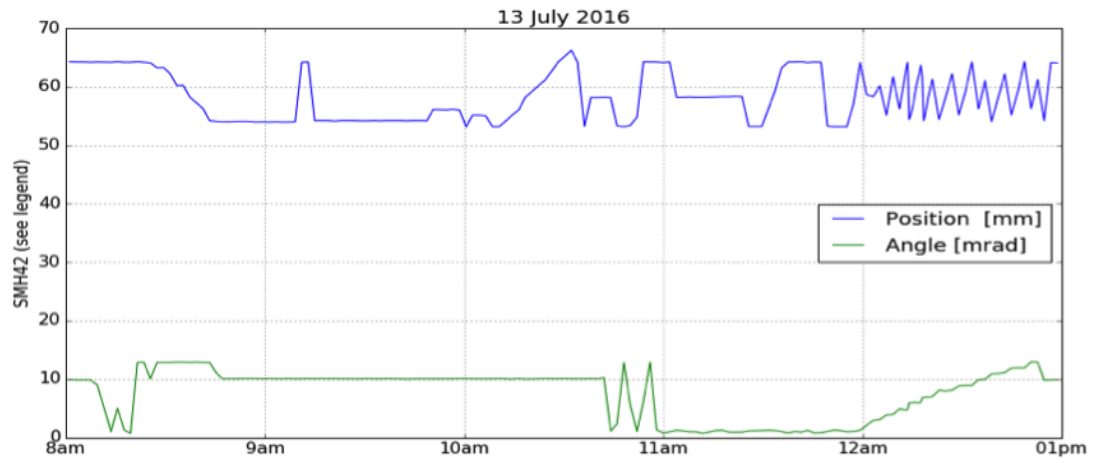


Figure 22: Acquisition of the septum position and angle variations during the MD for AD beam.

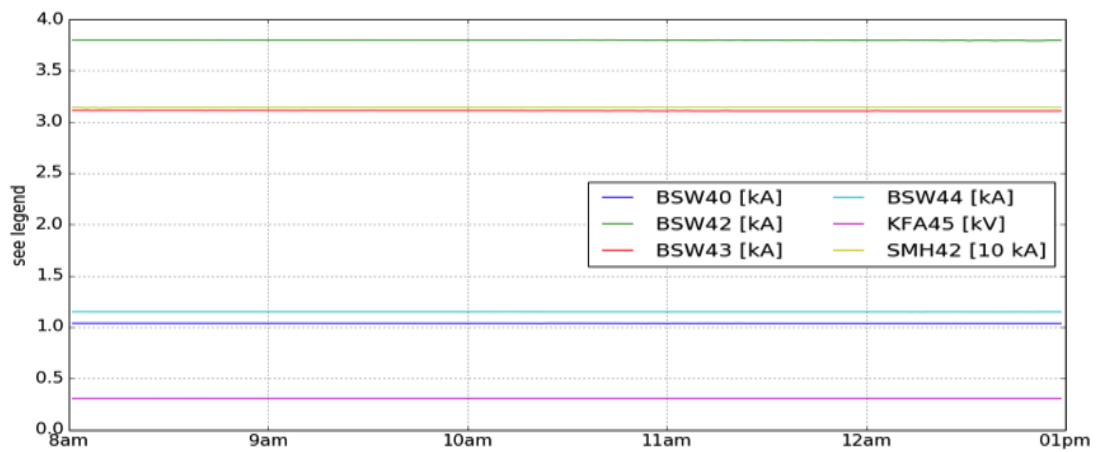


Figure 23: Bumpers, kicker and septum currents during the MD for AD beam.

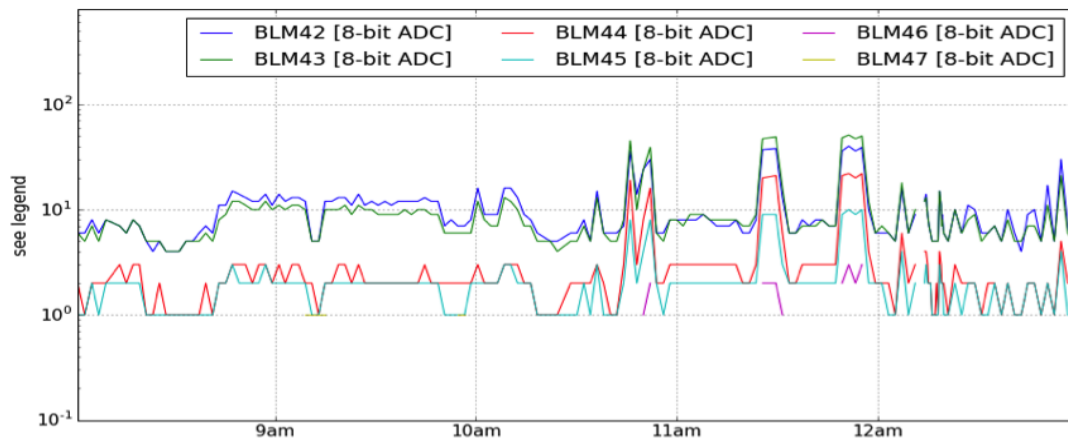


Figure 24: Measured losses in the BLMs downstream the injection section 42 for AD beam.

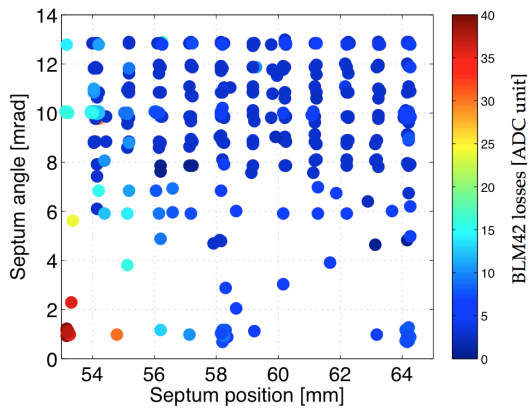


Figure 25: Results of the scan in position and angle for SFTPRO beam. The colour scale is the BLM42 signal.

CONCLUSION

A dedicated MD has been performed to optimise the septum position and angle in view of the LIU upgrade. The

results were very positive. They show that lowering the position of the septum and adjusting its angle it is possible to reduce losses in the injection area of the PS ring. This solution could be also applied to the present system with the drawback of increasing the septum strength by 4.2% and push it close to its maximum value.

ACKNOWLEDGEMENT

We wish to thanks the PS operation team for the support during the MD and Ewald Effinger for helping us in the setting of fast diamond BLM42.

REFERENCES

- [1] J. Borburgh *et al.*, “Specification for the 2 GeV PS Proton Injection Septa” in *EDMS*, 1477011
- [2] J. Abelleira and M. Serluca, “PS Injection Septum Position and Injection Bump at 2.0 GeV” in *EDMS*, 1557577 rev. 1.1
- [3] J. Borburgh, private communication, Jun. 2016.

LONGITUDINAL COUPLED-BUNCH INSTABILITY STUDIES IN THE PS

H. Damerau, L. Ventura*, CERN, Geneva, Switzerland

Abstract

The main longitudinal limitation for LHC-type beams in the PS are coupled-bunch instabilities. A dedicated prototype feedback system using a Finemet cavity as a longitudinal kicker has been installed. Extensive tests with beam have been performed to explore the intensity reach with this feedback. The maximum intensity with nominal longitudinal emittance at PS extraction has been measured, as well as the emittance required to keep the beam longitudinally stable at the design intensity for the High-Luminosity LHC (HL-LHC). A higher-harmonic cavity is a complementary option to extend the intensity reach beyond the capabilities of the coupled-bunch feedback. Preliminary machine development (MD) studies operating one 20 MHz or one 40 MHz RF system as a higher harmonic at the flat-top indicate the beneficial effect on longitudinal beam stability.

INTRODUCTION

To reach the beam parameters requested for the HL-LHC the PS is being upgraded in the framework of the LHC Injector Upgrade (LIU) project to deliver an intensity of $2.6 \cdot 10^{11}$ particles per bunch (ppb) with 25 ns bunch spacing. In the longitudinal plane the emittance must remain unchanged, hence doubling the longitudinal density with respect to the intensity threshold above which longitudinal coupled-bunch instabilities are observed after transition crossing and at the flat-top [1]. A prototype Finemet cavity [2] has thus been installed as a wide-band longitudinal kicker, driven by a functional prototype of the coupled-bunch signal processing covering all possible dipole oscillation modes [3,4].

An extensive series of MD studies has been performed in 2016 to understand and resolve technical issues related to the signal processing of the feedback and the Finemet cavity, as well as to explore the performance reach for LHC-type beams with the new feedback system. The technical issues include the frequent trips of the wide-band cavity due to over-current of the power amplifiers and the availability of a maximum number of the in total six acceleration gaps. On the low-level RF side the phasing of the filters of the signal processing and their reliable re-synchronization with respect to circulating bunch train has been treated. The first part of this contribution concentrates on the beam dynamics aspects, covering the measurements of coupled-bunch mode spectra and the maximum intensity reach.

For RF manipulations like bunch splitting and bunch rotation the PS is equipped with high-frequency RF cavities at 20 MHz, 40 MHz and 80 MHz. Due to their narrow bandwidth these cavities cannot sweep with the increasing revolution frequency during acceleration, but can only be operated

once flat-top energy has been reached. In the second part results of first studies operating a 20 MHz or 40 MHz cavity as higher-harmonic Landau cavity to longitudinally stabilize the beam at the flat-top are presented.

INTENSITY REACH WITH FEEDBACK

Maintaining the nominal longitudinal emittance of $\varepsilon_l = 0.35$ eVs per bunch, corresponding to about 4 ns (4σ Gaussian fit) bunch length at extraction, the intensity has been increased with the prototype wide-band coupled-bunch feedback. The important stability improvement is illustrated in Fig. 1. At an intensity of $2.0 \cdot 10^{11}$ ppb at extraction, the beam

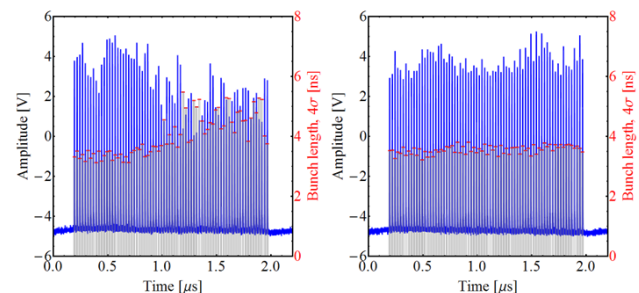


Figure 1: Beam profile during the last turn at $2.0 \cdot 10^{11}$ ppb together with the bunch length along the batch without (left) and with the coupled-bunch feedback switched on (right).

is longitudinally destroyed due to the coupled-bunch instability. Considering the short filling time of the 10 MHz cavities as dominant impedance source, the bunches at the tail of the batch are more strongly affected than the first bunches after the extraction kicker gap. The instabilities are fully suppressed when activating the dedicated feedback system. The bunch length at extraction remains below 4 ns all along the batch and no lengthening is observed for the tail bunches. The longitudinal beam quality reached at $2.0 \cdot 10^{11}$ ppb is equivalent to the beam quality at $1.3 \cdot 10^{11}$ ppb without the coupled-bunch feedback. It is worth noting that this performance has been maintained reliably under operational conditions during the 2016 accelerator run. Slightly higher peak intensity has been reached during short tests.

With the wide-band coupled-bunch feedback even higher intensity has only been achieved with larger longitudinal emittance so far. This emittance is too large for the SPS, but to exclude further longitudinal issues in the PS up to the intensity required for HL-LHC, measurements have been performed up to $2.6 \cdot 10^{11}$ ppb, which corresponds to a total intensity of almost $2 \cdot 10^{13}$ protons per pulse (ppp). Figure 2 shows intensity and transmission during a ramp-up test with a longitudinal emittance of about $0.45 \dots 0.5$ eVs.

Even at the intensity as requested at PS extraction for the HL-LHC project, the overall transmission stays at 97 %.

* New affiliation: Centre for Quantum Technologies, National University of Singapore

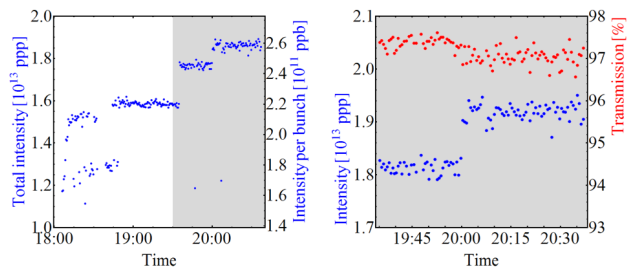


Figure 2: Total intensity together with intensity per bunch during the ramp-up (left), and overall transmission (right, ratio of extracted and sum intensity of both injections).

well above the 5% loss margin and does not degrade significantly with increased intensity. However, a number of technical difficulties was encountered which complicated the measurements. Only the absolute minimum number of cavity gaps of the 40 MHz (one cavity in straight section SS78) and 80 MHz (two cavities in SS88 and SS89) has been kept open. The remaining cavities would trip due to excessive beam-loading, even in the absence of a voltage program. Additionally, some 10 MHz cavities did not follow their voltage program and indicated an over-current of the final amplifier when tuning them from $h = 20$ to 7 at the end of the flat-bottom [5]. This was solved by activating the 1-turn delay feedbacks only later, at the start of acceleration, to reduce the final amplifier current. Although longitudinal emittance and bunch length required to keep the bunches longitudinally stable at extraction are yet too large for the SPS, the excellent overall transmission and beam quality show that no further show-stopper is in sight to reach the targeted intensity of $2.6 \cdot 10^{11}$ ppb.

QUADRUPOLE COUPLED-BUNCH OSCILLATIONS

While dipole coupled-bunch oscillations are well damped by the wide-band coupled-bunch feedback when increasing longitudinal density, quadrupole coupled-bunch oscillations can be excited during acceleration and at the flat-top. Figure 3 shows a typical measurement of bunch length oscillations with a phase advance from bunch to bunch observed after transition with an 18-bunch train accelerated on harmonic, $h = 21$. A discrete Fourier transform of amplitudes and phases of the bunch length oscillations reveals the mode spectrum (Fig. 4). The predominant mode number, $n_b = 2$, corresponding to a phase advance of $\Delta\phi = 2\pi n_b/18 = 2\pi/9$, is observed with 18-bunch trains during acceleration. This is very different from the dipole oscillation mode spectrum, where usually the low ($n_b = 1, 2$) and high ($n_b = 16, 17$) modes are strongest [1].

At the flat-top the longitudinal impedance of the PS changes for two reasons. While all 10 MHz cavities are needed during acceleration, the gaps of nine of these cavities are consecutively short-circuited with relays (two relays per cavity) at the flat-top. Secondly, due to the sweeping revolution frequency, the dominant spectral components of

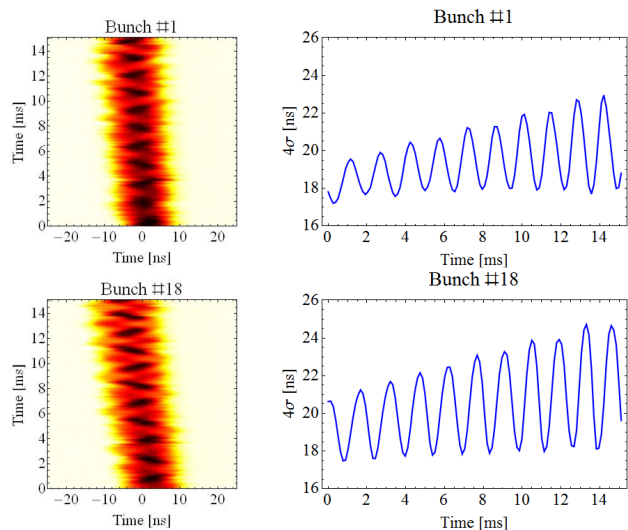


Figure 3: Bunch length oscillations of first and last bunch of an 18-bunch train during acceleration after transition crossing.

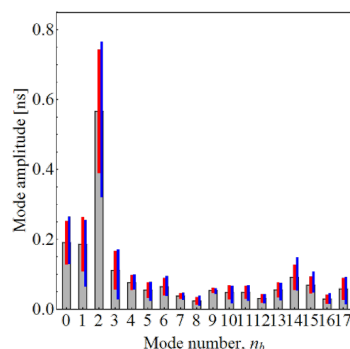


Figure 4: Average quadrupole coupled-bunch mode spectrum of ten cycles during acceleration. The red bars indicate the standard deviation, and the blue bars represent the total spread.

the beam at multiples of the RF frequency ($h = n \cdot 21$, $n = 1, 2, \dots$) move into the fixed resonances of the RF cavities at 40 MHz ($n = 4$) and 80 MHz ($n = 8$). The quadrupole coupled-bunch spectrum at the flat-top is shown in Fig. 5. Interestingly with the pre-dominant mode numbers around $n_b = 5$, the mode spectrum is extremely similar to the dipole mode spectrum (Fig. 6).

EFFECT OF 80 MHZ CAVITY IMPEDANCE

Part of the measurements have been acquired during parallel proton and lead ion operation. The influence of the impedance of the additional 80 MHz cavity for the bunch shortening with ions, tuned at 230 kHz below the frequency for protons, has been studied. A significant bunch lengthening, notably for bunches at the tail of the batch, becomes evident and had already been observed earlier [6].

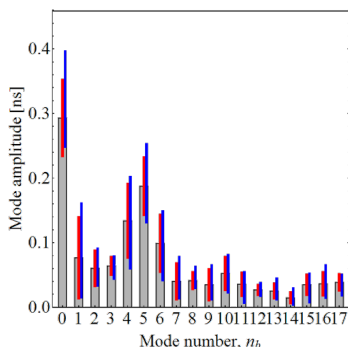


Figure 5: Average quadrupole coupled-bunch mode spectrum of ten cycles at the flat-top.

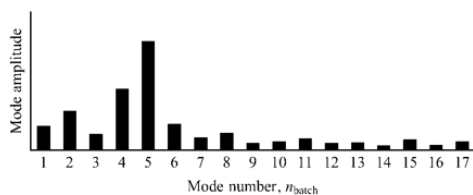


Figure 6: Average dipole coupled-bunch mode spectrum of ten cycles at the flat-top (from 2011 data).

The perturbation due to the impedance from an additional 80 MHz cavity can be directly seen during the last bunch pair splitting from $h = 42$ to 84 at the flat-top and with equivalent intensity of $1.6 \cdot 10^{11}$ ppb (Fig. 7). The high frequency

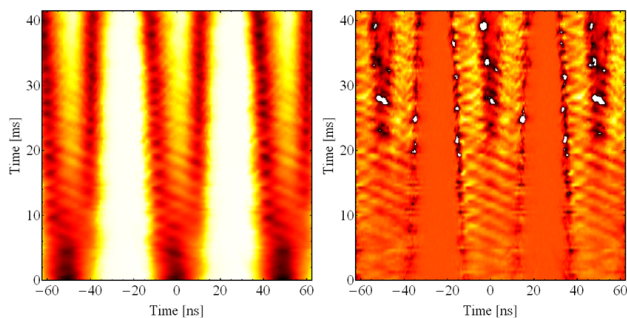


Figure 7: Mountain range plot of the bunch splitting from $h = 42$ to 84 with the gap of the third 80 MHz gap open (left). Averaging and subtracting this from the same data with the third cavity gap closed (right) clearly reveals the high frequency structure.

structure becomes much more pronounced with the gap of the 80 MHz cavity for ion operation open. Additionally, the relative phase of the high-frequency structure remains similar from cycle to cycle, confirming that the perturbation must be induced by the beam.

The degradation of the longitudinal beam quality becomes also evident from the bunch length along the batch at extraction, which is compared for two and three open gaps of 80 MHz cavities in Fig. 8. The average bunch length increases by about 300 ps due to the additional impedance, but up to 600 ps for the bunches at the tail of the batch.

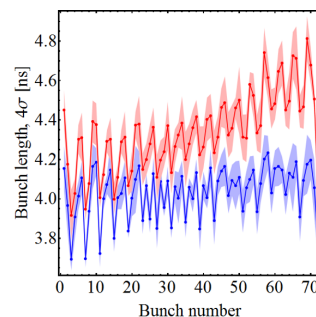


Figure 8: Bunch length along the batch at an intensity of $1.6 \cdot 10^{11}$ ppb with two (blue) and three (red) gaps of 80 MHz cavities open. The shaded areas indicate the spread of the ten cycles taken for the average.

These measurements underline the importance of the multi-harmonic feedback systems for the high-frequency cavities under development in the framework of the injector upgrades.

LANDAU RF SYSTEM STUDIES

While the PS presently has no tunable RF system that could be operated as a higher-harmonic RF system in addition to the ferrite-loaded cavities at $h = 21$, MD studies have been conducted at the flat-top using a 20 MHz or a 40 MHz at low voltage as a Landau RF system. Stopping the bunch splitting manipulations at the flat-top a beam with an equivalent intensity of $1.3 \cdot 10^{11}$ ppb (respectively four times that intensity without the splittings) develops a coupled-bunch oscillation when held at the low RF voltage of 20 kV at $h = 21$ with a single 10 MHz cavity.

Adding RF voltage at the second harmonic (20 MHz) of the principal RF system yields a slight improvement of the longitudinal stability when the higher-harmonic RF system is in counter-phase (bunch lengthening mode), confirming previous measurements under similar conditions [7].

However, only about 5 kV at $h = 84$ in phase (bunch shortening mode) from a 40 MHz cavity is sufficient to fully stabilize the beam and a significant stability improvement can be measured down to a higher-harmonic voltage as low as 2 kV. This technique is well known from the SPS where it is essential to stabilize the beams for the LHC [8]. With the harmonic number ratio of $84/21 = 4$, the beneficial effect is only seen in phase. Adding higher-harmonic RF voltage in counter-phase has a negligible effect on longitudinal stability as illustrated by the mode spectra shown in Fig. 9.

Figure 10 illustrates the synchrotron frequency distribution for the beneficial case of a harmonic number ratio of four and the given percentage of RF voltage at the higher-harmonic RF system with respect to the principal one. The synchrotron frequency spread is significantly increased in the relevant emittance range of up to $1.4 \text{ eVs} = 4 \cdot 0.35 \text{ eVs}$, even for a moderate voltage in the higher-harmonic cavity.

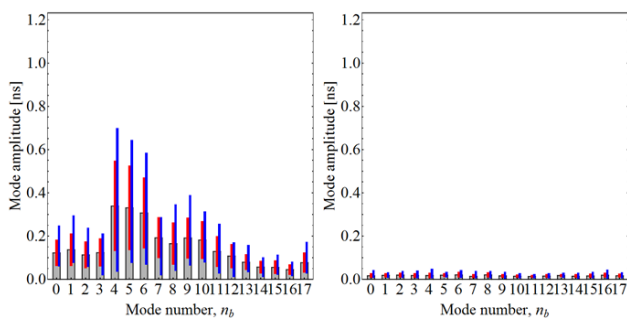


Figure 9: Coupled-bunch mode spectrum at the flat-top with an RF system at four times the fundamental harmonic and 5 kV RF voltage, i.e., one quarter of the 20 kV in the principal RF system. The higher-harmonic voltage has been brought up in counter-phase (left), as well as in phase (right).

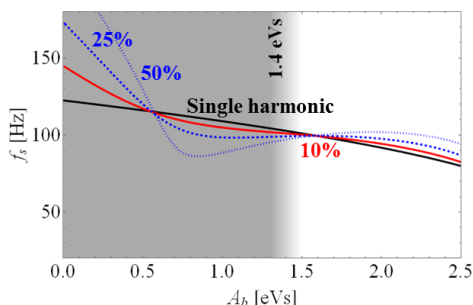


Figure 10: Synchrotron frequency versus single particle emittance for a harmonic ratio of four and different voltage ratios, given in percent of the principal harmonic voltage of 20 kV at $h = 21$. Both RF systems are in phase.

CONCLUSIONS

The MD campaign with the new wideband coupled-bunch feedback in 2016 has demonstrated that $2.0 \cdot 10^{11}$ ppb with 25 ns spacing and the nominal batch length of 72 bunches can be achieved and maintained under operational conditions. Beyond this intensity the longitudinal emittance must be blown-up further by almost 40% to keep the beam longitudinally stable up to the intensity of the HL-LHC request of $2.6 \cdot 10^{11}$ ppb. However, accelerating a total intensity of more than $72 \cdot 2.6 \cdot 10^{11}$ ppb $\approx 1.9 \cdot 10^{13}$ ppb with losses well below 5% shows that no further longitudinal show-stopper is expected.

Initial studies with higher-harmonic RF voltage from a 20 MHz or 40 MHz cavity indicate the beneficial effect on

longitudinal stability depending on the relative phase with respect to the principal RF system. In particular operating a 40 MHz in phase, as used in for LHC-type beams in the SPS, suppresses the coupled-bunch bunch oscillations efficiently. Further studies at higher intensity are foreseen in 2017.

ACKNOWLEDGEMENTS

The authors would like to thank Matthias Haase and Mauro Paoluzzi for their effort to maximise the availability of the Finemet cavity, as well as the operations team for the support of the studies. They are also grateful to Steven Hancock, Wolfgang Höfle and Elena Shaposhnikova for discussions.

REFERENCES

- [1] H. Damerau, S. Hancock, M. Schokker, “Longitudinal Performance with High-Density Beams for the LHC in the CERN PS,” ICFA-HB2010, Mohrschach, Switzerland, 2010, p. 193.
- [2] H. Damerau, M. Paoluzzi, “Design of the PS longitudinal damper,” CERN-ACC-NOTE-2013-0019, CERN, Geneva, Switzerland, 2013.
- [3] H. Damerau, M. Paoluzzi, D. Perrelet, L. Ventura, “Signal processing for the coupled-bunch feedback in the CERN PS,” LLRF’15, Shanghai, China, 2015.
- [4] H. Damerau, M. Migliorati, G. Sterbini, L. Ventura, “Excitation of Longitudinal Coupled-bunch Oscillations with the Wide-band Cavity in the CERN PS,” IPAC’16, Busan, Korea, 2016, p. 1724.
- [5] H. Damerau, L. Ventura, “Studies with the PS coupled-bunch feedback and recent simulations,” Unpublished presentation at Machine Studies Working Group, CERN, Geneva, Switzerland, 2017, <https://indico.cern.ch/event/603263/contributions/2433359/attachments/1406779/2149871/CoupledBunchStudies2016MSWG.pdf>.
- [6] H. Damerau, “Bunch Length along the Batch of the LHC Beam at Extraction from the PS,” AB-Note-2008-052 (MD), CERN, Geneva, Switzerland, 2008.
- [7] C. M. Bhat, F. Caspers, H. Damerau, S. Hancock, E. Mahner, F. Zimmermann, “Stabilizing Effect of a Double-harmonic RF System in the CERN PS,” PAC’09, Vancouver, Canada, 2009, p. 4670.
- [8] T. Bohl, T. Linnecar, E. Shaposhnikova, “Beam Transfer Functions and Beam Stabilisation in a Double RF system,” PAC’05, Knoxville, USA, 2005, p. 2300.

LOSSES ON SPS FLAT BOTTOM AND BEAM LOADING WITH LHC BEAMS

H. Bartosik*, T. Bohl, S. Cettour Cave, K. Cornelis, H. Damerau, B. Goddard, V. Kain, A. Lasheen, G. Rumolo, E. Shaposhnikova, H. Timko, CERN, Geneva

Abstract

Losses at SPS flat bottom with the LHC proton beams had been studied since the earliest days the LHC beams became available in the SPS. Some of the loss mechanisms involved could be identified and over the years of operation with the nominal 25 ns LHC beam, the losses could be gradually reduced. Nevertheless, in machine studies with high intensity 25 ns LHC beams it is still observed that the transmission degrades with intensity. As summarised in this paper, a series of studies have been performed in 2016 with the aim of further characterising the loss mechanisms and eventually finding mitigation measures in view of the LHC injector upgrade project (LIU).

INTRODUCTION

Losses at SPS flat bottom with the LHC proton beams had been studied since the earliest days the LHC beams became available in the SPS. The conclusions of four reports are summarized below to illustrate the understanding of the losses at certain times.

Historical context

2000 In 2000 the following was reported [1]: A total intensity of 1×10^{13} in three batches was accelerated to top energy with a transmission efficiency of 70%. Continuous particle losses are observed on the flat bottom for high intensities. The reason is not clear. The high intensity beam is unstable on the flat top independent of the final voltage value, however the situation seems to be worse for lower voltage. Limitations to the intensity are a) too large a longitudinal emittance sent by the PS for intensities above 3×10^{12} per batch, b) the acceptance of the SPS in connection with this large injected emittance and c) possibly noise in RF loops (causing additional emittance blow-up).

2004 In 2004 the following was reported [2]: While nominal LHC beams have been accelerated in the SPS, transmission loss is important for future intensity increases. Capture losses are due to a combination of injected bunch length, injection errors and bucket size reduction due to energy loss. The losses along the injection plateau are not fully understood. The effect of coherent lines in the presence of white noise, the effect of the transverse working point, and the influence of low-amplitude instabilities on parts of the batch have been seen but do not explain the whole picture. In addition the possible presence of ions could have an effect, which should be studied. Similar effects in the LHC itself could have serious consequences, the injection plateau at

450 GeV/c being 20 min long with no synchrotron radiation damping, which conversely will have a significant effect at 7 TeV.

2006 The following was reported at the LHC Machine Advisory Committee [3] in December 2006: A reduction of the low energy losses from >10 to 7-8% was achieved by a) a new RF voltage programme (end of 2003) and b) a new working point compatible with larger momentum spread (end of 2004) and large vertical chromaticity required to fight the ECI (see Fig. 1). Short lifetime on the injection plateau was observed even after optimization of the working point. The longitudinal lifetime dominates (capture losses due to real part of the longitudinal impedance and the bunch shape), which should be improved by impedance reduction and optimization of the bunch shape from PS. The difference in lifetime between the head and the tail of the batch recovers as the intensity decreases: Bunches are getting shorter particularly at the tail of the batch ... while the electron cloud signal disappears. Need to understand better the blow-up and loss mechanisms at the beginning of the ramp (mainly on the tail of the 4th batch).

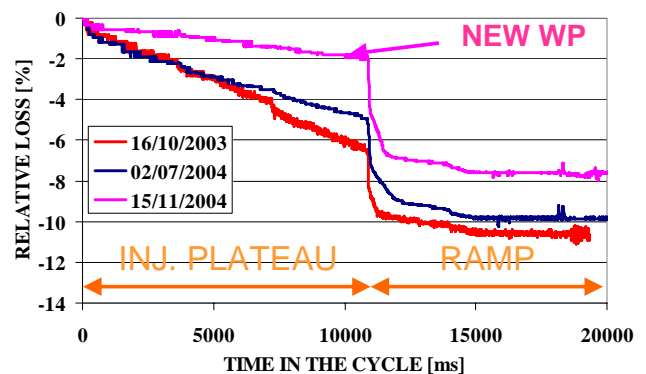


Figure 1: Losses for different working points, taken from [3].

2012 In 2012 the following was reported [4]: Detailed simulations of the PS-to-SPS longitudinal beam transfer determined the main longitudinal beam loss mechanism in the SPS. The simulated longitudinal phase-space distribution of a typical bunch after the PS rotation, at injection into the SPS bucket is shown in Fig. 2. The simulations demonstrated that using the minimum bunch length at PS-to-SPS transfer as a criterion for best transmission is not necessarily appropriate; instead, the phase-space bunch distribution should be optimised as a function of the bunch rotation timings used in the PS. Systematic measurements with 36 bunches of LHC-type

* hannes.bartosik@cern.ch

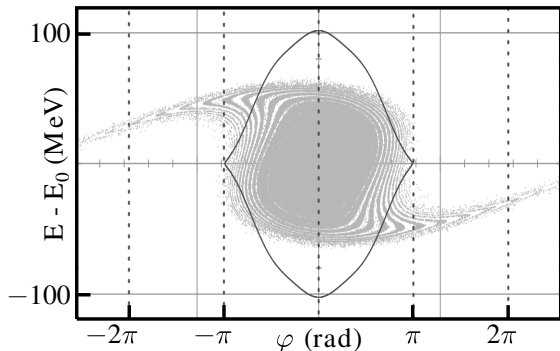


Figure 2: Simulated particle phase-space distribution at injection into the SPS bucket (V_{200} MHz = 2 MV and V_{800} MHz = 0.34 MV in bunch-shortening mode) under operational conditions [4].

50 ns beam in a short cycle gave reproducible, consistent results. The predicted optimal timings and the qualitative transmission and bunch length behaviour obtained from simulations is in excellent agreement with experimental results. With the spare 40 MHz cavity, a significant loss reduction of about 50% can be achieved with bunches that are shorter than operational. Alternatively, the longitudinal emittance can be increased by 40% while keeping the operational transmission, which allows for a stable beam in the PS even at significantly higher intensities. To better estimate the transmission and emittance requirements at the ultimate intensity required by the high luminosity LHC, simulations including impedance effects are underway. Due to the recent failure of a 40 MHz cavity in the PS, the new bunch rotation settings could not yet be tested under operational conditions, but they shall be tested as soon as it will be possible.

Studies in view of the LHC injector upgrade

The LHC injector upgrade project (LIU) [5] aims at consolidating and upgrading the existing injector chain at CERN in view of the beam parameters required for the High Luminosity LHC (HL-LHC) era. The aim is to provide 2.3×10^{11} p/b at LHC injection with about twice the brightness compared to today's operation. To reach these parameters, an extensive upgrade of the SPS RF system during Long Shutdown 2 will resolve intensity limitations from insufficient beam loading compensation. The LIU parameters require $\leq 10\%$ losses from PS extraction to SPS extraction.

Electron cloud is one of the issues encountered especially in the early years of operation with 25 ns beams. Although some conditioning of the machine has been achieved through scrubbing runs and machine operation over the years, it is still not fully clear if the e-cloud effect will pose a limitation on the beam performance in the HL-LHC era. In the last years extensive studies have been performed in the frame of the LIU project. The last high intensity scrubbing run was performed in 2015. During that period the Q20 optics [6] (implemented and operational for LHC beams since 2012 to

mitigate transverse single bunch transverse instabilities at injection) was used. With 4 batches of the 25 ns LHC beam and 2×10^{11} p/b the losses on the flat bottom alone already exceeded the target of 10%. As discussed in what follows, a series of measurements were therefore performed in 2016 in order to further investigate the loss mechanisms involved. Also the open question of the contribution from e-cloud effects was addressed.

STUDIES OF LOSSES IN THE SPS IN 2016

The machine studies in 2016 concentrated on 25 ns beams on a special MD cycle, which has a 7.8 s long injection plateau at 26 GeV/c and a 7.8 s long intermediate plateau at 28 GeV/c. This allowed distinguishing losses due to uncaptured beam on the injection plateau from other losses when storing the beam at almost the same energy. All studies presented here were performed with the Q20 optics.

Losses as a function of longitudinal emittance

The dependence of the losses on the longitudinal emittance at PS extraction was studied for a single batch of a low intensity LHC25ns (standard) beam, i.e. with 72 bunches of about 6.9×10^{10} p/b injected, which is about half of the nominal intensity. This allowed reaching very low longitudinal emittances without rendering the beam unstable in the PS. The longitudinal emittance can then be varied with controlled blow-up along the PS ramp. The SPS cycle was programmed for a calculated bucket area of about 0.6 eVs as used in routine operation. The voltage on the 800 MHz RF was set to 1/10 of the voltage at 200 MHz and the phase set to bunch shortening mode.

Figure 3 summarizes the results of the measurements: The plot on the left shows the BCT intensities averaged for the different longitudinal emittance cases along the cycle and on the right plot the relative losses on the flat bottom are compared to the relative losses from injection up to the beginning of the 28 GeV/c plateau (i.e. including the losses during the first ramp). Losses of about 1% are observed for the smallest longitudinal emittance, i.e. 0.2 eVs. The transmission degrades with larger longitudinal emittance, since the large longitudinal tails resulting from the bunch rotation at PS extraction cannot be captured in the SPS RF bucket. Therefore the losses occur mainly during the ramp. It is interesting to note however that there are also some losses on the flat portions of the cycle. Furthermore losses are observed also on the second ramp. These losses also increase with the longitudinal emittance as the RF bucket becomes very full.

Losses as a function of SPS bucket area

Losses in the SPS as a function of the bucket area were studied using a BCMS beam with 48 bunches and 1.3×10^{11} p/b. The beam had a bunch length of 4 ns at injection corresponding to the canonical longitudinal emittance of 0.35 eVs. Figure 4 shows the resulting losses with the 800 MHz OFF and with the 800 MHz ON (voltage ratio

LOSSES ON SPS FLAT BOTTOM AND BEAM LOADING WITH LHC BEAMS

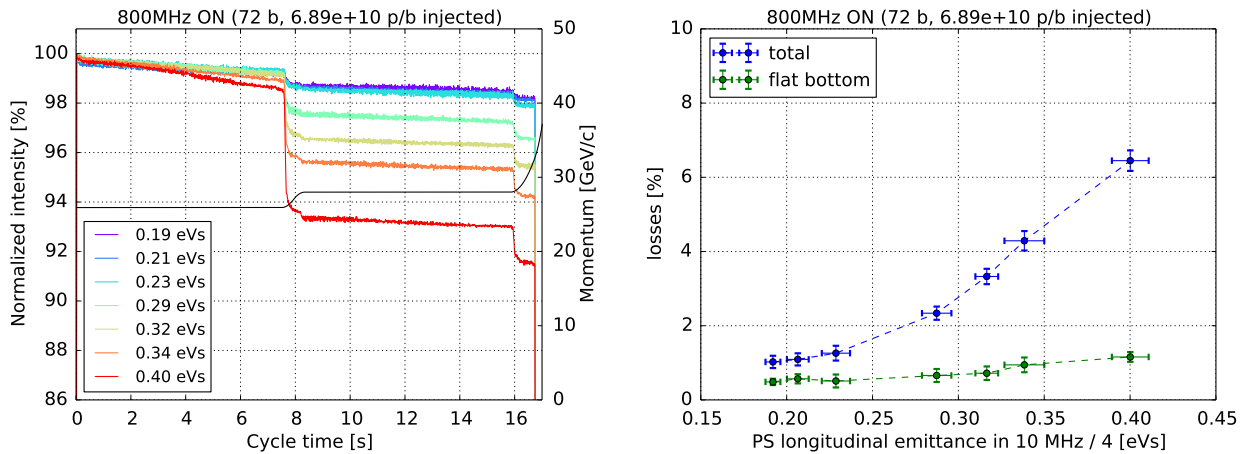


Figure 3: Losses as a function of longitudinal emittance as measured in the PS before bunch rotation. Left: Averaged BCT signal for different longitudinal emittances. Right: Relative losses on flat bottom compared to the relative losses from injection up to the beginning of the 28 GeV/c plateau.

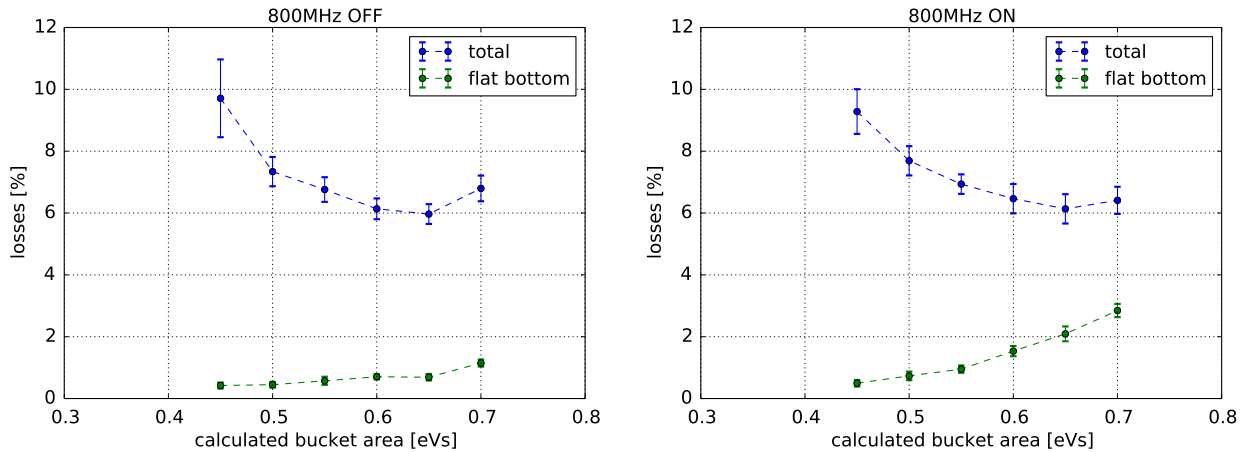


Figure 4: Losses on the flat bottom and total losses up to the beginning of the 28 GeV/c intermediate plateau as a function of the bucket area in the SPS for the case with 800 MHz RF system OFF (left) and ON (right) as described in the text.

1/10 with respect to the 200 MHz voltage, bunch shortening mode). With 800 MHz OFF the losses on the flat bottom show a slight but monotonic increase with larger bucket area (i.e. larger voltage), while the total losses including the ramp to 28 GeV/c show a minimum at the operational setting of 0.65 eVs: For smaller bucket areas the capture losses dominate; for larger bucket area the losses are also higher, most likely because particles in the bucket start reaching the momentum aperture limitation with the large dispersion in the Q20 optics. In the case with 800 MHz ON the total losses show a very similar behaviour, however the flat bottom losses in this case significantly increase as a function of the bucket area. In other words, in the case with the 800 MHz ON the flat bottom losses are enhanced without affecting the total losses. This was further investigated as described below.

Effect of 800 MHz RF on losses

To distinguish losses due to uncaptured beam from losses due to particles inside the RF buckets, the SPS vertical tune

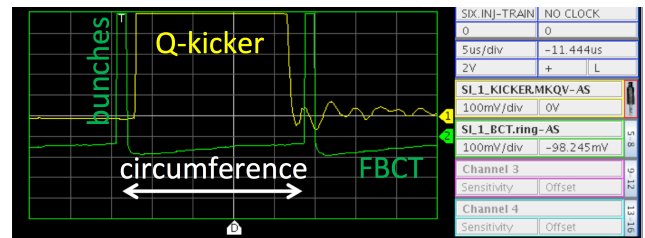


Figure 5: Adjustment of MKQV kicker waveform to clean uncaptured beam.

kicker MKQV was used at full kick strength to clean the part of the SPS circumference without bunches. To this end, the waveform of the kicker was carefully adjusted to pulse in a single turn in between the passage of the bunch train as illustrated in Fig. 5. Such a kick with the MKQV can be applied once per cycle. Figure 6 shows the intensity evolution with 800 MHz RF OFF compared to the case

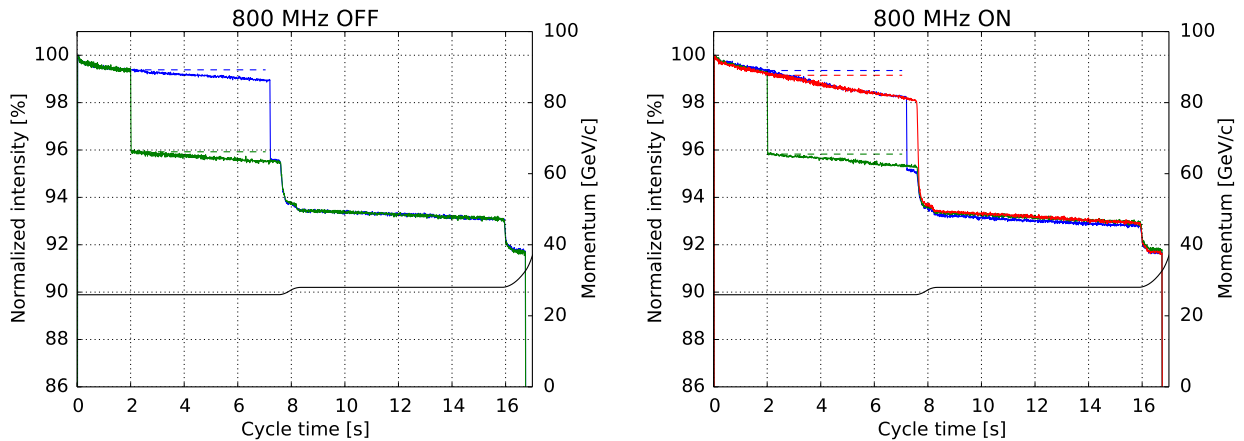


Figure 6: Intensity along the cycle when the uncaptured beam is cleaned with the MKQV tune kicker at 2 s or at 7.2 s for the case with 800 MHz OFF (left) and ON (right).

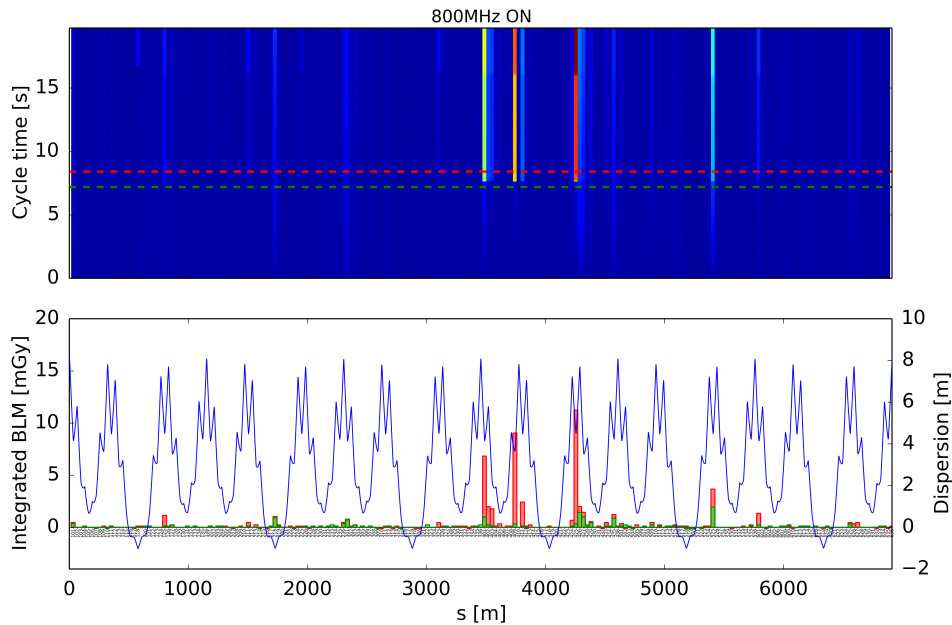


Figure 7: Losses around the SPS circumference as a function of time (top graph, color code indicates increasing losses from blue to red) and for two moments in the cycle (bottom graph, end of flat bottom in green, end of the first ramp in red).

with 800 MHz ON. As mentioned above, higher losses are observed on the flat bottom in case the 800 MHz is ON. When cleaning the uncaptured beam with the kicker at 2 s in the cycle, the losses along the remaining part of the flat bottom are very similar for both 800 MHz ON and OFF. One can therefore conclude that the uncaptured beam is lost faster with the 800 MHz RF ON, but these particles would be lost anyhow during acceleration. This is confirmed by the fact that the intensity at the end of the cycle is the same in both cases. It is interesting to note that even when cleaning the uncaptured beam a few ms before acceleration, there are still about 2% losses observed during the ramp. This could be either because not all uncaptured beam can be cleaned with the kicker (e.g. particles in the azimuthal region of the

bunches are not kicked), or rather because particles close to the separatrix are lost when the bucket shape changes at the beginning of the ramp. Figure 7 shows the distribution of losses around the machine. Both the accumulated losses along the flat bottom and the losses during the first ramp are concentrated in regions with large dispersion. This is another indication that the losses are mostly related to particles with large momentum offset, such as uncaptured beam.

25 ns standard vs. 8b4e beam

To assess the possible contribution of e-cloud to the SPS flat bottom losses, the 25 ns standard beam with 72 bunches of 1.3×10^{11} p/b was compared to the 8b4e beam [10] with 48 bunches of 1.9×10^{11} p/b at injection. Like this the total

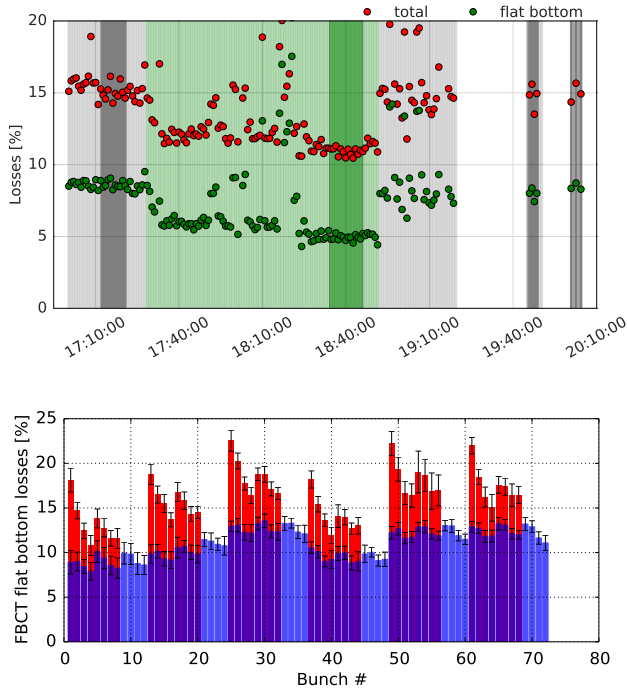


Figure 8: Losses as function of time in the MD session, where green background corresponds to times with the 25 ns standard beam and grey background to the 8b4e beam (top), and a comparison of the average bunch-by-bunch losses on the flat bottom between the two beams (bottom) taken during the time periods indicated by dark green and dark grey background.

intensity as well as the transverse emittance is the same for the two beams. In the case of the 8b4e beam the e-cloud build-up in the SPS should be negligible due to the gaps in the bunch train. Figure 8 shows the losses as function of time in the MD session (top) and a comparison of the average bunch-by-bunch losses on the flat bottom between the two beams (bottom). These average losses correspond to the periods indicated by the dark shaded time periods in the top plot (grey for 25 ns standard beam and green for the 8b4e beam). It is interesting to note that the losses along the batch show a similar pattern for the two beams, however the losses in the 8b4e beam are higher as compared to the standard beam. In addition, the losses are higher at the beginning of each group of each bunches and decrease along the sub-batches. The observations with these two beam types point towards the fact that SPS RF hardware limitations could play an important role for the losses, as discussed below.

SPS RF HARDWARE LIMITATIONS

As the review in the introduction shows, the losses along the flat bottom had been mainly discussed in the context of beam dynamics limitations and PS RF hardware limitations. In the following the SPS RF hardware limitations as far as they are relevant for losses at flat bottom and beam loading will be discussed.

200 MHz hardware

The relevant 200 MHz hardware in the SPS consists of

- four 200 MHz travelling wave structures with two structures of length $l_1 = 16$ m and two structures of length $l_2 = 20$ m
- a 1-turn delay feedback per travelling wave structure
- a feed-forward per travelling wave structure
- two longitudinal dampers, one acting through a travelling wave structure of length l_1 and one acting through a travelling wave structure of length l_2

The travelling wave structure parameters of interest here are the impedances Z_1 and Z_2 . The total voltage, as seen by the beam is given by [7]

$$V = V_{\text{RF}} + V_b,$$

with $V_{\text{RF}} = Z_1 i_g$ and $V_b = Z_2 i_b$. With

$$Z_1 \propto \frac{\sin \tau/2}{\tau/2} l,$$

$$Z_2 \propto - \left[\left(\frac{\sin \tau/2}{\tau/2} \right)^2 - j 2 \frac{\tau - \sin \tau}{\tau^2} \right] l^2$$

and

$$\tau = \frac{l}{v_g} (\omega - \omega_0).$$

Here l is interaction length, v_g is the group velocity given as $v_g/c = 0.0946$ and ω_0 the angular cavity centre frequency.

The main characteristics of the travelling wave structures is that the impedances Z_1 and Z_2 are completely different as function of frequency as illustrated in Fig. 9. This means that the beam induced voltage at certain frequencies cannot be properly compensated.

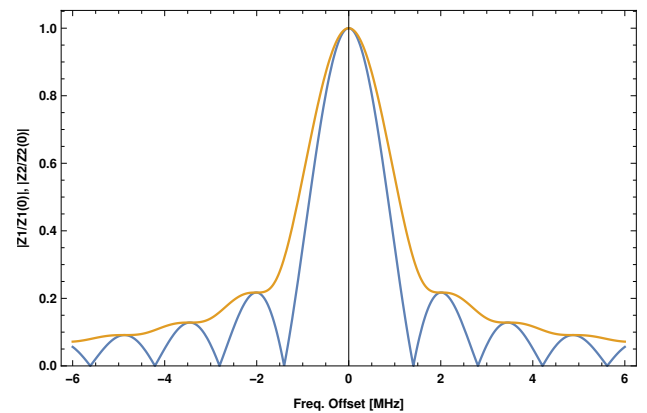


Figure 9: blue: $|Z_1(f)/Z_1(0)|$, yellow: $|Z_2(f)/Z_2(0)|$ for the case of a 5-section travelling wave structure.

To compensate the beam induced voltage in the travelling wave structures there are three elements: a polar loop, a 1-turn-delay feedback and a feed-forward. The amplitude and

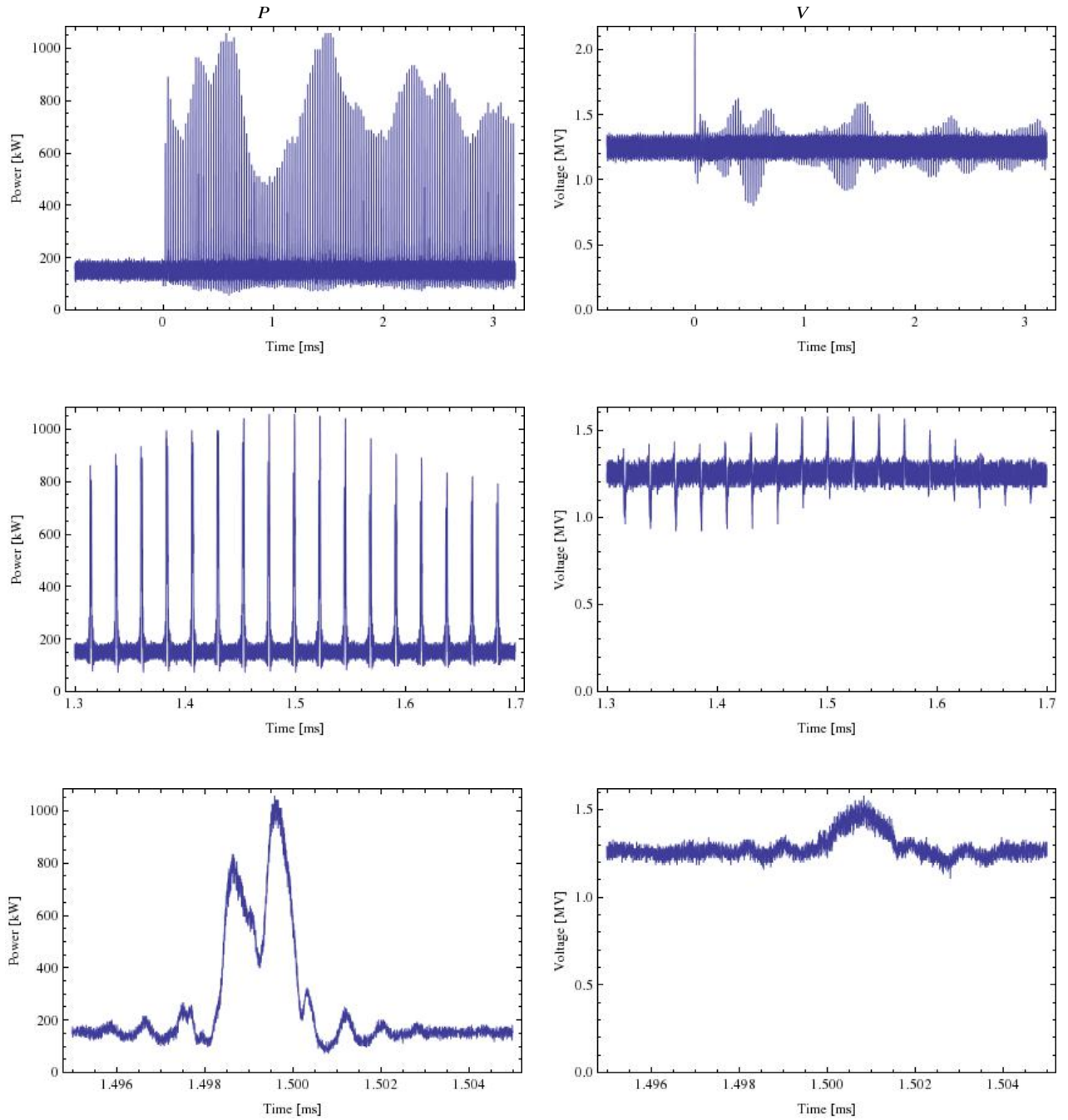


Figure 11: RF power delivered, P , and V of a 5-section travelling wave structure.

Example 2 Here a comparison of the beam loading effects at injection, $p = 26$ GeV/c, will be made using the standard 25 ns beam of 72 bunches per batch and the 8b4e beam [10] with the Q20 optics ($\gamma_t = 17.95$).

The standard 25 ns beam had the following parameters

- $N_Q = 1.3 \times 10^{11}$, $N_{Q,tot} = 9.1 \times 10^{12}$
- $l_{batch} = 1.775 \mu s$

The 8b4e beam had the following parameters

- $N_Q = 1.9 \times 10^{11}$, $N_{Q,tot} = 9.1 \times 10^{12}$

- $l_{batch} = 1.675 \mu s$

The total voltage in a 5-section travelling wave structure, V , at the first turn is shown in Fig. 12. The time of the arrival of the batch in the travelling wave structure and when it leaves the travelling wave structure can be clearly seen. Note that there is no beam loading compensation on the first turn. The power required for the beam loading compensation during the first 2 ms is shown in Fig. 13 (top). It is significantly higher for the case of the 8b4e beam. With a perfect beam loading compensation the voltage in the travelling wave structure should be constant whether the beam is

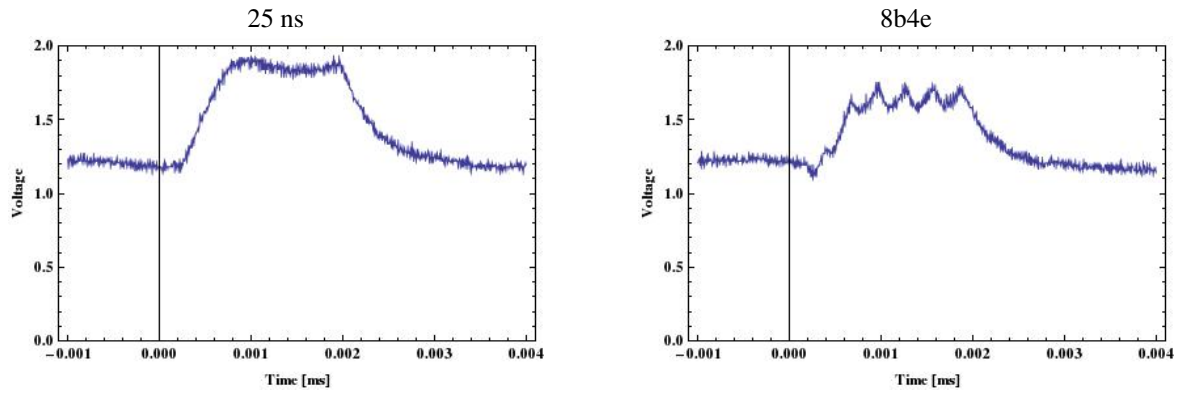


Figure 12: V at the first turn (scale: MV) for the two beams.

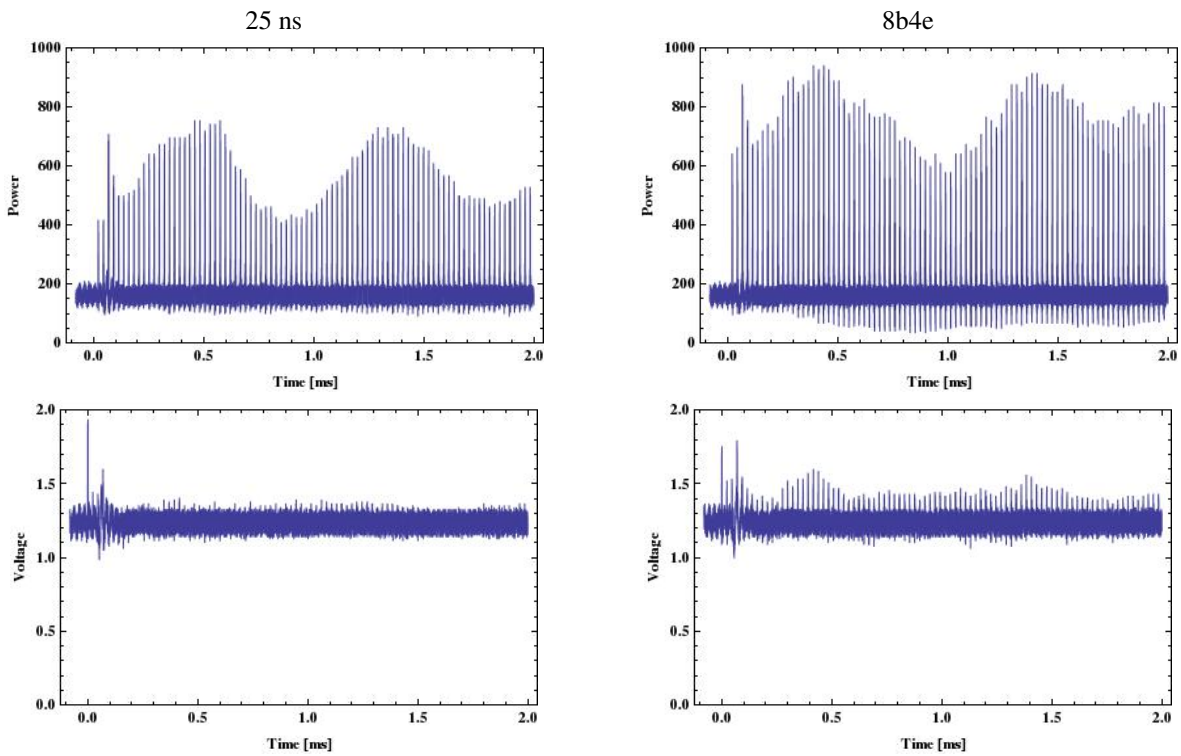


Figure 13: At the top the RF power delivered to the travelling wave structure during the first 2 ms (scale: kW) and on the bottom V during the first 2 ms (scale: MV) for the two beams.

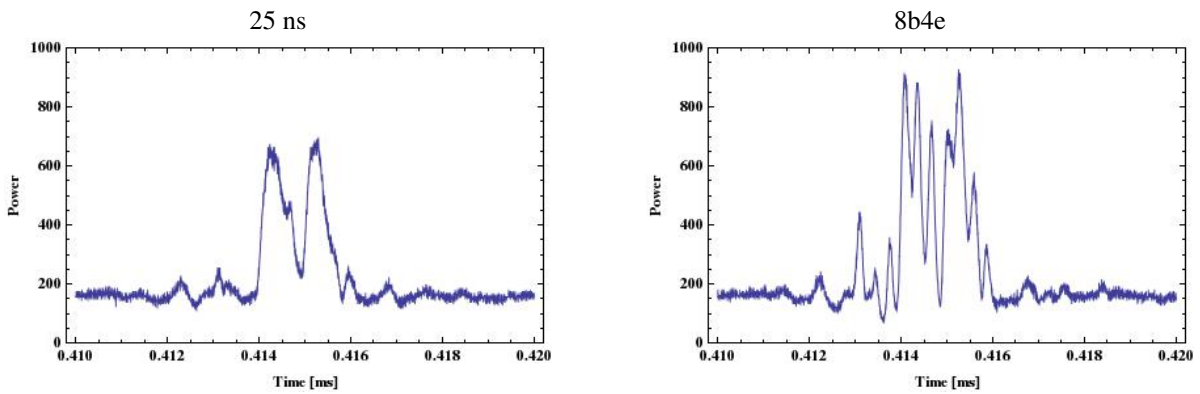


Figure 14: RF power delivered to the travelling wave structure at about $400 \mu\text{s}$ after injection (scale: kW) for the two beams.

inside the structure or not. Figure 13 (bottom) shows that this is not the case. In the case of the 25 ns beam the beam loading compensation is good after about 10 turns ($25 \mu\text{s}$). In the case of the 8b4e beam a residual error exists still after 2 ms.

A look at the power demand at about $400 \mu\text{s}$ after injection shows that the temporal structure is very different for the two beams, Fig. 14. This difference is related to the different time structures of the two beams. The frequent gaps of 8b4e require a larger bandwidth for beam loading compensation than it is necessary for the continuous beam of 72 bunches.

Longitudinal dampers

With respect to the losses at flat bottom, it is not only the beam loading in the travelling wave structures which plays a role. The two longitudinal dampers acting through the travelling structures #1 and #3 measure the bunch by bunch phase and damp longitudinal coupled bunch instabilities of low order (limited by the bandwidth of the travelling wave structures), see Fig. 10. In addition they provide the injection damping for the second and following injections of the beam as the phase loop measures only the first injected batch. Apart from the bandwidth limitation, there is another one. The longitudinal dampers had been designed for typical values of the synchrotron frequency for the Q26 optics. In the case of the Q20 optics with typically values twice or larger the damping is not any more optimal.

800 MHz hardware

The two 800 MHz travelling wave structures are now equipped with a new beam control and with a 1-turn delay feedback. The beam loading amplitude is reduced by about 26 dB and the phase variation due to beam loading is reduced to about 1° at 800 MHz. With the presently available beams there are no known limitations related to beam loading.

With respect to losses at flat bottom it had been observed that the loss rate depended on whether the 800 MHz RF system had been in use or not (see previous section). This seems to be the only point which needs to be investigated further.

Impact of LLRF settings on losses

From the above description of the SPS RF hardware it becomes clear that a global optimization of all LLRF settings requires careful measurements and multi-parametric scans. On the other hand, it can be easily tested what happens if one of the systems is switched OFF. This was done as shown in Fig. 15. For this study the 25 ns standard beam with 72 bunches of 1.33×10^{11} p/b with a bunch length of 4.1 ns at injection was used and the 800 MHz RF system was ON. The graph shows the total losses until reaching the 28 GeV/c plateau. Switching the longitudinal damper OFF had no impact on the losses, only when increasing the gain above certain levels was driving the beam unstable resulting in enhanced losses. This means that the damper is indeed not very effective in the Q20 optics as expected from the hardware limitations explained above. The biggest impact

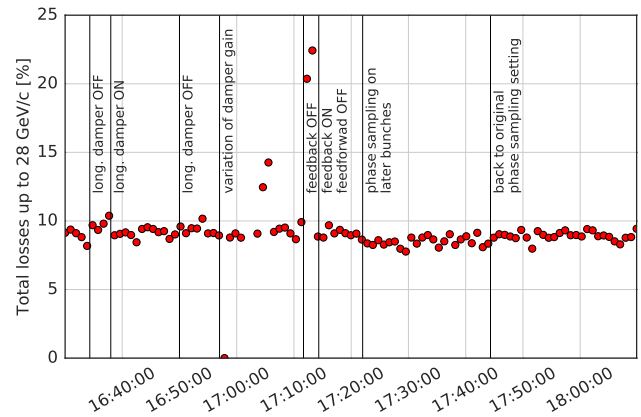


Figure 15: Losses from injection to the start of the intermediate plateau at 28 GeV/c as function of time in the MD session. The vertical bars indicate the changes in the RF settings as indicated by the labels.

on losses was observed when the 1-turn delay feedback was switched OFF, which increased the losses from 10% to more than 20%. Switching only the feed-forward OFF had no effect. This is not really expected and needs to be further studied in future MD sessions. Changing the phase loop sampling from the usual position in the beginning of the train towards the center of the batch did not change the losses.

Outlook

The hardware limitations which have been discussed will be overcome after the Long Shutdown 2. The 200 MHz 5-section travelling wave structures will be shortened and there will be only 3-section and 4-section long structures, optimal for the envisaged future beam currents. There will be two more travelling wave structures installed together with new RF power plants which will deliver higher power levels than the present ones. There will be new cavity controllers for the 200 MHz travelling wave structures with a polar loop around the RF power amplifiers, improved 1-turn delay feedback and feed-forward. In addition there will also be new longitudinal dampers which will not be limited to a particular synchrotron frequency.

In how far the beam dynamics limitations mentioned in the first part of the paper will be overcome remains to be seen.

SUMMARY AND CONCLUSIONS

Losses on the flat bottom and injection of LHC beams into the SPS are still an issue for reaching the ambitious intensity targets for the HL-LHC era. A part of the losses can clearly be attributed to capture losses due to the peculiar shape of the longitudinal distribution after the bunch rotation in the SPS, which is required at the transfer from the PS 40 MHz to the SPS 200 MHz RF structure. However, additional losses are observed on the SPS flat bottom and during the ramp. These losses seem to increase with the bunch intensity and may

not necessarily be directly related to electron cloud effects, as a comparison of the 25 ns beam with the 8b4e has shown. Instead the discussed SPS RF hardware limitations could play an important role, which however should be mitigated with the RF upgrade as part of the LIU project.

REFERENCES

- [1] P. Baudreghien, T. Bohl, T. Linnecar, E. Shaposhnikova, "Raising intensity of the LHC beam in the SPS. Longitudinal plane", SL-Note-2000-044 MD, July 2000.
- [2] T. Linnecar, T. Bohl, E. Shaposhnikova and J. Tückmantel, "Capture Losses Caused by Intensity Effects in the CERN SPS", HIGH INTENSITY AND HIGH BRIGHTNESS HADRON BEAMS: 33rd ICFA Advanced Beam Dynamics Workshop on High Intensity and High Brightness Hadron Beams. AIP Conf. Proc. 773, pp. 345-349, 2004.
- [3] G. Arduini, "Status & performance of the LHC (proton) Injector Complex", LHC Machine Advisory Committee, 2006-12-07.
- [4] H. Timko *et al.*, "Longitudinal beam loss studies of the CERN PS-TO-SPS transfer". ICFA Workshop HB2012, China, September 2012.
- [5] "LHC Injectors Upgrade Technical Design Report, Volume 1: Protons", EDMS 1451384, CERN, Geneva, Switzerland (2014).
- [6] H. Bartosik, G. Arduini and Y. Papaphilippou, "Optics considerations for lowering transition energy in the SPS", IPAC11 (2011) and references therein.
- [7] G. Dôme, "The SPS acceleration system travelling wave drift tube structure for the CERN SPS", CERN, Geneva, CERN-SPS/ARF/77-11, May, 1977.
- [8] D. Boussard and G. Lambert, "Reduction of the apparent impedance of wide band accelerating cavities by RF feed-back", IEEE Transactions on Nuclear Science, Vol. NS-30, No. 4, August 1983.
- [9] P. Baudreghien and G. Lambert, "Reducing the impedance of the travelling wave cavities. Feed-forward and one turn delay feed-back", Proc. of 10th Workshop on LEP-SPS Performance, Chamonix, France, January 2000.
- [10] H. Damerau *et al.*, "LIU: Exploring alternative ideas", Review of LHC and Injector Upgrade Plans Workshop (RLIUP), 29-31 October 2013, Centre de Convention, Archamps.

BEAM MEASUREMENTS OF THE SPS LONGITUDINAL IMPEDANCE

A. Lasheen*, E. Shaposhnikova, CERN, Geneva, Switzerland

This contribution is an extract from the following article published in Phys. Rev. Accelerators and Beams [1].

Abstract

Longitudinal instabilities are one of the main limitations in the CERN SPS to reach the beam parameters required for the High Luminosity LHC project. In preparation to the SPS upgrade, possible remedies are studied by performing macroparticle simulations using the machine impedance model obtained from electromagnetic simulations and measurements. To benchmark the impedance model, the results of simulations are compared with various beam measurements. In this study, the reactive part of the impedance was probed by measuring the quadrupole frequency shift with intensity, obtained from bunch length oscillations at mismatched injection into the SPS. This method was applied over many last years to follow up the evolution of the SPS impedance, injecting bunches with the same bunch length. A novel approach, giving significantly more information, consists in varying the injected bunch length. The comparison of these measurements with macroparticle simulations allowed to test the existing model and identify some missing SPS impedance and to obtain its possible dependence on frequency.

INTRODUCTION

One of the main challenges for future physics projects relying on particle accelerators is the need for high beam intensity, which can be limited by different collective effects. The High Luminosity LHC (HL-LHC) project at CERN needs twice higher beam intensity than achieved so far [2]. The Super Proton Synchrotron (SPS) is the last accelerator of the LHC injector chain and is the main bottleneck in terms of intensity due to beam loading and longitudinal instabilities. As the required step in performance in the SPS is high, one of the goals of the LHC Injector Upgrade (LIU) project [3] is to identify the sources of this limitation and find solutions.

The instabilities are driven by the interaction of the beam with its environment. Changes in the vacuum chamber geometry lead to electromagnetic perturbations, modeled by a beam coupling impedance \mathcal{Z} . An accurate impedance model of the ring is needed to identify the most critical contribution. A survey of all elements in the machine has been done and their impedance was found using electromagnetic simulations and bench measurements. It includes now the contribution from most of the significant sources, such as the Traveling Wave RF cavities (TWC) and their High-Order Modes (HOM), the injection/extraction kickers, the vacuum flanges (the biggest contributors correspond to the type near the focusing magnets QF), the pumping ports, and many other smaller sources [4,5]. At low energy in the

SPS, longitudinal space charge $(\text{Im}\mathcal{Z}/n)_{\text{SC}}$ is not negligible and needs to be correctly evaluated [6]. The present SPS impedance model is used in beam dynamics simulations and is presented in Fig. 1.

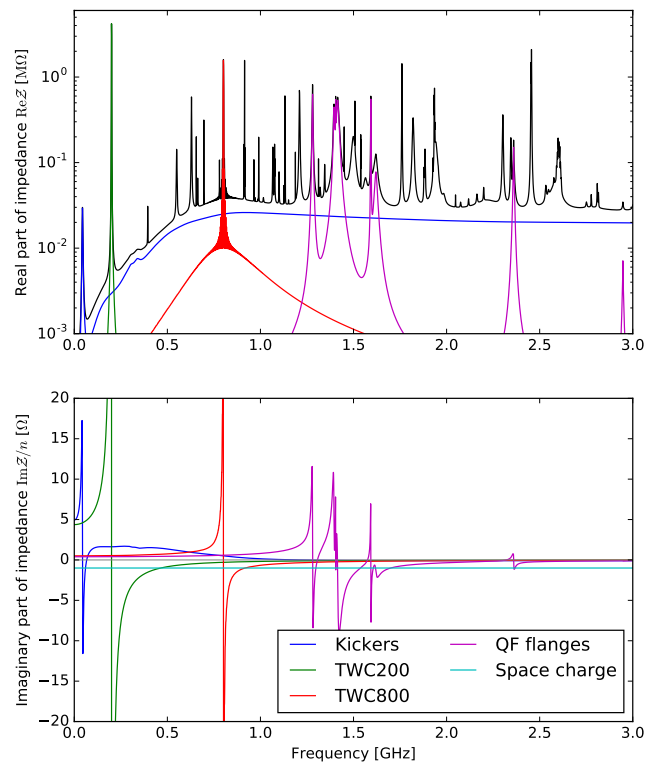


Figure 1: The present SPS longitudinal impedance model (top: resistive part, bottom: reactive part). The total impedance is represented in black (only for the real part for clarity purposes) while subsets are shown in various colors

The comparison of beam measurements performed to probe the whole impedance with macroparticle simulations can give indications about the completeness of the impedance model. The reactive part of the machine impedance can be evaluated from the measurements of the synchrotron frequency shift with intensity. Various approaches were used in different accelerators. For example, the Peak-Detected Schottky signal (e.g. in the LHC [7]), or measurements of the beam transfer function (e.g. in the PS [8]) can be used to directly observe the synchrotron frequency distribution, and the frequency shift is obtained by scanning the bunch intensity.

The method presented below relies on the measurements of bunch length oscillations at injection, initiated by a mismatched RF voltage. The frequency of these oscillations f_{s2} is approximately twice the linear synchrotron frequency and depends on the reactive part of the impedance as well as on the bunch intensity and length. Examples of recent measure-

* alexandre.lasheen@cern.ch

ments performed using bunches with different parameters are shown in Fig. 2.

The synchrotron frequency depends on the voltage seen by the beam, which is modified due to the voltage induced in the impedance sources. For bunches performing coherent oscillations, the induced voltage contribution coming from the stationary part of the bunch distribution can be separated from the one coming from the mismatched part. The frequency of coherent oscillations can be presented in the following form [9]:

$$f_{s,m}(N_b) \approx m f_{s0} + m \Delta f_{\text{inc}}(N_b) + \Delta f_{\text{coh},m}(N_b), \quad (1)$$

where N_b is the bunch intensity (number of particles in the bunch ppb), m is the mode of the oscillations ($m = 1$ is dipole or bunch position oscillations, $m = 2$ is quadrupole or bunch length oscillations), f_{s0} is the synchrotron frequency for small amplitude of oscillations, Δf_{inc} is the incoherent frequency shift due to induced voltage from the stationary bunch distribution and $\Delta f_{\text{coh},m}$ the coherent frequency shift defined by the perturbation due to the mismatched part. For dipole oscillations, the coherent and the incoherent shifts are exactly compensating each other for a parabolic bunch [10, Section 6.4] (which is a common distribution for proton bunches in the SPS), meaning that no information could be extracted so bunch length oscillations are used in this case.

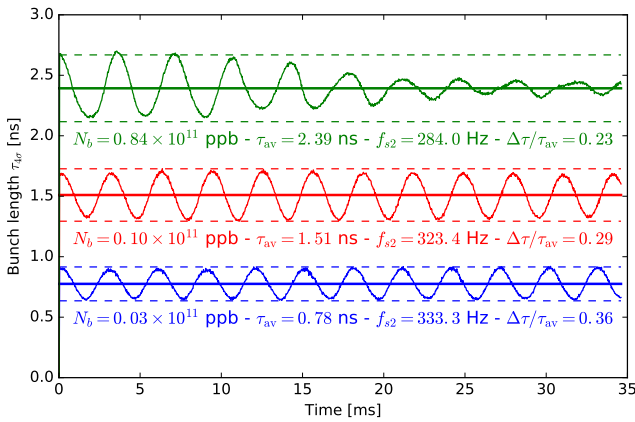


Figure 2: Examples of bunch length oscillations at SPS injection measured in the Q26 optics for different average bunch lengths τ_{av} and intensities N_b .

Since 1999, this method was used to monitor the evolution of the SPS impedance as many pieces of equipment were shielded, removed or installed [11]. The evolution of the measured quadrupole frequency shift with intensity is shown in Fig. 3 (represented by the slope b). In 1999, the main impedance contribution was from the pumping ports and the measured shift as a function of intensity was large ($b = -5.6$ Hz). The pumping ports were also the source of microwave instability in the SPS, a major limitation to reach the required beam parameters for the LHC. Therefore, their impedance was reduced by shielding in 2000. In 2001, the measured quadrupole frequency shift was lower ($b = -1.8$ Hz), proving that the impedance reduction was

successful. The shift with intensity was measured several times between 2003 and 2007 after the installation of kicker magnets for extraction to the LHC (2003 and 2006), followed by their impedance reduction (2007). However, while the large changes were easy to see, the small variations in the quadrupole frequency shift were difficult to measure. Studies showed that the measured shift b also strongly depends on the longitudinal emittance, and the lack of reproducibility in the average bunch length during measurements led to inconsistent results (e.g. the measured shift b increased in 2007, although the SPS impedance was reduced).

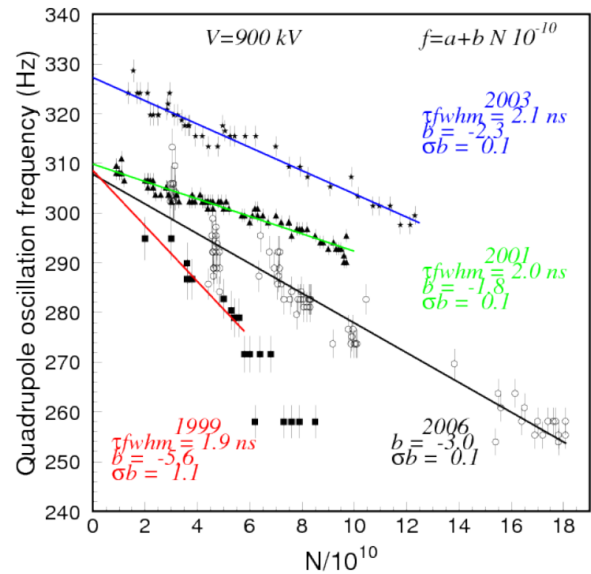


Figure 3: Measurements of the quadrupole synchrotron frequency shift at 26 GeV/c in the SPS since 1999 [11].

During the Machine Development (MD) sessions of 2016, measurements were extended to scanning both the bunch intensity and the average bunch length. The dependence on bunch length could be used to extract additional information about the frequency characteristics of the SPS impedance. By comparing measurements with macroparticle simulations using the present SPS impedance model, deviations were exploited to estimate possible missing impedance contributions.

MEASUREMENTS OF THE QUADRUPOLE FREQUENCY SHIFT

Setup

The quadrupole oscillation frequency f_{s2} was measured at injection in the SPS (kinetic energy $E_k = 25$ GeV) and its dependences were analyzed by exploring a broad range of bunch intensities and lengths. The RF parameters in the SPS injectors were adjusted to scan the injected bunch properties [12]. In the SPS, the RF voltage was set for the injected bunch to be slightly mismatched hence initiating bunch length oscillations. The dipole oscillations were re-

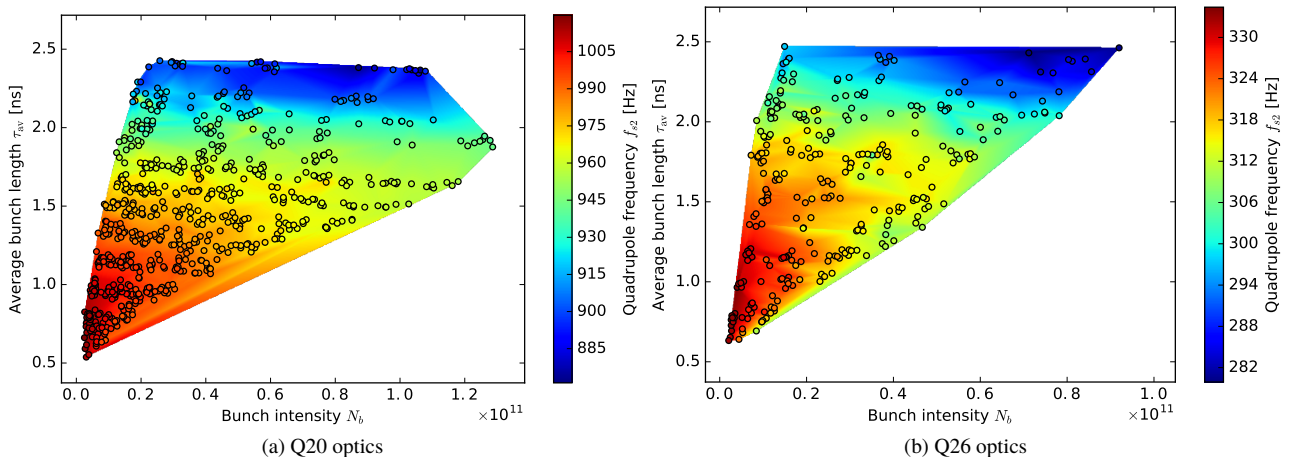


Figure 4: Measured quadrupole frequency f_{s2} as a function of bunch length and intensity in both Q20 (left) and Q26 (right) optics. Each point corresponds to a single measurement, and the colored surface corresponds to the quadrupole frequency.

duced thanks to the RF phase loop and this effect is considered negligible below. The longitudinal bunch profiles were acquired every turn using a Wall Current Monitor for an amount of turns covering approximately ten quadrupole oscillations periods.

The measured bunch length is increased, mainly due to the perturbation from the cables between the Wall Current Monitor and the oscilloscope used for the measurements. The perturbation from the Wall Current Monitor on bunch length is negligible, and the perturbation from the cables transfer function is small: the measured bunch profile is lengthened by 5-10%. The lengthening comes from short coaxial cables in the measurement line, the main part of the cables consist in a long fiber optic link, which has a negligible impact on the measured bunch profile. The Wall Current Monitor and cables transfer functions were measured, and the bunch profile was systematically corrected [13, 14]. The profiles were fitted with the binomial function

$$\lambda(\tau) = \frac{2\Gamma(3/2 + \mu)}{\tau_L \sqrt{\pi} \Gamma(1 + \mu)} \left[1 - 4 \left(\frac{\tau}{\tau_L} \right)^2 \right]^\mu, \quad (2)$$

$$\lambda(|\tau| > \tau_L/2) = 0,$$

where τ_L is the full bunch length, and where $\mu = 3/2$. The bunch length for the rest of the paper is defined as $\tau_{4\sigma} = 4\sigma_{\text{rms}}$, where σ_{rms} is the rms bunch length of the fitting profile. We note τ_{av} and $\Delta\tau$ corresponding to the average bunch length and the peak-to-peak amplitude of the bunch length oscillations. The frequency of the bunch length oscillations f_{s2} was obtained from the maximum component of the Fast Fourier Transform. The bunch intensity N_b was measured using a DC Beam Current Transformer and an averaged value was taken. Finally, each acquired SPS cycle associates the quadrupole frequency f_{s2} with an average bunch length τ_{av} , a peak-to-peak amplitude of oscillations $\Delta\tau$ and a bunch intensity N_b . Examples of these acquisitions were shown in Fig. 2.

Two different optics are available in the SPS, named after the transverse tune: Q20 and Q26. The main difference is the different γ_t and therefore a different synchrotron frequency for the same bucket area \mathcal{A}_b . Another difference is the longitudinal space charge effect which is larger in the Q26 optics with respect to the Q20 optics. This is due to the different dispersion function which gives a smaller horizontal bunch size in the Q26 optics for the same transverse emittance [6]. Measurements were performed in both optics, for the same bucket area (by adjusting the RF voltage V_{RF}). The raw data of the quadrupole frequency as a function of intensity and the average bunch length is shown in Fig. 4. The corresponding beam and machine parameters are shown in Table 1.

Table 1: The SPS beam and machine parameters for the two different SPS optics.

Optics	γ_t	V_{RF} [MV]	f_{s0} [Hz]	\mathcal{A}_b [eVs]	$\left(\frac{\text{Im}Z}{n}\right)_{\text{SC}}$ [Ω]
Q20	17.95	2.8	517.7	0.473	-1.0
Q26	22.77	0.9	172.4	0.456	-1.27

Data analysis and results

The dependence of the quadrupole frequency f_{s2} on intensity was studied by selecting the data with the same average bunch length τ_{av} (within ± 50 ps). For each set, the dependence on intensity is obtained from the fit by a linear function $f_{s2} = a + b N_b$. The origin of the fit a corresponds to the quadrupole frequency without intensity effects, while the slope b contains the information about the reactive impedance. Examples of measured quadrupole frequency f_{s2} as a function of intensity for different sets of average bunch length τ_{av} together with fits are shown in Fig. 5.

The dependence of the quadrupole frequency on bunch length can be studied from the fitted parameters a and b

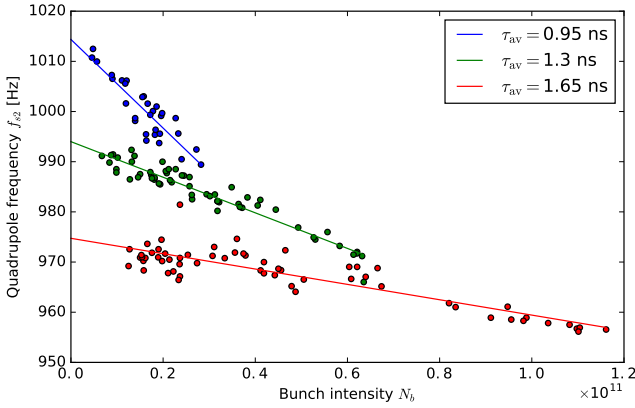


Figure 5: Examples of measured quadrupole frequency f_{s2} as a function of intensity for selected average bunch lengths τ_{av} (within ± 50 ps) in the Q20 optics. The lines correspond to a linear fit.

obtained for each set of τ_{av} . The measured quadrupole oscillations are mainly performed by the mismatched particles from the outer part of the distribution. The first consequence is that the quadrupole frequency without intensity effects a (τ_{av}) should follow [1]:

$$a(\tau_{av}) \approx 2f_{s0} \left[1 - \frac{(\omega_{RF}\tau_{av})^2}{64} \right], \quad (3)$$

where $f_{RF} = \omega_{RF}/(2\pi)$ is the RF frequency and where the right-hand side of the equation is noted $2f_s^{(0)}$, which is the quadrupole frequency including the effect of the non-linearity of the RF voltage. The comparison of measurements with the expected analytical formula is shown in Figs. 6a and 6b for both optics. They are in good agreement, confirming that the measured quadrupole frequency is dominated by contributions from particles with large synchrotron oscillation amplitudes. The small discrepancy between measurements and the expected scaling comes from the fact that Eq. (3) is valid for particles with maximum oscillation amplitude, while in measurements the frequency is determined by the sum of all the particles defining the mismatch.

It is possible to extrapolate the value of $2f_{s0}$ from the measured a ($\tau_{av} \rightarrow 0$) which gives the actual amplitude of the RF voltage during measurements (this parameter has an uncertainty of $\approx 5\%$). For both Q20 and Q26 optics the measured values ($2f_{s0} \approx 1035$ Hz in the Q20 optics and $2f_{s0} \approx 342$ Hz in the Q26 optics) are in good agreement with the values expected in theory in Table 1. The measured slope b is shown in Figs. 6c and 6d and it scales approximately as $\propto 1/\tau_{av}^3$, in accordance to the expected scaling of the synchrotron frequency shift for large particle oscillation amplitudes [1].

In previous studies of the synchrotron frequency shift as a probe of the reactive impedance, only the slope b was taken to compare measurements and simulations. However, the strong dependence on bunch length of the slope b implies that small deviations in the measured bunch length could lead to important differences between measurements and

simulations (e.g. due to perturbations in the measured profile from the measurement line, see *Setup* paragraph). Therefore, it was found preferable to use as a figure of merit the equivalent impedance which dependence on bunch length is less strong, even if the measured bunch profile was corrected regarding perturbations in the measurement line. The analyzed parameters $a = 2f_s^{(0)}$ and $b = -2\Delta f_{inc}/N_b$ are recombined to obtain the equivalent reactive impedance as [1]:

$$(\text{Im}\mathcal{Z}/n)_{eq} = \frac{\omega_{rev}^2 V_{RF} h}{6q} \frac{b}{a} \tau_{av}^3, \quad (4)$$

where $f_{rev} = \omega_{rev}/(2\pi)$ is the revolution frequency, q the charge of the particles, h the RF harmonic number. The results are shown in Figs. 6e and 6f. Note that the equivalent impedances $(\text{Im}\mathcal{Z}/n)_{eq}$ are very similar for the Q20 and Q26 optics since the dependence on the machine parameters V_{RF} and η was removed.

For the measured equivalent impedance $(\text{Im}\mathcal{Z}/n)_{eq}$ we can distinguish three different bunch length intervals. For $\tau_{av} < 1.7$ ns, the results are similar in pattern and value between the Q20 and Q26 optics and correspond to the ideal bunch length range for these measurements. At $\tau_{av} \approx 1.7$ ns, the measured equivalent impedance $(\text{Im}\mathcal{Z}/n)_{eq}$ in the Q20 and Q26 optics starts to be different. For the Q20 optics, the measured values keeps decreasing increase whilst the equivalent impedance grows in the case of the Q26 optics. For $\tau_{av} > 2$ ns the measured equivalent impedance $(\text{Im}\mathcal{Z}/n)_{eq}$ in Q20 is completely unusable. This is explained by the motion of a mismatched bunch in phase space which is heavily affected by the non-linearities of the RF bucket for large bunch lengths. As shown in Fig. 2, the consequence is that the bunch profile changes with time and bunch length oscillations are quickly damped due to filamentation. In addition, the bunch is shortened in the SPS injector (PS) by a fast RF voltage increase (bunch rotation in phase space). For large bunch lengths, the distribution in phase space is distorted during the bunch rotation in the longitudinal phase space and has an "S-shape" [15], making the filamentation effects even more difficult to reproduce. Moreover, the spectrum of a filamenting bunch has components at high frequency, which could affect the synchrotron frequency shift. In those conditions the results are varying from one acquisition to another. Nevertheless, the main observation is that for large bunch lengths the equivalent impedance $(\text{Im}\mathcal{Z}/n)_{eq}$ for $\tau_{av} > 2$ ns is increasing, implying that long bunches are mainly sampling inductive impedance.

PARTICLE SIMULATIONS

BLoND simulations

The dependence of the quadrupole frequency shift on the SPS impedance can be studied more precisely by macroparticle simulations that include the RF non-linearities and induced voltage. The simulation code BLoND was written at CERN to simulate longitudinal beam dynamics in synchrotrons and was successfully benchmarked with measurements in various accelerators and physics cases. including

BEAM MEASUREMENTS OF THE SPS LONGITUDINAL IMPEDANCE

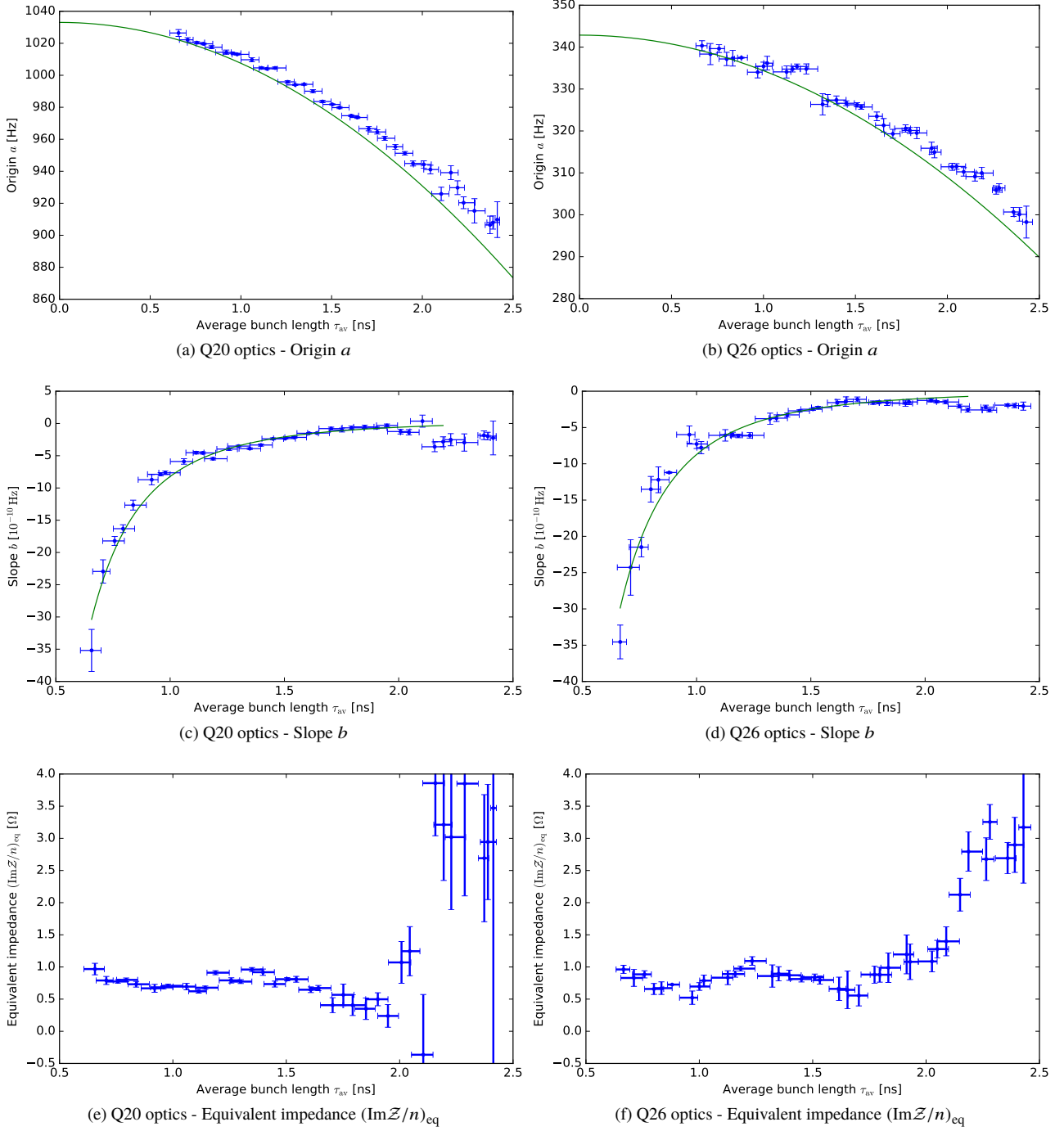


Figure 6: The fitted origin a (top), slope b (middle) and their expected scaling from theory (green, respectively from Eq. (3) and $\propto -1/\tau_{av}^3$). The Eq. (4) is used to get the corresponding equivalent impedance $(\text{Im}\mathcal{Z}/n)_{eq}$ (bottom) of the quadrupole frequency shift with intensity, as a function of the average bunch length τ_{av} , in the Q20 (left) and Q26 (right) optics.

the synchrotron frequency shift with intensity [16]. All simulations were done using the SPS impedance model presented in Fig. 1 (both resistive and reactive parts).

The SPS machine parameters were set in simulations to be the same as in measurements (for both optics in Table 1). To cover the same range of longitudinal emittances and bunch intensities obtained in measurements, each acquisition was

reproduced in simulations by taking the injected bunch profile and reconstructing the bunch distribution in phase space using the Abel transform [17]. To get in simulations a mismatch close to the one in measurements, the bunch distribution in phase space was generated and the energy spread was iteratively adjusted so that the peak-to-peak bunch length oscillations $\Delta\tau$ are similar to the corresponding acquisition.

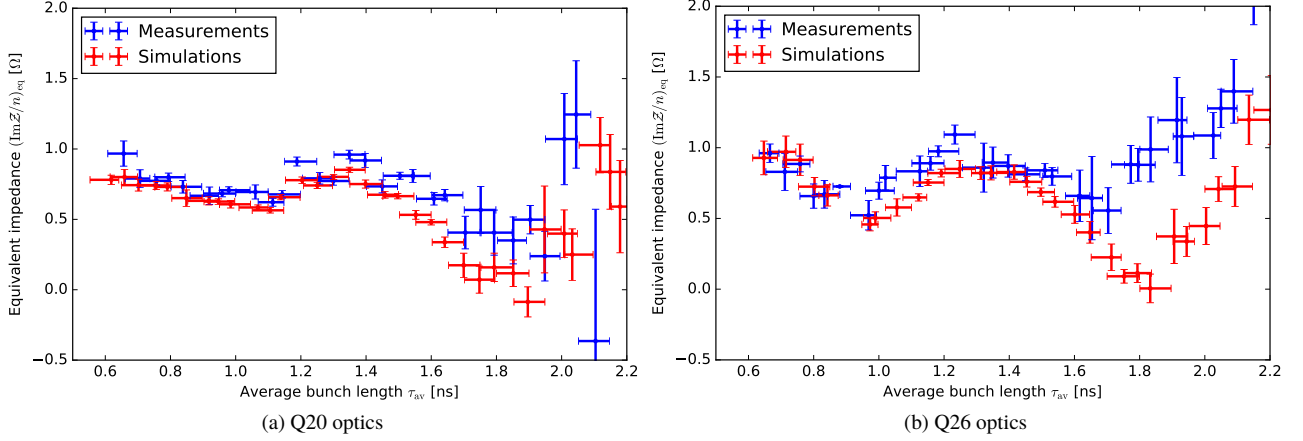


Figure 7: Equivalent impedance $(\text{Im}\mathcal{Z}/n)_{\text{eq}}$ as a function of bunch length obtained from measurements (blue) and simulations (red) using the full SPS impedance model in the Q20 (left) and Q26 (right) optics.

For small bunch lengths, this approach is good enough to get input distributions close to the ones extracted from the PS without having to simulate the bunch rotation in the PS. Simulation results analyzed applying exactly the same method as used for measurements are presented in Fig. 7.

Overall, simulations using the present SPS impedance model are in good agreement with measurements and the non-trivial dependence of the equivalent impedance $(\text{Im}\mathcal{Z}/n)_{\text{eq}}$ on bunch length is well reproduced in both optics. Nevertheless, some systematic deviations can be noticed. First, the equivalent impedance $(\text{Im}\mathcal{Z}/n)_{\text{eq}}$ is in general lower in simulations than in measurements, suggesting that some impedance is still missing in the SPS impedance model. Next, the discrepancy is higher for $\tau_{\text{av}} \approx 1.6$ ns, indicating that the missing impedance has a particular frequency dependence. The results for $\tau_{\text{av}} > 1.7$ ns are less accurate due to the limitations described above and may not be suitable to draw reliable assumptions on possible missing impedance.

Evaluation of the missing impedance

To define possible missing impedance sources, the simulations were reiterated by adding a variable amount of constant inductive impedance $\text{Im}\mathcal{Z}/n$. Results are shown in Fig. 8. The present SPS impedance including space charge is represented in blue and the deviations between measurements and simulations could be explained by an additional inductive impedance in the order of $\text{Im}\mathcal{Z}/n \approx (0 - 1.5)$ Ω depending on the bunch length. This is comparable to the longitudinal space charge impedance of $(\text{Im}\mathcal{Z}/n)_{\text{SC}} \approx -1$ Ω . Omitting the longitudinal space charge impedance in simulations would correspond to the red line. In this case, the interpretation would have been opposite, since we would have concluded that the inductive impedance in the present model is in excess. Therefore, the longitudinal space charge effects are indeed not negligible and should be included in simulations at flat bottom in the SPS. An accurate evaluation

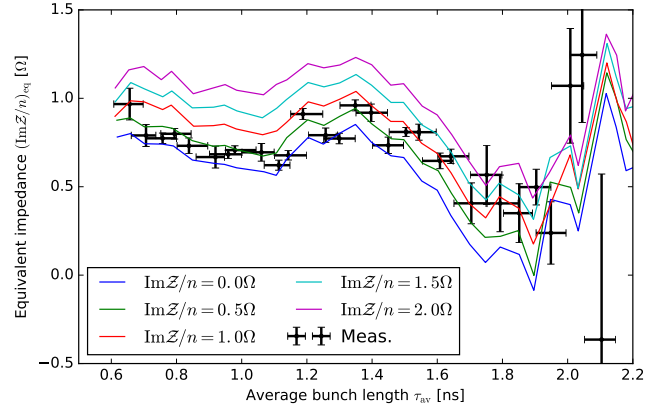


Figure 8: Measured equivalent impedance $(\text{Im}\mathcal{Z}/n)_{\text{eq}}$ (black) in the Q20 optics compared with simulations (colored lines) adding a variable amount of inductive impedance in the range $\text{Im}\mathcal{Z}/n = (0 - 2)$ Ω to the full SPS impedance model.

of the longitudinal space charge impedance was done [6], leading to the values shown in Table 1 for both optics.

By using the previous scan in simulations adding a variable amount of constant inductive impedance $\text{Im}\mathcal{Z}/n$, it is possible to determine for each bunch length the necessary impedance value to reach a perfect agreement between simulations and measurements. Results are shown in Fig. 9 for both optics.

For $\tau_{\text{av}} < 1.4$ ns, the missing impedance is constant in first coarse approximation and it is necessary to add $\Delta(\text{Im}\mathcal{Z}/n) \approx 0.3$ Ω in the Q20 optics and $\Delta(\text{Im}\mathcal{Z}/n) \approx 0.5$ Ω in the Q26 optics to remove the deviations. For this large range of bunch lengths, a broadband impedance source could be the missing contribution, as determined in the previous section. Whilst non negligible, this missing contribution is still small in comparison with the full impedance budget and could be explained by an underestimation of a source in the model or some contributions that were not included.

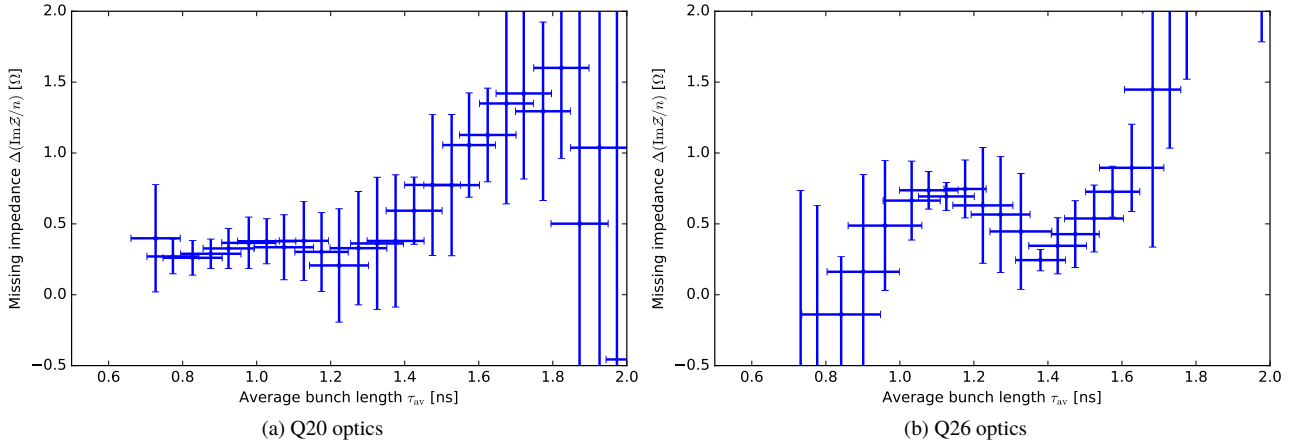


Figure 9: Missing inductive impedance $\Delta(\text{Im}\mathcal{Z}/n)$ as a function of bunch length needed to get a perfect agreement between measurements and simulations shown in Fig. 7 for both Q20 (left) and Q26 (right) optics.

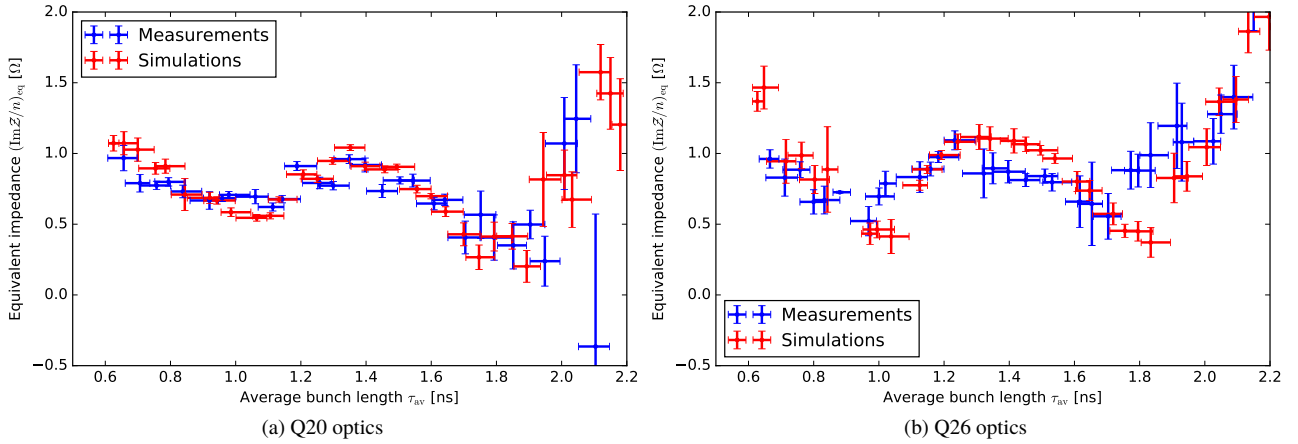


Figure 10: Equivalent impedance $(\text{Im}\mathcal{Z}/n)_{\text{eq}}$ in measurements and simulations after adding an extra resonator with $f_r = 350$ MHz, $R/Q = 3$ k Ω and $Q = 1$ to the SPS impedance model to compensate for deviations from measurements in both Q20 (left) and Q26 (right) optics.

For τ_{av} in the range (1.4 – 1.7) ns, the missing impedance is increasing linearly, suggesting that an impedance source as a resonator could also be missing. Simulations were done with an additional resonator and its resonant frequency f_r and impedance R/Q were scanned to further reduce the discrepancy (with $Q = 1$). The best agreement was found for a resonator with $f_r \approx (350 \pm 50)$ MHz and $R/Q \approx (3 \pm 1)$ k Ω , leading to an almost perfect agreement in the Q20 optics as shown in Fig. 10a. While in the Q26 optics the agreement is also improved, some small deviations are still present at $\tau_{\text{av}} \approx 1.0$ ns and $\tau_{\text{av}} \approx 1.5$ ns (see Fig. 10b). Adding a single resonator is most probably not enough to correct all the deviations between measurements and simulations. A perfect description of the missing impedance is a multi-parametric task which requires a very large amount of measured data with small error-bars. Moreover, the realistic frequency dependence of a device contributing to the machine impedance could be more complex than that of a single resonator. Nevertheless, clear indications for the

missing effective impedance as a function of bunch length can be exploited to get hint and direction for further searches. The missing contribution, depending on its frequency, could also be critical to have a reliable SPS impedance model for the bunch stability studies required for the SPS upgrade.

CONCLUSIONS

The measured quadrupole frequency shift with intensity has been used to probe the reactive part of the SPS machine impedance. Being very sensitive to the average bunch length because of the non-linearities of the RF bucket and the induced voltage, this method can nevertheless be used to have an estimate of the missing impedance and its frequency dependence. Measurements were done in the SPS in two different optics and allowed, from good agreement with particle simulations, to show that the present SPS impedance model is satisfactory to reproduce the measured synchrotron frequency shift. The agreement can be further increased by adding a resonant impedance at $f_r \approx 350$ MHz with

$R/Q \approx 3 \text{ k}\Omega$ and $Q = 1$, the real source to be investigated. As the studies for the HL-LHC project rely on the accurate reproduction of beam instabilities, any missing impedance could be crucial and this method is an effective way to test the existing impedance model. Beyond the evaluation of the longitudinal impedance model, the study of the synchrotron frequency shift is also important as it is a key component to determine the instability mechanisms related to the loss of Landau damping.

ACKNOWLEDGMENTS

We would like to thank the impedance working group at CERN for the development of the SPS impedance model and in particular T. Kaltenbacher, C. Zannini and B. Salvant. We would also like to thank T. Bohl for helping during the measurements in the SPS and S. Hancock for the help in the preparation of the necessary cycles in the PSB and PS. We are grateful to the MD coordinators for providing with beam time and the operation team for setting up the cycles. Finally we would like to thank BLoND developers for their contributions to the simulation code.

REFERENCES

- [1] A. Lasheen and E. Shaposhnikova, "Evaluation of the cern super proton synchrotron longitudinal impedance from measurements of the quadrupole frequency shift," *Phys. Rev. Accel. Beams*, vol. 20, p. 064401, Jun 2017.
- [2] G. Apollinari, I. Béjar Alonso, O. Brüning, M. Lamont, and L. Rossi, "High-Luminosity Large Hadron Collider (HL-LHC): Preliminary Design Report," Tech. Rep. CERN-2015-005, CERN, Geneva, Switzerland, Dec 2015.
- [3] H. Damerau, A. Funken, R. Garoby, S. Gilardoni, B. Goddard, K. Hanke, A. Lombardi, D. Manglunki, M. Meddahi, B. Mikulec, G. Rumolo, E. Shaposhnikova, M. Vretenar, and J. Coupard, "LHC Injectors Upgrade, Technical Design Report, Vol. I: Protons," Tech. Rep. CERN-ACC-2014-0337, CERN, Geneva, Switzerland, Dec 2014.
- [4] J. E. Campelo, T. Argyropoulos, T. Bohl, F. Caspers, J. Esteban Müller, J. Ghini, A. Lasheen, D. Quartullo, B. Salvant, E. Shaposhnikova, and C. Zannini, "An Extended SPS Longitudinal Impedance Model," in *Proceedings of IPAC2015*, no. MOPJE035, (Richmond, VA, USA), pp. 360–362, May 2015.
- [5] J. E. Campelo, "Longitudinal Impedance Characterization of the CERN SPS Vacuum Flanges," in *Proceedings of IPAC2015*, no. MOPJE036, (Richmond, VA, USA), pp. 363–365, May 2015.
- [6] A. Lasheen, "Longitudinal Space Charge in the SPS," Tech. Rep. CERN-ACC-NOTE-2016-0074, Dec 2016.
- [7] E. Shaposhnikova, T. Bohl, and T. Linnecar, "Longitudinal Peak Detected Schottky Spectrum," in *Proceedings of HB2010*, no. TUO1C04, (Morschach, Switzerland), pp. 363–367, September 2010.
- [8] M. Migliorati, S. Persichelli, H. Damerau, S. Gilardoni, S. Hancock, and L. Palumbo, "Beam-wall interaction in the cern proton synchrotron for the lhc upgrade," *Phys. Rev. ST Accel. Beams*, vol. 16, p. 031001, Mar 2013.
- [9] J. L. Laclare, "Bunched beam coherent instabilities," in *Proceedings of CAS 1985 Vol. I*, (Geneva, Switzerland), pp. 264–326, 1987.
- [10] A. W. Chao, *Physics of collective beam instabilities in high energy accelerators*. New York, NY: Wiley, 1993.
- [11] E. Shaposhnikova, T. Bohl, H. Damerau, K. Hanke, T. Linnecar, B. Mikulec, J. Tan, and J. Tückmantel, "Reference Measurements of the Longitudinal Impedance in the CERN SPS," in *Proceedings of PAC09*, no. FR5RFP056, (Vancouver, Canada), pp. 4667–4669, May 2009.
- [12] S. Hancock, "Improved Longitudinal Blow-up and Shaving in the Booster," Tech. Rep. CERN-ATS-Note-2013-040 MD, CERN, Jul 2013.
- [13] T. Bohl, "APWL-10 transfer function," Tech. Rep. Note-2006-37, CERN, 2006.
- [14] T. Bohl, "Pulse response of SPS APWL signal chain via FO Link No. 1," Tech. Rep. Note-2011-09, CERN, 2011.
- [15] H. Timko, T. Argyropoulos, T. Bohl, H. Damerau, J. F. Esteban Müller, S. Hancock, and E. Shaposhnikova, "Longitudinal transfer of rotated bunches in the cern injectors," *Phys. Rev. ST Accel. Beams*, vol. 16, p. 051004, May 2013.
- [16] H. Timko, J. E. Müller, A. Lasheen, and D. Quartullo, "Benchmarking the Beam Longitudinal Dynamics Code BLoND," in *Proc. of International Particle Accelerator Conference (IPAC'16), Busan, Korea, May 8-13, 2016*, no. 7 in International Particle Accelerator Conference, (Geneva, Switzerland), pp. 3094–3097, JACoW, June 2016. doi:10.18429/JACoW-IPAC2016-WEPOY045.
- [17] P. W. Krempf, "The Abel-type Integral Transformation with the Kernel $(t^2-x^2)^{-1/2}$ and its Application to Density Distributions of Particle Beams," Tech. Rep. CERN Note MPS/Int. BR/74-1, CERN, 1974.

FIXED TARGET BEAMS

V. Kain, H. Bartosik, S. Cettour-Cave, K. Cornelis, M. A. Fraser,
L. Gatignon, B. Goddard, F. Velotti, CERN, Geneva, Switzerland

Abstract

The CERN SPS (Super Proton Synchrotron) serves as LHC injector and provides beam for the North Area fixed target experiments. At low energy, the vertical acceptance becomes critical with high intensity large emittance fixed target beams. Optimizing the vertical available aperture is a key ingredient to optimize transmission and reduce activation around the ring. During the 2016 run a tool was developed to provide an automated local aperture scan around the entire ring.

The flux of particles slow extracted with the 1/3 integer resonance from the Super Proton Synchrotron at CERN should ideally be constant over the length of the extraction plateau, for optimum use of the beam by the fixed target experiments in the North Area. The extracted intensity is controlled in feed-forward correction of the horizontal tune via the main SPS quadrupoles. The Mains power supply noise at 50 Hz and harmonics is also corrected in feed-forward by small amplitude tune modulation at the respective frequencies with a dedicated additional quadrupole circuit. The characteristics of the SPS slow extracted spill in terms of macro structure and typical frequency content are shown. Other sources of perturbation were, however, also present in 2016 which frequently caused the spill quality to be much reduced.

INTRODUCTION

The Super Proton Synchrotron (SPS) at CERN delivers beam to the North Area fixed-target experiments using resonant slow extraction. It serves also as LHC injector and provides beam to the HiradMat [1] and AWAKE [2] facilities. The proton beams for fixed target physics are injected at a momentum of 14 GeV/c and need to cross transition in the early part of the acceleration to the 400 GeV/c extraction momentum. The requested intensities for fixed-target physics range from 3 to 4×10^{13} protons per cycle with typically 3300 cycles per day. Due to the high intensity and high duty cycle of the fixed-target beams, beam loss in the SPS has to be kept as low as possible to limit activation of the ring and maximising the acceptance of the machine is crucial.

The other challenge with fixed target beams in the SPS is to provide adequate spill quality for the North Area experiments. For an ideal slow extracted spill, the rate of extracted particles dN/dt should remain constant over the 4.8 s long extraction plateau. The spill is corrected in feed-forward by adjusting the tune directly through the main quadrupoles all around the SPS [3]. Also the fluctuations at 50 Hz and its harmonics are corrected in feed-forward. The servo-quadrupole system in long straight section 1 of the SPS is equipped with a 50, 100, 150 and 300 Hz current modulation of adjustable phase and amplitude for that purpose.

AUTOMATIC LOCAL APERTURE MEASUREMENT

The shape of the vacuum chambers follows the beam size variation around the ring circumference and the aperture with the flat vacuum chambers in the dipole magnets is optimised to accommodate the horizontal beam size during transition crossing and slow extraction. By design the acceptance in the vertical plane is smaller than in the horizontal plane. At low energy any further reduction of the vertical aperture due to orbit and misalignments directly translates into increased losses. The SPS vertical aperture bottleneck is expected to be at the TIDVG internal beam dump (vertical aperture of 42 mm).

The local aperture measurement tool

The automatic local aperture measurement tool is based on applying three-corrector-bumps at all quadrupole locations around the SPS. The bump amplitudes are increased linearly during the measurement period and the evolution of the beam intensity in the SPS is recorded. The amplitude is either increased from 0 mm to the maximum corresponding to the corrector circuit current limit or decreased from 0 mm to the minimum.

The mechanical aperture at a given location corresponds to the bump amplitude, where the intensity drops to zero as the entire beam is scraped off. A typical intensity evolution during a bump scan is plotted in Fig. 1. This method is independent of the transverse beam distribution, that can vary from shot to shot, but requires sufficient corrector strength.

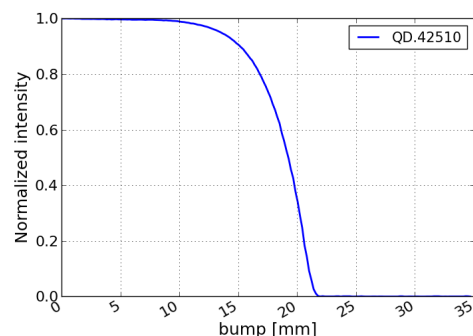


Figure 1: Intensity evolution during the scan of the amplitude of a three-corrector bump at location of QD.42510.

Limitations

The SPS orbit corrector magnets are limited to ± 3.5 A. For proton fixed-target beams, injected at 14 GeV/c and optics Q26, the maximum possible three-corrector-bump amplitude is thus ± 35 mm. This is sufficient for the vertical plane to

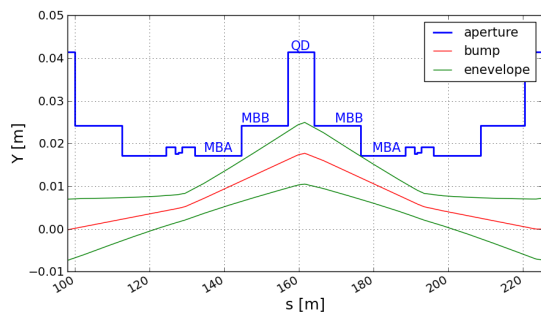


Figure 2: Mechanical aperture in the FODO cell of the SPS in the vertical plane with three-corrector bump and beam envelope. The bump will touch the aperture at the MBA to MBB or QD to MBB transition before reaching the QD aperture.

probe the mechanical aperture, but not for the horizontal one given the vacuum chamber dimensions.

The other limitation arises from the fact that the three-corrector-bumps span two SPS FODO cells and the mechanical aperture changes along a cell. In fact the bump as used during the scan does not probe the aperture of the defocusing quadrupole QD, but of the transitions from the QD to MBB main dipole vacuum chamber or from the MBB to MBA type of main dipoles as indicated in Fig. 2. In the current implementation of the tool the location of potential aperture bottlenecks that are found during the aperture scans cannot be better localised than to the region comprising the half cell upstream and downstream of the QD. The option to apply asymmetric bumps with four correctors to further localise the aperture restriction could be made available in an upgraded version of the local aperture measurement tool.

Results

The above introduced aperture measurement technique was developed, tested and finally deployed during the SPS run 2016. Low intensity $2 \mu\text{s}$ long MTE [4] beam of an intensity of $2 - 3 \times 10^{11}$ protons was used in a test cycle with a 3.6 s long 14 GeV/c plateau. The locations of all 108 defocussing quadrupoles of the SPS were scanned in positive and negative direction. Each scan was repeated 3 times for statistics. The error bars in the plots only contain the statistical errors.

The CERN accelerator control system provided all building blocks required for the automatic aperture scan. The YASP steering program [5] includes an automatic bump scan routine. YASP relies on the LHC software architecture (LSA) framework [6] which allows to configure knobs, i.e. bumps, to be applied in a user defined manner over time. An additional JAVA application had to be prepared to record the beam intensity measurement through the cycle and associate the data with the bump amplitude and the bump location name.

Two measurement series were carried out towards the end of the run in 2016, one on 18th of October and the second one on 22nd of November. The aperture was analysed as total aperture per location by combining the result of the positive and negative scan to be independent of the actual orbit on the test cycle. The total aperture measured at the different QD locations for the two scans is shown in the upper plot of Fig. 3. At the locations where no measurement point is indicated, the aperture was either never reached or the quality of the measurement was inadequate. In the long straight sections of every sextant, the QDs of half cells 17 and 19 are not neighboured by dipoles. Thus the aperture is larger than elsewhere and the correctors there are not strong enough to reach the mechanical aperture of the QD chamber itself. The exception is LSS1 where the SPS internal beam dump TIDVG is installed. The aperture at location QDA.11910 is much reduced because of it. Table 1 summarises the 4 locations found in the scans with the smallest vertical aperture around the ring.

As can be seen from the upper plot of Fig. 3, the aperture measurement is reproducible within typically better than 0.5 mm. Part of the measurement accuracy limitation comes from the noise on the BCT, which is in the order of $\approx 5 \times 10^8$ protons. The error bars in the plot do not indicate the error from the BCT resolution. More studies need to be carried out in 2017 to define the systematic error of the new measurement technique.

The consistency of the obtained results was cross-checked by scaling the obtained bump values at the QD locations to the locations of the MBB-to-MBA transitions as indicated in Fig. 2, where the beam loss should occur. Ideally the scaled values should be equal to the MBA aperture at this location. The aperture is however smaller than it should be at almost every location, see Fig. 3 (lower plot).

Table 1: The four locations with the smallest vertical aperture in the SPS in 2016.

location	aperture [mm]	error [mm]
QD.13310	43.1	± 0.5
QD.10710	43.3	± 0.2
QD.33110	44.6	± 0.6
QD.42310	45.2	± 0.7

The local aperture measurements suggest that the aperture bottleneck of the SPS is not at the beam dump, but at locations close to QD.10710 and QD.13310. Roughly 4 mm of aperture are missing at these locations. The total aperture measured at location QDA.11910 of 48.2 mm corresponds to ≈ 42.5 mm aperture at the center of the internal beam dump TIDVG, but 45.3 mm at the exit of the TIDVG, where the aperture bottle neck is supposed to be located. The theoretical aperture there is 42 mm. This inconsistency will have to be further investigated in 2017.

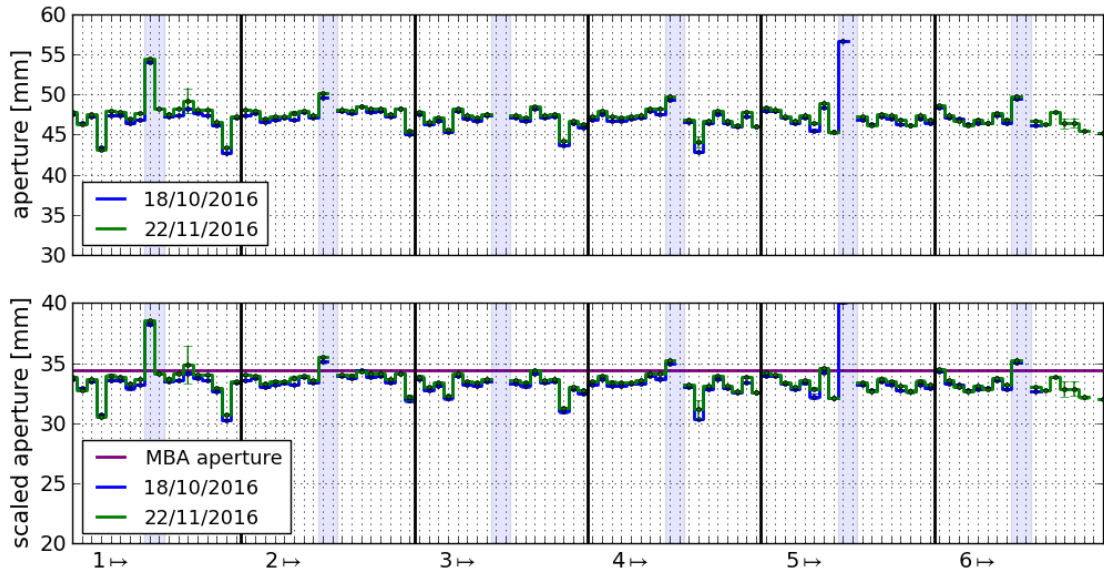


Figure 3: Total aperture measured at all defocusing quadrupole locations on 18th of October in blue and on 22nd of November in green. The numbers 1 - 6 on the bottom of the plot indicate the number of the corresponding sextant. The shaded areas correspond to the LSS. The lower plot shows the aperture measurements scaled to the location of the MBB-MBA transitions. The aperture of the MBA vacuum chamber is also indicated

SPILL QUALITY

The feed-forward based spill control was introduced in 2015 to remove the continuous trajectory changes on the North Area targets caused by the feedback controlled slow extraction [3]. The feed-forward is calculated only upon request. On a shot-by-shot basis, the spill quality relies on the reproducibility of the machine.

The hysteresis of the SPS magnets is not sufficiently modelled in the SPS control system. Any changes to the set of magnetic cycles played one after the other, the so-called super-cycle, have an impact on the beam parameters and hence on the flux of extracted particles during slow extraction. A measure of the uniformity of the spill is the "effective spill length" [7] which is defined as:

$$t_{efs} = \frac{[\int_{t_1}^{t_2} f(t) dt]^2}{\int_{t_1}^{t_2} [f(t)]^2 dt} \quad (1)$$

where $f(t)$ is the extracted intensity as a function of time. Fig. 4 and 5 show the evolution of the circulating intensity and extracted intensity calculated from the decay of the intensity during the extraction flat-top. The extracted intensity ramp-up at the beginning of the spill is introduced on purpose as the RF structure takes roughly ≈ 500 ms to diminish to an acceptable level for the North area experiments. Any events during this time are not taken into account. The situation in

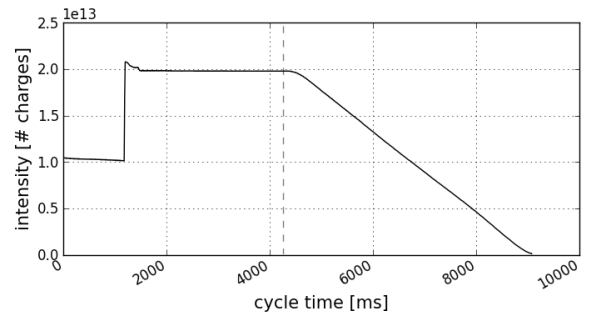


Figure 4: Evolution of the intensity through the fixed target cycle in the SPS in 2016. The dashed line indicates the moment at which the slow extraction starts.

Fig. 4 corresponds to a well adjusted spill and the effective spill length calculated according to (1) is $t_{efs} \approx 4500$ ms. If LHC 450 GeV/c cycles are added to the super-cycle or the dynamic economy mode is enabled, where the cycles are not fully played in case no beam is injected, the beam parameters will change. The effect on the extracted intensity before running the feed-forward algorithm is shown in Fig. 6 and 7. The effective spill length is reduced to 3800 ms for that case.

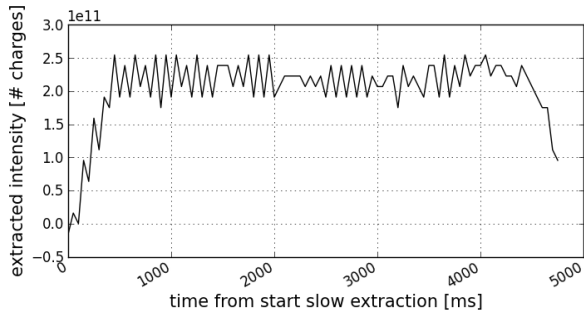


Figure 5: Extracted intensity as function of time on the extraction plateau of the fixed target cycle calculated from the intensity evolution in Fig. 4.

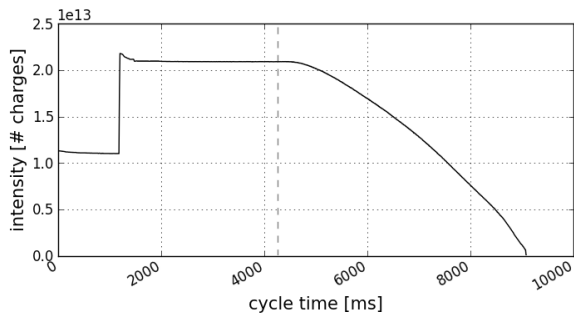


Figure 6: Evolution of the intensity through the fixed target cycle in the SPS in 2016 after a super cycle change. The dashed line indicates the moment at which the slow extraction starts. The beam is not extracted with a constant rate.

2016 Effective spill length

The typical value of the effective spill length for the 10.8 s long fixed target cycle in the SPS with a 4800 ms flat-top was ≈ 4500 ms. Due to hysteresis reasons, as explained above, the expected spill length could however be much reduced for extended periods. Fig. 8 shows the evolution of the effective spill length during 24 h where the LHC was in machine development (MD) and LHC beam had to be provided frequently by the SPS leading to many super-cycle changes. Whereas the first few hours of Fig. 8 are representative for a so-called production super-cycle with high duty cycle for the North Area, the period of the first shaded

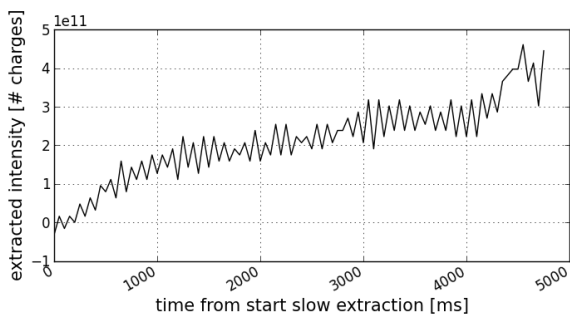


Figure 7: Extracted intensity as function of time on the extraction plateau of the fixed target cycle calculated from

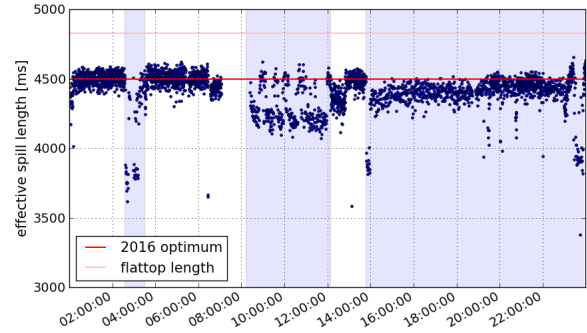


Figure 8: Evolution of the effective spill length during 24 h on 6th of October 2016. The shaded areas indicate times where LHC beam production cycles were in the SPS super-cycle. The first periods included LHC cycles with beam dedicated to the LHC with the LHC not continuously requesting beam such that the dynamic economy was played. During the last extended period a setting-up cycle for LHC beam was in the super-cycle with constant beam request.

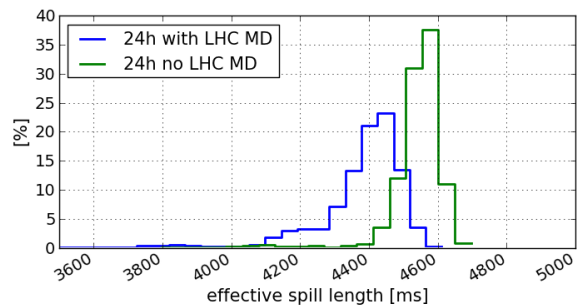


Figure 9: Distribution of effective spill length over 24 h on 6th of October, 2016, with MD in the LHC and 24 h on 16th of October, 2016, without MD in the LHC.

area is typical for an LHC filling super-cycle in terms of effective spill length. Fig. 9 shows the comparison of the distribution of effective spill lengths over 24 h with LHC MD (6th of October 2016) and a typical day with the occasional LHC filling or infrequent super-cycle changes in the SPS (16th of October 2016). Not surprisingly, the more stable running period without LHC MD leads to a narrower effective spill length distribution and also a slightly higher average effective spill length.

The hysteresis of the main dipoles seems to be the main cause of the spill macro structure variations with super-cycle changes [8]. In 2017 online field measurements of the reference magnets will be available. It is hoped that the analysis of this data will allow to build an automated correction algorithm.

Spill frequency content

As was discussed in [3] the SPS slow extracted spill is strongly modulated at 50 Hz and its harmonics. Without active correction the intensity fluctuations can be as high as 100 %. The amplitude and phase of the 50 Hz and higher

FIXED TARGET BEAMS

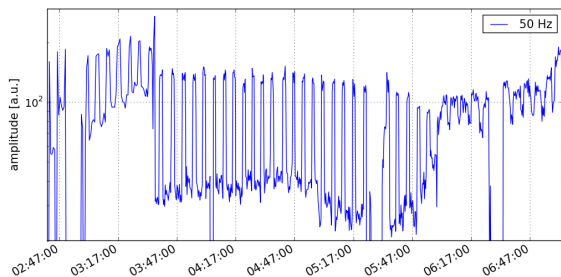


Figure 10: Evolution of the amplitude of the 50 Hz content in the spill. The 50 Hz amplitude bursts occur every few minutes.

harmonics modulations drift over time and the correction has to be frequently adjusted. In 2016 the system used to feed forward a small amplitude compensating tune modulation was calibrated for its spill phase response. As a result of this campaign a deterministic automatic algorithm could be put in place to adjust the modulation parameters. The adequate amplitude of the modulation is derived from an automatic scan.

Despite the more performant tools, the 50 Hz spill ripple seemed to be uncorrectable at times. Recording the evolution of the 50 Hz amplitude without changing the correction revealed the cause of this issue. The amplitude of the 50 Hz ripple does not slowly drift over time, but its amplitude is increased by up to a factor 5 for a short period of a few minutes and then decreased again. These bursts re-occur with a period of several minutes. Fig. 10 shows an example of such an observation. The bursts are not always present. For the time being no correlation with any modes of operation could be established.

Another problem in 2016 was the fact that strong modulation of the extracted intensity did not only occur at 50 Hz and higher harmonics thereof, but also at about 30 Hz or 65 Hz. The amplitudes of the peaks at these frequencies could be as high as of the 50 Hz lines, Fig. 11, but no active correction is available at these frequencies. The origin of these disturbances need to be found and corrected at the source. The FFT of the current of the QF main quadrupole circuit in the SPS also showed ≈ 30 Hz in the spectrum when the disturbance was strong on the spill, see Fig. 12. When the quadrupole power supply was swapped towards the end of the run in 2016, the 30 Hz issue disappeared.

SUMMARY & CONCLUSION

Optimising the vertical acceptance in the SPS is fundamental for minimising losses with high intensity fixed-target beams at low energy. An automated tool for measuring the local aperture at all defocusing quadrupoles was developed and tested in 2016. The results show that the vertical aperture bottleneck of the SPS is not at the internal beam dump TIDVG, but in the vicinity of QD.13310 and QD.10710. Also in sextant 3 and 4 bottlenecks were found.

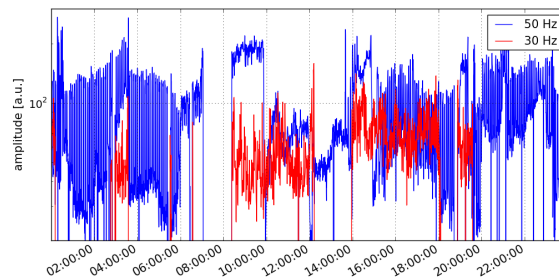


Figure 11: Evolution of the amplitude of the 50 Hz and 30 Hz content in the spill on 6th of October 2016. 50 Hz bursts are also present during most of the time of the observation time.

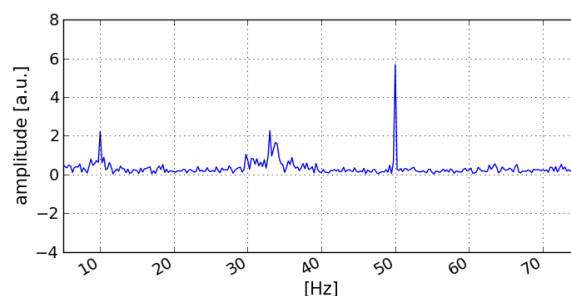


Figure 12: FFT of the current of the QF circuit during the slow extraction plateau on 6th of October 2016. Lines with large amplitude at 50 Hz as well as around 30 Hz can be seen in the spectrum.

The SPS slow extracted spill can be well corrected with feed-forward algorithms controlling the rate of extracted intensity as well as the 50 Hz and higher harmonics spill ripple. Good spill quality on a shot-by-shot basis relies however on reproducibility and several effects lead to that neither the spill macro structure nor the harmonic content of the spill were stable. Uncompensated hysteresis effects of the main field might be the origin of the macro structure changes. Work is underway to understand and model the hysteresis better and make it part of automated correction algorithms. Noise in the spill at 30 and 65 Hz is most probably induced by the main power supplies. Swapping the QF power supply already removed the 30 Hz ripple. More performant tools are now available to correct the 50 Hz and harmonics modulation of the spill. To really profit from these tools though, the origin of the 50 Hz bursts will have to be found and removed.

REFERENCES

- [1] N. A. Tahir et al., *New J. Phys.* 10, 073028 (2008)
- [2] E. Gschwendtner, et al., "Feasibility Study of the Awake Facility at CERN", IPAC, Shanghai, China, 2013
- [3] V. Kain et al., "New spill control for the slow extraction in the multi-cycling SPS", IPAC2016, Busan, North Korea.
- [4] M. Giovannozzi, et al., "Operational Performance of the CERN Injector Complex with Transversely Split Beams", *Phys. Rev. Accel. Beams* 20, 014001 (2017)
- [5] J. Wenninger, "YASP: Yet Another Steering Program"
- [6] D. Jacquet et al., "LSA - The High Level Application Software of the LHC and its Performance during the first 3 years of Operation", ICALEPCS, San Francisco, USA, 2013.
- [7] H. Weisberg, "Effective spill length monitor", AGS division technical note, Brookhaven National Laboratory, New York, 1980.
- [8] F. Velotti et al., "Investigation of the remanent field of the SPS main dipoles and possible solutions for machine operation", these proceedings.

SLOW EXTRACTION AT THE SPS: EXTRACTION EFFICIENCY AND LOSS REDUCTION STUDIES

M.A. Fraser*, F. Addesa, G. Cavoto, F. Galluccio, S. Gilardoni, B. Goddard, F. Iacoangeli, V. Kain, D. Mirarchi, S. Montesano, F. Murtas, S. Petrucci, S. Redaelli, F. Roncarolo, R. Rossi, W. Scandale, L.S. Stoel, F.M. Velotti

INTRODUCTION

Elevated activation levels in LSS2 were first reported during an intervention on the SPS extraction septum (ZS) in September 2015. The increase was attributed to higher intensity Fixed Target (FT) operation and poorer extraction efficiency, and reported to the IEFM [1]. Since this event the awareness of the impact of slow extraction losses on the operation and maintenance of the SPS has been heightened. This is particularly pertinent in light of tightening limits on dose to personnel and recent requests for increased intensities, as well as ambitious future experimental proposals in the North Area (NA), such as the SPS Beam Dump Facility (BDF) [2]. To follow up these issues the SPS Losses and Activation Working Group (SLAWG) was formed.

The MD programme for 2016 was originally foreseen to test the faster spill on a 1.2 second flat-top for the BDF and benchmark simulations of the extraction process, but this was not possible due to the restrictions imposed by the TIDVG. Nevertheless, during operational set-up and re-alignment of the electrostatic septum (ZS) the extraction efficiency could be studied parasitically. The first re-alignment of the ZS actually took place during dedicated MD time in May, before moving to physics time.

The application of bent crystals used in different configurations and modes of operation for slow extraction is being studied [3, 4]. Bent crystals offer promising solutions for reducing the activation of the SPS LSS2 extraction region that is induced by the small fraction of beam that unavoidably impinges the ZS during the conventional resonant slow extraction process. In 2016, the slow extraction of a low intensity coasting 270 GeV proton beam into the TT20 extraction line towards the NA of the SPS was demonstrated in dedicated MDs using the extraction septa in LSS2 and a bent crystal, provided by the UA9 collaboration as part of their experimental installation in LSS5.

TIDVG Restrictions

The TIDVG fault in 2016 limited the scope of slow extraction MD plans. Extraction tests that could be carried out as part of operational set-up were carried out, such as the alignment of the ZS, checking spiral step size, extraction bump amplitude, profile measurements, aperture measurements, etc. The following MDs were largely put on hold or severely limited due to the intensity limit:

- MD181: Deployment of new SPS BDF cycle and extraction tests

* mfraser@cern.ch

- MD183: Deployment of new SPS BDF optics for TT20

- MD186: Investigation of slow-extraction losses and optimisation studies

Fortunately, the restriction on single-bunch coasting MD's at 270 GeV was relaxed and crystal-assisted slow extraction MDs could be carried out:

- MD953: Crystal-assisted slow extraction through LSS2

The requests for the MD programme in 2017 will reflect the time lost in 2016.

MD186: INVESTIGATION OF SLOW EXTRACTION LOSSES AND OPTIMISATION STUDIES

Extraction losses at the ZS were improved in 2016 with beam-based alignment campaigns, however a local hotspot discovered in the end-of-year RP survey indicated that the losses had been pushed downstream. Although the TPST is a dedicated absorber the situation must be better ameliorated in 2017 and studies are on-going to understand the cause of the hotspot. The re-alignments were slow, taking over 8 hours. With the possibility to scan the up and the downstream ends of each of the 5 ZS tanks it was challenging to minimise the measured loss on BLMs in an efficient manner. This type of alignment is a potential use case for machine learning algorithms, which will be pursued to improve the efficiency in 2017. It is also expected to re-align by moving the beam instead of the ZS to correct for orbit drifts.

The extraction inefficiency could be measured parasitically as ZS position was scanned during the realignments and could therefore be carried out despite the TIDVG restrictions. The objective was to experimentally quantify the efficiency of the SPS slow extraction process and make a first attempt to calibrate the secondary emission foils (BSI) foils in TT20 using the ring BCT. The BSI foils are used to determine transmission through the NA transfer lines and to determine the Protons on Target (POT) sent to the experiments. Significant discrepancies in the calibration of these foils have been reported but the source of the discrepancy is not understood. The titanium foils in the first two BSI's of the TT20 extraction line, which are normally permanently inserted into the extracted beam, were used in the calibration tests, as shown in Fig. 1: BSI.210216 (used for the servo spill control) and BSI.210279.

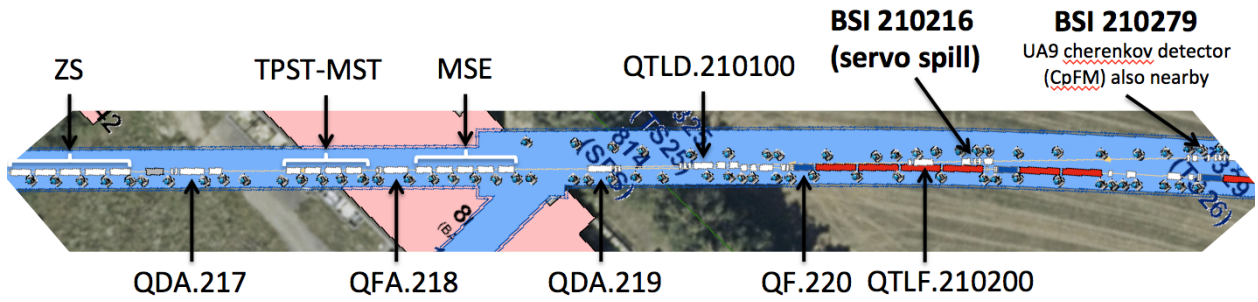


Figure 1: Layout of the LSS2 extraction region and location of the BSI's.

Extraction Inefficiency Measurement Concept

The inefficiency measurement used the more reliable ring BCT intensity measurement to calibrate both the BLMs and BSIs as the extraction efficiency was deliberately varied by misaligning the ZS. The concept relies on the assumption that losses do not appear somewhere that the BLM system does not cover and that the results can be extrapolated over a rather large range. The concept is based on investigations made at the AGS in Brookhaven during the 1980's [5], as shown in Fig. 2.

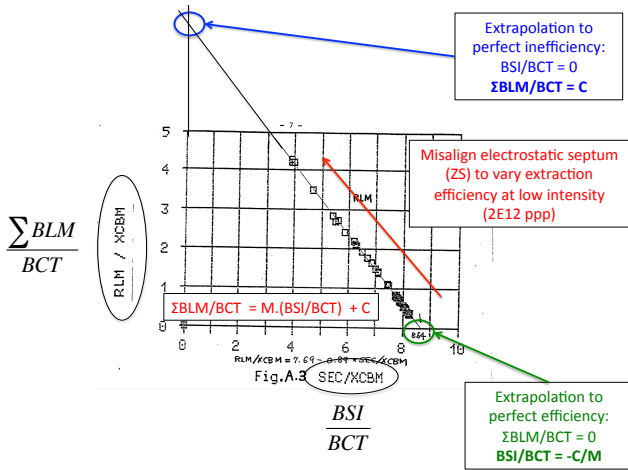


Figure 2: Measurement concept with AGS data [5].

The septum is deliberately skewed, as is done anyway to find the optimum position during re-alignment, and the resulting beam losses are correlated to the measured beam intensity extracted into the transfer line, normalised to the total intensity in the ring before extraction measured on the BCT. The correlation is closely linear and one can compute the extraction efficiency and check the calibration of the BSI against the BCT by extrapolating and computing the intercepts with each of the axes as shown in Fig. 2.

A low intensity beam of 2×10^{12} ppp was extracted during the MD to avoid damaging the ZS and to avoid unnecessary activation. It was important to remove the beam intensity lost at injection and dumped after the extraction to properly normalise the loss and extracted beam intensity data. A total of 160 shots were measured as the downstream end of the

ZS girder was scanned by ± 1.5 mm, i.e. both towards and away from the circulating beam. A screenshot of the ZS scan application is shown in Fig. 3, where the BLM response is recorded as function of the downstream girder position.

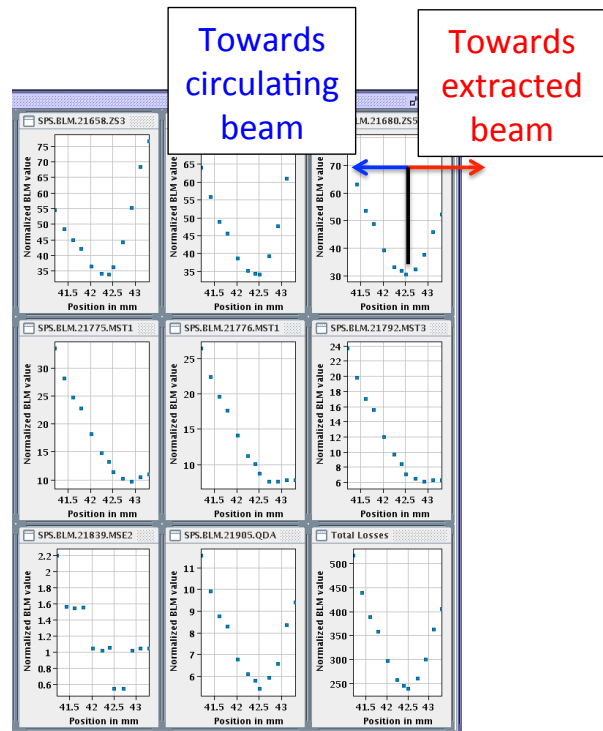


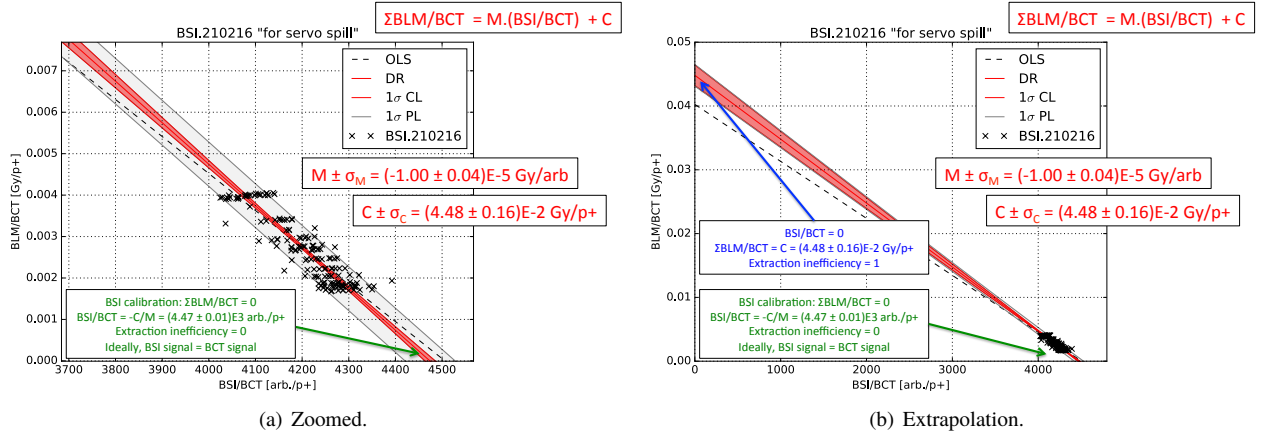
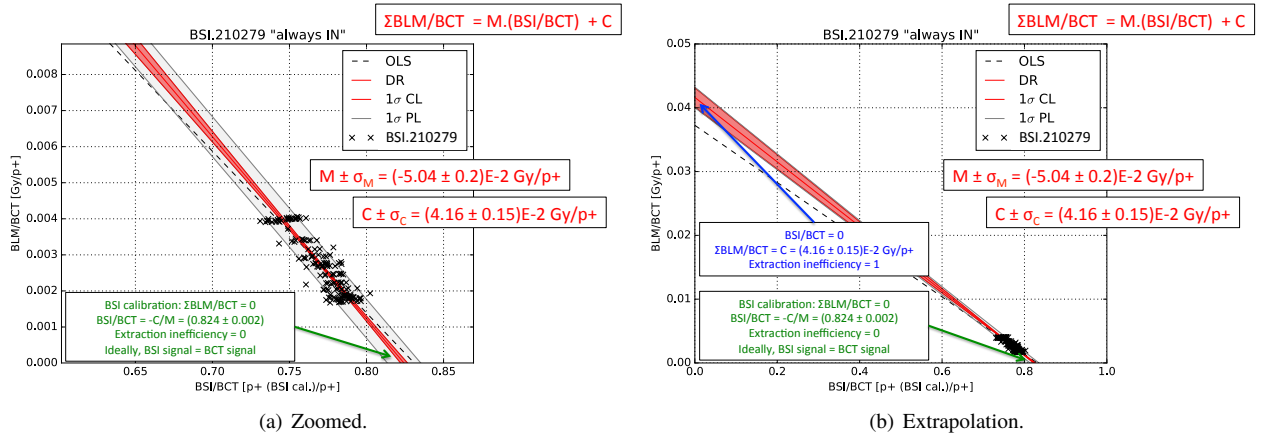
Figure 3: Screenshot of the ZS scan application for girder movement. The normalised loss (per extracted proton) measured on different BLMs in LSS2 are displayed as a function of the downstream ZS girder position.

Extraction Inefficiency Results

The results collected on the two different BSIs are shown in Figs. 4 and 5, and summarised in Table 1. In order not to introduce any additional non-linear effects it was decided not to adjust the gain of the BSI even though relatively low intensities were being extracted. This is the source of the poor signal-to-noise on the BSI measurement data. The measurement errors in both the BLM and BSI measurements

Table 1: Summary of extraction inefficiency measurements

BSI #	Comment	Extraction Inefficiency [%]	Calibration Error
210216	servo spill, Ti, always IN	4.0 ± 0.2	n/a
210279	second in TT20, Ti, always IN	3.6 ± 0.2	-17.6 ± 0.2


 Figure 4: Results for BSI.210216 (used for the servo spill control): downstream girder position scanned ± 1.5 mm.

 Figure 5: Results for BSI.210279: downstream girder position scanned ± 1.5 mm.

were taken carefully into account when carrying out the least-squares regression analysis:

$$\frac{\sum BLM}{BCT} = M \frac{BSI}{BCT} + C \quad (1)$$

The extraction inefficiency was computed by normalising the sum BLM signal for the well-aligned case with the extrapolated y-intercept:

$$\text{Ext. inefficiency} = \frac{\left. \frac{\sum BLM}{BCT} \right|_{ZS \text{ aligned}}}{C} \quad (2)$$

The electronics of BSI.210216 used for the spill control is different to the other BSI's in the line and is not used for intensity measurements, only spill fluctuations, therefore no calibration constant is available to compare with the

ring BCT. The calibration of BSI.210279 showed a discrepancy of close to 18% compared to the BCT, as shown by the intercept of the regression with the horizontal axis. In both cases the slow extraction inefficiency was measured at approximately 4.0%.

Discussion & Outlook

Care must be taken in the interpretation of the results as systematic errors are rather unknown, e.g. transmission losses between the SPS and the BSI location will systematically shift the calibration measurements. However, an 18% loss of beam intensity between the ring and the transfer line is unlikely and doesn't agree with the measured 4% extraction inefficiency. In order to better understand the calibration of the BSI, the titanium foil in question (in BSI.210279), was

removed from TT20 and installed in TT10 during the shutdown where a BCT is present. Dedicated measurements of its secondary emission yield are planned in 2017 to further investigate these results.

MD953: CRYSTAL-ASSISTED SLOW EXTRACTION AT THE SPS

The possibility of extracting highly energetic particles from the SPS by means of silicon bent crystals has been explored since the 1990's. The channelling effect of a bent crystal can be used to strongly deflect primary protons and hence direct them onto an internal absorber or, with additional deflection elements, eject them from the synchrotron. Many studies and experiments have been carried out to investigate crystal channelling effects. As summarised in [6–9], diffusion extraction of 120 and 270 GeV proton beams has already been demonstrated in the SPS with dedicated experiments located in the ring. At present in the SPS, the UA9 experiment is performing studies to evaluate the possibility to use bent silicon crystals to steer particle beams in high energy accelerators [10–14]. Recent studies on the feasibility of extraction from the SPS have been made using the UA9 infrastructure with a longer-term view of using crystals to help mitigate slow extraction induced activation of the SPS. During three dedicated MD sessions in 2016 the possibility to eject particles from the SPS and into the extraction channel in Long Straight Section (LSS) 2 using the bent crystals was tested.

Extraction Concept

The location of the bent crystals in LSS5 is 3.5 km from the slow extraction channel in LSS2, which makes the extraction process highly sensitive to the working point of the machine. The crystals are positioned on the inside of the ring and deflect inwards. Detailed studies [15] failed to identify a suitable working point that provides the required phase advance for the channelled beam to jump the wires of the electrostatic septum, on the outside of the ring, on the first turn. However, they did identify the potential of the operational Fixed Target working point ($Q_x = 26.62$, $Q_y = 26.58$) to extract the beam at the ZS on the second turn, with a fractional phase advance of 252° . The extraction scheme chosen is shown schematically in Fig. 6, where the electrostatic and magnetic septa (ZS, MST and MSE) are shown, along with a dedicated Cherenkov for Proton Flux Measurement (CpFM) detector installed upstream of the extraction dump (TED) in the TT20 transfer line. The channelled beam performs almost 41 betatron oscillations before reaching the ZS.

With the machine configured to store a single bunch at constant energy, the transverse halo can be slowly and non-resonantly extracted as it diffuses into the crystal, is channelled and deflected into the extraction septa. The advantage of such an extraction concept for these first development tests is that the channelled beam passes the UA9 experimental area a second time, allowing the exploitation of the

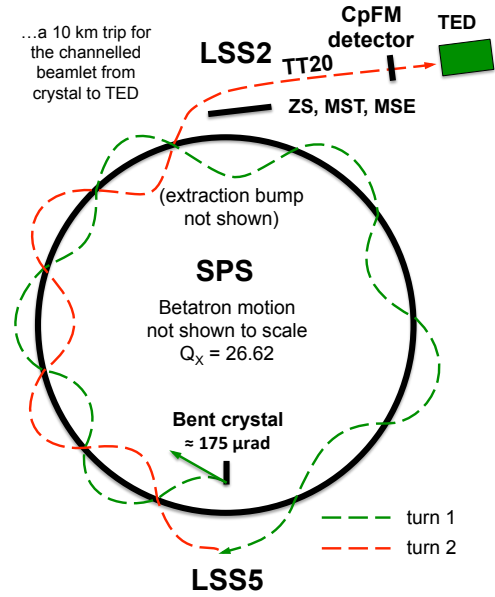


Figure 6: Schematic of the crystal-assisted extraction scheme.

specialised beam diagnostics systems to verify the phase advance of the channelled beam in the absence of suitable systems in LSS2.

In order to simulate the dynamics of the extraction, the SPS was implemented in MADX and particle tracking carried out in combination with the pycollimate [16] scattering routine, where the crystal interaction was modelled using single-pass UA9 measurement data [17]. More details of how the simulations were implemented are found in [15]. The presentation of the beam at the entrance to the ZS is shown in Fig. 7 after being tracked through the crystal and the SPS, where the distribution is approximated as a hollow halo beam to save computation time. In Fig.7 the crystal is aligned at -6σ with a channelling angle of $-160 \mu\text{rad}$, where positive denotes a direction towards the outside of the ring. The simulations were used to design the LSS2 extraction bump, ensuring its closure, and to set the strengths of the extraction septa such that the channelled beam enters TT20 on the nominal trajectory.

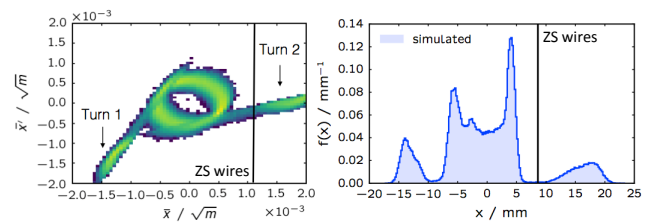


Figure 7: Beam distribution (hollow halo approximation) at ZS: normalised phase space (left) and horizontal projection (right) [15].

Experimental Setup

A schematic view of the UA9 installation is shown in Fig. 8 comprising two goniometers for a multi- and a single-crystal setup, different detectors used to precisely align the crystals to the beam and to measure different observables, as well as absorbers and scrapers to intercept the channelled beam. The collimators and absorbers are named TCXHW, QD517, QF518, QD519, TCSM, TACW, QF520, MBA-MBB, MBB, QD521 and TAL.

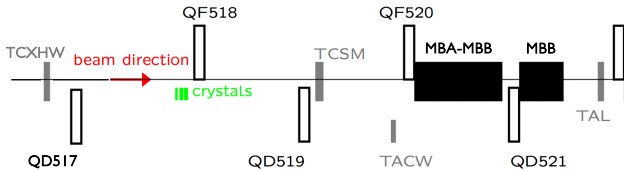


Figure 8: Schematic of the UA9 experiment's installation.

TCSM, TACW and TAL, and all of them are equipped with LHC Beam Loss Monitors (BLMs), which are significantly more sensitive than the standard SPS BLMs. The TCSM is an LHC prototype collimator with two horizontal jaws, composed of 1 m long blocks of graphite, and equipped with a Beam Position Monitor (BPM) at its entrance. The TACW is an old SPS collimator, which was equipped with a single 60 cm tungsten jaw to suit the needs of the UA9 experiment, used to stop the crystal-channelled beam during data taking. The experimental installation starts with the TCXHW, a 10 cm long double-sided tungsten scraper, and terminates with a station in the high dispersive area, which includes the TAL (10 cm long double-sided tungsten scraper) and a Roman Pot containing two Timepix high-precision pixel detectors [18, 19]. In conjunction with UA9's absorbers and scrapers, the channelled beam could be stopped from circulating after a given number of turns and its position and transverse size measured on its return to LSS5, turn-by-turn. To directly detect the presence of channelled beam in the TT20 extraction line a dedicated CpFM detector [20, 21] was installed that is capable of measuring single-particle events and therefore very low extraction rates.

Experimental Results

A low intensity LHC-type single-bunch of 1.6×10^{10} protons was used throughout the tests in order to guarantee the protection of the fragile wires of the ZS from damage. The effect of the imperfect closure of the LSS2 extraction bump was tested and shown not to significantly perturb the channelling efficiency. The BPM at the TCSM observed a 0.1 mm movement as the extraction bump was powered to its nominal value of 57 mm at the ZS, inducing a spike in the channelling rate and increasing BLM readings in LSS5. To avoid this type of dynamic effect it was decided to turn on the extraction bump before aligning the crystal with the beam. The alignment of the UA9 equipment was carried out as usual [22]. The crystal was positioned at 6σ and aligned by scanning the angle of its goniometer and using scintillators and BLM loss levels as observables to determine the optimal orientation of the crystal. The bending angle of the crystal used was measured in a previous MD in 2016

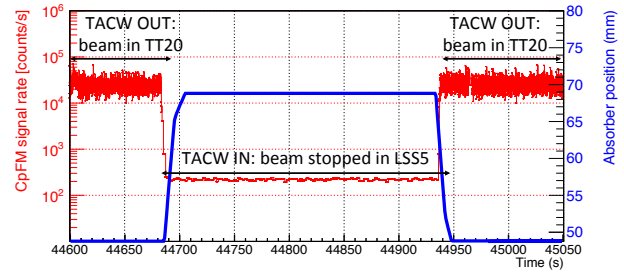
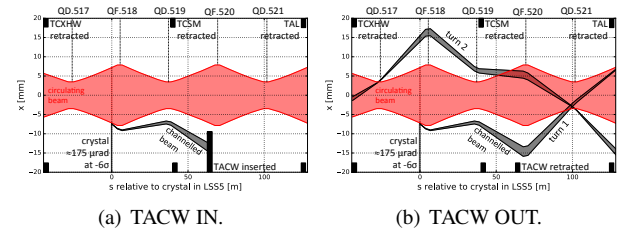


Figure 9: TT20 CpFM signal rate (red) vs. TACW position (blue) [21].

as $175 \pm 2 \mu\text{rad}$, consistent with [10]. Once the TACW absorber was retracted and the channelled beam was free to circulate, it was immediately detected by the CpFM in the TT20 extraction line. After small steering corrections the beam could be centred on the nominal beam axis at the CpFM. The extraction could be ceased by reinserting the TACW and stopping the channelled beam in LSS5 as shown in Figs. 9 and 10.



(a) TACW IN. (b) TACW OUT.

Figure 10: LSS5 absorber configuration for extraction.

The horizontal beam size of the extracted beam at the CpFM was also measured at $\sigma = 0.6 \text{ mm}$ by scanning the quartz bar of the CpFM through the extracted beam in the horizontal plane, as shown in Fig. 11. The signal reaches its maximum value when the quartz bar samples the entire beam. The calibration of the CpFM is on-going in order to quantify the exact extraction rate in terms of protons extracted per second.

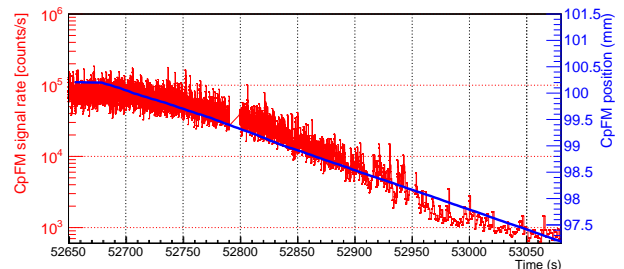


Figure 11: TT20 CpFM signal (red) and position (blue) vs. time as it is moved out of the extracted beam [21].

Further tests were made to guarantee that the extracted beam was indeed channelled by the crystal. These involved (i) inserting the outer TCSM jaw and TAL inner jaw to stop the channelled beam on the second turn in LSS5, also allowing beam profiles to be reconstructed. (ii) changing the

angular alignment of crystal and (iii) adjusting the diffusion rate by exciting the beam with the transverse damper and checking the measured extraction rate on the CpFM. The aforementioned direct checks using the CpFM behaved as expected with the most elegant validation being an indirect measurement carried out with the Timepix detector. With the extraction bump turned off, and the TCXHW inserted to intercept the channelled beam from circulating after its fourth pass of LSS5, the channelled beam was imaged on the Timepix detector on its third pass of LSS5, as shown in Fig. 12(a). When the extraction bump was turned on the channelled beam disappeared from the image as it was pushed over the septum wires of the ZS and extracted into TT20, as shown in Fig. 12(b). The extraction was again confirmed by the CpFM.

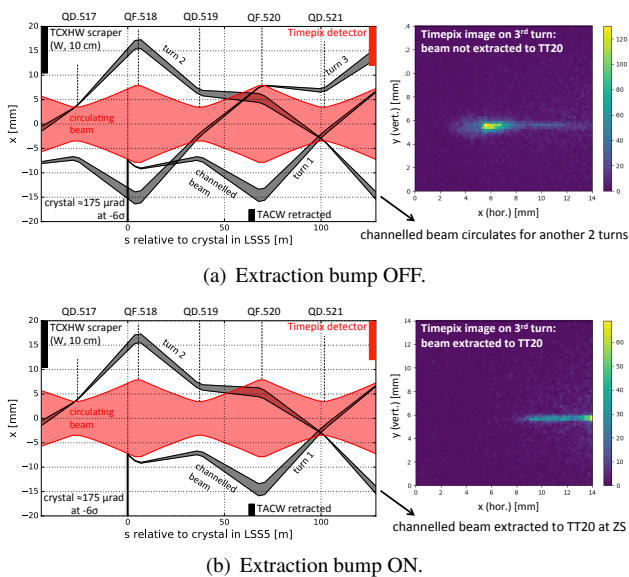


Figure 12: Timepix images showing the disappearance of the channelled beam in LSS5 when extracted in LSS2.

Conclusion & Outlook

The non-resonant crystal-assisted slow extraction of a 270 GeV proton beam from the SPS towards the North Experimental Area has been demonstrated during dedicated MD tests in 2016. The low intensity beam was extracted from the halo of a circulating LHC-type single-bunch of 1.6×10^{10} protons and its presence validated and characteristics probed with a dedicated CpFM detector in the extraction line. This is the first time in the SPS that a bent crystal has been used in conjunction with the extraction systems to bring the beam into a transfer line towards an experimental area. In light of future experimental requests for Fixed Target physics at 400 GeV, this is an important step in the application of bent crystals at the SPS for the mitigation of slow extraction induced activation.

The MD programme will continue in 2017 to increase the extraction rate, characterise the extracted beam, quantify and compare the losses for different extraction techniques.

and calibrate the CpFM with a beam synchronous trigger to improve the signal-to-noise ratio. The application of bent crystals to shadow the wires of the ZS during a conventional resonant slow extraction is being actively studied [23] and the installation of a dedicated crystal to test this proposal in MD sessions is presently being discussed.

Acknowledgements

We are grateful to the other members of the UA9 collaboration for their support and their contribution to the development of the experimental apparatus used in this study. This work has been partially supported by the ERC CoG CRYSB-EAM G.A. 615089. We would also like to thank the SPS operation, beam instrumentation, septa and RF teams for their support, as well as the Experimental Areas and Physics co-ordinators for their flexibility and understanding in the scheduling of the dedicated MD sessions.

REFERENCES

- [1] M.A. Fraser *et al.*, Follow-up on the SPS Activation Levels, Presentation at the 157th IEFC Meeting, 13th November 2015.
- [2] A. Golutvin *et al.*, "A Facility to Search for Hidden Particles (SHiP) at the CERN SPS", CERN, Geneva, Switzerland, Rep. CERN-SPSC-2015-016 (SPSC-P-350), Apr. 2015.
- [3] M.A. Fraser *et al.*, "SPS Slow Extraction Losses and Activation: Challenges and Possibilities for Improvement", in *Proc. IPAC'17*, Copenhagen, Denmark, May 2017, paper MOPIK045.
- [4] W. Scandale, "Bent crystals in particle accelerators", Seminar at the 19th ABT Engineering Forum, CERN, Geneva, 28th November 2014.
- [5] M. Tanaka *et al.*, SEB Extraction Study I-III, December 1986 to March 1987, AGS Studies Reports #219,222 and 229.
- [6] W. Herr, "Diffusion of particles induced by transverse noise and its application to crystal extraction experiments", CERN, Geneva, Switzerland, Rep. CERN-SL-92-53-AP, Nov. 1992.
- [7] H. Akbari *et al.*, "First results on proton extraction from the CERN-SPS with a bent crystal", *Phys. Lett. B*, vol. 313, pp. 491 - 497, Sep. 1993.
- [8] K. Elsener *et al.*, "What did we learn from the extraction experiments with bent crystals at the CERN SPS?", in *Proc. EPAC'98*, Stockholm, Sweden, June 1998, pp. 239 - 241.
- [9] K. Elsener *et al.*, "Proton extraction from the CERN SPS using a bent crystal", *Nucl. Instrum. Meth. B*, vol. 119, pp. 215 - 230, Oct. 1996.
- [10] W. Scandale *et al.*, "First results on the SPS beam collimation with bent crystals", *Phys. Lett. B*, vol. 692, pp. 78 - 82, Aug. 2010.
- [11] W. Scandale *et al.*, "Comparative results on collimation of the SPS beam of protons and Pb ions with bent crystals", *Phys. Lett. B*, vol. 703, pp. 547 - 551, Aug. 2011.
- [12] W. Scandale *et al.*, "Strong reduction of the off-momentum halo in crystal assisted collimation of the SPS beam", *Phys. Lett. B*, vol. 714, pp. 231 - 236, Aug 2012.

- [13] W. Scandale *et al.*, “Optimization of the crystal assisted collimation of the SPS beam”, *Phys. Lett. B*, vol. 726, pp. 182 - 186, Oct. 2013.
- [14] W. Scandale *et al.*, “Observation of strong leakage reduction in crystal assisted collimation of the SPS beam”, *Phys. Lett. B*, 748, pp. 451 - 454, Sept. 2015.
- [15] F.M. Velotti, “Higher brightness beams from the SPS for the HL-LHC era”, Ph.D. thesis, EPFL, Lausanne, Switzerland, 2017.
- [16] F.M. Velotti *et al.*, “SPS-To-LHC transfer lines loss map generation using pycollimate”, in *Proc. of IPAC'15*, Richmond, VA, USA, May 2015, paper THPF09, pp. 3934 - 3937.
- [17] R. Rossi, G. Cavoto, D. Mirarchi, S. Redaelli, W. Scandale, “Measurements of coherent interactions of 400 GeV protons in silicon bent crystals”, *Nucl. Instrum. Meth. B*, vol. 355, pp. 369 - 373, July 2015.
- [18] D. Turecek, T. Holy, J. Jakubek, S. Pospisil, Z. Vykydal, “Pixelman: a multi-platform data acquisition and processing software package for Medipix2, Timepix and Medipix3 detectors”, *J. Instrum.*, vol. 6 pp. C01046, Jan. 2011.
- [19] V. Kraus, M. Holik, J. Jakubek, M. Kroupa, P. Soukup, Z. Vykydal, “FITPix - Fast Interface for Timepix Pixel Detectors”, *J. Instrum.*, vol. 6, pp. C01079, Jan 2011.
- [20] S. Montesano *et al.*, “The Cherenkov detector for proton flux measurement (CpFM) In the UA9 experiment”, in *Proc. IBIC'16*, Barcelona, Spain, Sept. 2016, paper TUPG40, pp. 430 - 433.
- [21] F.M. Addesa, “Cherenkov light in vacuum beam monitor for crystal-assisted beam manipulations”, Ph.D thesis, La Sapienza Università di Roma, Roma, Italy (in preparation).
- [22] S. Montesano and W. Scandale, “Apparatus and experimental procedures to test crystal collimation”, in *Proc. of IPAC'12*, New Orleans, Louisiana, USA, May 2012, paper THEPPB011, pp. 3254 - 3256.
- [23] F.M. Velotti *et al.*, “Reduction Of Resonant Slow Extraction Losses With Shadowing Of Septum Wires By A Bent Crystal”, in *Proc. of IPAC'17*, Copenhagen, Denmark, May 2017, paper MOPIK050.

WIDEBAND FEEDBACK SYSTEM PROTOTYPE VALIDATION

K. Li*, H. Bartosik, E. Bjorsvik, W. Hofle, G. Kotzian, B. Salvant
CERN, Switzerland

J. Fox, C. Rivetta, O. Turgut
SLAC, Menlo Park, California, USA

Abstract

A wideband feedback demonstrator system has been developed in collaboration with US-LARP under the joint leadership of CERN and SLAC. The system includes wideband kicker structures and amplifiers along with a fast digital reconfigurable system up to 4 GS/s for single bunch and multi bunch control. Most of the components have been installed in recent years and have been put into operation to test both intra-bunch damping and individual bunch control in a multi bunch train. In this note we report on the MD program, procedure and key findings that were made with this system in the past year.

INTRODUCTION – HISTORY, MOTIVATION AND OVERVIEW

A wideband feedback system has been proposed in the past and has been under study to be used in the SPS for instability mitigation. This was mainly motivated by the hard limit in the maximum reachable bunch intensity imposed by the transverse mode coupling instability (TMCI) threshold. Another limitation arises from electron cloud formation from multipacting which can also drive coherent instabilities and drastically limit the machine performance. These coherent instabilities would prevent reaching the beam parameters required by the LHC Injector Upgrade (LIU) in preparation for HL-LHC. In both cases, the instabilities feature coherently growing intra-bunch motion. Given the typical bunch length in the SPS which is in the range of 3 ns at injection energy, this renders signals in the 100 MHz up to the 1 GHz range. Conventional transverse feedback systems as used in the LHC or the SPS to-date operate with a roll off starting at already 1 MHz, thus, the frequencies exhibited by the aforementioned instabilities are way beyond the reach of these feedback systems.

Whereas a conventional transverse damper is ideally able to sample and act on the individual bunch centroid motion, a wideband feedback system is fast enough to sample individual time slices within a single bunch. This allows it to act distinctively on individual slices and thus to control coherent intra-bunch motion. The challenges with these systems, however, are multifold. For one, it is non-trivial to design kicker structures that can generate signals of up to 1 GHz with enough power to provide an adequate correction kick (or integrated deflecting voltage). The same holds true for the power amplifiers used to power the kicker structures which

need to deliver high power in a very broad frequency range and with a correspondingly flat phase response. Moreover, the high sampling rate, noise filtering and the presence of synchrotron motion make the digital processing and finding suitable control algorithms very demanding.

Nevertheless, a system was devised and developed which features wideband kicker structures powered by wideband amplifiers with a frequency reach up to 700 MHz and 1 GHz, respectively. In conjunction with this, a fast digital signal processing unit which is fully reconfigurable and can run at a sampling rate of up to 4 GS/s allows the implementation of a variety of control techniques for sophisticated intra-bunch control.

It has been shown in simulations that a wideband feedback system can work to ameliorate both TMCI and e-cloud driven instabilities [1–4]. The simulations include a sophisticated model to mimic a realistic feedback system. This system was added on top of the basic chain of components to correctly simulate the beam dynamics of collective effects including important beam and machine parameters, impedances and electron cloud effects. Thus, the numerical proof of principle was at hand and to be complemented by an experimental realization. Fig. 1 displays an example of a simulation which shows an e-cloud instability being damped by a 500 MHz wideband feedback system. Beam centroid motion and transverse emittance are plotted as a function of the number of turns for different feedback gains. From a certain gain onward, the system mitigates the e-cloud driven intra-bunch coherent motion.

The project has been reviewed twice. Following the presentations during the last review, we will focus here on the key findings made during MDs. In the following two sections we will briefly describe the main components of the system and then discuss the MD program and results for single bunch and multi bunch studies.

SYSTEM INSTALLATION

The wideband feedback system installed in the SPS currently comprises of 2 stripline kickers with a bandwidth of up to 700 MHz which are each powered by two 250 W amplifiers with a bandwidth of 5 – 1000 MHz. A slotline kicker which can provide more kick strength in the range of 1 GHz is currently under construction [5, 6]. The digital signal processing unit has been developed and deployed and contains all the hardware, firmware and interfaces necessary to implement excitation signals or perform closed loop control for single as well as for multiple bunches in a 25 ns

* kevin.shing.bruce.li@cern.ch

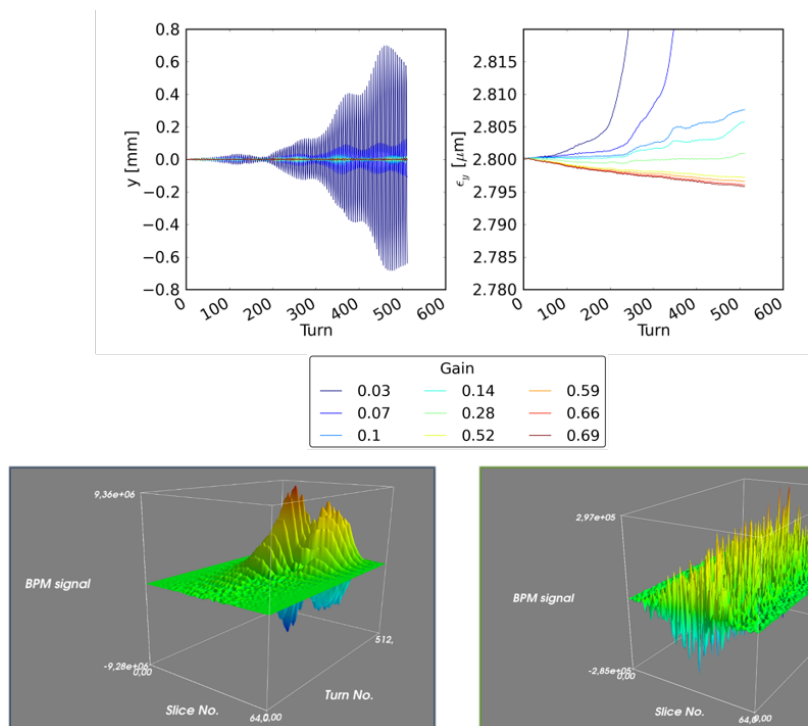


Figure 1: Simulation of an e-cloud driven instability. The top plot shows the beam centroid motion and transverse emittance plotted as a function of the number of turns for different feedback gains for a 500 MHz wideband feedback system. The bottom plots show the time evolution of the intra-bunch motion for a gain of 0 (left side) and a gain of 0.4 (right side).

bunch train. Different filters have been designed and implemented to cope with the different optics configurations, namely the classical Q26 as well as the Q20 optics which features by a factor 2.5 increased synchrotron frequency. Fig. 2 shows a schematic of the location of the installed components, all located around BA4 of the SPS. The system uses an exponential coupler as pickup [7, 8].

MD PROGRAM AND RESULTS

The aim of the wideband feedback demonstrator system is the experimental verification of damping of TMCI and e-cloud-like instabilities. Therefore, one of the main goal of the MDs was to show damping of intra-bunch motion for both single and multi-bunch instabilities in order to verify the frequency reach of the system. As explained above, this is the part which poses the most challenging requirements on the entire feedback chain.

Going for the most straightforward option of setting the machine to operate somewhere beyond the TMCI threshold and using the wideband feedback system to cure the instability is, unfortunately, not a viable strategy. For cost reasons, the system had to be built with reduced specifications and in particular with the power amplifiers being one of the main cost drivers, the output power of the system is very limited and not able to handle the fast rise times of a typical TMCI, in particular during transients at injection and with the presently achieved noise floor. Therefore, the strategy chosen instead was to identify a working point that would exhibit an intra-bunch motion while at the same time being

slow enough such that it could be handled by the wideband feedback system with its reduced power. It is known from simulations as well as measurements that this working point, or rather region of working points, does exist in the SPS [9] and the task for the single bunch studies was to find this point in the machine, set up the wideband feedback system and then to close the loop on the instability to hopefully regain the beam stability.

The multi bunch studies involve the injection of up to 4 batches of 72 bunches into the SPS. For this reason these latter studies required dedicated MD time. Due to reduced machine availability, only about 50% of the dedicated MDs could be realized as planned.

Single bunch instabilities

As mentioned above, the first step in using the wideband feedback system for single bunch studies was to find the right working point for exciting an intra-bunch instability at sufficiently low growth rates, such that the instability could still be handled within the limitations of the system. Fig. 3 shows simulations from [9] where the left plot shows the growth rates of an instability as a function of the longitudinal emittance and the bunch population. The sharp yellow boundary separates the regions of the classical fast TMCI in red from the more stable regions in blue. Within the stable regions, it is possible to make out a light blue island which features comparatively low growth rates. The plot on the right hand side shows the turn-by-turn signal along the bunch as it would be picked up by a wide band beam position

WIDEBAND FEEDBACK SYSTEM PROTOTYPE VALIDATION

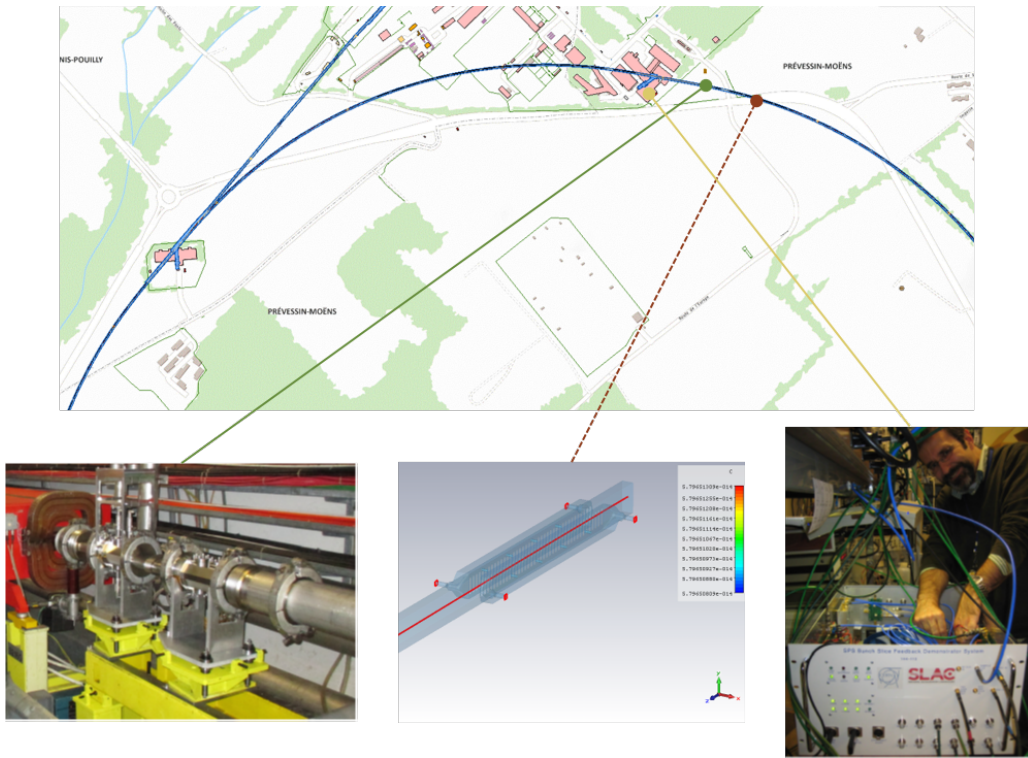


Figure 2: Location of the stripline kickers (green) and the feedback box (yellow). A slotline kicker is still under fabrication but is foreseen to be installed close to the stripline kickers.

monitor. The signal features a single node and an oscillation along the bunch with a phase shift of about 180 degrees from the tail to the head. The regime clearly shows coherent intra-bunch motion suitable for demonstrating the frequency reach of the wideband feedback system.

To obtain the same instability in practice, the machine had to be set up very carefully using a variety of parameters. To make the beam more susceptible to instabilities without the need of pushing the intensities too far, it was decided to conduct the studies using the Q26 optics. Therefore, the required machine parameters were not expected to exactly match the region of working points found in the simulation mentioned above. The longitudinal emittance was typically somewhat below 0.3 eVs. The transverse emittance was chosen to be rather large, above $3 \mu\text{m}$ in order to suppress space charge forces as much as possible as it is not entirely clear how exactly space charge would influence the pure TMCI. The intensity was tuned around 1.6×10^{11} ppb. The main diagnostics used was the FBCT to detect losses occurring due to instabilities as well as the fast losses application to distinguish slower headtail-like instabilities from TMCI. Finally, the headtail monitor, basically a scope with a high sampling rate connected to a large memory buffer for turn-by-turn acquisition along the bunch was used to detect coherent intra-bunch motion. This instrument could be used in addition to the internal ADC of the feedback box, the latter one which could be gated to read out on an individual bunch.

The chromaticity was then carefully adapted to move it as close as possible to zero while still remaining positive. Typically the bunch was stable at intermediate chromaticity values and became unstable when the chromaticity was lowered. Unfortunately, the arising instabilities were exclusively of mode type zero and did not feature any intra-bunch coherent mode pattern. It became clear that by using just the chromaticity it was not possible to isolate an instability which would feature any coherent intra-bunch motion. Instead, the main RF voltage proved to be an important knob to adjust, and by lowering the RF voltage it was possible to induce instabilities that did contain a distinguishable amount of intra-bunch motion. Still, the signals were dominated by a strong coherent motion of the bunch centroid which would quickly saturate the wideband feedback system rendering it virtually ineffective upon closing the loop. To ameliorate this situation, we then added the conventional transverse damper [10] to control and remove the centroid component and prevent saturation of the wideband feedback system. Doing this, finally, it was possible to isolate a clean coherent intra-bunch instability in a reproducible manner. Fig. 4 shows a snapshot from a headtail monitor acquisition. The signal looks very similar to the once predicted in the simulations.

It is to be noted, that the conventional damper was active during this time during growth of the intra-bunch motion. The coherent intra-bunch instability ultimately leads to losses which could be seen on the BCT. It is in this configuration, that the wideband feedback loop was closed. Fig. 5

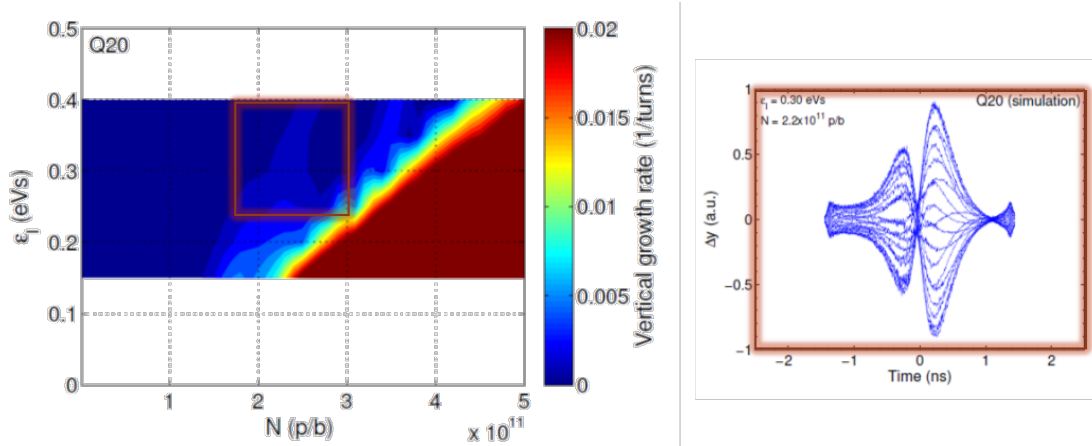


Figure 3: Simulations of the single bunch growth rate (colour-coded) as a function of the longitudinal emittance and the bunch intensity. The red frame indicates a good potential working area to test a wideband feedback system. The plot on the right hand side displays the BPM signal produced by instabilities arising from operation close to this working point and features a clearly visible coherent intra-bunch motion.

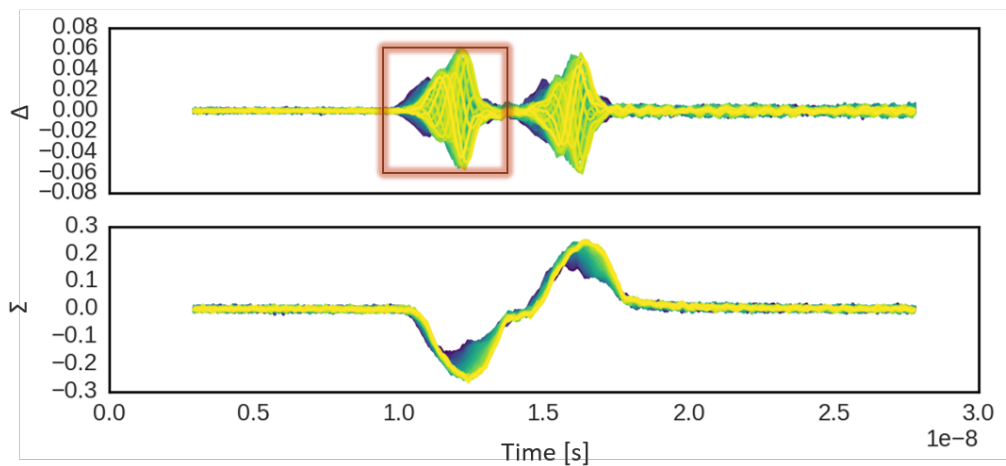


Figure 4: A snapshot of the instability produced in the SPS acquired with the headtail monitor. The top plot shows the Δ -signal and features the single node very similar to what has been computed in simulations as show in Fig. 3 (red frame). The second signal is an artifact from the reflected signal in the headtail monitor as becomes clear also from the bottom plot which shows the Σ -signal.

WIDEBAND FEEDBACK SYSTEM PROTOTYPE VALIDATION

shows the typical signature of this instability with the top plots showing the beam intensity lost over a few 100 μs and the bottom plots showing the signal acquired up by the internal ADC of the feedback box. The bottom plot shows the delta signal which clearly features the single node and the 180 degrees face shift from head to tail which is characteristic for the coherent intra-bunch motion. The observed signal corresponds to what is seen by the headtail monitor – note that here the ordering of the channels is inverted in time.

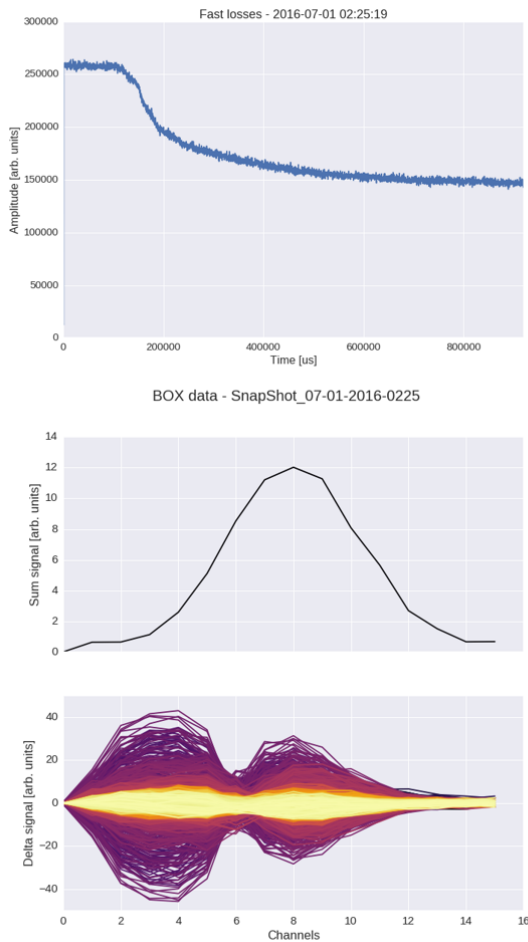


Figure 5: Open loop signature and acquisition of the internal ADC. Fast losses are visible accompanied by a distinct coherent intra-bunch oscillation shown in the bottom plot which displays the turn-by-turn delta signal across the bunch.

After recording the instability above, the loop was closed for the following supercycle. The signature of the instability with the loop closed is shown in Fig. 6. The beam does no longer exhibit any signs of instabilities. The intensity is similar, but no losses are visible. The ADC shows initial coherent motion corresponding to the injection oscillations. These are damped rapidly by the transverse damper after which the growth of the coherent intra-bunch motion featured in Figs. 4 and 5 is entirely suppressed. The loop was opened and closed randomly several times during the following 30

minutes and the picture remained absolutely consistent in that the intra-bunch motion rose each time the loop was opened and was damped when the loop was closed.

With this, the experimental verification of intra-bunch damping at high frequencies was achieved, however, keeping in mind that the machine had to be carefully tuned in order to be compatible with the reduced specifications of the wideband feedback system. As the system was built to also help mitigation of e-cloud instabilities, the next step was to show multi-bunch control in a batch of several bunches.

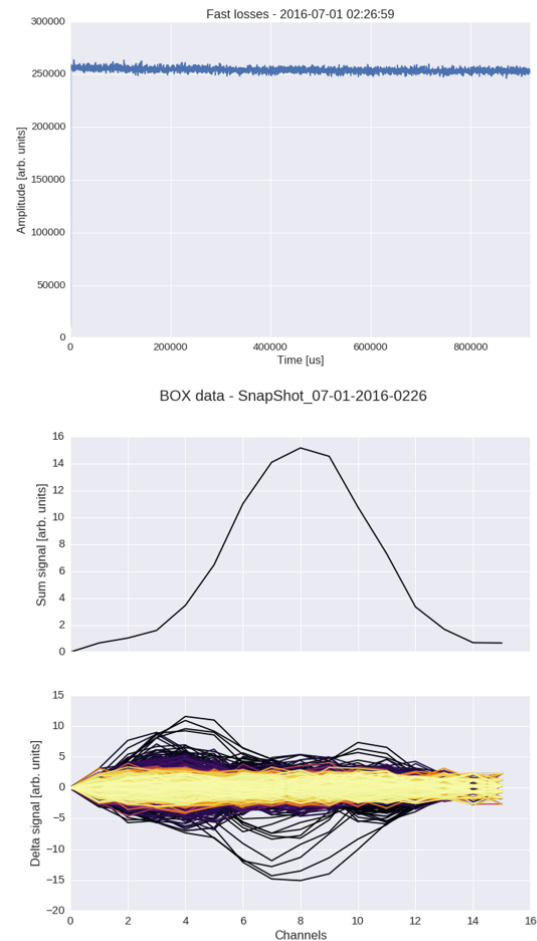


Figure 6: Closing the loop fully restores beam stability. Losses are fully mitigated and the coherent intra-bunch oscillations are no longer seen in the ADC.

Multi bunch instabilities

Multi bunch instabilities occur at certain conditions in the SPS when several trains of 72 bunches at high intensity are injected (approaching 2×10^{11} ppb for Q20 optics). Normally, the transverse damper should take care of coupled bunch instabilities of any order in the SPS. If the instability is not of coupled bunch type and contains intra-bunch motion then the transverse damper will be ineffective against these instabilities. however. During the SPS scrubbing runs

in 2014 and 2015, multi-bunch instabilities were routinely observed despite having the transverse damper set up and active. It is assumed, that these instabilities are generated by e-cloud. During the scrubbing runs, chromaticity and even octupoles had to be employed in order to stabilize the beam. These, however have undesirable side effects as the large tune spread can substantially decrease the beam lifetime.

With e-cloud being the likely origin of the observed instabilities, finding a good working point to test the wideband feedback demonstrator system with limited power becomes very hard. As conditioning and de-conditioning of the inner vacuum surfaces takes place continuously and dependent on the composition of the supercycle or the operational program, e-cloud effects are intrinsically not reproducible.

The strategy here was to prepare a high intensity scrubbing beam at close to 2×10^{11} ppb and inject batches of 72 bunches into the SPS with the Q20 optics and high chromaticity. Having the transverse damper active is mandatory here to suppress coupled bunch instabilities. Slowly lowering the chromaticity at a certain point leads to losses. Looking at the headtail monitor or at the LHC BPMs one can observe the last bunches of the later batches starting to oscillate.

One can use the headtail monitor to also look into the intra-bunch motion of individual bunches in the batch. Figs. 7 shows a zoom into the last bunches of an unstable batch. One can see the last bunches going unstable. A zoom into an individual bunch reveals that the type of instability corresponds rather to a mode 0-like instability, meaning rather a pure centroid motion and less of a coherent intra-bunch pattern. In principle, this kind of pattern can be damped by the conventional damper, however, with several adjacent bunches oscillating at random phases this can be difficult for the transverse damper to handle.

Given the fact that unstable bunches are preferably located towards the end of batches and that the instability grows despite the presence of the transverse damper suggests that the instability is likely to be a result of e-cloud effects. With the high bandwidth and the advanced control algorithms of the wideband feedback system, this device is ideally suited to control individual bunches within a batch entirely separated from each other. As shown in the previous experiment with single bunches it could even damp intra-bunch motion. The observed types of instabilities in the multi-bunch configuration did not show this feature however.

Nevertheless, the instability provided a good test for the multi-bunch controller of the wideband feedback system. For this test, we set up the machine to exhibit a multi-bunch instability as described above keeping the wideband feedback loop open. Once a reproducible condition was reached for the instability, the loop was closed.

Figs. 8 shows one of the unstable bunches in an unstable batch in terms of the signal acquired by the internal ADC of the feedback box, once with the feedback loop open on the left hand side, and then with the feedback loop closed on the right hand side. The growth of the bunch centroid motion and the mode 0-like pattern can be seen on the left plot and corresponds to what has been observed on the same

instability with the headtail monitor. Upon closing the loop, the instability is perfectly damped. This was the case for all bunches within the batch meaning that the multi-bunch instability was perfectly mitigated by the wideband feedback system. Several measurements were taken, again randomly opening and closing the loop and the instability appeared and was suppressed in a reproducible manner.

SUMMARY AND NEXT STEPS

The experiments above show that the wideband feedback system in principle is able to damp intra-bunch instabilities as well as to independently control individual bunches in a multi-bunch batch. This implies that it is also possible to damp very high frequency multi-bunch or coupled bunch intra-bunch motion.

The multi-bunch studies were very difficult to reproduce from one dedicated MD to the next mainly because both the scrubbing beam and the machine could not be set up in a very reproducible manner. This is not surprising since the scrubbing beam was rarely deployed and usually needs dedicated preparation and setup throughout the injector chain starting from the PS Booster up to the SPS. One of the goals for the future will be to utilize the wideband feedback system to stabilize an actual scrubbing beam such that it can be run at low chromaticity and without making use of octupoles. For this, more tests should be done on multi-bunch batches to gain experience and confidence with the multi-bunch firmware and the configuration of the feedback box. A single batch could be enough for this. These types of MDs could potentially be run as parallel MDs with 72 bunches. Once the box is well set up it can be deployed during high intensity runs in the SPS.

For the single bunch studies it will be of high interest to see how the system can perform with modified optics and, in particular, with the Q22 optics which is foreseen to be tested in 2017. For this, new filters will have to be designed, implemented and tested. The Q22 optics has the potential to ameliorate certain limitations for the RF but at the same time it comes with a lower TMCI threshold close to the nominal intensity for LIU beams. This could ultimately prohibit the use of these optics. A wideband feedback system could be used to mitigate the TMCI, thus removing this limitation and opening up the parameter space for a successful deployment of these optics.

Both the single bunch as well as the multi-bunch operation modes still suffer from a lack of output power and it is not clear whether the kick strength is sufficient for the feedback system to work for operational beams. This will need to be tested. In addition, a slotline kicker structure is in fabrication and is planned to be installed during the 2017 YETS to complement the 2 stripline kickers probably with the same set of power amplifiers aimed to double the available kick strength.

One of the points not mentioned so far are the diagnostic possibilities of the system. With the signal acquisition and digital processing system at hand there are a variety of diag-

WIDEBAND FEEDBACK SYSTEM PROTOTYPE VALIDATION

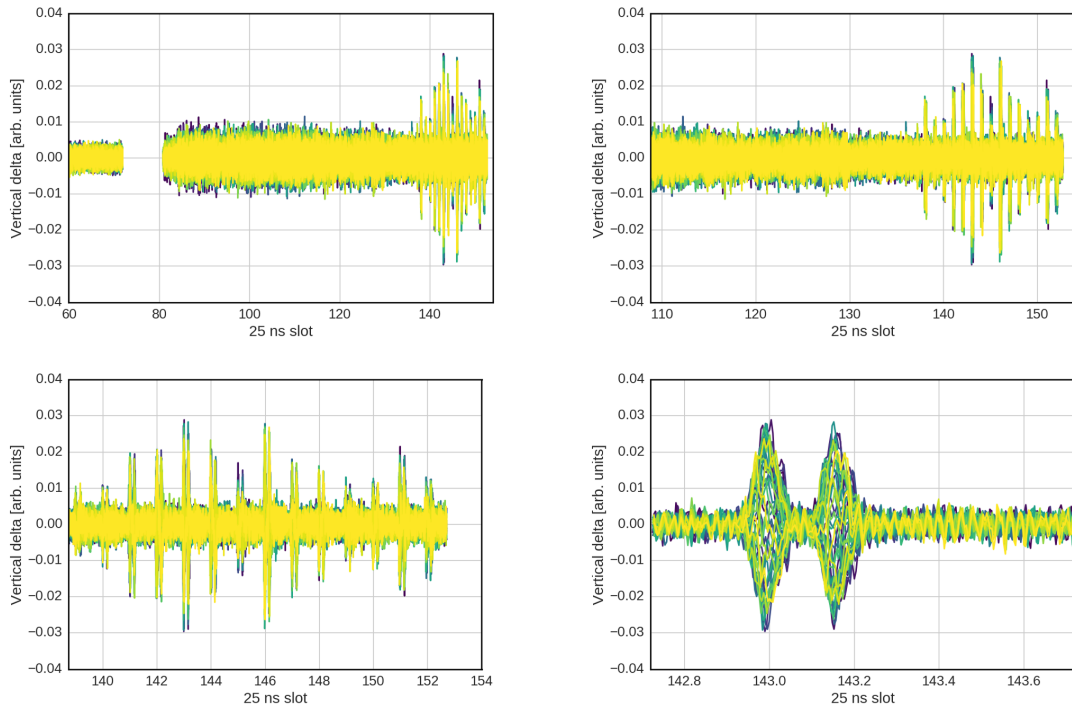


Figure 7: The plots above show a step-wise zoom into the final bunches of an unstable batch from the top-left to the bottom-right. Top left shows the headtail monitor acquisition of the entire batch with the last couple of bunches going unstable. The bottom right plot is a final zoom into an individual unstable bunch. For this bunch, the coherent centroid motion is well visible as well as the absence of any coherent intra-bunch structure. This is true also for all other unstable bunches in the batch.

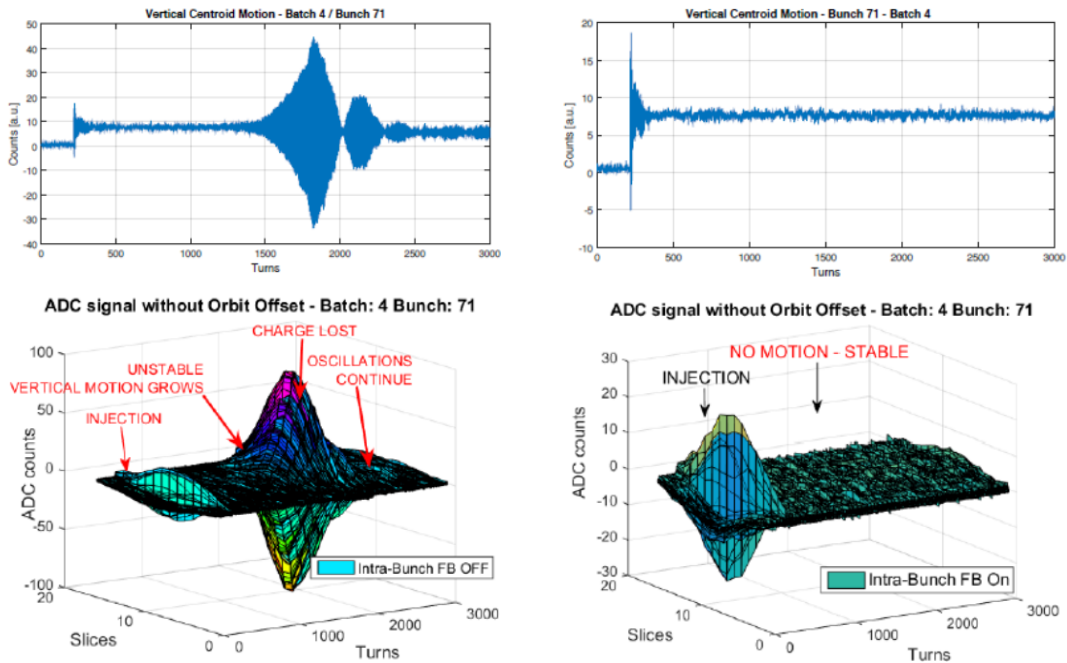


Figure 8: The bunch signal acquired by the internal ADC of the feedback box gated on bunch 71 in an unstable batch of 72 bunches. The left plot shows the growth of the centroid motion and the coherent mode 0-like bunch pattern when the feedback loop is open. The right plot shows the suppression of the same instability upon closing the feedback loop (note the different vertical scales).

nostic tools that one could think of designing. In particular, in combination with the kickers, the system can expand the present diagnostic capabilities for impedance and instability measurements to new regimes. The feedback system can be thought of as a programmable impedance and could be used to drive the beam at various modes to then check the beam response and thus probe impedances or also machine non-linearities.

In conclusion, at this point, important experimental proofs-of-principle for the wideband feedback system were made such as demonstrating the damping of intra-bunch motion as well as individual bunch control in a multi-bunch batch. The system holds lots of promise for the future applications but further R&D is required for a full understanding of its limitations and how to best overcome them such that it can be used for operational beams.

ACKNOWLEDGEMENTS

We wish to thank the SPS OP team for their support before and during the MDs.

REFERENCES

- [1] J.R. Thompson *et al.*, "Initial Results of Simulation of a Damping System for Electron Cloud-Driven Instabilities in the CERN SPS", Proceedings of PAC 2009, Vancouver, British Columbia, Canada, 2009.
- [2] K. Li *et al.*, "Instabilities Simulations with Wideband Feedback Systems: CMAD, HEADTAIL, WARP", Proceedings of ELOUD'12, 5-9 June 2012, La Biodola, Isola d'Elba.
- [3] K. Li *et al.*, "Modeling and Studies for a Wideband Feedback System for Mitigation of Transverse Single Bunch Instabilities", Proceedings of the 4th International Particle Accelerator Conference, Shanghai, China, 12–17 May 2013.
- [4] K. Li *et al.*, Wideband Feedback System, LIU-SPS Wideband Feedback Review, CERN, 20 September 2016.
- [5] J. Cesaratto *et al.*, "SPS Wideband Transverse Feedback Kicker: Design Report", CERN-ACC-NOTE-2013-0047/SLAC-R-1037, 20 December 2013.
- [6] M. Wendt *et al.*, Wideband Feedback System, LIU-SPS Wideband Feedback Review, Proceedings of the 8th International Particle Accelerator Conference, Copenhagen, Denmark, 14–19 May 2017.
- [7] T. Linnekar, CERN-SPS-ARF-SPS/78/17, CERN, Geneva, 1978.
- [8] R. De Maria *et al.*, "Performance of Exponential Coupler in the SPS with LHC Type Beam for Transverse Broadband Instability Analysis, Proceedings of DIPAC09, Basel, Switzerland, 2009.
- [9] H. Bartosik, "Beam dynamics and optics studies for the LHC injectors upgrade", CERN-THESIS-2013-257, 2013.
- [10] G. Kotzian, "SPS damper", MSWG Meeting, CERN, 13 February 2015

SPS BATCH SPACING OPTIMISATION

F.M. Velotti, W. Bartmann, E. Carlier, B. Goddard, V. Kain, G. Kotzian

INTRODUCTION AND MOTIVATIONS

Until 2015, the LHC filling schemes used the batch spacing as specified in the LHC design report. The maximum number of bunches injectable in the LHC directly depends on the batch spacing at injection in the SPS and hence on the MKP rise time.

As part of the LHC Injectors Upgrade project for LHC heavy ions, a reduction of the batch spacing is needed. In this direction, studies to approach the MKP design rise time of 150 ns (2-98%) have been carried out. These measurements gave clear indications that such optimisation, and beyond, could be done also for higher injection momentum beams, where the additional slower MKP (MKP-L) is needed.

After the successful results from 2015 SPS batch spacing optimisation for the Pb-Pb run [1], the same concept was thought to be used also for proton beams. In fact, thanks to the SPS transverse feed back, it was already observed that lower batch spacing than the design one (225 ns) could be achieved. For the 2016 p-Pb run, a batch spacing of 200 ns for the proton beam with 100 ns bunch spacing was requested and finally used.

Thanks to the good performance of the 200 ns scheme, this was proposed as operational scenario for 2017 p-p physics with BCMS beams.

In order to confirm the first observations and to evaluate the operational settings, the 2016 MD sessions were carried out.

SPS INJECTION SYSTEM

The SPS injection system is composed by a horizontal septum, MSI, and kicker, MKP. The MSI steers the beam coming from TT10 onto the nominal closed orbit (CO) and the MKP adjusts the angle to match the one of the circulating beam.

The MKP system is composed of four tanks, each of them connected to a high voltage generator. The first three tanks host 12 magnets of small aperture type with a rise time of 150 ns. The last tank hosts 4 large types which have a rise time of 225 ns (from specifications). Each generator is connected to two thyatron switches where each of them is connected to two magnets.

The total rise time, which then directly translates in the minimum batch spacing, is the result of the proper synchronisation of the individual magnets field waveforms. To this, ageing effect of the thyatron should also be added, because they will increase the response time of the switches and hence increase the rise time. Another source of error which contributes to the rise is the jitter of the triggering. All this can add up to several tens of ns.

ROAD TO 200NS batch spacing

To aim to have 200 ns batch spacing at injection, two possible optimisations are possible: fine synchronisation of each individual switches, optimal sharing of residual oscillations between injected and circulating batch. The main constraints are given by emittance growth and large intensity reduction due to high populated tails during scraping (or transport).

Fine synchronisation

The overall rise time depends on the individual rise times and on the synchronisation of them with respect to the beam passage. Theoretically, the optimum overlap is obtained when the individual delays are calculated accounting for the beam time of flight from one magnet to another.

The stability of the waveform then depends on the reproducibility of each individual waveform and on the stability of the conduction time of each individual switches. This can translate in a jittering optimum, which, if it becomes comparable to the bunch spacing, makes the optimum delay very unstable. Hence, switches health is a key parameter to achieve a clean and durable short rise time. In Fig. 1 an example of terminating magnet resistor (TMR) current measurements is shown, when the delay are set as the time of flight between individual magnets.

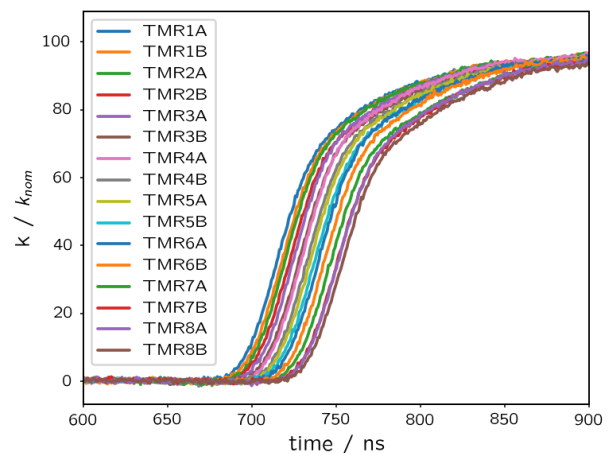


Figure 1: Example of TMR measurements accounting for perfect delay, calculated as time of flight between magnets.

Optimum delay

The other parameter to adjust to achieve a good injection with tighter batch spacing is the delay of the whole MKP system with respect to the injected batch. The optimum is reached when the residual oscillation is evenly shared between the last bunch of the circulating batch and the first of the injected one. as shown in Fig. 2.

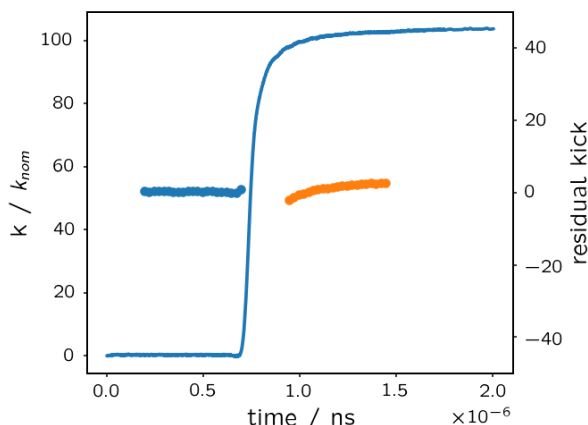


Figure 2: Schematic view of synchronisation of the normalised MKP waveform with injected batch (orange) and circulating one (blue).

In the SPS, the emittance growth that could be produced by such a residual kick is too small to be measured with the present profile measurements available. One way to evaluate how much each individual bunches are kicked by the MKP is to use the LHC BPMs in LSS5. These are BPMs which can resolve position bunch-by-bunch and turn-by-turn (Fig. 3).

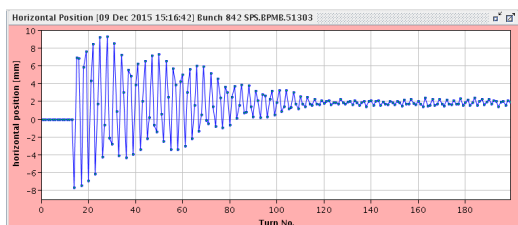


Figure 3: Example of horizontal position evolution of the first injected bunch as measured with one of the LHC BPMs.

The figure of merit used to evaluate the residual oscillation on the first injected and the last circulating bunch is the half amplitude:

$$A_{osc} = \left| \frac{x_{max} - x_{min}}{2} \right| \quad (1)$$

where x_{min} and x_{max} are the minimum and maximum horizontal amplitude excursions recorded around the injection event. The delay for which A_{osc} is the same for both bunches under analysis represents the optimum. In Fig. 4, the results for 225 ns and 200 ns batch spacing are shown. The increase in the residual oscillation when passing from 200 to 225 ns is only 1.5 mm.

The beam obtained with 200 ns batch spacing was then delivered to the LHC, where the final conclusion on the quality of such a scheme can be drawn. In Fig. 5, the intensity bunch-by-bunch is compared between 250 (top) and 200 ns (bottom) after injection into the LHC. No significant differences between the two schemes could be observed. In Fig. 6, the emittance bunch-by-bunch, as measured with the BSRT.

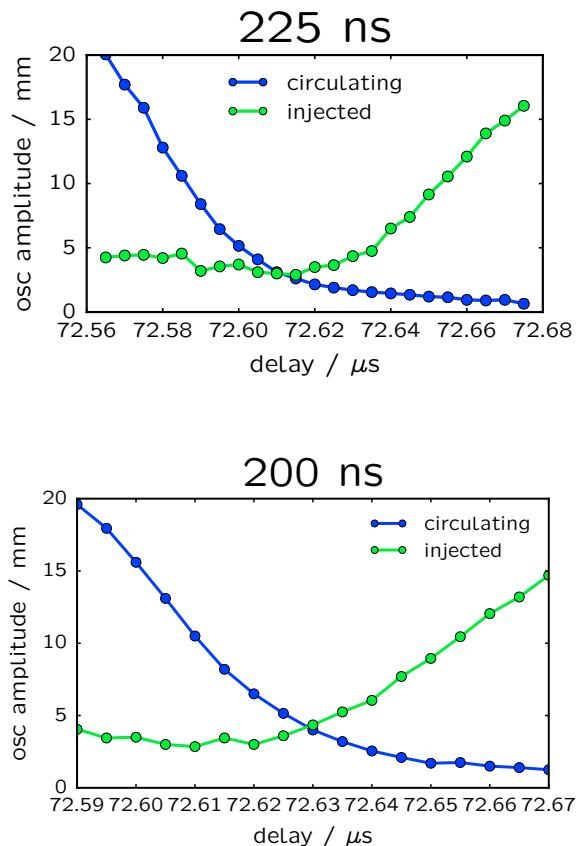


Figure 4: Results of delay scan with 225 ns (top) and 200 ns (bottom).

is shown when a 200 ns batch spacing beam is injected. The emittances of the bunches at the discontinuity are in the range of the intra-bunch jitter.

Such good results are combination of kicker synchronisation with beam and transverse feed back performances. A clear indication of the importance of the SPS transverse damper is shown in Fig. 7. In the top plot, the intensity bunch-by-bunch in the LHC with SPS damper off is shown and compared with the case with damper on (bottom). An intensity reduction of about 20% on the bunches close to the batch gap is observed. In comparison, essentially no reduction in intensity was observed in the LHC when the SPS damper is active.

CONCLUSIONS

The second part of 2016, the LHC proton physics run was carried out with 225 ns SPS batch spacing. In the 2016 Pb-p run instead, the 200 ns SPS batch spacing was already used.

For 2017 operation, the 200 ns SPS batch spacing has been proposed for operation, where, when combined with LHC batch spacing reduction (800 ns), an overall gain in luminosity of about 16% is foreseen [2]. With 200 ns batch spacing, the injection quality is more sensitive to the switches

SPS BATCH SPACING OPTIMISATION

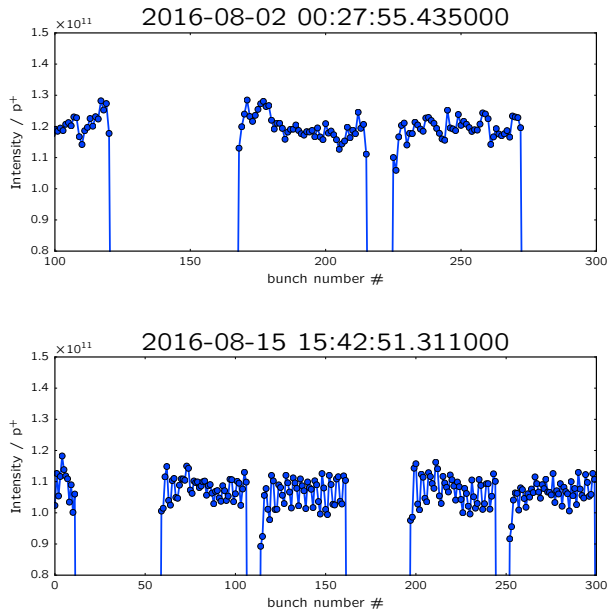


Figure 5: Bunch-by-bunch measurements with 250 (top) and 200 ns batch spacing at injection in the LHC.

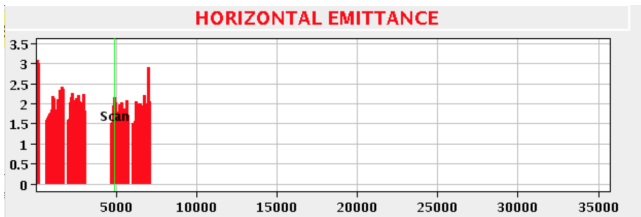


Figure 6: Emittance measurement done with the BSRT in the LHC at injection for 200 ns scheme.

drift, hence a constant monitoring of the individual delays is needed.

The MD time dedicated to this topic has been essential for both LHC Pb-Pb, Pb-p and proton physics of the last two years.

REFERENCES

- [1] B. Goddard, *et al.*, “SPS Injection and Beam Quality for LHC Heavy Ions With 150 ns Kicker Rise Time”, in *Proc. 7th Int. Particle Accelerator Conf. (IPAC'16)*, Busan, Korea, May 2016, paper TUPMR048, pp. 1360–1362, <http://jacow.org/ipac2016/papers/tupmr048.pdf>, doi:10.18429/JACoW-IPAC2016-TUPMR048, 2016.
- [2] W. Bartmann, *et al.*, “Impact of LHC and SPS Injection Kicker Rise Times on Lhc Filling Schemes and Luminosity Reach”, in *Proc. 8th Int. Particle Accelerator Conf. (IPAC'17)*, Copenhagen, Denmark, May 2017, paper TUPVA007, pp. 2043–2046, <http://jacow.org/ipac2017/papers/tupva007.pdf>, <https://doi.org/10.18429/JACoW-IPAC2017-TUPVA007>, 2017.

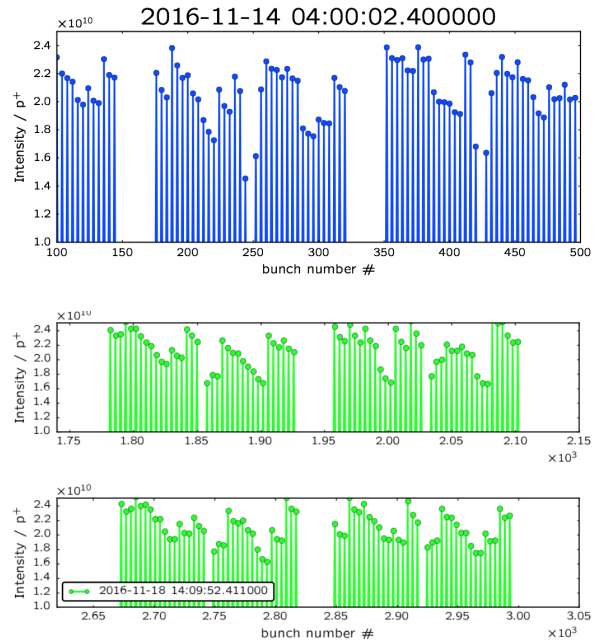


Figure 7: Bunch-by-bunch intensity comparison of the 200 ns scheme with damper off (top) and on (bottom).

EMITTANCE GROWTH IN COAST IN THE SPS

A. Alekou^{1,2}, F. Antoniou^{1,3}, H. Bartosik¹, R. Calaga¹

¹CERN, Geneva, Switzerland, ²University of Manchester, UK, ³University of Liverpool, UK

Abstract

The CERN SPS will be used as a test-bed for the LHC prototype crab-cavities, which will be installed and tested in the SPS in 2018. As the time available for experimental beam dynamics studies with the crab cavities installed in the machine will be limited, a very good preparation is required in advance. One of the main concerns is the induced emittance growth, driven by phase jitter in the crab cavities. In this respect, several machine development (MD) studies were performed during the past years to quantify and characterize the emittance evolution of proton beams in coast in the SPS. In these proceedings, the experimental observations from past years are summarized and the MD studies from 2016 are presented. Finally, a proposal for an experimental program for 2017 is discussed.

INTRODUCTION

For the LHC upgrade, the use of a crab-crossing scheme is foreseen aiming to restore an effective head-on collision at the interaction regions. When particles pass through a crab cavity (CC), they receive a z-dependent transverse kick. They can thus be used in order to compensate the crossing angle at the interaction region, minimizing in this way the geometric luminosity loss which otherwise arises from the crossing angle [1,2].

The crab cavities have been successively operated in KEKB [3] but have never been tested in high energy and high current proton machines. It is therefore of paramount importance to test them in another hadron machine before their full installation into the LHC. For this reason, two LHC prototype CC will be installed in the SPS during the technical stop at the end of 2017 and will be tested in 2018 in special machine development sessions. The SPS test is the only way to get conclusive answers on several aspects, like emittance growth, machine protection, RF non-linearity, instabilities, etc.

One of the main concerns that needs to be addressed in the SPS experiments is the induced emittance growth, driven by phase jitter in the crab cavities. A good understanding and characterization of the natural emittance growth in the SPS is thus very important in order to distinguish from the effect of crab cavity noise. Several machine development sessions with coast beams in the SPS were devoted in the past years to the natural emittance growth studies [4]. In these proceedings, the results from past studies are summarized and the machine development studies of 2016 are presented. Finally a proposed experimental program for 2017 is discussed.

PREVIOUS STUDIES

Several experimental sessions were carried out in the past, aiming to characterize the long-term natural emittance growth in the SPS. Three different energies have been studied and the results until 2012 are summarized in [4]. The main conclusions from those studies were:

- The natural emittance growth in the SPS is substantial at low energies and moderate at higher energies for coasting beams.
- The emittance growth appears to be primarily a single bunch effect.
- The effect of the working point is minimal with very low intensity bunches, even in the proximity of the 3rd order resonance.
- Chromaticity had strong effect and the growth was approximately proportional to Q' .

While in the experiments up until 2012 both horizontal and vertical emittances had similar growth slopes, a different behavior was observed in 2015. The results from the MD of October 2015 are presented in fig. 1, showing a much larger horizontal growth compared to the vertical one. A similar trend was observed in the MD of May 2015 as well.

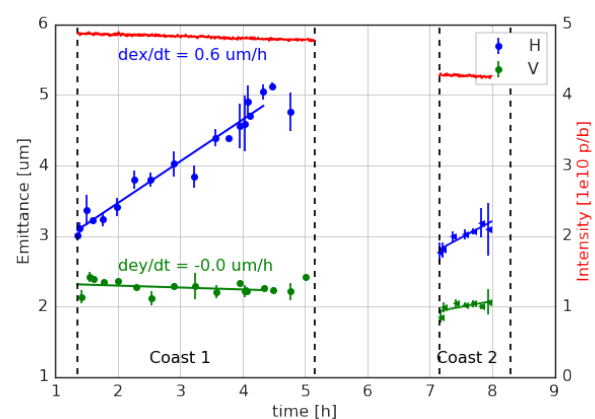


Figure 1: Emittance growth studies in coast beam in the SPS at 270 GeV, in 2015.

MD STUDIES IN 2016

In 2016, two machine development slots were dedicated in the natural emittance growth studies in coast beams at 270 GeV, aiming to reproduce the observations of 2015.

July 2016

The first MD study took place on the 13th of July 2016. A low intensity bunch of 2.35×10^{10} protons/bunch was injected in the SPS and a closed orbit of 5 mm was measured. The chromaticity was set to 2.5 in both H and V planes, in order to be similar to the values of the October 2015 experiment. The linear wire-scanners (517H, 517V) were used to measure the natural emittance evolution. Figure 2 shows the intensity (gray) and the horizontal (blue) and vertical (green) emittance evolution in time. After around 2 h in coast, a sudden jump was observed in the emittance evolution and the bunch got de-bunched, as shown in fig. 3. On the multiQ, a coherent oscillation was observed, for which the origin was not known. It is also interesting to notice, that even though almost no losses were observed in the BCT-DC data (red line in fig. 3), the Mountain Range Sum data (purple) indicate slow off bucket losses, of the order of 20 % within 1.6 h. At the same time, a bunch length increase of around 10 % is indicated by the Mountain Range Bunch Length data (green).

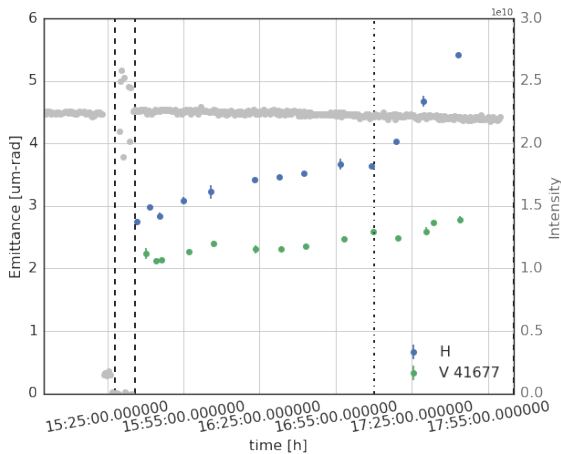


Figure 2: Intensity (gray) and horizontal (blue) and vertical (green) emittance evolution during the MD on coast in the SPS at 270 GeV in July 2016.

For the analysis of the emittance evolution, only the data of the first 1.6 h were used, thus before the sudden jump in bunch length. A linear fit was applied to the emittance data for both horizontal and vertical planes, and the results are shown in fig. 4 and summarized in Table 1.

Even though the experimental conditions were very similar to the ones of October 2015, both horizontal and vertical emittance growth were observed. The vertical emittance growth rate though, is slower than the horizontal one, by a factor of 2.5.

December 2016

The second MD of 2016 took place on the 7th of December and was carried out with a single bunch at 270 GeV. During the MD the evolution of the horizontal emittance was recorded with a rotational wire-scanner (519H) while

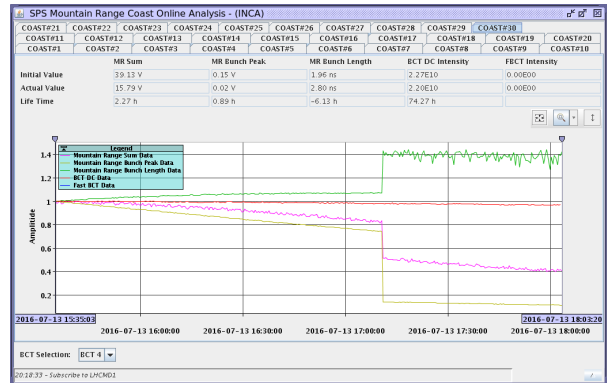


Figure 3: Mountain Range Data, showing the sudden de-bunching of the bunch after around 2 h in coast and the slow de-bunching during the first 2 h in coast.

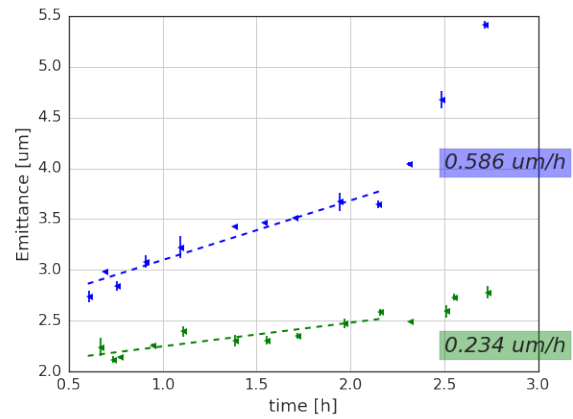


Figure 4: Linear fits and estimation of the emittance growth in the horizontal (blue) and vertical planes (green), before the debunching.

the vertical emittance evolution was recorded with a rotational (416V) and a linear (517V) wire-scanner.

A first coast (Coast 1) was injected with a single bunch intensity of 4.25×10^{10} ppb. The chromaticity of the machine was corrected to 0.5 and 1 in the horizontal and vertical planes respectively. After 1.8 hours in Coast 1, the beam was dumped and a fresh beam was injected (Coast 2), with a lower bunch intensity of 1.65×10^{10} ppb and same chromaticity values. The bunch evolution was recorded for 2.5 h under the same conditions while later the chromaticity was increased by 2 units in both planes. Figure 5 shows the evolution of the bunch intensity (gray), and the horizontal (green) and vertical (blue and cyan) emittances during the MD.

In [5], the impact of the multiple coulomb scattering effect on the transverse emittance growth during the wire scans is discussed. Emittance measurements from 2004 were corrected to the expected growth due to the wire scans, showing negligible or no growth in the vertical plane after this correction. Aiming to verify those observations, the rate of acquisition of vertical beam size profiles with the

EMITTANCE GROWTH IN COAST IN THE SPS

Table 1: Summary results from the MD of July 2016

Parameter	Value
Init. emittance H/V [$\mu\text{m}\cdot\text{rad}$]	2.85/2.16
Intensity [ppb]	2.25×10^{10}
Chromaticity H/V	2.5/2.5
Time [h]	1.6
$d\epsilon_x/dt$ [$\mu\text{m}/\text{h}$]	0.59
$d\epsilon_y/dt$ [$\mu\text{m}/\text{h}$]	0.23

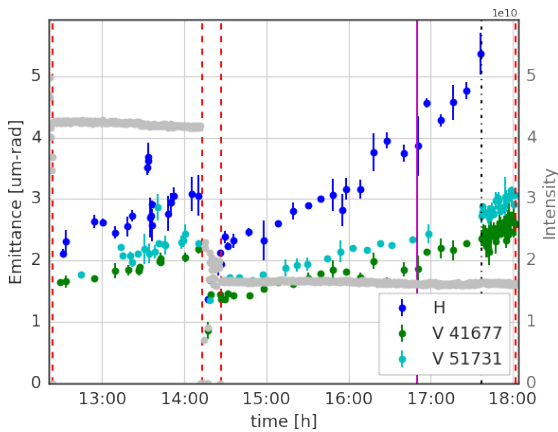


Figure 5: Data from the MD with coast beam in the SPS of December 2016. Horizontal (green) and vertical (blue (WS416) and cyan (WS517)) emittance evolution and intensity (gray) evolution.

linear wire-scanner was drastically increased during the last 15 min in Coast 2; in the first part of Coast 2 10 WS were performed in 1.8 h while in the last 15 min of the MD 24 WS were performed.

Figure 6 shows the snapshots from the Mountain Range application in the control room for both coast 1 and coast 2. Similar to the July MD, even though almost no losses were observed in the BCT-DC data (red), the Mountain Range Sum data (purple) indicate slow off bucket losses and a bunch length increase (green). For coast 1, off-bucket losses of the order of 25% and a 20% bunch length blow up were observed within the 1.8 h. For coast 2, the observations are similar for the first 1.8 h while later, the bunch length decreases and the total machine losses start to increase as well. At the same time, an increase in the horizontal emittance is also observed.

The MD data were divided in 4 groups and a linear fit was applied to the horizontal and vertical emittances versus time for each period:

1. Coast 1
2. Coast 2 before the chroma change
3. Coast 2 after the chrom change, before the multiple WS
4. Coast 2 during the multiple WS

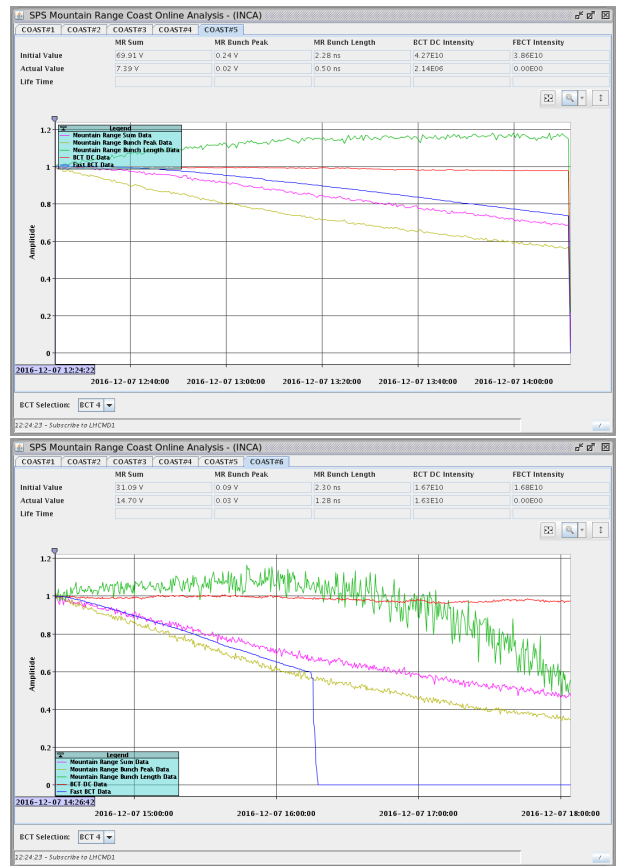


Figure 6: Data from the December 2016 MD with coast beam in the SPS. Mountain Range Data, showing the slow de-bunching of the bunch during coast 1 (top) and coast 2 (bottom).

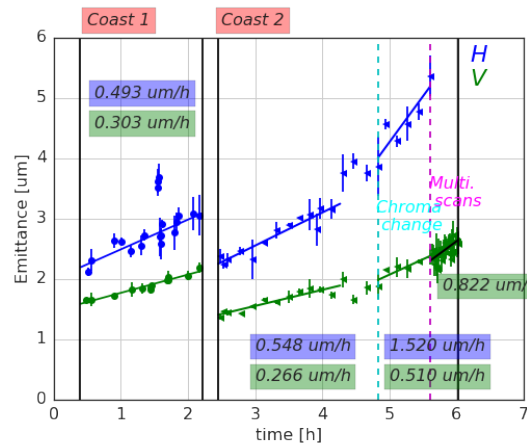


Figure 7: Fit results for the 4 different periods of the MD of December 2016.

The 4 periods and the fit results are presented in fig. 7 and summarized in Table 2. The main conclusions coming from this analysis are:

- Comparing the slopes between coast 1 and the first part of coast 2. no slope increase was observed even

though the intensity was reduced by almost a factor of 4. Note that for coast 2, the same time interval of measurements was used as for Coast 1.

- After the chromaticity change, a clear slope increase was observed in both planes; a factor of 2 increase in the vertical plane and a factor of 3 in the horizontal one.
- During the multiple wire-scans, a slight increase in the vertical emittance growth slope was observed. However, the time interval of those measurements was small and the spread of the data is large. In order to extract conclusive results, the experiment has to be repeated in a more systematic way, for a longer time period and for lower chromaticity values.
- Slow de-bunching was observed in both coasts, similar to the MD of July, which needs to be understood.

Table 2 summarizes all the observations from this MD.

EXPERIMENTAL PROGRAM FOR 2017

As the available time for experimental beam dynamics studies with the crab cavities installed in the SPS will be limited, a very good preparation in advance is essential. In this respect, several studies are proposed for 2017 in dedicated or parallel Machine Development slots and are listed below.

Natural emittance growth in coast

The characterization of the natural emittance growth in the SPS is very important in order to disentangle it from the induced emittance growth from the crab cavities. With this in mind, the following studies are proposed, in dedicated MD sessions:

- Study the impact of the vacuum levels on the natural emittance growth. An MD at the beginning of the year, where the vacuum levels are expected to be worse and one at the end of year, after degrading the vacuum.
- Systematic chromaticity scan to identify the horizontal and vertical chromaticity values that result in the smallest emittance growth.
- Study different intensities.
- Multiple Wire Scan experiment in a more systematic way.
- Commissioning and cross-calibration of the Beam Gas Ionization monitor.
- Identify the effect of the damper on the emittance evolution on coast without the CC.
- Vacuum and power supply monitoring during each MD.

Head Tail monitor

The Head-tail monitor is the most sensitive instrument available in the SPS and is foreseen to be used for the crabbing validation. In this respect, several studies are proposed in preparation for the 2018 measurements:

- Study the accuracy of the instrument at different intensities.
- Identify the minimum kick that can be measured.
- Simulations are currently in progress to be used as a guideline.

Closed orbit correction

In past MDs an rms orbit of 3-5 mm has been measured.

- Verify if we can correct further the orbit.
- Verify if the normal YASP can be used efficiently at 270 GeV or if it is more efficient to use the extraction kickers.
- Identify the optimal kickers and the sensitivity of the BPMs around the crab location.

Collimation studies

- Verify if the collimation system works properly

Studies with shorter bunch length

- Look at the effects of the non-linearities of the RF curvature due to the different frequencies of the SPS main RF system (200 MHz) and the Crab Cavities (400 MHz).

SUMMARY

Two LHC prototype crab cavities will be tested in the SPS in 2018. After the installation of the CC in the SPS, only a limited time will be available for dedicated beam dynamics studies, thus a good preparation in advance is essential for an efficient testing in 2018. With this in mind, during the last years several machine development sessions were dedicated to the characterization of the natural emittance growth in the SPS. In these proceedings, the results from the 2016 studies have been presented. A clear dependence on the chromaticity has been concluded, with the emittance growth rate increasing with the chromaticity increase. On the other hand, for the emittance growth correlation with the number of wire scans was not very conclusive and needs to be repeated in a more systematic way. Based on the observations from the previous years and the tests that need to be performed in 2018, an experimental program for 2017 has been proposed.

EMITTANCE GROWTH IN COAST IN THE SPS

Table 2: Summary results from the MD of December 2016

Parameter	Period 1	Period 2	Period 3	Period 4
Init. emittance H/V [$\mu\text{m}\cdot\text{rad}$]	2.23/1.61	2.25/1.41	4.0/1.98	/2.30
Intensity [10^{10} p/b]	4.25	1.65	-	-
Chromaticity H/V	0.5/1	0.5/1	2.5/3	2.5/3
Time [h]	1.8	1.8	0.8	0.4
$d\epsilon_x/dt$ [$\mu\text{m}/\text{h}$]	0.49	0.55	1.52	-
$d\epsilon_y/dt$ [$\mu\text{m}/\text{h}$]	0.30	0.27	0.51	0.82
Number of linear WS	17	10	-	24
$d\epsilon_y/\text{scan}$ [nm/scan]	31.2	63.5	-	14.3

REFERENCES

- [1] R. Calaga, LHC-PW, Chamonix 2012.
- [2] Y. Sun et al., Phys. Rev. ST Accel. Beams 12, 101002 (2009).
- [3] Y. Funakoshi, Operational experience with Crab Cavities at KEKB, arXiv:1410.4036v1
- [4] R. Calaga et al, Proton-beam emittance growth in SPS coasts, Proceed. of IPAC2012, New Orleans, Louisiana, USA.
- [5] F. Roncarolo, CERN-THESIS-2005-082.

SOURCE AND LINAC3 STUDIES

G.Bellodi, CERN, Geneva, Switzerland

Abstract

In the framework of the LHC Ion Injector Upgrade programme (LIU), several activities have been carried out in 2016 to improve the ion source and Linac3 performance, with the goal to increase the beam current routinely delivered to LEIR. The extraction region of the GTS-LHC ion source was upgraded with enlarged vacuum chamber apertures and the addition of an einzel lens, yielding higher transmission through the rest of the machine. Also, a series of experiments have been performed to study the effects of double frequency mixing on the afterglow performance of the source after installation of a Travelling Wave Tube Amplifier (TWTA) as secondary microwave source at variable frequency. Measurements have been carried out at a dedicated oven test stand for better understanding of the ion source performance. Finally, several MD sessions were dedicated to the study and characterization of the stripping foils, after evidence of degradation in time was discovered in the 2015 run.

SOURCE EXTRACTION UPGRADE

In the framework of the LHC Injector Upgrade project, which aims to improve the performance of the CERN accelerator chain in preparation for future high luminosity operation of the LHC, several studies for beam intensity improvement at Linac3 have been launched, with the goal of increasing the extracted intensity by 20% by LS2. Simulations of beam formation and extraction from the 14.5GHz Electron Cyclotron Resonance (ECR) GTS-LHC ion source and subsequent beam tracking in the low-energy part of the Linac revealed significant beam losses from collimation on the chamber walls due to the very high beam divergence at source extraction. In order to address this issue, a re-design of the source extraction system was launched and implemented during YETS 2015-2016. This consisted in 1) the removal of the beampipe aperture limitation, with increase of the chamber diameter from 65 to 100mm; and 2) the installation of an electrostatic einzel lens as additional focusing element between the existing source extraction electrodes and the first beamline solenoid (see Fig.1). A 20% beam transmission increase through the LEBT was expected from simulations of upgrade 1), which was nicely confirmed in operation, with an increase in the average lead beam current measured at the RFQ input from 170mA during the 2015 run to 210mA in 2016 (Fig.2).

A thorough campaign of beam measurements was carried out to characterize beam parameters. Transverse emittances were measured indirectly via a quadrupole scan technique and tomographic reconstruction of the beam distribution from profile measurements at the SEMgrid in the LEBT section.

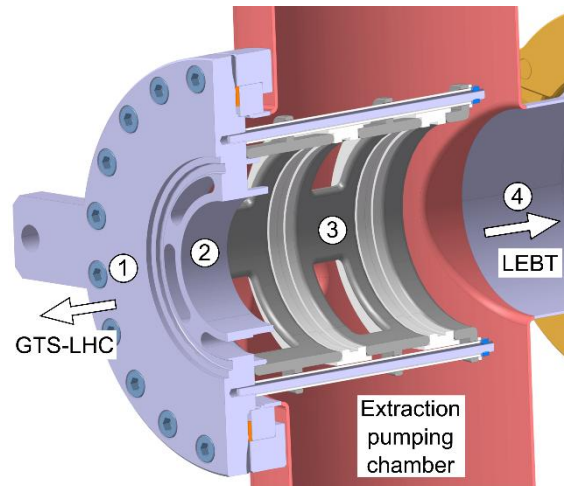


Figure 1 Mechanical design of the source extraction upgrade.

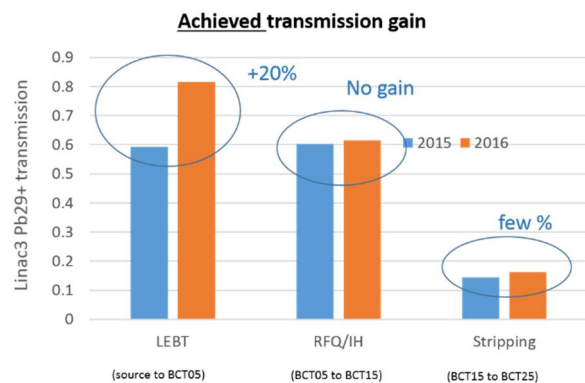


Figure 2 Transmission gain along Linac3 from 2015 to 2016 operation.

Beam emittances at the RFQ input were found to vary between 0.18 and 0.25 mm mrad (RMS normalised values) in both horizontal and vertical planes. This exceeds the design transverse acceptance of the RFQ (200 mm mrad), making this the next transport bottleneck in Linac3 (with 60% average transmission in operation at nominal voltage).

LINAC3 ACTIVITIES IN 2016

A systematic campaign of beam measurements was carried out in 2016, for more precise characterization of beam parameters at Linac3 and validation of the simulation models assumed to study the machine. Several methods to improve beam performance and intensity delivered to LEIR were investigated throughout the year, as listed here in the following.

Einzel lens studies

The einzel lens has been designed to be operated in accelerating or decelerating mode with absolute voltages up to 20kV. Simulation studies of beam extraction in presence of the einzel lens predicted an additional gain in the beam intensity transported downstream, on top of the one achieved by increasing the vacuum chamber aperture. The main benefit of the einzel lens installation was however expected to come from enhanced control of the beam properties via the separation between the ion source tuning and beam transport optimisation, providing higher flexibility to the ion source operation and potential to improve performance. Linac3 has effectively been run in 2016 with different source settings than in the past, leading to better beam matching to the rest of the accelerator. No remarkable gain in transmission through the spectrometer was however observed when applying non-zero (positive or negative) voltages to the einzel lens, as was instead expected from simulation studies (see Fig.3).

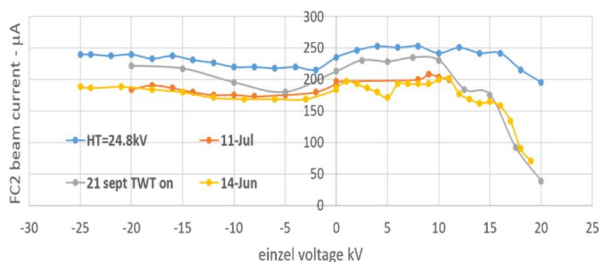


Figure 3 Measured beam transmission after the Linac3 LEBT spectrometer while scanning the voltage applied to the einzel lens. The orange and yellow curves correspond to standard settings, the blue curve has been taken for higher extraction voltage from the source, and the grey curve is for operation with the TWTA switched on.

Double frequency operation

Using multiple discrete frequencies simultaneously for ECR plasma heating is a well-established method to improve ion source performance with high charge state production. Experiments have however mainly been conducted with ECR ion sources operated in CW mode. Investigations have been carried out this year at the GTS-LHC source to study the effects on afterglow operation.

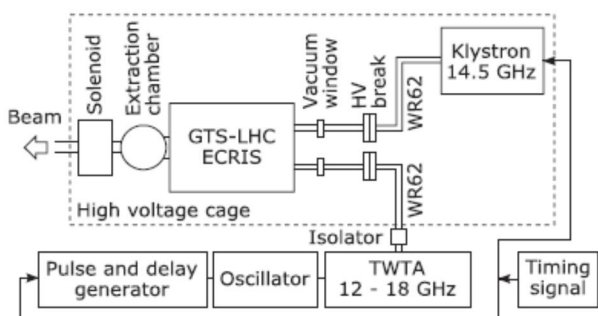


Figure 4 Double-frequency measurement setup at Linac3.

The measurements setup is shown in Fig.4. The primary 14.5GHz microwave radiation is provided by a klystron amplifier at 10Hz repetition rate and 50% duty factor. The spare waveguide is connected to a Travelling Wave Tube Amplifier (TWTA) to deliver microwaves at variable secondary frequency (in a 12-18 GHz range). The maximum power delivered from the amplifier was ~300W. The input signal was generated by a variable frequency oscillator and the pulse generator was triggered by the klystron timing signal, thus allowing pulsed operation of the TWTA. A first assembly was installed in April 2016 with borrowed units; these were later on purchased and made the object of a second installation in September 2016.

A shift to higher charge states was indeed observed when the secondary frequency was chosen to be lower than the primary one, whereas the effect was much weaker in the opposite case. It was also verified that the shift was not just due to an increased total microwave power. The best results for Pb²⁹⁺ were obtained with 14.2GHz pulsed secondary frequency, with beam current improvements of 10% after the RFQ and 5% downstream of the IH linac after re-matching. No significant changes were observed in measured beam parameters (mainly transverse emittance and RFQ transmission) with the TWTA ON or OFF.

Some negative effects were however observed in the overall beam stability out of the source, justifying an interruption of the double frequency operation when beam was finally delivered to the LHC for the physics run.

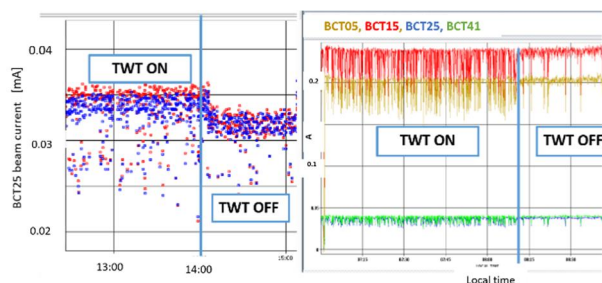
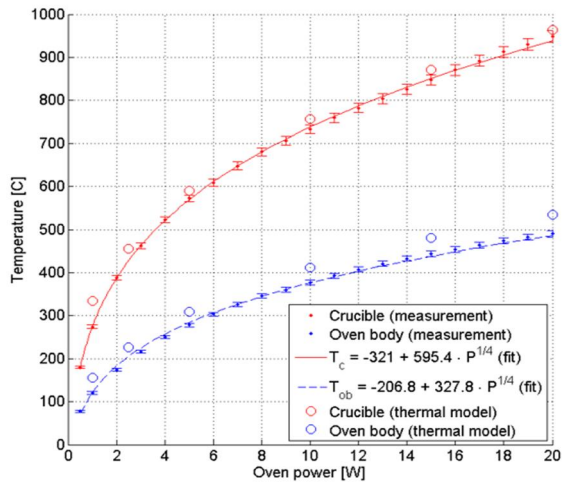


Figure 5 TWTA effect on transmission downstream of the IH, as measured on the BCT25 current transformer (left), and on beam stability (right).

Oven test stand studies

The Linac3 Lead ion beams are produced in the GTS-LHC source using resistively heated ovens, consisting of an aluminium oxide crucible, tantalum heating filament and oven body and stainless steel cane allowing insertion through the ion source. In order to study oven performance and get better understanding of failure mechanisms, a dedicated off-line test stand has been constructed in the South Hall of bldg. 152 with the goal of measuring oven temperatures and Lead evaporation rates in varied input conditions. Fig.6 shows the measured temperature characterization of the oven. For operational values of the input power between 6W and 20W, the crucible temperature varies between 600 °C and 950 °C, following a $T \sim P^{1/4}$ relationship characteristic of radiative losses. The response to input power changes is slow, as observed in operation.



$$T_{crucible} = 54.6 + 1.8 T_{oven\ body}$$

Figure 6 Measured crucible and oven body temperatures as function of the oven input power, compared to model predictions.

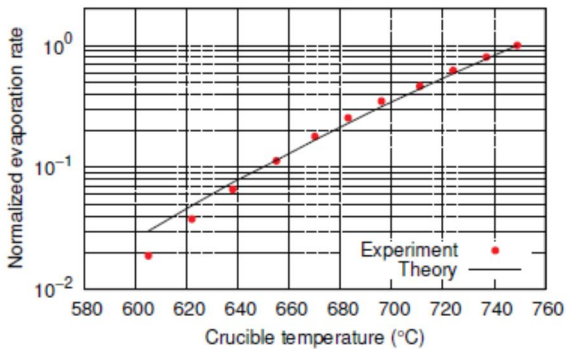


Figure 7 Evaporation rates as function of the crucible temperatures.

Measurements of the lead evaporation rate (Fig.7) show a steady response of the output as a function of the crucible temperature, as predicted by theory. At constant power, on the other hand, the oven output is observed to decrease steadily over time as seen in operation, where a regular power adjustment is needed to keep the necessary lead evaporation rate for beam production.

A numerical thermal model of the oven has also been developed with the ANSYS code to complement the measurements and provide insight on the temperature distribution inside the oven. Simulation results have been compared to temperature measurements at selected locations and found to be in good agreement with them. Fig.9 shows ANSYS results for the case of 10W and 15W heating power. They show good temperature uniformity in the lead

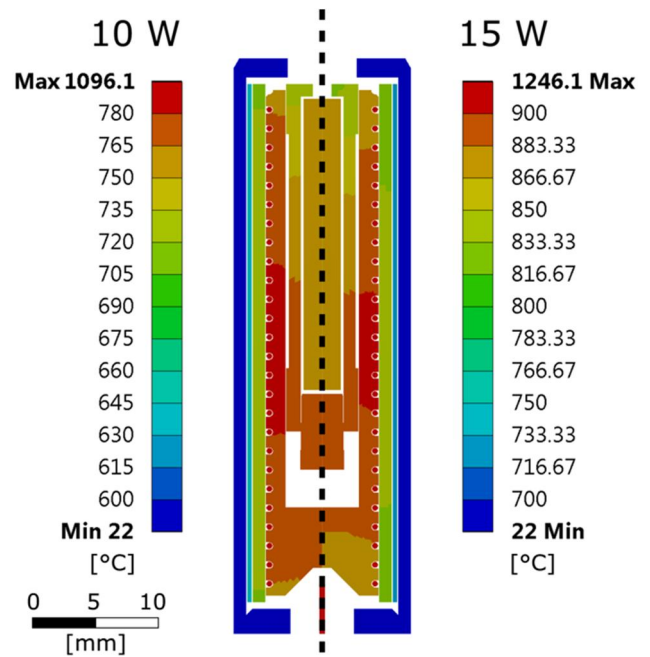


Figure 8 ANSYS simulations of the temperature distribution inside the oven.

sample, with a significantly colder tip of the oven, which could explain the oven blockages experienced in operation.

Stripping foil studies

Several Linac3 MD sessions were dedicated to the characterization of stripping foils, after 2015 measurements showed measurable signs of degradation after few weeks of usage. The stripped beam average energy and energy spread are calculated from beam profile measurements in the ITFS spectrometer line, with the ramping cavity at zero-crossing phase. Measurements taken at the end of the 2015 run (see Fig.9) show clearly a shift to higher values of the average beam energy and considerable energy spread broadening of the beam passing through the three foils used during the year at different periods with respect to the unused foils.

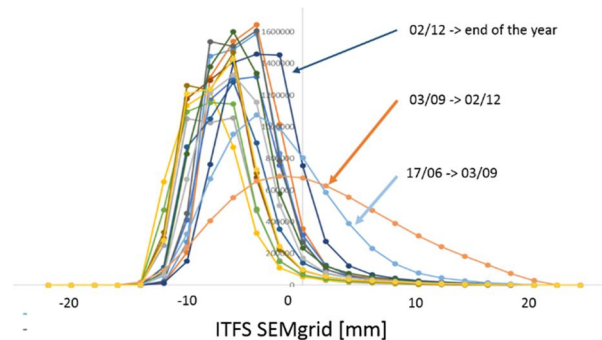


Figure 9 2015 beam profiles measurements in ITFS line.

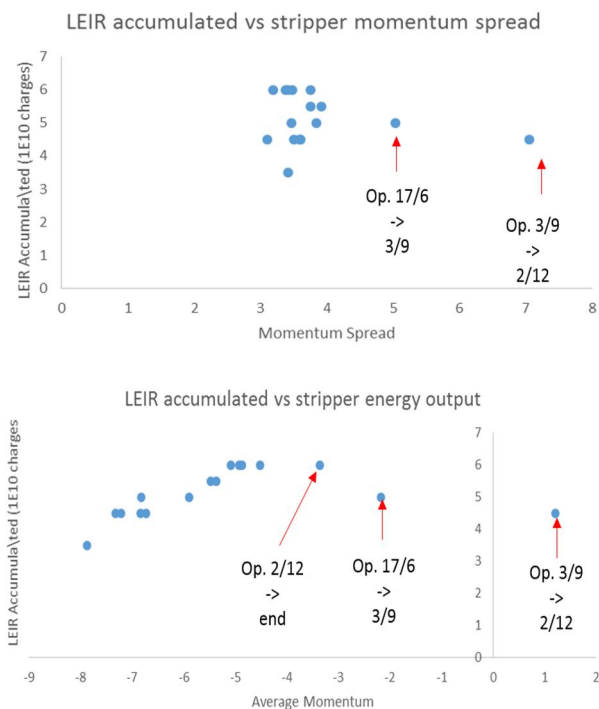


Figure 10 Correlation of LEIR accumulated intensity with stripper energy and momentum spread output.

These measurements were correlated with accumulated intensity in LEIR without changing the linac energy nor transfer beam-line settings (see Fig.10). The accumulation efficiency is found to be nearly independent of the energy spread, with only a small reduction for foils in use for a longer time. The average energy instead was found to be of major importance for the injection efficiency, with a plateau width of <10 keV/u.

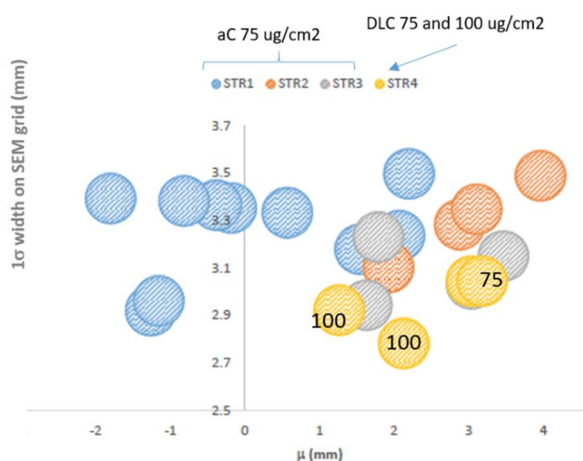


Figure 11 Measured variation in average energy and energy spread of the stripped beam (end of May 2016).

Fig.11 summarises some foil characterization measurements taken in 2016 after several weeks of beam operation.

Four Diamond-Like-Carbon (DLC) foils were installed at the time, with a thickness of 75 and 100 $\mu\text{g}/\text{cm}^2$ (in yellow). All the other twelve foils are of the amorphous-Carbon (aC) type, with a thickness of 75 $\mu\text{g}/\text{cm}^2$ (and a tolerance of <5 $\mu\text{g}/\text{cm}^2$). Different colours are used for foils on different arms. Also, two to three measurements at different positions within the foil were carried out for the STR1 foils, which explains the ten blue points in the diagram.

The mean energy out of the aC foils varies within a range of 27 keV/u between the foils (assuming 4.5 keV/u/mm conversion factor of the spectrometer line), which is significant compared to the calculated energy loss of 42 keV/u through a 75 $\mu\text{g}/\text{cm}^2$ foil. Variation within a single foil when positioning the beam at different spots is relatively modest, less than 5 keV/u, but differences from foil to foil can be quite significant, suggesting that thickness could vary significantly between different foils. Charge State Distribution (CSD) scans measured for all different foils hint to the fact that DLC foils might be too thin (even if the calculated equilibrium thickness is ~ 75 $\mu\text{g}/\text{cm}^2$). There is also indication that DLC foils are less robust and performant than aC foils.

CONCLUSIONS

Thanks to the upgrade of the GTS-LHC source extraction region during YETS2015-6, higher beam currents are now routinely delivered to LEIR satisfying the Linac3 output intensity goal set in the LIU project. A dedicated campaign of measurements has been pursued in 2016 to achieve better understanding of the beam dynamics in Linac3 and for validation of the machine model in the simulation codes used. The effects of additional einzel lens focusing and of double frequency mixing in the source plasma have started to be investigated with the goal of achieving either an even higher intensity or just a more robust and reliable beam operation. This latter point has now become the main objective of LIU-related studies at Linac3, which will develop along three main directions:

- i. Understanding of the source performance (oven test stand activities, double-frequency heating, einzel lens and development of an application for automatic regulation of the source)
- ii. Machine model validation (space charge compensation studies in the LEBT, studies for a higher extraction voltage)
- iii. Understanding of the stripper foils performance (characterization of degradation, monitoring of beam trajectory/energy evolution, foil swapping procedures etc.)

The 2017 scheduled operation of Linac3 is with Xenon ions; though adapted to the different particle species, the Linac3 study campaign will continue with regular weekly MD sessions, profiting from the better beam stability and regularity.

SPACE CHARGE AND WORKING POINT STUDIES IN THE CERN LOW ENERGY ION RING

A. Huschauer, H. Bartosik, S. Hancock, V. Kain, CERN, Geneva, Switzerland

INTRODUCTION

The Low Energy Ion Ring (LEIR) is at the heart of CERN’s heavy ion physics programme and was designed to provide the high phase space densities required by the experiments at the Large Hadron Collider (LHC). LEIR is the first synchrotron of the LHC ion injector chain and it receives a quasi-continuous pulse of lead ions (Pb^{54+}) from Linac3, exploiting a sophisticated multi-turn injection scheme in both transverse and longitudinal planes. Seven of these pulses are injected and accumulated, which requires continuous electron cooling (EC) at low energy to decrease the phase space volume of the circulating beam in between two injections. Subsequently, the coasting beam is adiabatically captured in two bunches, which are then accelerated and extracted towards the Proton Synchrotron (PS). Figure 1 shows the LEIR magnetic cycle and the different steps required for beam production.

To achieve the ion intensity requirements of the High-Luminosity LHC (HL-LHC), i.e., 8.1×10^8 ions/bunch at LEIR extraction [1, 2], the major LEIR intensity limitation had to be overcome. Past studies showed that up to 50% of the beam was lost after radio-frequency (RF) capture and during the first part of acceleration and, furthermore, the total extracted intensity was reported to be limited to a maximum of 6×10^8 ions/bunch (see dashed line in Fig. 1). Various possible sources limiting the LEIR intensity reach were identified, such as hardware related problems, effects related to direct space charge or collective instabilities of the ion beams [3]. In the framework of the LHC Injectors

Upgrade (LIU) project, dedicated studies were started at the end of 2015 to understand the underlying loss mechanism and to find possible mitigation measures. These studies revealed the important interplay of betatron resonances and direct space charge effects during the bunching process [4].

In this paper, the results of more recent experimental and simulation studies, which further emphasize the importance of space charge effects, are summarized and the impact of these studies on the LEIR performance increase is discussed.

CHARACTERIZATION OF THE PERFORMANCE LIMITATION

Figure 2 shows a comparison of the intensity evolution along the LEIR cycle for three different longitudinal phase space distributions. In all three cases the RF voltage functions were programmed such as to perform an iso-adiabatic capture of the coasting beam. The longitudinal emittance of the coasting beam was adjusted prior to RF capture using a periodic modulation of the electron gun voltage. This allowed tailoring the longitudinal emittance of the two bunches after capture. In two cases the beam was captured in single harmonic. The losses clearly decrease with increasing bunching factor (BF), i.e. the average line density divided by peak line density. In other words, enhanced losses are observed for high peak line charge densities. Note that the incoherent tune spread due to direct space charge is directly proportional to the peak line charge density, or inversely proportional to the BF.

RESONANCE IDENTIFICATION STUDIES

In order to characterize resonances close to the operational working point $(Q_{x_0}, Q_{y_0}) = (1.82, 2.72)$, low-intensity tune scans were performed. A single pulse from Linac3 with roughly 2×10^{10} charges was injected and cooled at

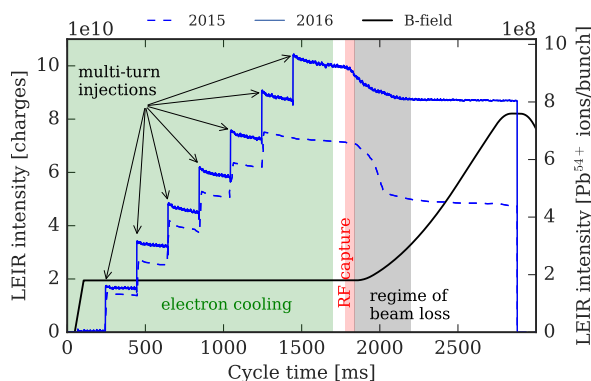


Figure 1: LEIR magnetic cycle of the nominal beam production scheme for heavy ion physics at the LHC. The intensity measurement represented by the solid line corresponds to values that were typically achieved during the 2016 p-Pb LHC run. In earlier years up to 50% of the beam intensity was lost during the first part of acceleration (shown by the dashed line).

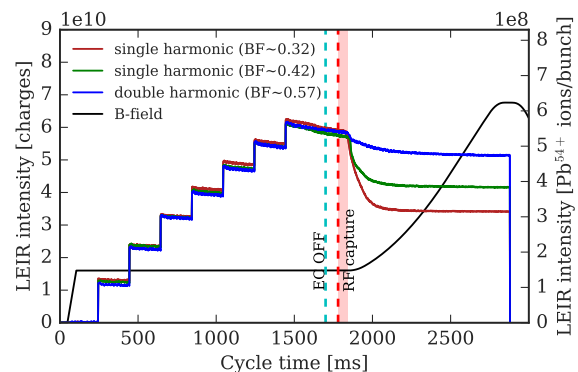


Figure 2: Dependency of beam loss on the longitudinal line density. Losses are significantly reduced for large BF's.

these nominal tunes, before the working point was moved to perform the scan. To respect this sequence of events is important for the following two reasons: i) performing a tune scan by changing the tunes at injection is not meaningful as the injection efficiency crucially depends on the tune settings; ii) resonance crossing immediately leads to beam loss in LEIR, which can be significantly mitigated by active EC during the crossing process. Scans with bunched and unbunched beams, which were stored for 500 ms at constant energy, were performed and the beam loss over this period was considered as figure of merit. Figure 3 illustrates the measurement procedure.

This procedure was repeated for multiple working points with bunched and unbunched beams, and the results are shown in Fig. 4. The skew and the normal sextupolar resonances $3Q_y = 8$ and $Q_x + 2Q_y = 7$, respectively, are revealed to be especially strong. In addition, significant beam loss is observed close to the diagonal and the $4Q_y = 11$ resonance for bunched beams. For large horizontal tunes, i.e., $Q_x > 1.9$, beam loss is intrinsic to the way the lattice functions are controlled in LEIR, as the optical β -functions increase drastically. An additional bunched beam tune scan was performed using higher intensity and the corresponding results are shown in Fig. 5. Overall, the same resonance pattern as in Fig. 4 is apparent, but beam loss is significantly increased due to the increased direct space charge tune spread.

An independent way to identify excited resonances is based on the measurement of transverse profiles. In LEIR, horizontal and vertical beam gas ionisation (BGI) profile monitors are available and allow parasitic measurements of the beam size. In order to investigate the effect of the strong skew and normal sextupolar resonances on the beam, the beam size evolution at different working points was studied along the magnetic cycle and the results are shown in

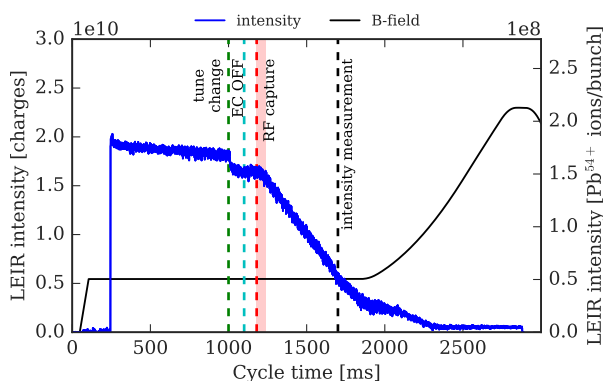


Figure 3: Illustration of the measurement technique for low-intensity tune scans. A single Linac3 pulse was injected at nominal tunes and subsequently cooled. The working point was changed during the EC process to mitigate beam loss when crossing a resonance. Furthermore, the RF capture was advanced by 500 ms with respect to the operational settings.

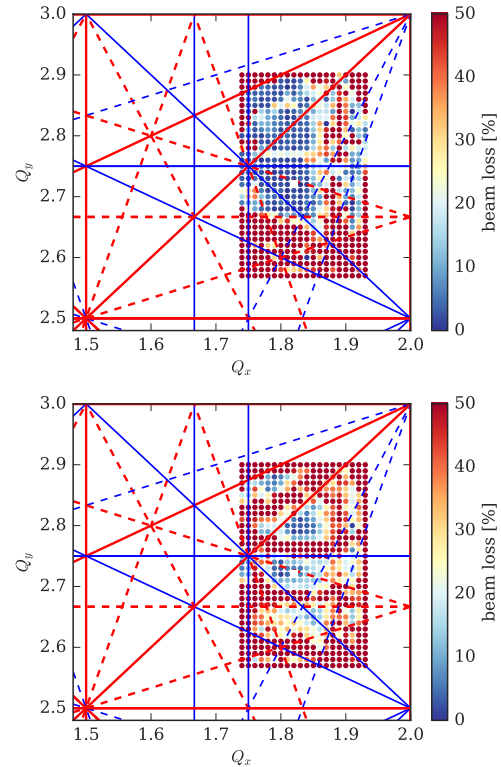


Figure 4: Measured tune diagram in the vicinity of the operational working point (indicated by the white square) for unbunched (top) and bunched beam (bottom). The color scale shows beam loss after 500 ms of storage time. Systematic resonances are shown in red, solid and dashed lines correspond to normal and skew resonances, respectively.

Fig. 6. In addition to the already discussed sextupolar resonances, an effect of the resonance $2Q_x + 2Q_y = 9$ is visible. Furthermore, for decreasing horizontal and vertical tunes, the horizontal beam size experiences a significant growth, possibly due to the resonance $4Q_x = 7$.

The driving term of these resonances remains unknown today. The presence of the electron cooler and its multitude of magnetic elements was expected to significantly contribute to the excitation of resonances. Therefore, an additional study using the bare machine was performed. To perform this test, the main solenoid of the electron cooler as well as the corrector solenoids, all additional magnetic elements of the cooler, the correction of the orbit distortion around the electron cooler and all chromatic and harmonic sextupoles were switched off.

Using this configuration, the skew sextupolar resonance $3Q_y = 8$ was crossed and no significant differences in terms of beam loss when crossing the resonances were observed (see Fig. 7). Therefore, the electron cooler was excluded as source of skew sextupolar errors and a possible source is yet to be determined. Furthermore, the normal sextupolar resonances are expected to be excited by magnetic errors in the main bending dipoles.

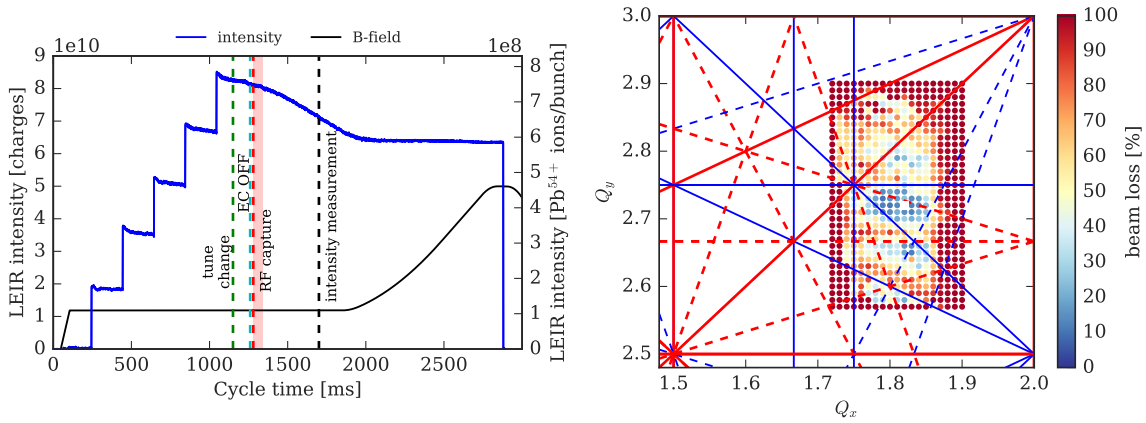


Figure 5: Measured high-intensity tune diagram for bunched beam. Left: Illustration of the measurement technique likewise to Fig. 3. Right: Measurement results in the vicinity of the operational working point (indicated by the white square). The resonance pattern is very similar to the one observed in Fig. 4.

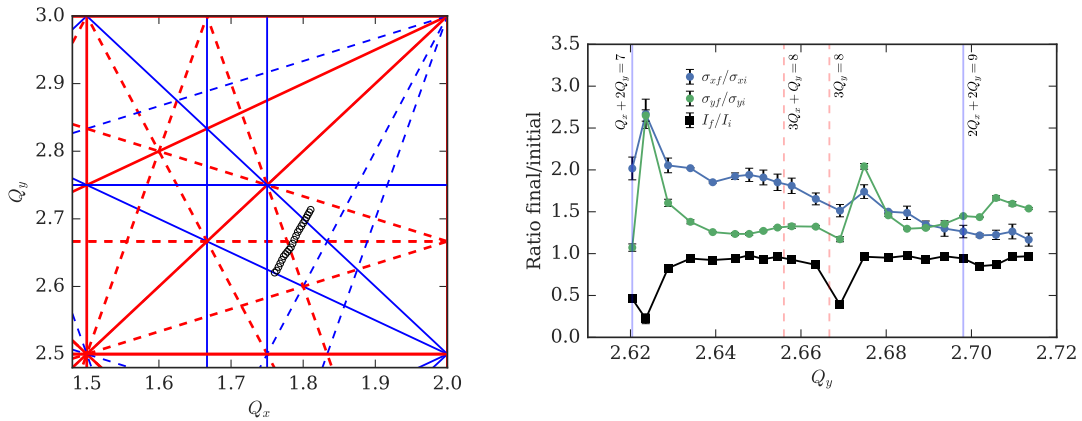


Figure 6: For each working point indicated in the tune diagram on the left, the ratio between final and initial beam sizes for each transverse plane and the corresponding intensity are shown on the right. The observed shift between maximum blow-up and theoretical position of resonance lines (blue and red vertical lines in the background) is compatible with the maximum direct space charge tune spread $\Delta Q_x \approx \Delta Q_y \approx -3 \times 10^{-2}$. The error bars correspond to the statistical fluctuations over three consecutive measurements.

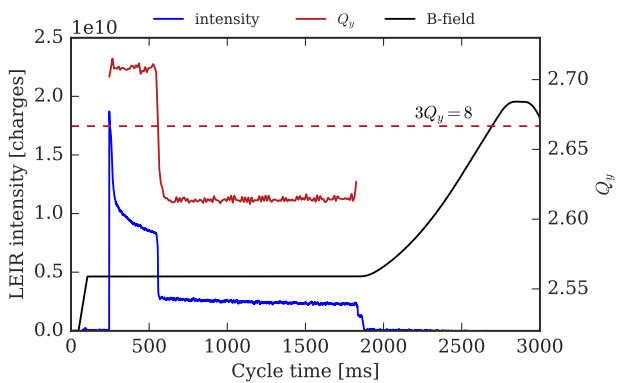


Figure 7: Also in the absence of the magnetic effects of the electron cooler, significant beam losses are observed when crossing the resonance $3Q_y = 8$. The significant drop of intensity right after injection is due to the large beam size in the absence of EC.

Given the fact that the direct space charge tune spread $\Delta Q_{x,y}$ of operational beams reaches values larger than 0.1 during the RF capture process (see also [4]), particles experience the effect of multiple resonances simultaneously, which might lead to emittance blow-up and beam loss at the main aperture restriction of LEIR, i.e., the vacuum chambers inside the bending magnets. Therefore, additional studies, which are presented in the following, were performed to compensate or avoid the resonances. The latter can be achieved by modification of the machine optics.

RESONANCE COMPENSATION

With the current operational setup of LEIR, it is essential to control the transverse tunes precisely. One possible means to relax this constraint is to compensate resonances, which can be attempted by using either the eight installed chromatic or the two harmonic sextupoles. In fact, the latter

are a combination of normal and skew sextupoles in a single element.

A first proof of principle has been presented in [4], where a reduction of the current in the chromatic sextupoles was observed to lead to reduced beam loss close to the resonances. Subsequently, a more systematic approach was pursued: using the Polymorphic Tracking Code (PTC [5]) library inside MAD-X [6], the resonance driving terms (RDTs) of the different sextupoles were computed and suitable pairs of sextupoles for compensation studies were determined (see Fig. 8). The feasibility of compensation with several of these pairs was then studied by programming the working point to lie on top of the $Q_x + 2Q_y = 7$ resonance, while scanning the current in the sextupoles and recording beam loss simultaneously. The results are shown in Fig. 9: for any combination of two chromatic sextupoles, but also by using one chromatic and one harmonic sextupole, resonance compensation can be achieved for certain currents. Surprisingly, however, no compensation could be achieved by using the pair of harmonic sextupoles, even though their functionality has been verified. This issue will be further investigated in the future. In Fig. 10 the results from Fig. 9 are displayed in a different way, namely by transforming the measured sextupole currents into the RDT-space. As expected, the phase and amplitude of the resonance, which corresponds to the area of maximum beam survival, is observed to be identical for different combinations of sextupoles.

In addition, the impact of resonance compensation on the evolution of the transverse profiles was studied. A low-intensity beam was injected, cooled and stored with active resonance compensation (corresponding to the optimum settings found for the scan using SXFN11 and SXFN32 in Fig. 9) for several hundreds of milliseconds. Subsequently, the compensating sextupoles were switched off during the cycle and the evolution of the beam size during the entire magnetic cycle was recorded using the BGI monitor. In Fig. 11, the suppressed growth of the beam size during the first part of the cycle is clearly visible.

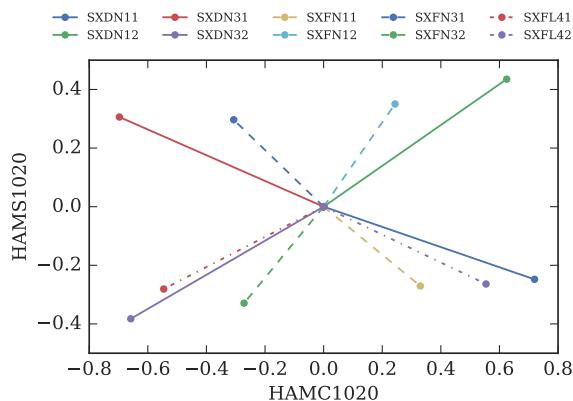


Figure 8: Hamiltonian RDTs for the different sextupoles installed in LEIR. Pairs of sextupoles whose vectors are at an angle of 90 degrees are well suited elements for compensation.

OPERATION AT A DIFFERENT WORKING POINT

The LEIR machine optics configurations are significantly constrained by the multi-turn injection and EC processes [7–9]. In order to modify the lattice optics and move the working point to a quadrant of the tune diagram that is less resonance dominated, a dedicated simulation study was performed and a suitable stable solution was obtained for the tunes $(Q_x, Q_y) = (2.18, 3.28)$. In Fig. 12, the optics functions for both setups are compared and the main difference concerns the β_y -functions at the entrance and exit of the bending magnets. Considering this fact, the optics modification is clearly unfavorable. However, if the overlap between the direct space charge tune spread and excited resonances is significantly reduced, emittance growth during the RF capture is also expected to be mitigated, resulting in an overall reduction of beam loss.

To investigate the resonance excitation in this new optics configuration, an additional measurement was performed. The result is shown in Fig. 13 and the resonance free area is found to be significantly increased compared to the measurements in the nominal configuration (see Fig. 2).

The continuation of the optimization of this new machine setup and the investigation of transverse emittance blow-up and beam loss are subject of future studies.

CONCLUSIONS AND OUTLOOK

The early part of LEIR operation in 2016 was fully dedicated to deepening the understanding of the performance limitations and to investigating mitigation possibilities. The combination of the results presented in this paper in combination with the excellent performance of Linac3 [10], and additional modifications of the RF capture process [11], led to the unprecedented Pb^{54+} -intensity of more than 10^{10} charges at LEIR extraction (see Fig. 14). Therewith, the HL-LHC ion intensity requirement has been operationally demonstrated in LEIR and the major remaining challenge is to maintain this high performance of the machine and Linac3, and to reduce the sensitivity of the performance to the various machine settings by exploiting resonance compensation or the modified optics configuration. Furthermore, the reduction of the time between two subsequent injections into LEIR and operation with increased electron current in the cooler is being studied to increase the accumulated intensity and provide more margin for future operation [12].

REFERENCES

- [1] J. Coupard *et al.* (eds.), “LHC Injectors Upgrade, Technical Design Report, Vol. II: Ions”, CERN-ACC-2016-0041 (2016).
- [2] H. Bartosik *et al.*, “The LHC Injectors Upgrade (LIU) Project at CERN: Ion Injector Chain”, Proc. of IPAC’17, Copenhagen, Denmark (2017), TUPVA020, pp 2089-2092.
- [3] M.A. Bodendorfer, M.E. Angoletta, J. Axensalva, D. Manglunki, and S. Pasinelli, “Beam Loss in the Low Energy Ion Ring (LEIR) in the Light of the LHC Injectors Upgrade for

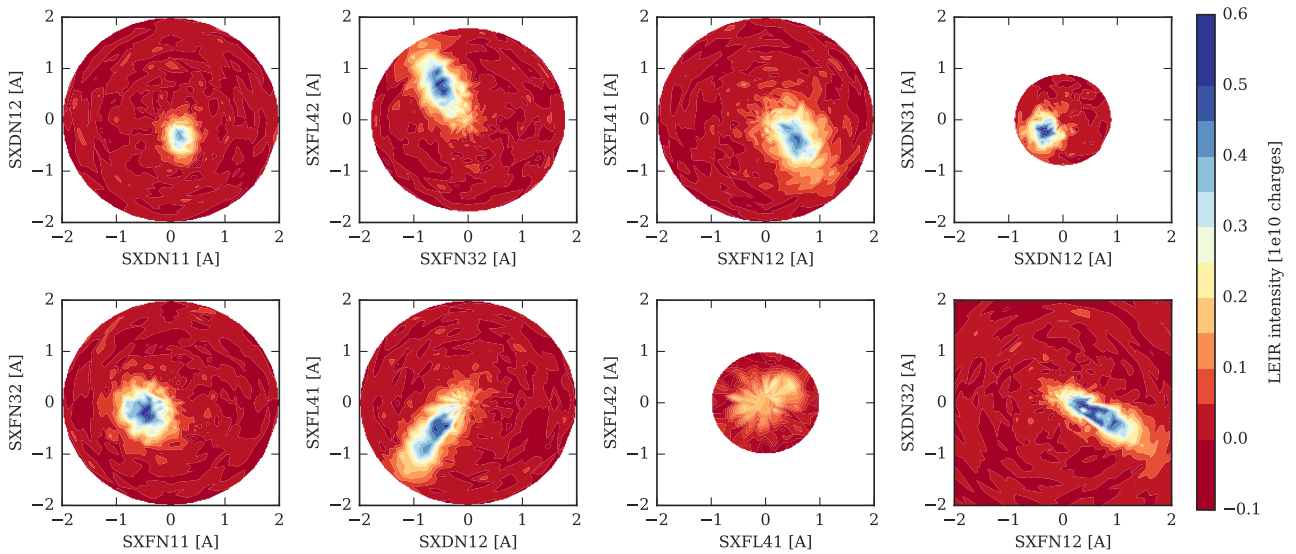


Figure 9: Beam survival after 600 ms of storage time as a function of current in the sextupoles. A combined use of harmonic (SXFL*) and chromatic (SXFN*/SXDN*) sextupoles clearly reveals reduced resonance excitation. Contrary to expectations, no such effect can be observed by using pairs of harmonic sextupoles only.

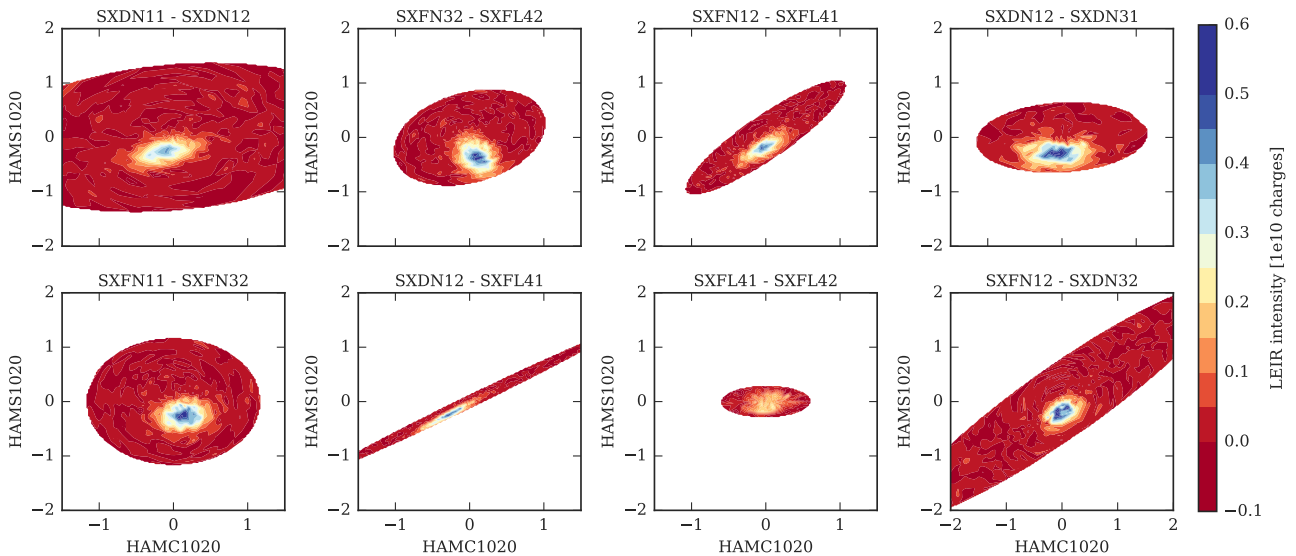


Figure 10: Measurement results of Fig. 9 transformed into RDT-space. Amplitude and phase of the resonance are in very good agreement for the different scans.

- Ions (LIU-Ions)", in *Proc. of HIAT15*, Yokohama, Japan (2015), pp. 115-117.
- [4] H. Bartosik, S. Hancock, A. Huschauer, and V. Kain, "Space Charge Driven Beam Loss for Cooled Beams and Mitigation Measures in the CERN Low Energy Ion Ring", in *Proc. of HB2016*, Malmö, Sweden (2016), pp. 272-277.
- [5] F. Schmidt, E. Forest, and E. McIntosh, "Introduction to the polymorphic tracking code: Fibre bundles, polymorphic Taylor types and "Exact tracking", CERN-SL-2002-044-AP, KEK-REPORT-2002-3 (2002).
- [6] W. Herr and F. Schmidt, "A MAD-X Primer", CERN-AB-2004-027-ABP (2004).
- [7] M. Benedikt, P. Collier, V. Mertens, J. Poole, and K. Schindl (eds.), "LHC Design Report", Volume III, Chapter 35, CERN, Geneva, Switzerland (2004).
- [8] C. Carli, S. Maury, and D. Mohl, "Combined longitudinal and transverse multiturn injection in a heavy ion accumulator", in *Proc. of PAC97*, Vancouver, Canada (1997), pp. 976-978.
- [9] J. Bossert, C. Carli, M. Chanel, R. MacCafferri, S. Maury, D. Möhl, G. Molinari, G. Tranquille, "Electron cooling of PB⁵⁴⁺ ions in the low energy ion ring (LEIR)", in *Proc. of EPAC98*, Stockholm, Sweden (1998), pp. 1073-1075.
- [10] G. Bellodi, "Source and Linac3 studies", elsewhere in these proceedings.

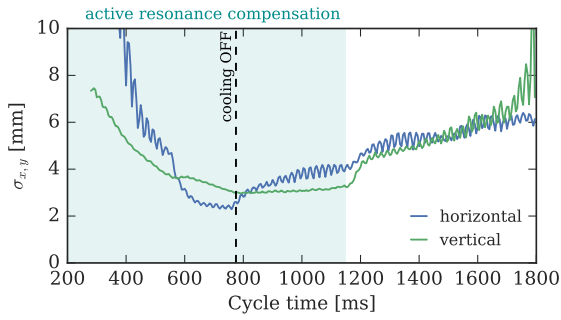


Figure 11: Impact of resonance compensation on the evolution of the horizontal and vertical beam sizes, σ_x and σ_y , respectively. Once the sextupoles are switched off, the beam immediately grows in both transverse planes.

- [11] S. Albright *et al.*, “LEIR Longitudinal dynamics studies”, elsewhere in these proceedings.
- [12] R. Scrivens *et al.*, “100 ms injection into LEIR”, elsewhere in these proceedings.

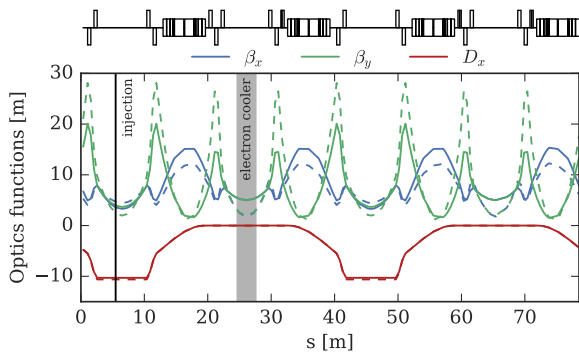


Figure 12: LEIR optics functions for the nominal (solid lines) and modified (dashed lines) settings.

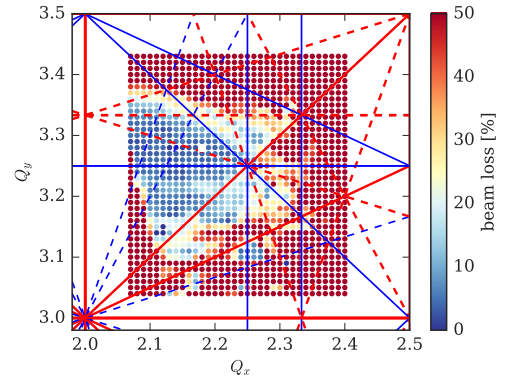


Figure 13: Measured tune diagram for the modified LEIR optics configuration. The design working point for this machine setup is indicated by the white square.

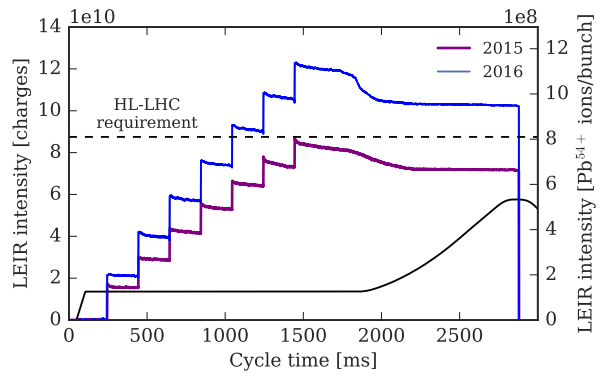


Figure 14: In 2016, the extracted intensity out of LEIR was increased by 40% compared to the performance at the end of 2015.

LEIR LONGITUDINAL STUDIES

S. Albright, S. Hancock, M. E. Angoletta, CERN, Geneva, Switzerland

Abstract

Towards the end of 2015 and during 2016 there were extensive studies of longitudinal beam dynamics in LEIR aimed at improving extracted intensities. As the driving source of losses early in the ramp was shown to be transverse space charge tune spread a significant improvement came from flattening the beam profile to increase the bunching factor by offsetting the RF frequency from the beam revolution frequency. Further benefits were provided by modulating the RF frequency during capture, leading to emittance blow-up and improved reproducibility. The use of two RF cavities during operation was studied to try and further increase the captured emittance, however after careful alignment of the RF it was found that a hard limit in the bunch height of approximately 7 MeV exists. Due to the acceptance limit there was no operational benefit to using both cavities simultaneously.

INTRODUCTION

This paper summarises the studies that were carried in the longitudinal plane in LEIR at the end of 2015 and during 2016. The paper comprises three sections, the first related to line density reduction, the second to two cavity operation, and the third to longitudinal acceptance limitations.

LINE DENSITY REDUCTION

The RF frequency in LEIR is calculated based on the measured B-Train, however during capture an additional offset can be used to correct for differences between the design frequency and the revolution frequency of the coasting beam. Under the assumption that the revolution frequency is constant an offset can therefore be used to center the bucket on the center of the coasting beam. However, it was found in operation that having an offset between the RF and the beam during capture lead to reduced losses.

Figure 1 shows the capture process with the RF frequency (F_{RF}) equal to the coasting beam revolution frequency (F_{beam}), and with an offset between them. Whilst the centered case (Fig. 1a) is clearly smooth and much neater the transmission is better in the case where $F_{RF} \neq F_{beam}$ (Fig. 1b).

After further optimising the voltage function and frequency offset the capture process was designed such that the coasting beam was captured in such a way as to produce hollow bunches, dubbed the "Lone Ranger" effect shown in Figure 2 [1]. The Lone Ranger phase space distribution shows a low density part of the beam within the inner separatrix, with the majority of the particles on the outer edge of the inner separatrix. The difference between the beam and RF frequencies must be chosen carefully, if the core is too dense or the outer part of the beam too far from the inner

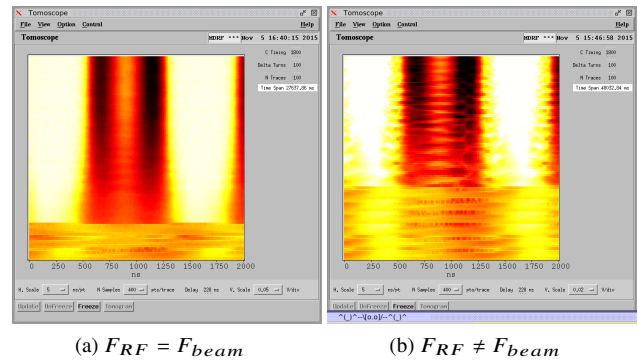


Figure 1: Waterfall plots of capture with the RF centered on the coasting beam, and with an offset.

separatrix the profile will not be flat, thus increasing the line density.

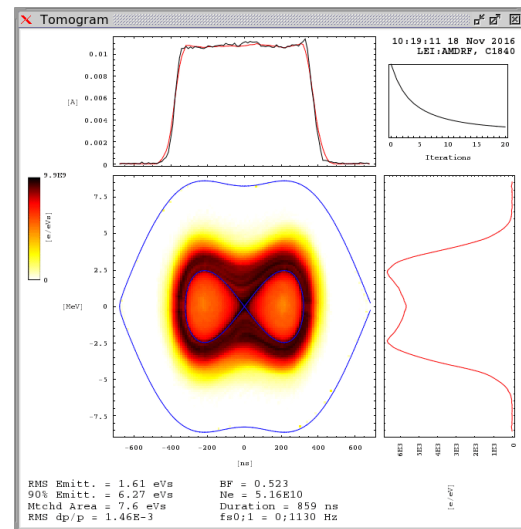


Figure 2: The Lone Ranger phase space distribution.

Whilst the Lone Ranger effect was able to provide lower line densities than otherwise achievable the sensitivity to changes in coasting beam revolution frequency meant regular adjustment was necessary. Along with slow changes in the average revolution frequency, which were corrected by regular tuning, there is also shot to shot variations that cannot be compensated for. An alternative method of capture using frequency modulation during the capture process was found to greatly improve the reproducibility of the captured bunch.

Modulating the RF frequency during capture causes the bucket to sweep through the coasting beam giving a more reproducible and uniform distribution than otherwise possible. Compared to fixed frequency capture this produces significantly improved reproducibility. Unfortunately the intensity

in initial studies was not as high. The Full Width at 25% Maximum of the captured bunch is shown in Fig. 3, the flat frequency data was taken before Lone Ranger became the operational norm.

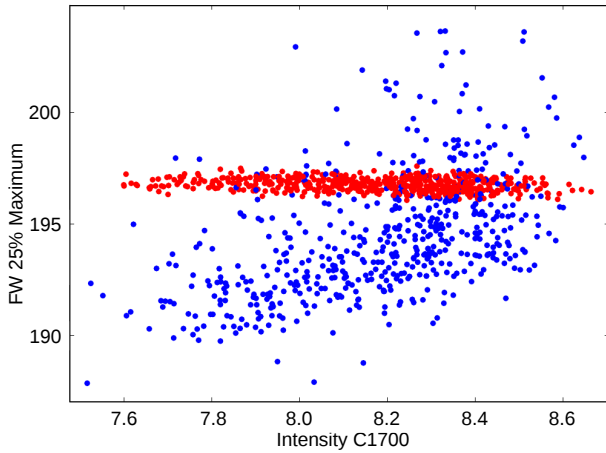


Figure 3: A comparison of captured Full Width at 25% Maximum vs intensity with modulated RF frequency (red) and flat RF frequency (blue) during capture.

As modulated capture provided larger longitudinal emittances and lower line densities it was expected that the transmission would be higher, however this was not the case. After a significant amount of optimisation and study it was found that modifying the working point in the vertical direction throughout the cycle was needed to capitalise on the benefits as shown in Fig. 4. The need for a modified working point was put down to a shift in the density of the tune foot print, which changed the density in tune space near resonance lines.

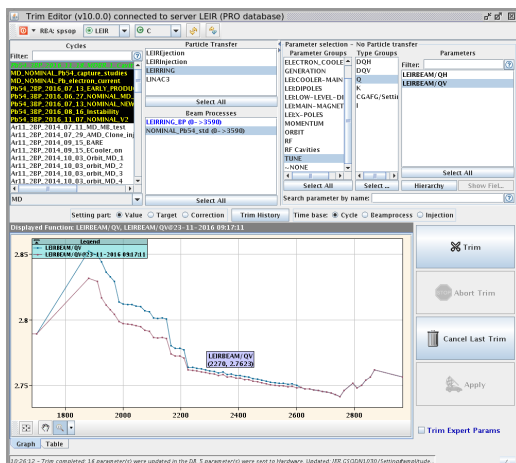


Figure 4: Original (red) and new (blue) vertical tune used to maximise transmission with modulated capture.

After implementing the new working point a comparison of modulated capture with Lone Ranger capture (Fig. 5) showed that better, and more reproducible, transmission could be achieved. As a result modulated capture was used

operationally for approximately the last half of the 2016 p-Pb run.

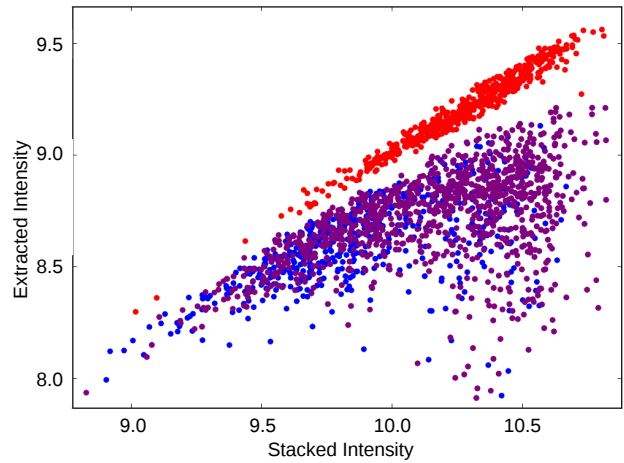


Figure 5: Extracted versus stacked intensity with modulated capture (red) and Lone Ranger (purple and blue).

TWO CAVITY OPERATION

In LEIR there are two Finemet cavities, with one used operationally and the other maintained as a hot spare. After it was demonstrated that frequency modulated capture could be used to provide reproducible longitudinal emittance blow-up it was decided to try using both cavities simultaneously. By using both cavities the RF acceptance would be increased, potentially allowing even larger bunches to be produced.

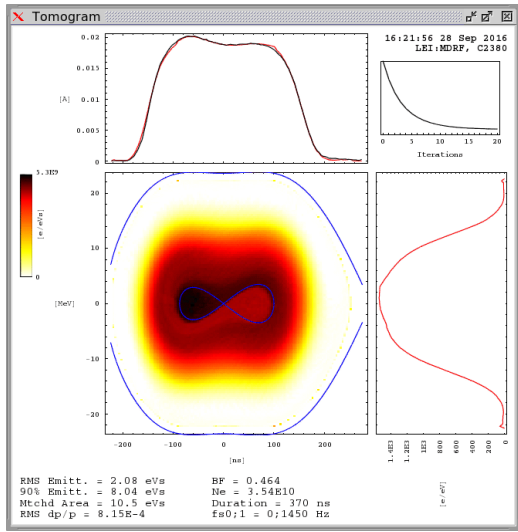
To use both cavities they must first be phased correctly relative to each other. The first coarse tuning brought the phases very close to correct alignment without beam, afterwards a fine tune with beam made a small additional correction. Using modulation during capture allowed for a highly reproducible distribution in phase space, it was therefore possible to use bunch profiles and tomography to adjust the LLRF and bring the harmonics into alignment.

To align the cavities using the beam an initial measurement was taken with both harmonics in a single cavity, shown in Fig. 6a. The $h=2$ voltage was then set to 0 in the first cavity and set to the operational program in the second cavity. The conditions prior to fine tuning are shown in Fig. 6b, whilst the result is very close to the single cavity case there is a visible difference. Fine tuning of the alignment of the cavities resulted in a near identical bunch as can be seen in Fig. 6c.

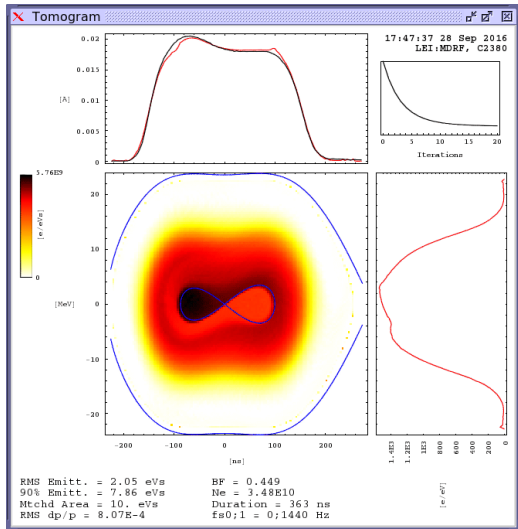
LONGITUDINAL ACCEPTANCE LIMITATION

After dual cavity operation was shown to be effective frequency modulation was used to try and further increase the captured emittance, taking advantage of the increased longitudinal acceptance. It was discovered that the emittance could not be increased past a hard limit, at which point losses were unavoidable with no further blow-up. As it was not

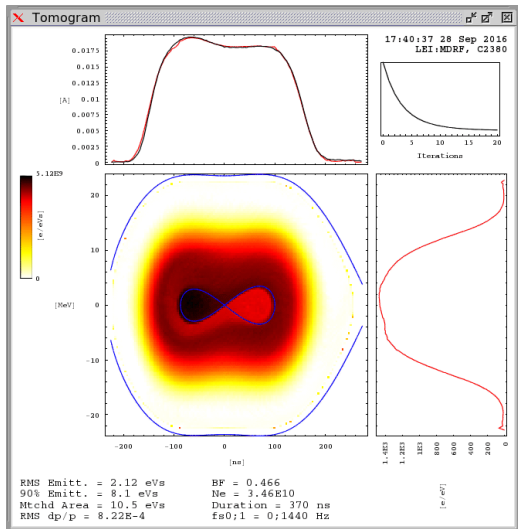
LEIR LONGITUDINAL STUDIES



(a) Single Cavity



(b) Dual Cavity Initial



(c) Dual Cavity Final

Figure 6: Phase spaces produced with single cavity (6a), two cavities before fine tuning (6b) and two cavities after fine

clear if the losses were due to an acceptance limitation or related to the transition from the flat bottom to the ramp the capture was first moved earlier in the cycle to allow distinguishing the end of capture from the start of the ramp.

Separating capture from the ramp allowed two distinct losses to be seen as shown in Fig. 7. First a fast loss can be seen at C1780, the end of capture, and a second larger loss is seen at the start of the ramp at C1850. The localisation of losses at capture appeared to indicate that the longitudinal momentum spread was responsible for lost beam, this was shown to be the case by capturing a fixed emittance and then increasing the voltage to stimulate losses.

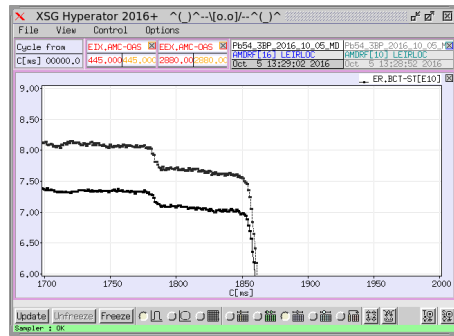


Figure 7: Distinct losses at the end of capture and the start of the ramp.

For a given emittance an increase in the RF voltage will lead to a larger dp/p and a smaller bunch length. After capture the two harmonics were increased to a peak and then decreased (peak at 100ms shown in Fig. 8) causing an increase in the bunch height and the losses shown in Fig. 9 with no fast loss at the start of the ramp.

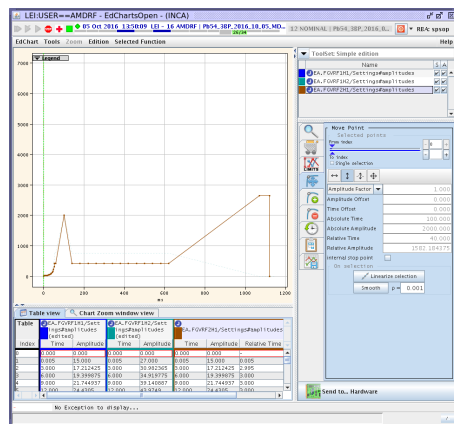


Figure 8: Voltage spike used to increase bunch height.

Figure 10 shows the phase space reconstructions at C1800 (Fig. 10a), C1820 (Fig. 10b) and C1830 (Fig. 10c), where the emittance decreases with approximately constant $\frac{dp}{p}$. The constant $\frac{dp}{p}$ shows that there is a hard limit in the maximum energy deviation, which therefore causes the emittance to be reduced with increasing voltage due to losses.

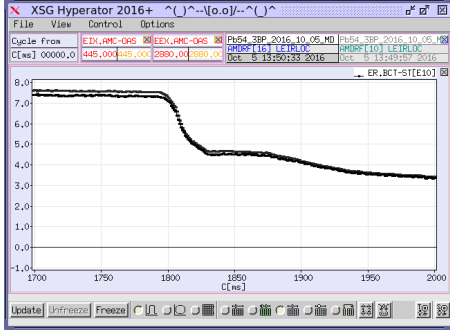


Figure 9: Losses during voltage spike.

The acceptance limitation demonstrated that the maximum bunch height after capture must be less than 7 MeV, as a result the use of two cavities would not be able to improve transmission. Working with a single cavity the voltage program was adjusted such that the ratio $V_{h=2} : V_{h=1}$ maximised $\frac{A_B}{h_B}$, where A_B is the bucket area and h_B is the bucket height. The maximum of $\frac{A_B}{h_B}$ on the flat bottom was found to be at approximately 1.1 : 1 voltage ratio.

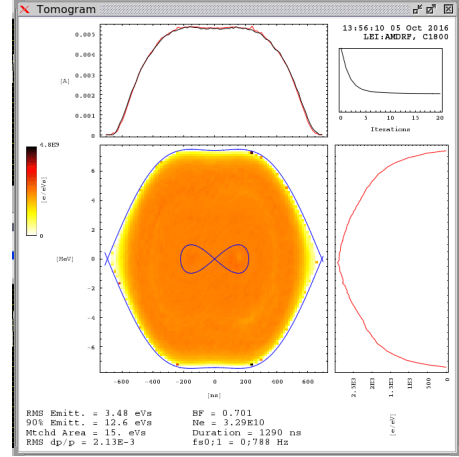
CONCLUSION

There were extensive studies in the longitudinal plane of LEIR during 2016. A series of studies and developments are summarised in this paper, which resulted in highly reproducible beams with large emittances being produced through frequency modulation during capture.

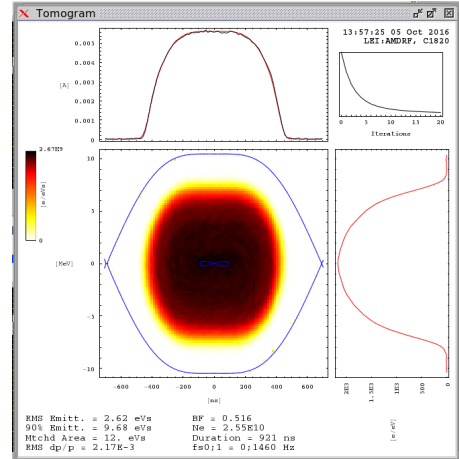
Initially a constant offset between the RF frequency and the design frequency was used to increase the captured emittance. Further improvements to this lead to the production of the “lone ranger” distribution, in which the beam is smeared around the edge of the inner separatrix giving a high bunching factor and very flat profile. Later it was shown that modulating the frequency offset during the capture process lead to larger emittances and improved reproducibility, combined with an adjustment to the working point this then allowed better and more reproducible transmission.

There are two cavities in the LEIR ring, with only one used in operation. The use of two cavities was studied as a possible way to further increase the longitudinal acceptance, allowing greater emittance blow-up during capture. After careful alignment of the voltage in the cavities it was found that a limit in the longitudinal acceptance existed due to the energy spread of the beam, rather than the bucket area. Since the maximum energy deviation on the flat bottom was approximately 7 MeV, corresponding to an RMS $\frac{dp}{p}$ slightly above 2×10^{-4} there was no operational benefit to using two cavities.

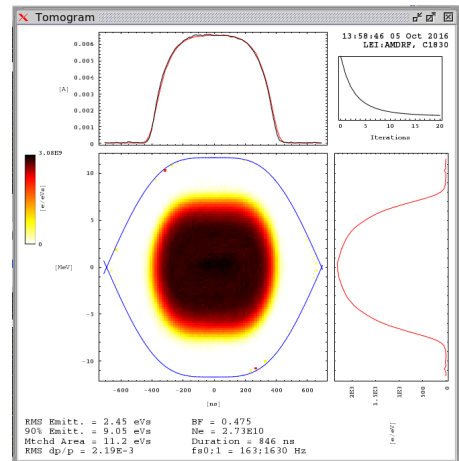
Finally in the second half of the LHC p-Pb run frequency modulated capture with a single cavity and voltage functions designed to maximise the bucket area within the acceptance limit became the operational norm.



(a) C1800, $\epsilon_l = 15$ eVs, $\frac{dp}{p} = 2.13 \times 10^{-4}$



(b) C1820, $\epsilon_l = 12$ eVs, $\frac{dp}{p} = 2.17 \times 10^{-4}$



(c) C1830, $\epsilon_l = 11$ eVs, $\frac{dp}{p} = 2.19 \times 10^{-4}$

Figure 10: Phase spaces during an increase in the RF voltage showing an approximately constant $\frac{dp}{p}$ with decreasing longitudinal emittance (ϵ_l) demonstrating the existence of a longitudinal acceptance limitation independent of RF voltage.

ACKNOWLEDGEMENTS

The authors would like to thank the all members of the LIU-IONS team and all those involved in LEIR operations who enabled this work to happen.

REFERENCES

- [1] the New LEIR Digital Low-Level RF System, M. E. Angoletta et al, *IPAC2017, THPAB144*

LEIR IMPEDANCE MODEL AND COHERENT BEAM INSTABILITY OBSERVATIONS

N. Biancacci, E. Métral, T. L. Rijoff (CERN, Geneva, Switzerland),
M. Migliorati (University of Rome “La Sapienza” and INFN-Roma I)

Abstract

The LEIR machine is the first synchrotron in the ion acceleration chain at CERN and it is responsible to deliver high intensity ion beams to the LHC. Following the recent progress in the understanding of the intensity limitations, detailed studies of the machine impedance started. In this work we describe the present LEIR impedance model, detailing the contribution to the total longitudinal and transverse impedance of several machine elements. We then compare the machine tune shift versus intensity predictions against measurements at injection energy and summarize the coherent instability observations in the absence of transverse feedback.

INTRODUCTION

The LEIR machine is the first ion synchrotron accelerator along the CERN ion accelerators chain and it was conceived in order to deliver high brightness bunches to the LHC [1]. The machine is equipped for this purpose, with an electron cooler that, together with the 2.5 planes stacking injection mechanism (transverse phase spaces and longitudinal momentum space), allows for accumulation of high intensity beams at the injection plateau of 4.2 MeV/nucleon.

Once injected and accumulated, the coasting beam is captured by the RF system [2], accelerated to 72 MeV/nucleon and sent to the PS ring.

During the capture process, high losses were systematically observed for high intensity beams, leading to performance degradation in terms of delivered bunch intensity [3, 4]. At the end of 2015 an extensive beam study program was started in order to understand the underlying mechanism and the main driving source was identified as direct space charge effects in combination with the lattice sextupolar resonances [5, 6]. Thanks to special shaping of the longitudinal line density during the RF capture and optimized resonance compensation, the LIU/HL-LHC design intensity goal of $8.1 \cdot 10^8$ ions/bunch has been reached in 2016 [6, 7].

In order to ensure a stable LEIR machine performance with enough margin with respect to the LIU baseline, further studies are presently ongoing [8] (working point and electron cooling optimization, resonance compensation, bunching factor increase, etc.). Among these, the development of the transverse impedance model is taking place in order to improve the general understanding of the machine with respect to collective effects.

In this work we will detail the development status of the LEIR transverse impedance model, we will compare the measured transverse tune shift versus intensity with the cor-

responding predictions and summarize the transverse coherent instabilities that are observed in coasting beam mode in the absence of the transverse feedback.

LEIR TRANSVERSE IMPEDANCE MODEL

The process of developing an impedance model for an accelerator has been recently summarized in [9]. Concerning the LEIR machine, the vacuum envelopes of the following elements have been considered so far for the impedance calculations [10–12]: dipoles, quadrupoles, vacuum drift tubes, septa, beam position monitors, electron cooler main and transition pipes (computed with IW2D [13] considering the corresponding flat or round stainless steel beam pipe), kickers (modeled with the Tsutsui formalism [14]), stripline pick-up (computed using Ng formulae [15]). The total integrated length calculated so far is 68.37 m, i.e. $\approx 87\%$ of the total machine circumference (78.54 m).

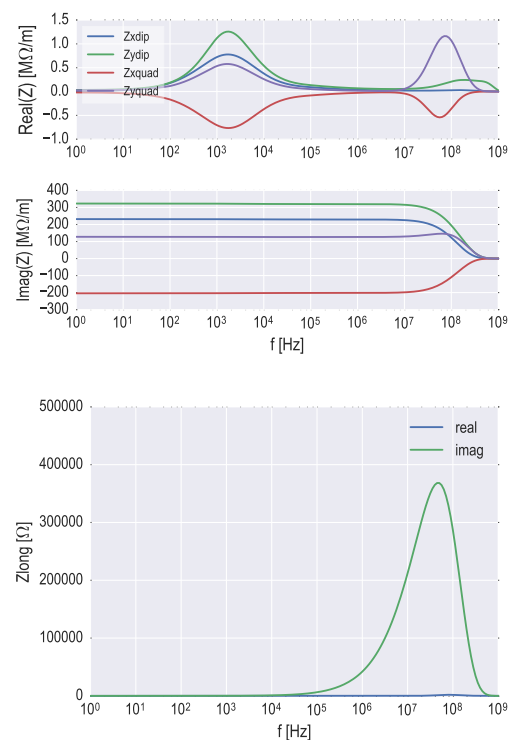


Figure 1: Left: Real and imaginary part of the dipolar (driving) and quadrupolar (detuning) LEIR impedance model. Right: Real and imaginary part of the longitudinal LEIR impedance model.

The left side of Fig. 1 shows, as an example, the total impedance budget in the transverse planes for real and imaginary part of dipolar (or driving) and quadrupolar (or detuning) impedances. A typical bunched beam in LEIR has a rms bunch length of $\sigma_{\tau}^{rms} \simeq 200$ ns corresponding to $\sigma_f^{rms} \simeq 1$ MHz considering a Gaussian profile. Considering tune shift calculations, for example, only the inductive part of the impedance would be relevant. The machine total impedance budget (i.e. dipolar plus quadrupolar) is 442 M Ω /m in the vertical plane and 27 M Ω /m in the horizontal plane¹.

Due to the low machine energy, the indirect space charge impedance is dominant and mainly driven by the vacuum chamber in the dipoles (60%) and the quadrupoles (20%).

TUNE SHIFT MEASUREMENTS

The impedance model presented in the previous section was used to predict the tune shifts in coasting and bunched beam regimes. The coasting beam angular frequency shift $\Delta\omega_n$, from Laclare's theory [16] can be evaluated in the (vertical) plane, as

$$\Delta\omega_n = \frac{Q}{A} \frac{j\beta c^2 I_0}{4\pi Q_y f_0 C E_t / e} Z_y^{dip}(n), \quad (1)$$

where the number of ion charges over the number of mass ratio Q/A is 0.26 for Pb^{54+} , $I_0 = Ne f_0$ is the beam current with N total number of charges, e the elementary charge and f_0 the revolution frequency, β the relativistic factor ($\simeq 0.1$ at injection and 0.37 at extraction), c the speed of light in vacuum, Q_y the betatron tune, C the machine circumference, E_t the total beam energy per nucleon, Z_y^{dip} the dipolar impedance sampled at the coasting beam spectral lines given by

$$f_n = (n + Q_y)f_0, \quad \text{with } n \in (-\infty, +\infty). \quad (2)$$

When the coasting beam is kicked, coherent betatron oscillations build up and the coherent frequency shift is proportional to the total transverse impedance $Z_y^{tot} = Z_y^{dip} + Z_y^{quad}$.

The predicted tune shift and growth rate for a coasting beam of $N = 10^{10}$ charges calculated for the vertical plane (most critical) with reference to the working point $Q_x = 1.82$, $Q_y = 2.72$ are respectively of $2.75 \cdot 10^{-4}$ and 0.25 s^{-1} , the latter corresponding to the spectral line f_{-3} driven by the resistive wall impedance.

Tune shift versus intensity measurements were done in the machine during 2016 with both coasting and bunched beams following a first assessment done in [10]. High intensities available in LEIR allow for several injections from Linac3 followed by electron cooling. The electron cooler introduces an average momentum shift which depends on the intensity and may lead, by itself, to a tune shift through chromaticity. As it is difficult to set chromaticity exactly to zero, a different approach was followed in order to perform

a coasting beam intensity scan: once the maximum intensity is accumulated into the machine to about 10^{10} charges, the vertical damper is turned off for an adjustable time in order to let the coherent instability (see next section) develop and scrape the beam onto the vacuum chamber. Figure 2 on the left shows measured and predicted tune shifts in agreement within 80%.

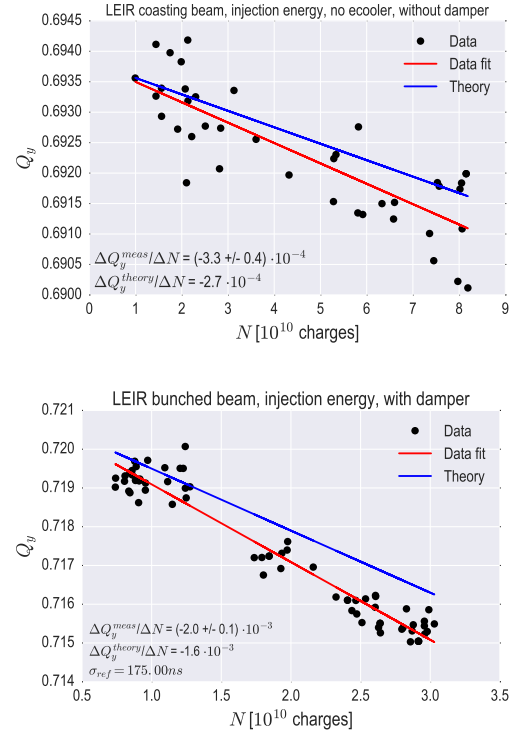


Figure 2: Coasting beam (left) and bunched beam (right) transverse tune shift versus intensity.

The measurements with bunched beams were performed after capturing the coasting beam using a double harmonic RF system. Despite the losses at capture described in the introduction, a maximum intensity of $3 \cdot 10^{10}$ charges within $\sigma_{\tau}^{rms} = 175$ ns bunch length was achieved. This produces a tune shift versus intensity of $-2 \cdot 10^{-3}$ (per 10^{10} charges) to be compared with $-1.6 \cdot 10^{-3}$ predicted scaling Eq. (1) by the inverse of the bunching factor $B_f = \sqrt{2\pi}\sigma_{\tau}^{rms} f_0 = 0.16$ between coasting and bunched beam measurements. The measurement results are shown in Fig. 2 on the right and are in agreement with prediction within 80%, in line with the coasting beam measurements.

INSTABILITY OBSERVATIONS

When the transverse feedback is not in operation, a fast vertical instability is observed in coasting beam, still unexplained by the impedance model outlined so far. We present here a characterization of the instability in terms of resonator impedance based on beam measurements.

Figure 3 shows the instability observed analyzing the turn-by-turn data acquired with a wide band pick-up of the trans-

¹ We accounted for an additional $1/\beta$ factor multiplying the impedance of IW2D in order to be compatible with the theory of [16] used later.

verse feedback system. A single line growth can be observed at ≈ 1.9 MHz which corresponds to the coasting beam spectral line f_{-8} . The growth rate is $\approx 40\text{s}^{-1}/10^{10}$ charges and according to Eq. (1) would correspond to a transverse impedance with a real part of $28\text{ M}\Omega/\text{m}$, larger than the impedance model predictions of $\approx 0.1\text{ M}\Omega/\text{m}$ in this range of frequencies. In the hypothesis of having a localized reso-

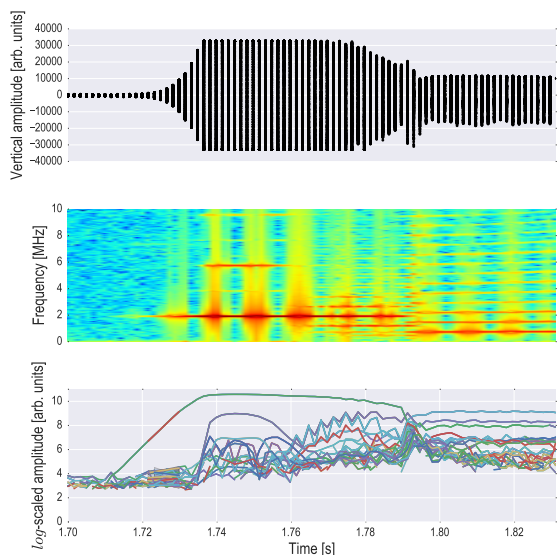


Figure 3: Turn-by-turn data (top) with moving window FFT (middle) and amplitude growth per coasting beam spectral line of the observed vertical instability: the linear growth (in log scale) corresponds to the f_{-8} spectral line.

nant mode in the machine at this frequency, we performed a Q -factor characterization studying the variation of growth rate with respect to a change in the machine tune Q_y . This can be seen as a frequency scan as the unstable mode line f_{-8} will move according to Eq. (2). As shown in Fig. 4 for different chromaticities², a resonator with a $Q \approx 50$ can describe the observations within the accuracy of the measurement.

In order to damp the instability, it is possible to enhance the transverse Landau damping by means of increasing chromaticity [16]. For this purpose, a scan in Q' was done for a fixed value of the vertical tune. Figure 5 shows the growth rate of the instability for different values of Q' : the frequency f_{-8} is unstable for $Q' \in (-10, 4)$ whereas for $Q' > 4$ only higher order lines are observed to be unstable.

As the stabilizing betatron spread from chromaticity S is

$$S_n = \left(f_n - \frac{Q'}{\eta} f_0 \right) \eta \Delta p / p, \quad (3)$$

with $\eta = -0.87$ the slip factor at injection and $\Delta p/p \approx 10^{-3}$ momentum spread, S_{-8} cancels for $Q' = 4.5$. On the contrary, the threshold effect observed in Fig. 5, is still under

² The ones indicated are programmed chromaticities corrected with -3 units to account for the difference between real and programmed values [17].

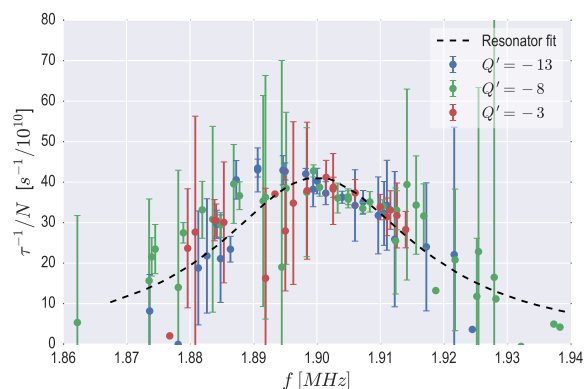


Figure 4: Instability growth rate versus frequency (i.e. Q_y) for Q' values of -3, -8, -13. The fit with a resonator model is done at the frequency of 1.9 MHz with $Q \approx 50$ and growth rate of $40\text{s}^{-1}/10^{10}$.

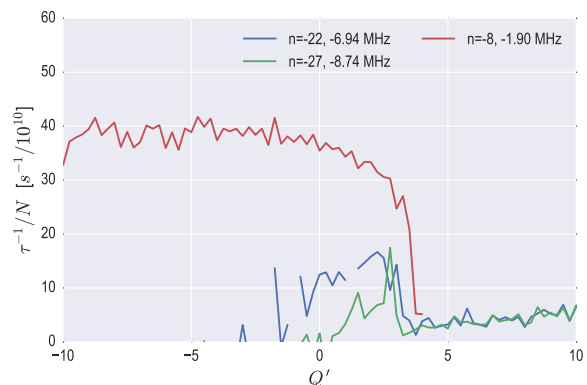


Figure 5: Instability growth rate versus Q' : the f_{-8} line is unstable for $Q' < 4$.

investigation and could be related to the effect of direct space charge [18].

CONCLUSIONS

The LEIR impedance model has been largely developed and accounts for $\approx 87\%$ of the total machine elements. Studies are ongoing in order to include the remaining elements and update the tune shift predictions that are, so far, in agreement within 80% with coasting and bunched beam transverse tune shift measurements.

The vertical coherent instability observed in coasting beam without damper is not yet predicted by the model and studies are ongoing in order to localize possible sources of resonant modes (cavities, kickers, electron cooler, etc.).

By means of tune and chromaticity parametric scans it was possible to derive the parameters of an equivalent resonator describing the instability having shunt impedance of $28\text{ M}\Omega/\text{m}$, a resonant frequency at 1.9 MHz, corresponding to the f_{-8} coasting beam line, and a Q -factor of ≈ 50 .

The stabilization of the instability is measured for $Q' > 4$ revealing a threshold effect in contrast with theory compatible with a local reduction of Landau damping. Further measurements, in particular of the beam transfer function in coasting, will help clarifying the role of space charge in the stabilizing mechanism and defining the corresponding stability margins for possible future intensity upgrades.

ACKNOWLEDGEMENTS

The authors would like to thank H. Bartosik, G. Favia, A. Huschauer, J. Lacroix, M. Paoluzzi, B. Salvant, R. Scrivens, L. Teofili, and G. Tranquille for the help and suggestions received during the development of the LEIR impedance model and the SPS-LEIR operation team for the support during the beam measurements.

REFERENCES

- [1] O. Brüning and others (editors). *LHC design report Vol.1: The LHC main ring*. CERN-2004-003-V1. CERN, Geneva, Switzerland, 2004.
- [2] M. Paoluzzi et al. The LEIR RF system. LHC-Project-Report-818, CERN, Geneva, Switzerland, July 2005.
- [3] M. Bodendorfer et al. "Is Pb⁵⁴⁺ in LEIR limited by space charge?" . Space Charge Collaboration Meeting, CERN, Geneva, Switzerland, 20 May 2014. https://indico.cern.ch/event/292362/contributions/669646/attachments/546507/753289/2014_05_20_SC_collaboration_mbodendorfer.pdf.
- [4] M. Bodendorfer et al. Beam loss in the low energy ion ring (LEIR) in the light of the LHC Injector Upgrade for Ions (LIU-Ions). In *Proceedings, 13th Heavy Ion Accelerator Technology Conference*, pages 115–117, paper TUM1C01, Yokohama, Japan, September 7-11, 2015.
- [5] R. Scrivens, D. Manglunki, et al. LIU-IONS PS injectors: baseline, outcome from 2015 operation and next steps. In *LHC Performance Workshop*, Chamonix, France, January 25-28, 2016. https://indico.cern.ch/event/448109/contributions/1942044/attachments/1217907/1780095/Chamonix_2016_Scrivens.pdf.
- [6] A. Huschauer et al. LIU-ions for PS injectors status and outlook. In *LHC Performance Workshop*, Chamonix, France, January 23-27, 2017. https://indico.cern.ch/event/580313/contributions/2359565/attachments/1401709/2139617/LIU-ions_for_PS_injectors_status_and_outlook.pdf.
- [7] H. Bartosik et al. The LHC injectors upgrade (LIU) project at CERN: ion injector chain. In *8th International Particle Accelerator Conference*, paper TUPVA020, Copenhagen, Denmark, 14-19 May 2017.
- [8] A. Huschauer et al. Progress in the understanding of the performance limitations in the CERN Low Energy Ion Ring. In *8th International Particle Accelerator Conference*, paper THPAB049, Copenhagen, Denmark, 14-19 May 2017.
- [9] E. Métral and Y. H. Chin (editors). *Collective effects in particle accelerators*. ICFA Beam Dynamics Newsletter no.69, Chapter 2.9, December 2016.
- [10] T. Rijoff et al. Tune shift measurements in LEIR. HSC Meeting, CERN, Geneva, Switzerland, 14 March 2016. https://espace.cern.ch/be-dep-workspace/abp/HSC/Meetings/HSC_LEIR_Impedance.pptx.
- [11] M. Migliorati et al. LEIR impedance model. LIU-IONS PS Injectors - Beam Performance Meeting, CERN, Geneva, Switzerland, 19 July 2016. <https://indico.cern.ch/event/556983/contributions/2245274/attachments/1311523/1962698/20160719LEIR.pdf>.
- [12] N. Biancacci et al. LEIR impedance and instability measurements. Injectors MD days, CERN, Geneva, Switzerland, 24 March 2017. https://indico.cern.ch/event/598300/contributions/2417621/attachments/1396793/2129641/LEIR_impedance_17012016.pdf.
- [13] N. Mounet. *The LHC Transverse Coupled-Bunch Instability*. PhD thesis, Ecole Polytechnique, Lausanne, March 2012.
- [14] H. Tsutsui and L. Vos. Transverse coupling impedance of a simplified ferrite kicker magnet model. *LHC-PROJECT-NOTE-234*, CERN, Geneva, Switzerland, September 2000.
- [15] K. Y. Ng. Impedances of stripline beam position monitors. *Part. Accel.* 23 (1988), pages 93–102, 1988.
- [16] J. L. Laclare. Introduction to coherent instabilities: coasting beam case. *CAS - CERN Accelerator School, Gif-sur-Yvette, France, 3 - 14 September 1984*.
- [17] A. Huschauer. Beam dynamics studies on LEIR. LIU-IONS PS Injectors - Beam Performance Meeting, CERN, Geneva, Switzerland, 30 October 2015. https://indico.cern.ch/event/458938/contributions/1127652/subcontributions/100810/attachments/1179818/1707584/2015.10.30_LIU-LEIR.pdf.
- [18] K. Y. Ng. Landau damping of space-charge dominated Fermilab Booster beam. In *42nd Advanced Beam Dynamics Workshop*, pages 168–177, Paper WGA32, Nashville, USA, 25-29 August 2008.

100MS INJECTION INTO LEIR

R, Scrivens*, N. Biancacci, A. Huschauer, D. Manglunki, G. Tranquille, CERN, Geneva, Switzerland

Abstract

Results of machine developments for 100ms spaced injections from Linac3 into LEIR are presented.

INTRODUCTION

The LIU project aims to increase the number of ions [1] injected into the LHC, and one of the limitations to be overcome is to increase the number of ions available from the pre-injector, Linac3, as well as to accumulate and accelerate this higher intensity in LEIR. One of the methods to increase the number of Pb54+ ions available from Linac3, is to decrease the spacing between the 200us long pulses, and if the same length of LEIR injection plateau is kept, the number of pulses that can be transferred from Linac3 to LEIR increases from 7 to 13. Additionally, it could be conceived to inject a smaller number of injections in a much shorter time, and reduce the LEIR cycle from 3.6 to 2.4s. In order to decrease the injection spacing to 100ms, the following was demonstrated to be possible with the presently installed equipment:

- the Linac3 ECR source already operates at 100ms spaced pulses,
- most of Linac3 was designed to run at 10Hz,
- the injection system of LEIR was designed for 10Hz operation,
- the electron cooling beam current could be doubled from the operational value of 220mA.

Within the LIU project, the following actions were made to allow remaining equipment to run at 100ms spaced pulses.

- pulsed quadrupole and corrector dipole power converters were upgraded to 10Hz,
- these pulsed magnets had thermal interlocks added,
- Ventilation was improved on the RF racks to give additional cooling.

All of these measures were anyway limited to proving up to 13 pulses in a 3.6s cycle, as well as allowing for continuous 5Hz operation. In this regard, the consolidation of the ventilation system of Linac3 is also needed to allow continuous operation at these higher repetition rates.

The results presented in the following sections are based on two MD sessions.

Table 1: Parameters used for comparison of intensity at 100 and 200ms space injections

	NOMINAL 200ms	AMD 100
Spacing (ms)	200	100
# Injections	7	14
Electron cooler (mA)	220 Non-uniform beam (too high current)?	510
Accum Intensity (Charges Total)	9.5E10	12.0E10
Extracted Intensity (Charges Total)	8.0E10	8.0E10

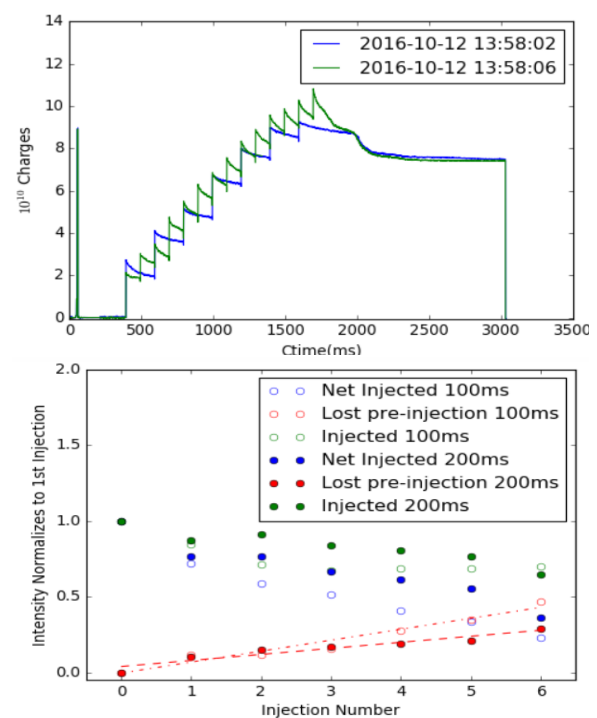


Figure 1: Top: Beam intensity stored in the ring for 14x 100ms injection (green) and 7x 200ms injections (blue); Bottom: Comparison of the first 7 injections into LEIR when spaced by 100ms (open circles) and 200ms (closed circles). Linear fits are shown to the intensity lost pre-injection.

INTENSITY

On 12/10/2017, the optimized cycle being used for operation (*USER=NOMINAL*) was cloned and the injection rate decreased to 100ms along with the number of injections being increased to 14. The electron cooler was increased in beam intensity and optimization of the injection and stacking process was done (including injection line trajectories, orbit

* richard.scrivens@cern.ch

during accumulation, electron beam energy etc.), details are given in Table 1.

The intensity during a LEIR cycle is shown in Figure 1 (left) where it can be seen that slightly more beam is accumulated with the 100ms injections, but this is limited due to two loss mechanisms:

- fast loss of the beam stacked in the ring when the injection bump is opened,
- loss of the accumulated beam between injections.

The fast loss was measured using the fast Beam Current Transformer (BCT) and comparing the reduction in signal in the 100 μ s before the injection beam starts. Comparison of the magnitude of the beam lost, to the intensity injected on the first injection is shown in Figure 1 (right) where it can be seen that for 100ms spaced injections, the amount of stacked beam lost is increasing more rapidly with injection number, reaching approximately 50% of the intensity of the first injection intensity, by injection number 8.

The slow loss of accumulated beam in between the injections is also more pronounced when the beam is injected with 100ms spacing (Figure 1 (left)). This loss is composed of two components, one of the order of milliseconds, and the second the order of seconds. writing this as:

$$I = I_{fast} e^{-\frac{t}{\tau_{fast}}} + I_{slow} e^{-\frac{t}{\tau_{slow}}} \quad (1)$$

and at an intensity of 8E10 charges circulating, the (fast,slow) decay times are (20ms,4500ms) for 200ms and (20ms,2000ms) for 100ms spaced injections, the slow decay time is 2.5 times shorter for the higher injection rate.

This can be initially compared to the ion loss rate for Pb54+ ions that was measured at LEAR in 1996 [2] and the total beam decay rate (for both electron cooling losses and vacuum losses) was calculated to be 7seconds.

TRANSVERSE COOLING RATE

The transverse cooling of the circulating beam can be measured with the Ionization Profile Monitor [3]. The projected beam profile can be measured every 1ms to which a gaussian fit is made to calculate an rms beam size. A fit of the decay of the beam size is then made, i.e.:

$$\sigma = \sigma_0 e^{-\frac{t}{\tau_{cool}}} \quad (2)$$

where the time window 11 ms after each injection are not included in the fit due to the often seen large beam size oscillations measured after the injection process.

Measurements of the beam profile as a function of time in the cycles were made with the parameters in table 2, and the resulting cooling times are reported in Figure 2 (right). Contrary to the data in table 1 in this case for 100ms spaced injections the electron cooling current was 430mA. In Figure 2 (right) the lines shown are not fits, but only guides for the eye.

The following conclusions are drawn from this result:

Table 2: Parameters used for comparison of transverse beam cooling rates at 100 and 200ms space injections

	NOMINAL 200ms	AMD 100ms
Spacing (ms)	200	100
# Injections	7	13
Electron cooler (mA)	220	430
Accum Intensity (Charges Total)	9.5E10	9.5E10
Extracted Intensity (Charges Total)	8.0E10	5.0E10

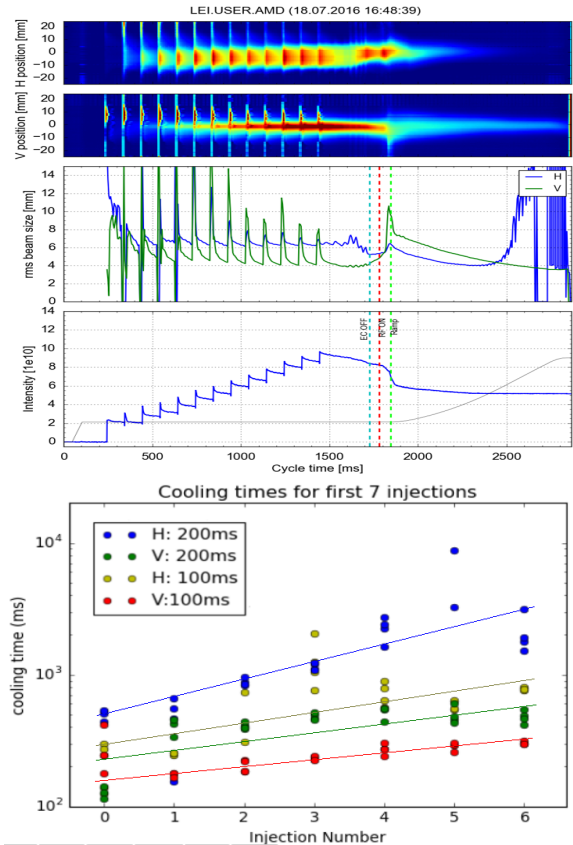


Figure 2: Top: Plots of the beam profile measured with the Ionization Profile Monitor; Bottom: Transverse cooling times for the circulating beam following 100 and 200ms spaced injections, first 7 injections shown.

- the cooling times increase as a function of injection number, but the effect on the measurement of the already stacked and cooling beam is not known
- the vertical cooling time is measured to be 2 - 3 times faster than the horizontal plane (however, this may be affected by the losses in the vertical plane),
- the increased electron cooling current improves the cooling time by a factor 1.5 - 2.

FUTURE MEASUREMENTS

In 2017 only xenon will be available in LEIR, and the performance of the beam is expected to be significantly different and it is not foreseen to spend effort understanding limitations of the xenon beam as the required intensity for physics is low. However studies will be possible to understand some of the processes, these are listed below:

- Preliminary testing of 150ms cycling of the Linac3 source,
- measurement of xenon cooling times from IPM after its repair,
- measurement of the effect of injection bump on circulating beam,
- inclusion of dispersion into the analysis of cooling rate for the horizontal IPM,
- benchmarking of cooling simulations, including parametric studies.

ACKNOWLEDGEMENTS

Thanks is due to the teams from EPC, MPE, MSC and RF who upgraded equipment in Linac3 and the transfer line in order to allow the beam to be produced with 100ms spacing.

REFERENCES

- [1] LHC Injectors Upgrade: Technical Design Report - Volume 2: Ions, Eds J. Coupard et al, LIU-PM-RPT-0025, <https://edms.cern.ch/document/1626950/>
- [2] J. Bosser, Review of Recent Work on Electron Cooling at LEAR, CERN-PS/96-13(AR), 1 April 1996.
- [3] C. Bal, V. Prieto, R. Sautier, G. Tranquille, First Results from the LEIR Ionisation Profile Monitors, Proc DIPAC 2007, Venice, Italy, TUPB24, <https://accelconf.web.cern.ch/accelconf/d07/papers/tupb24.pdf>

YASP FOR LEIR TO PS INJECTION

V. Kain, J. Axensalva, H. Bartosik, A. Huschauer, D. Jacquet, D. Nicosia, S. Pasinelli, J. Wenninger

Abstract

The steering program YASP was introduced in the LEIR injection as well as the extraction lines in 2016 to correct the trajectories with well-known model based correction algorithms such as MICADO or SVD. In addition a YASP configuration was prepared to correct the extraction line together with the first turn of the PS. In this way the injection oscillations can be corrected while keeping the trajectory reasonable in the PS injection line.

INTRODUCTION

The steering program YASP [1] provides well-known trajectory and orbit correction algorithms as well as the option to calculate trajectory or orbit bumps for a given shape and amplitude. The optics of the beam line or ring have to be provided such that response matrices can be calculated. The required correction is given in angles for the different bending magnets and steerers.

YASP makes use of the LSA [2] framework, where an optics can be defined and uploaded to a database for a so-called *particle transfer* (which is a combination of one or several accelerator zones). Also, all magnets can be associated with normalized strength parameters (e.g. k for quadrupoles and angle for dipoles) within LSA. The momentum or $B\rho$ is defined as part of an LSA cycle which is associated with a timing user. Together with this information and calibration functions, LSA calculates the required power supply currents with *makerules* and sends the required current value or function to the hardware. In short, a correction in YASP *trims* the parameter angle of one or more dipole magnets and LSA calculates and *drives* the associated current values.

PREPARATION OF LSA FOR THE LEIR TRANSFER LINES

Figure 1 shows the layout of the LEIR synchrotron with its transfer lines. The injection line consists of the lines ITH, ITE, the bi-directional line ETL as well as EI. The extraction line is made up of the lines EE, ETL in the other direction and ETP. One obvious complication for modelling this layout in LSA is the bi-directionality of ETL. Another one is the fact that the lines contain a mixture of PPM as well as non-PPM power supplies, which mostly expect scalar values as settings, but in one case (ETL.BHN10) a function. *Accelerator zones* were created for the different parts of the lines in LSA. In most cases there is a one-to-one match between the physical line and the accelerator zone (e.g. line EE corresponds to accelerator zone EE). The exception is ETL which became three different accelerator zones: ETL_INJ, ETL_EJ and ETL. The hardware actually follows this zoning. In fact the ETL scalar power supplies are equipped with two FESA classes. one to pilot the current for the injected beam and

one for the extracted beam. The function power supply of ETL.BHN10 is contained in the accelerator zone ETL.

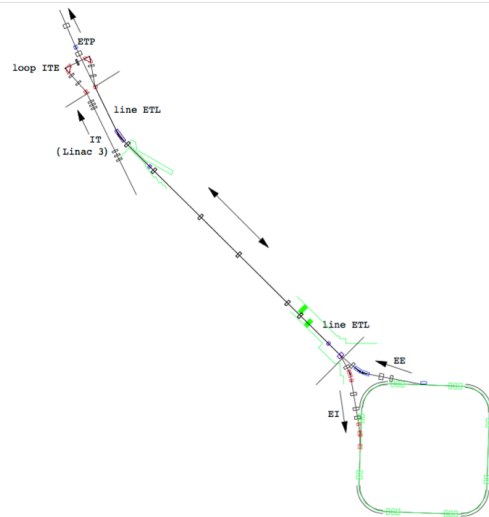


Figure 1: LEIR and its transfer lines

These different accelerator zones were associated with two particle transfers: LEIRInjection and LEIREjection. Different beam processes were then prepared for the particle transfers with the line optics. Discrete beam processes are used for the scalar type power supplies and function beam processes for the function type power supply. At YASP start-up one has to decide whether one wants to work with either the discrete or function beam process. As most of the correctors are scalar type power supplies the usual configuration is to use the discrete beam process.

JMad models have been prepared to upload the optics into LSA.

In order to have all settings required to control the line associated with a particular cycle, virtually ppm current parameters had to be prepared for the non-ppm power supplies in LSA. These virtually ppm current settings are sent to the hardware as if coming from the *non-multiplexed context*. If trims from different cycles occur, the last one wins.

The transfer functions had been collected from Norma and through other sources. Special makerules and linkrules for ETL.BHN10 had to be written. The makerule for the scalar power supplies is `LeirK2CurrMakeRule.java` in the package `lsa-ext-leir`, the makerule for ETL.BHN10 is `K2CurrMakeRule.java` in the same package and the linkrule is `EtLinkRule.java`. The advantage of this linkrule is that no matter which current is used during the beam passage, $|dI/dt|$ for the ascent and descent is always the same.

LEIR TO PS STEERING

YASP can be configured to acquire the BPMs in the LEIR to PS transfer line at the same time as the injection oscillations in the PS (= first turn minus closed orbit at time 0 ms).

In this mode the horizontal pickups in the PS are multiplied with -1 to take the reference system change into account from LEIR transfer line to PS ring. Thus the first pickup in the PS between the septum and the kickers has a large negative offset, where in reality it has a large offset towards the outside, i.e. positive offset. As the septum and kickers are also used for the injection oscillation correction in the horizontal plane, their response is also multiplied with -1. Kick

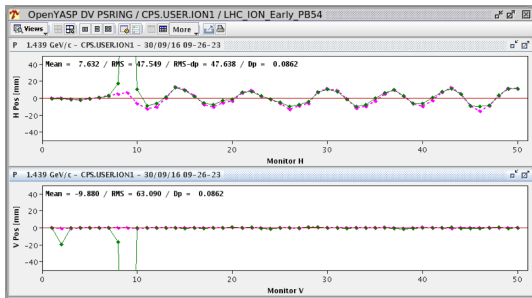


Figure 2: Result of horizontal kick response. The first roughly 10 pickups are in the line, the remainder in the PS.

response measurements were carried out to verify polarities and calibration of the different correctors. Whereas the obtained results were satisfying in the horizontal plane, see Fig. 2, the vertical response for all of the available correctors did not match, see Fig. 3. Optics issues are suspected and will need follow-up during the 2017 run.

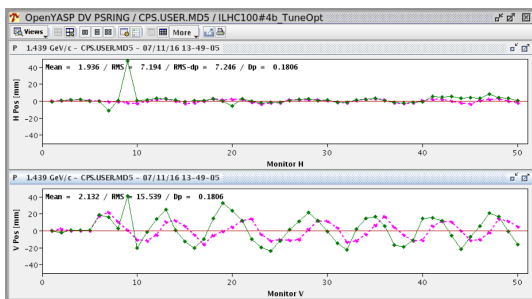


Figure 3: Result of vertical kick response with ETL.BVN10. The first roughly 10 pickups are in the line, the remainder in the PS.

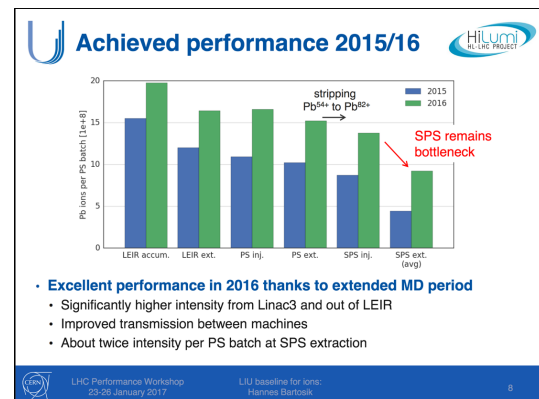


Figure 4: Slide of presentation on LIU baseline for ions by H. Bartosik at LHC performance workshop in Chamonix, January 2017.

This setup was used to steer the ion beam into the PS during the ion run 2016. The transmission from LEIR extraction to PS injection could be increased to essentially 100% in 2016, see Fig. 4.

OUTLOOK - LEIR TO PS STEERING

The potential optics issue needs to be understood to ensure convergence of corrections under all conditions (currently vertical corrections could only be carried out with low gain). Another improvement could be to remove the offset at the injection region BPM in the YASP configuration LEIR to PS steering to further reduce the complexity of the injection oscillation correction. Reference trajectories will have to be established for the coming ion runs.

REFERENCES

[1] J.Wenninger, "YASP: Yet Another Steering Program"
 [2] D. Jacquet et al., "LSA - The High Level Application Software of the LHC and its Performance during the first 3 years of Operation", ICALEPCS, San Francisco, USA, 2013.

BATCH COMPRESSION TO 50 NS SPACING AT PS FLAT-TOP

H. Damerou, CERN, Geneva, Switzerland

Abstract

The bunch spacing in the injector chain has a direct impact on the total number of bunches in the LHC and hence on its integrated luminosity. The baseline scheme for lead ion beams within the LHC Injector Upgrade (LIU) project foresees the transfer of multiple batches of four bunches spaced by 100 ns from the PS to the SPS. The bunch spacing will then be reduced by momentum slip-stacking from 100 ns to 50 ns. Studies have been performed in view of alternatively producing 50 ns spacing directly at extraction from the PS, with the aim of demonstrating a batch compression-like RF manipulation to approach two bunches. Additionally, the proof-of-principle tests allow to define the requirements for an additional RF system in the PS for the batch compression of four bunches to 50 ns spacing. Together with slip stacking in the SPS, this scheme would yield 25 ns bunch spacing with ions in the LHC.

INTRODUCTION

Reducing the bunch spacing of ion bunches in the injector chain has a direct impact on the total number of bunches which fit into the circumference of the LHC and hence on integrated luminosity. While the PS should deliver four bunches spaced by 100 ns for the LIU ion baseline scheme [1], the possibility to reduce the bunch spacing to 50 ns, beyond the LIU baseline, has been studied. In combination with the slip-stacking [2] in the SPS a bunch spacing of 25 ns would then become available to the LHC, significantly increasing the number of ion bunches per ring. Alternatively, generating the 50 ns bunch spacing directly in the PS could furthermore be considered as a back-up scenario for the momentum slip stacking in the SPS.

With proton beams a bunch spacing of 50 ns, as well as 25 ns is produced by bunch pair splitting at the flat-top in the PS [3] using dedicated RF systems at 20 MHz and 40 MHz. For lead ($^{208}\text{Pb}^{54+}$) ion beams such schemes are not feasible due to vicinity of the flat-top energy, $\gamma = 7.4$, to the energy of transition, $\gamma_{\text{tr}} = 6.1$. Even for low RF voltages in the range of 10 kV, the bucket filling factor remains small, which would require extremely precise relative phase control. In combination with the low synchrotron frequency the conditions for splitting are unfavourable. A test of bunch splitting from harmonic, $h = 21$, to $h = 42$ with lead ions in 2012 has illustrated the difficulties. In the middle of the process some particles were actually stuck at the unstable fixed-point during the separation of the two bunches [4]. The splitting scheme has therefore been abandoned.

Batch compression [5] at the flat-top has been studied as an alternative path to 50 ns bunch spacing at PS extraction. It does not suffer from the adiabaticity issues and excessive phase control precision as bunch splitting. During the RF manipulation all bunches stay within well defined sub-

buckets without the need for separation at an unstable fixed point. The process is also tolerant to phase errors as the bunches are just handed over from bucket centres at the initial harmonic to bucket centres at the final one. However, the main drawback of batch-compression RF manipulations is the large number of intermediate RF harmonics which is required. In the case of batch compression of four bunches from 100 ns to 50 ns spacing, RF voltage on at least four intermediate harmonics (e.g., $h = 25, 30, 36$ and 42) is needed in addition to $h = 21$. Following the batch compression, the four bunches spaced by 50 ns can then be rebucketed to $h = 85$, generated by a slightly detuned 40 MHz RF system, and finally to $h = 169$ for the bunch shortening prior to extraction. The simulated mountain range plot of the complete RF manipulation at the PS flat-top is shown in Fig. 1.

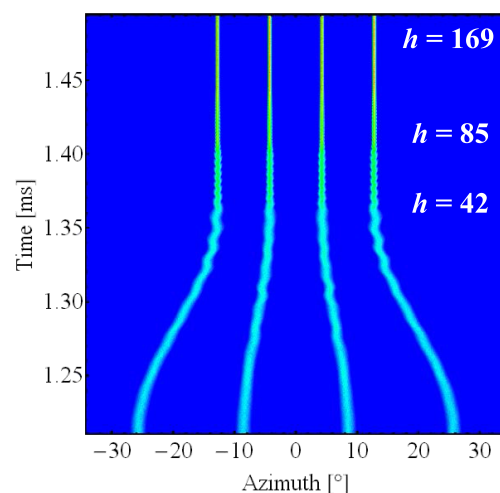


Figure 1: Simulated (ESME [6] without intensity effects) mountain range plot of the complete RF manipulation from $h = 21$ to $h = 169$ aiming at generating four short bunches with 50 ns spacing.

Since no RF system presently installed in the PS can deliver voltage at $h = 25, 30$ or 36 for a standard batch compression, a much simplified scheme has been tested with beam 2016. It allows to batch compress two bunches to 50 ns spacing, by starting from the first part of a bunch pair merging to approach the bunches combined with a hand-over to $h = 42$. The scheme is inherently limited to two bunches. The proof-of-principle tests permit nonetheless to evaluate voltage requirements and address the adiabaticity issues in case of moving bunches in azimuth at the flat-top in the PS.

In the following section the simulation results and measurements with beam for this simplified batch compression-like RF manipulations are presented. Special care has been taken to optimize the voltage programs such that, e.g., discontinuities of the synchronous phase are avoided when accelerating one bunch while decelerating the other during

the approach. Based on these experimental results the requirements for additional RF systems needed for the full production scheme, yielding four bunches spaced by 50 ns, are discussed.

TWO-BUNCH MERGING COMPRESSION

Two bunches in adjacent buckets at an initial harmonic can be brought closer together in time by increasing the harmonic number of the RF system or, assuming sufficiently large bucket area, by adding RF voltage at a lower harmonic. The latter method is actually the first part of a bunch pair merging [7, 8].

Figure 2 shows a tracking simulation of two lead bunches spaced by 100 ns approaching each other. Initially the

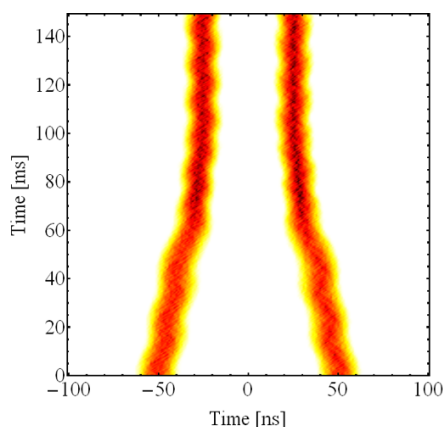


Figure 2: Simulated merging compression $h = 21 \rightarrow 21 + 7 \rightarrow 42$ using linear functions for the RF voltage programs.

bunches are held by a single harmonic RF voltage of 10 kV in $h = 21$. An additional RF voltage at $h = 7$ is then brought up linearly with time until the same voltage is reached for both RF harmonics. Both bunches are then close enough to be handed over to an RF system at $h = 42$, corresponding to 50 ns spacing. At the PS flat-top energy of 5.9 GeV/n this manipulation takes about 100 ms. However, due to the linear voltage functions the initially stationary bucket instantly becomes accelerating, respectively decelerating, at the start of the process and vice versa at its end. The corresponding stable phase jumps excite dipole oscillations as observed in Fig. 2.

These oscillations can be largely avoided by introducing non-linear voltage functions (with time) such that the bucket centres start to approach without jump in stable phase (Fig. 3). The reduction of the bunch spacing from 100 ns to 50 ns is again performed in 100 ms and the bunches follow the bucket centres smoothly.

DOUBLE HARMONIC $H=21+7$

Similar conditions have been studied with a lead ion beam at the flat-top in the PS. Two ion bunches are injected from LEIR, accelerated to an intermediate flat-top at a kinetic energy of approximately 0.38 GeV/u and split according to the nominal four-bunch scheme described in [1]. Two

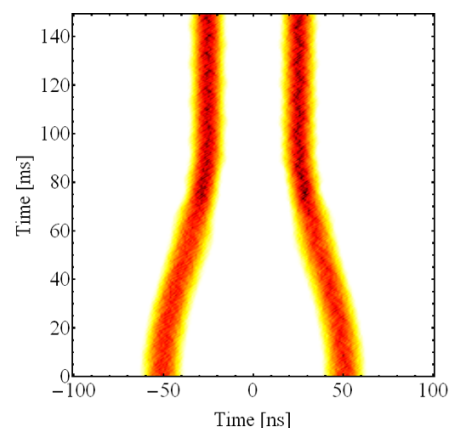


Figure 3: Simulated merging compression as in Fig. 2 using optimized voltage programs.

of the four bunches held at $h = 21$ are then removed by the extraction kicker and the remaining two bunches are accelerated on $h = 21$ to the flat-top. This is the initial condition for the approach from 100 ns to 50 ns. Although the manipulations also works at lower RF voltages, sufficient margin has been chosen to keep beam phase and radial loops closed properly. Therefore the first series of measurements was taken with an initial RF voltage of 60 kV at $h = 21$.

Figure 4 shows a mountain range plot of the approach of two bunches when linearly increasing the RF voltage at $h = 7$ from zero to 120 kV. The beam phase loop is kept

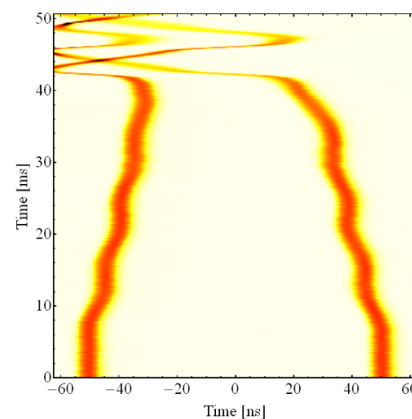


Figure 4: Measured merging compression $h = 21 \rightarrow 21 + 7$ in 40 ms using linear voltage programs.

at $h = 21$ and towards the end of the process, when both bunches already get too close to deliver a meaningful phase information, the phase loop locks out.

The dipole oscillations due to the abrupt start of the approach are clearly visible. They are caused by the sudden change from a stationary to a moving bucket (Fig. 5, blue trace) and back to a stationary bucket. As the oscillations are triggered directly at the start of the process, they persist even for a twice longer linear rise of the RF voltage on $h = 7$. However, a non-linear voltage rise can be computed such that the bucket centres move adiabatically (Fig. 5, red trace).

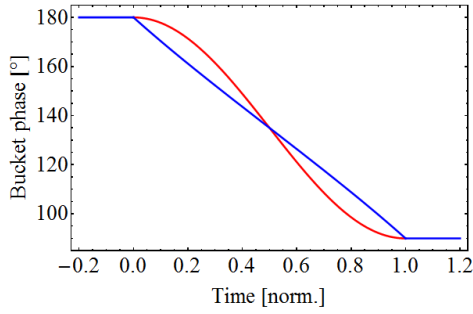


Figure 5: Bucket phase (in degrees of $h = 21$) for a linear (blue) and non-linear rise (red) of the RF voltage at $h = 7$, in combination with a constant RF voltage at $h = 21$. The non-linear voltage rise is evaluated numerically to achieve a sinusoidal approach of the buckets.

In this case they follow a sinusoidal function starting and ending with zero gradient. The corresponding non-linear voltage rise is plotted in Fig. 6, showing the detected voltages of the RF systems at $h = 21$ (constant) and $h = 7$.

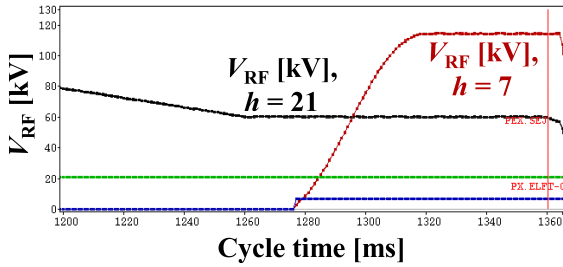


Figure 6: Detected RF voltages at $h = 21$ (black) and $h = 7$ (brown) together with the corresponding harmonic numbers (green and blue) yielding the evolution of the buckets centres according to Fig. 5 (red).

As expected, the dipole oscillations at the start of process (Fig. 4) disappear when the RF voltage on $h = 7$ is not raised linearly but according to the curve shown in Fig. 6. The same effect is observed for various durations of the RF

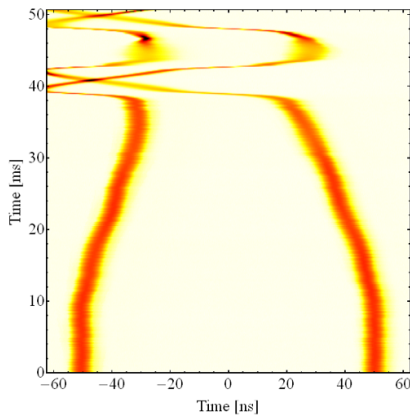


Figure 7: Measured merging compression $h = 21 \rightarrow 21 + 7$ in 40 ms using optimized voltage programs.

manipulations showing that the dipole oscillations are almost entirely due to the discontinuity at the beginning of the process. Two bunches can thus be adiabatically approached without significant impact on longitudinal beam quality.

REBUCKETING TO H=42

Approaching the two bunches from 100 ns to 50 ns spacing using only RF systems at $h = 21$ and $h = 7$ would require a twice larger RF voltage as at the lower harmonic as described in the previous section. However, for a rebucketing to $h = 42$ it is sufficient to approach the bunches close enough to hand them over into two adjacent buckets at $h = 42$. In a first step the RF voltage on $h = 7$ is therefore increased non-linearly to the same voltage at $h = 21$ (about 40 kV), which results in a bunch spacing of approximately 75 ns. Using a 20 MHz cavity tuned to 19.85 MHz, about 175 kHz below its frequency for protons, the RF voltage on $h = 42$ is then linearly increased to 20 kV. Finally, the voltages at both RF harmonics, $h = 7$ and $h = 21$ are simultaneously brought to zero, leaving two bunches spaced by 50 ns in a single-harmonic bucket at $h = 42$. Due to the limited beam time available for optimization, no attempt with non-linear voltage function during the re-bucketing part has been made.

The evolution of the detected RF voltages for the three harmonics during complete process is summarized in Fig. 8. The relative phases are adjusted such that the unstable fixed

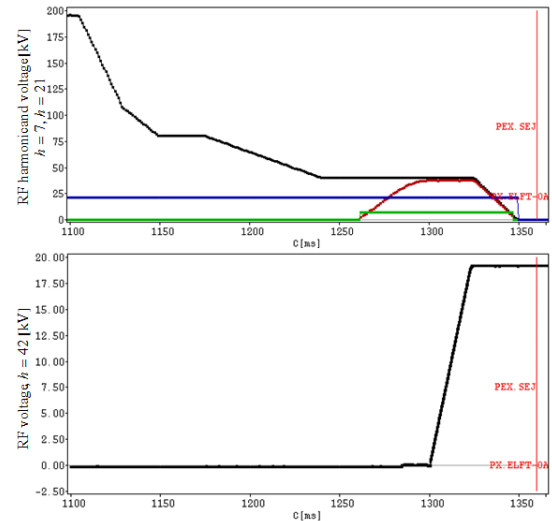


Figure 8: RF voltages at $h = 7$ (top, brown), 21 (top, black) and 42 (bottom) during the complete merging compression. The green and blue traces of the top plot are the measured harmonic numbers, $h = 7$ and $h = 21$.

point of initial ($h = 21$) and final ($h = 42$) buckets are aligned. The RF phase at $h = 7$ is programmed in counter-phase.

The resulting evolution of the bunch profiles during the RF manipulation is illustrated in Fig. 9. For a total duration of 100 ms the bunch distance is smoothly reduced and the longitudinal emittance blow-up remains below the measure-

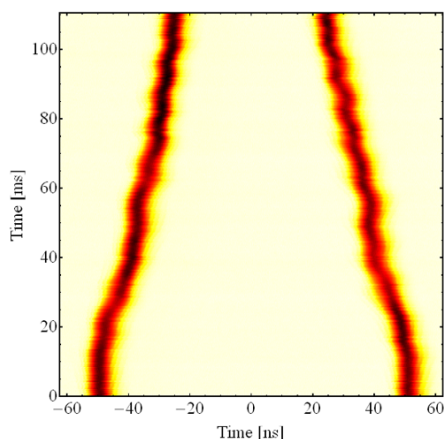


Figure 9: Measured mountain range plot of the complete RF manipulation from pure $h = 21$ to pure $h = 42$ in 100 ms.

ment precision of few percent. Executing the RF manipulation twice faster results in strong dipole oscillations of both bunches though.

Ideally the harmonic for the beam phase loop should also follow from $h = 21$ to $h = 42$ to avoid losing the phase information of the beam on $h = 21$. For technical reasons, a beam phase loop at $h = 42$ could not be provided easily and the phase loop harmonic was only switched to $h = 24$ instead. This is sufficiently high to keep the loop locked although the bunches are already held by a single-harmonic RF voltage at $h = 42$. It is worth noting that the cavity return to the beam phase loop was emulated by a beam synchronous RF source programmed at $h = 24$.

SCALING TO STANDARD BATCH COMPRESSION

The beam measurements of the merging compression demonstrate that the spacing of lead ion bunches can be reduced on the flat-top by means of batch compression despite the vicinity to transition energy.

The normalized bucket areas for the merging and standard batch compression are compared in Fig. 10, showing that very similar RF voltages are required for both schemes to achieve comparable conditions. For the full implementation of the standard batch compression of four ion bunches from 100 ns to 50 ns spacing, the PS would thus need to be equipped with wide-band RF systems, delivering about 20 kV in the frequency range of about 12 MHz to 20 MHz ($h = 25$ to $h = 42$). Since two harmonics are required simultaneously the total RF voltage of the installation would amount to 40 kV.

For the batch compression with four bunches the outer bunches must move three times the azimuth of the two inner ones. Additionally, the motion of the bucket centres can not be optimized for inner and outer bunches at the same time. Hence the duration of the adiabatic batch compression scheme with four bunches is expected to be three times longer compared to proof-of-principle scheme with only two

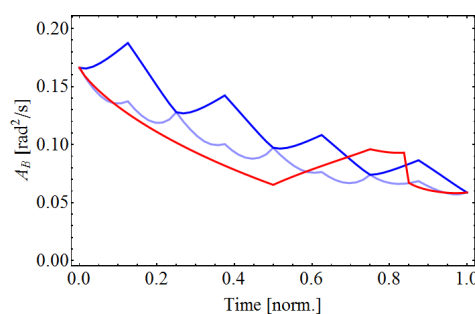


Figure 10: Comparison of normalized bucket area of the merging compression (red, $h = 21 \rightarrow 21 + 7 \rightarrow 42$) with the standard batch compression (inner bucket in dark blue, outer bucket in light blue, $h = 21 \rightarrow 25 \rightarrow 30 \rightarrow 36 \rightarrow 42$).

bunches, resulting in a duration of about 200 ms to 300 ms in total. This is slightly longer than expected from the tracking simulations. A detailed study must confirm if the duration is compatible with the maximum length of the flat-top in the PS. Additionally, the intermediate step of RF voltage at $h = 85$ from a detuned 40 MHz cavity to shorten the bunches for the re-bucketing to $h = 169$ has to be investigated.

CONCLUSIONS

Proof-of-principle beam tests have been performed with lead ion beams at the flat-top in the PS with the objective of producing 50 ns bunch spacing by batch compression. In the absence of RF systems at the necessary frequencies, a merging compression scheme has been set-up. It demonstrates that, despite the unfavourable conditions for RF manipulations at the flat-top, batch-compression is feasible. Furthermore, the beam measurements of the merging compression allow to specify the requirements of additional RF systems to produce four-bunch batches with 50 ns spacing: two RF systems covering the frequency range 12 MHz to 20 MHz with a voltage of about 20 kV. Based on the beam tests the total duration of the batch compression RF manipulation is estimated to be 200 ms to 300 ms.

ACKNOWLEDGEMENTS

The author would like to thank Michele Morvillo and Salvatore Energico for the tuning of the 20 MHz cavity for the beam tests with ions and the operations team for the support of the studies. He is also grateful to Wolfgang Höfle for valuable comments and corrections of the manuscript.

REFERENCES

- [1] J. Coupard, H. Damerau, A. Funken, et al., “LHC Injectors Upgrade, Technical Design Report, Vol. II: Ions”, CERN-ACC-2016-0041, CERN, Geneva, Switzerland, 2016.
- [2] D. Boussard, Y. Mizumachi, “Production of Beams with High Line-Density by Azimuthal Combination of Bunches in a Synchrotron”, PAC79, San Francisco, USA, 1979, p. 3623.
- [3] R. Garoby, “Multiple bunch-splitting in the PS: Results and plans”, LEP performance workshop, Chamonix, France, 2001, p. 32.

BATCH COMPRESSION TO 50 NS SPACING AT PS FLAT-TOP

- [4] Electronic accelerator logbook, <https://ab-dep-op-elogbook.web.cern.ch/ab-dep-op-elogbook/elogbook/secure/eLogbook.php?lgbk=11&date=20121109&shift=1>.
- [5] R. Garoby, "Proposal for a new process realizing longitudinal merging of bunches in the CPS, while conserving the total longitudinal emittance of the beam", CERN PS/RF/Note 83-15, CERN, Geneva, Switzerland, 1983.
- [6] J. A. MacLachlan, "Longitudinal Tracking With Space Charge and Inductive Wall Coupling Impedance", FERMI LAB-FN-446, Fermi National Accelerator Lab., Batavia, Illinois, 1987.
- [7] I. Bozsik, I. Hofmann, A. Jahnke, R. W. Müller, "Numerical Investigation of Bunch-Merging in a Heavy-Ion-Synchrotron", Proc. of Computing in Acc. Design and Operation, Berlin, Germany, 1983, p. 128.
- [8] R. Garoby, "New RF Exercises Envisaged in the CERN-PS for the Antiprotons Production Beam of the ACOL Machine", IEEE Trans. Nucl. Sci., Vol. NS-32, 1985, p. 2332.

TRANSVERSE STUDIES WITH IONS AT SPS FLAT BOTTOM

F. Antoniou, H. Bartosik, A. Huschauer and A. Saa Hernandez*, CERN, Geneva

Abstract

The LHC injectors upgrade project (LIU) aims at consolidating and upgrading the existing accelerator chain at CERN in view of the increased beam performance required for the High Luminosity LHC (HL-LHC) project. For the ion chain, the losses and emittance growth in the SPS impose presently the main performance limitation. The significant beam degradation encountered on the long injection plateau has been studied during the 2016 MD runs with Pb82+. In this report we present the systematic measurements of emittance, bunch length and transmission performed along the injection plateau for different bunch intensities. We present, as well, static and dynamic tune scans for the optimization of the working point and measurement of the loss rate at closeby resonances.

MOTIVATION AND MD RUNS

The LHC injectors upgrade project (LIU) aims at consolidating and upgrading the existing accelerator chain at CERN in view of the increased beam performance required for the High Luminosity LHC (HL-LHC) project. For the ion chain, the losses and transverse emittance growth in the SPS impose presently the main performance limitation [1]. The losses increase with the bunch intensity, as shown in Fig 1 for the case of 7 injections from PS as used in 2016 for the LHC p-Pb run. For comparison, the nominal bunch intensity for LIU is $3.6\text{e}+8$ Pb ions at SPS injection [1, 2].

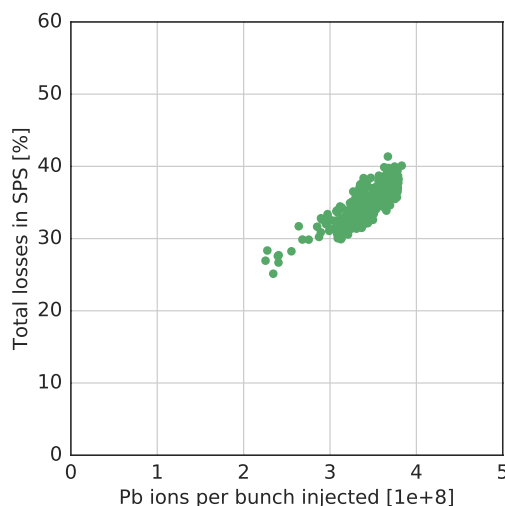


Figure 1: Total losses in the SPS as a function of bunch intensity. The nominal bunch intensity for LIU is $3.6\text{e}+8$ Pb ions.

A big fraction of the beam degradation occurs on the SPS injection plateau, also referred to as flat bottom (FB) in the

following. The FB length for LIU will be approximately 50 s in order to accumulate 14 injections from the PS. We suspect there are various sources for these losses; namely space charge, intrabeam scattering (IBS), RF noise, and aperture limitations. A series of machine development (MD) studies were performed during the Pb ion run between October and December of 2016 to study these effects. The FB duration of the parallel MD cycles used was 3 s. These short cycles were used to perform static and dynamic tune scans. Additionally, four dedicated MD runs took place in November 2016. The dedicated MD cycles had FB durations of 22 s, which enabled measurements of transmission, bunch length and emittance evolution along the longer injection plateau.

MEASUREMENTS

Four bunches from the PS (i.e. one batch) were injected at the beginning of the FB (defined as $t = 0$ s) of each MD cycle. Further injections were avoided in order to enable direct measurement of emittance and intensity evolution along the FB. The SPS was tuned to the default Pb-ion working point (WP) of $Q_x = 20.30$, $Q_y = 20.25$. All measurements were taken at this WP, unless stated differently.

Transverse emittances

The emittance of the beam cannot be directly measured. However, combining the measurements of the transverse beam sizes with the knowledge of the optical functions (from the lattice model or from measurements), the transverse emittances can be derived. In the SPS two sorts of diagnostic instruments were used to measure the beam size: a beam gaseous ionization monitor (BGI), which was still under commissioning, and rotational wire scanners (WS) in the horizontal and vertical planes. While the BGI enables several measurements along one cycle, the WS can only be fired twice along the same cycle. For this reason, WS measurements of the emittance evolution along the FB have been performed on different cycles. The measurements have been repeated between 5 and 15 times and the error bars indicate the standard deviation.

First the emittance evolution along the FB was studied for bunches with a constant intensity. The horizontal emittance measured shortly after injection was approximately 50% larger than the vertical one. The observed emittance evolution is also different for both planes; while it increases steadily in the vertical plane, the overall increase in the horizontal plane is much smaller, showing even a small decrease in the first half of the cycle, as plotted in Fig. 2. Measurements with the WS and the BGI show a qualitative agreement, even when taken for different bunch intensities.

Another set of emittance measurements was performed with different bunch intensities. The emittance measured at SPS injection increases linearly with the bunch inten-

* angela.saa.hernandez@cern.ch

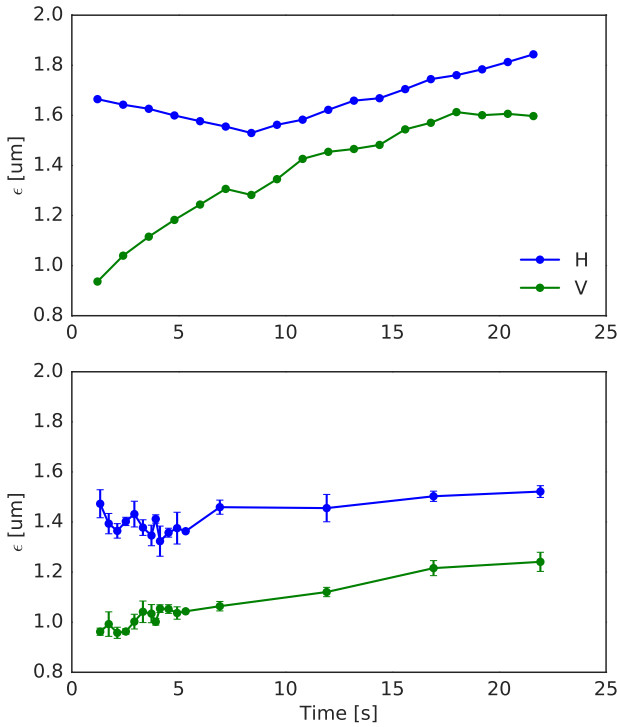


Figure 2: Emittance evolution along the FB measured with the BGI for a bunch intensity of 3.5×10^8 Pb ions/bunch at injection (top), and measured with the WS for a bunch intensity of 2.6×10^8 Pb ions/bunch at injection (bottom).

sity. This intensity dependence of the emittance is probably already created upstream in the injector chain (e.g. space charge effects at PS injection [3]). The emittance at the end of the SPS FB also increases linearly with bunch intensity as shown in Fig 3. In the vertical plane the emittance seems to grow by a constant amount, independent of intensity (at least in the range studied in the measurements). In the horizontal plane on the other hand there is minor blow-up for lower intensity but practically no emittance blow-up for the higher intensity bunches measured. The reason for this is not yet understood. The explanation might be linked to the observed degradation of the transmission for increasing intensity as shown in Fig. 4.

To further investigate the underlying mechanisms that define the emittance evolution on the SPS FB, it was attempted to vary the transverse emittance of the injected beam independently of the bunch intensity. However, the brightness at SPS injection (intensity/emittance ratio) remained unaffected despite 1) injecting only 3 instead of 7 Linac3 pulses into LEIR, 2) partially closing the slits placed in the transfer line between Linac3 and LEIR to decrease the bunch intensity, and 3) changing the cooling efficiency in LEIR by varying the closed orbit in the electron cooler. None of these methods enabled the independent variation of the emittance and bunch intensity, which is another indication that the dependence is created either in LEIR, or at PS injection.

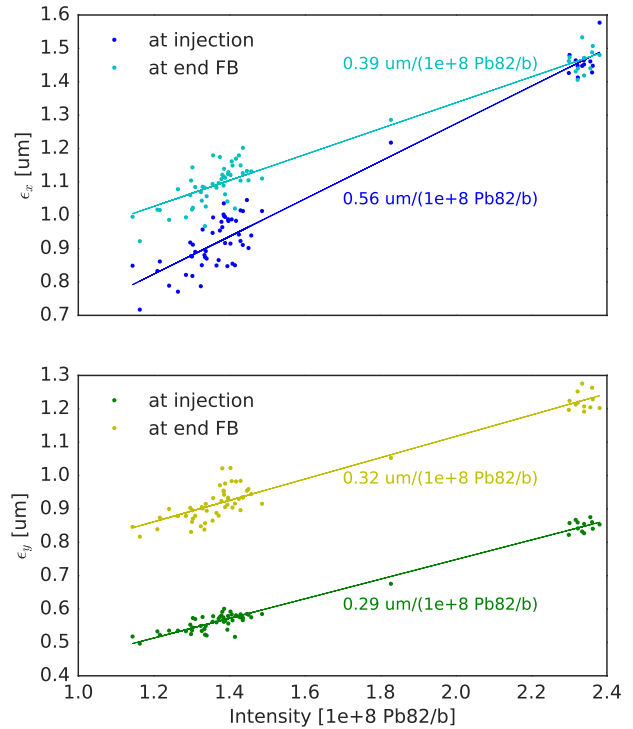


Figure 3: Emittances at injection and at the end of the FB as a function of bunch intensity for the horizontal (up) and vertical planes (down).

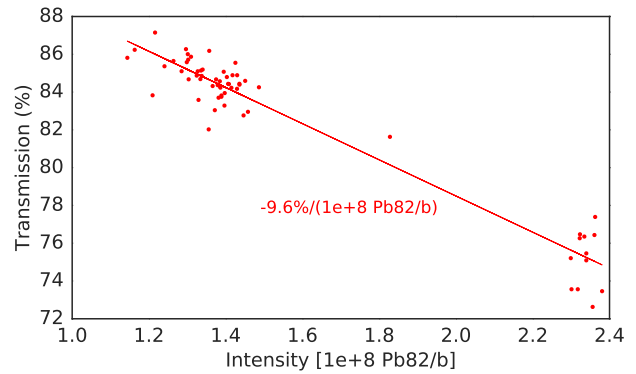


Figure 4: Transmission as a function of bunch intensity.

Bunch Length

The bunch length evolution along the FB was measured with the beam quality monitor (BQM), which is triggered at each injection timing (i.e. every 3.6 s). Additionally, the mountain range (MR) displays one trace per turn, for 50 consecutive turns. As for protons, the bunches are not perfectly matched at SPS injection due to the different RF frequency compared to the PS. Therefore, the bunch length evolution from the BQM data is only considered starting from $t = 3.6$ s (i.e. the moment where in principle a second batch could be injected) until the end of the FB at $t = 21.6$ s. A bunch length reduction of approximately 10% is observed, which slightly increases with intensity, as shown in Fig. 5. However it is important to note that longitudinal studies

of the Pb beam at the SPS have shown that the amount of uncaptured beam increases along the FB [4]. This implies that there is a continuous spill of particles out of the bucket (on the order of 5% in 20 s).

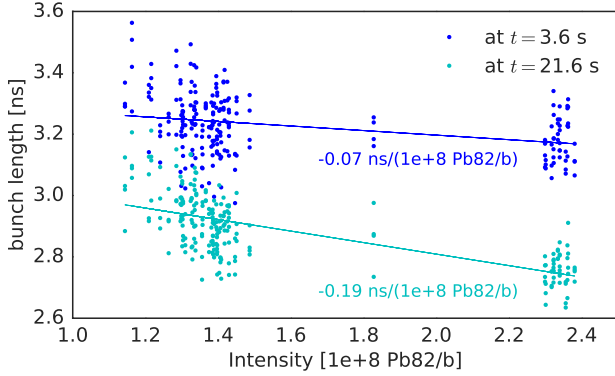


Figure 5: Bunch lengths at $t = 3.6$ s and at the end of the FB ($t = 21.6$ s) as a function of bunch intensity.

Observations without RF

It should be emphasized that the beam degradation described above, i.e. losses and emittance growth, is observed only for bunched beams. In the absence of RF (i.e. with an unbunched beam) the emittance blow-up is negligible and almost no losses are observed. This could be measured directly with the BGI when the RF tripped in the middle of a cycle as shown in Fig. 6. From this observation it seems that vacuum issues can be excluded as the source of beam degradation, since these would also affect unbunched beams. On the contrary, these observations point more towards IBS and space charge, which are negligible for the unbunched beam, and RF noise as potential sources.

Tune Scans

Dynamic and static tune scans were performed to measure the loss rate at the different resonances in view of optimizing the WP. The tune spread caused by space charge is proportional to the line density of the beam. In the case of the bunched Pb beam the tune shift at injection is large (about $\Delta Q_x = -0.2$, $\Delta Q_y = -0.3$ for the beam parameters during the MDs presented here). The resulting tune footprint overlaps many resonances, even the vertical integer, as shown in Fig 7. On the other hand, in the case of an unbunched beam the line density is so small that the tune spread created by space charge is negligible. The footprint is point-like and the resonances can be probed independently. Thus, we dynamically scanned the tune diagram while measuring the loss rate as function of the working point in the absence of RF. As shown in Fig. 8, the highest loss rates were measured at the point $Q_x = Q_y = 20.33$, where the diagonal ($Q_x - Q_y$), the third order integer ($3Q_x$) and the third order coupling ($Q_x + 2Q_y$) resonances cross. Also the third order coupling resonance ($Q_x - 2Q_y$) is clearly excited. Resonances other

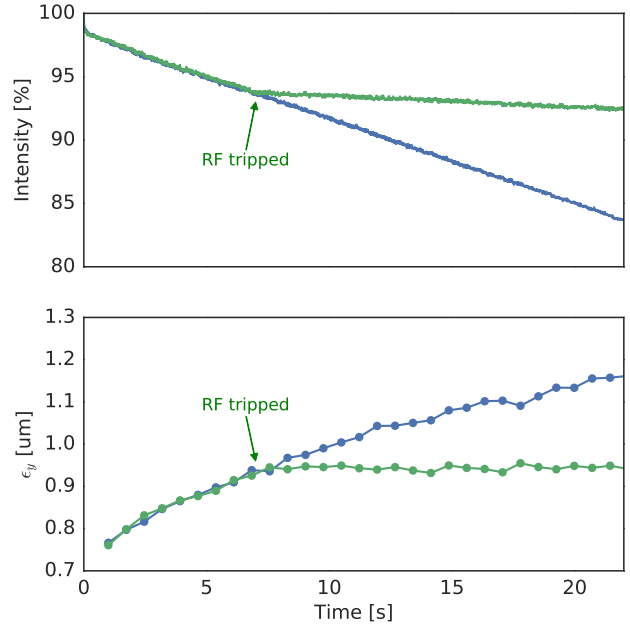


Figure 6: Comparison of losses (up) and emittance blow-up (down) along the FB for two consecutive cycles; the first one with the RF ON (blue) and a second one in which the RF tripped at $t = 7$ s (green).

than the normal third order resonances and the diagonal appear to be much weaker.

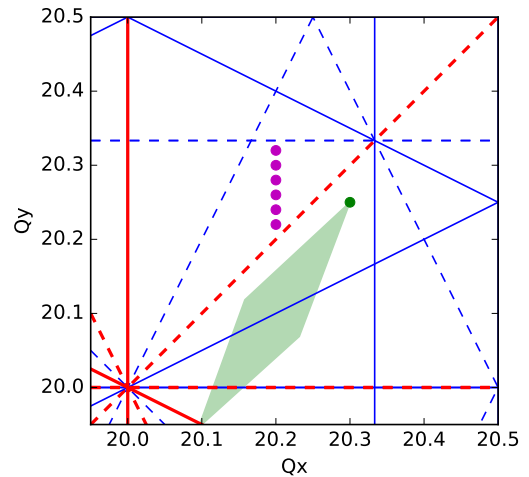


Figure 7: Tune diagram showing resonances up to third order. The standard WP is represented by a green dot. Other WP considered as alternatives are represented by pink dots. Solid line correspond to normal resonances and dashed lines to skew resonances, where systematic resonances are indicated by red colors and non-systematic by blue.

The standard WP for Pb-ions, $Q_x = 20.30$, $Q_y = 20.25$, is situated in an area of low loss rates. We also measured an area with low loss rates placed opposite of the diagonal. We explored some alternative WPs in this area, represented as pink dots in Fig 7, by measuring the transmission and

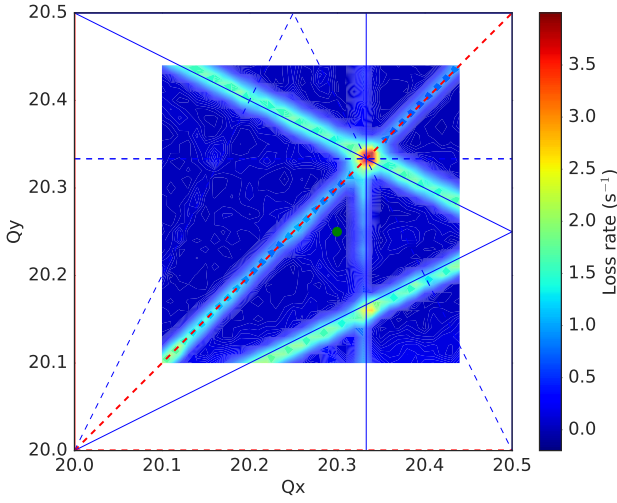


Figure 8: Dynamic tune scan using an unbunched beam.

transverse emittance blow-up along the 22 s FB in the case of a bunched beam. As shown in Fig. 9 all alternative WPs have a lower transmission compared to the standard WP. It is interesting to note that the standard WP has a lower horizontal emittance blow-up but a higher vertical emittance blow-up compared to the alternatives studies.

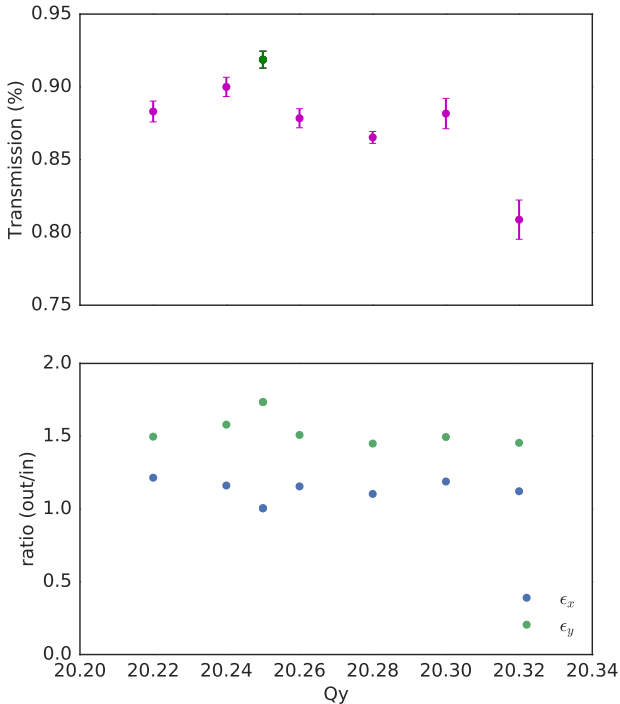


Figure 9: Top: transmission along the FB for the standard WP (green dot) and alternative WP (pink dots). Bottom: transverse emittance blow-up.

We repeated the transmission measurement along the FB for many more points on the tune diagram. However, the scan of a much larger area could only be done in parallel MDs using the cvcle with a 3 s long FB. In this case the

transmission difference between the standard and the alternative WP is not observed. Further analysis and investigations need to be done.

Closed orbit distortions from BGI magnets

An additional observation was done during the MD runs which we consider worth to be mentioned: the transmission along the FB decreased as a function of the BGI vertical dipole current. The transmission went down to 60% when the BGI magnets were powered to their maximum current, 60 A. Simultaneously, the BPMs show large deviations from the reference closed orbit (c.o.), which is a clear indication that the orbit bump created by the dipoles is not fully closed. After re-optimizing the correctors to minimize the orbit deviations the transmission could be recovered, as shown in Fig. 10. This shows that the vertical closed orbit correction is critical for the ion beams, as the beam size is large compared to the available aperture.

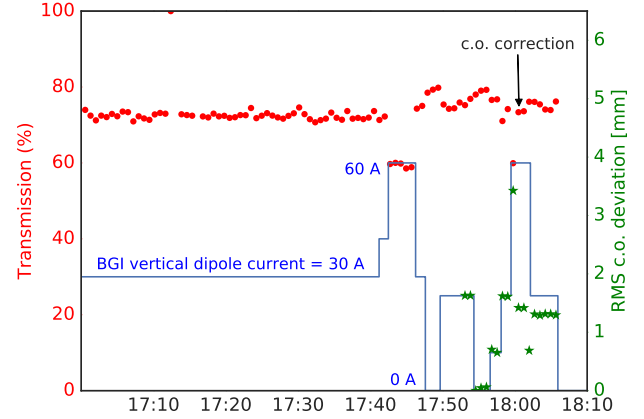


Figure 10: Transmission along the FB (red dots) and RMS c.o. deviation (green stars) for different current values of the BGI vertical dipoles.

CONCLUSIONS

Strong degradation of the Pb-ion beam is observed on the long injection plateau of the SPS, consisting of a significant reduction of the transmission and a transverse emittance blow-up. The transmission of the beam decreases linearly with the bunch intensity. For the beam parameters used during the MDs, i.e. about 50% larger horizontal than vertical emittance at injection, the emittance blow-up occurs mainly in the vertical plane. A bunch length reduction of the order of 10% has also been observed along the FB.

The beam degradation is most likely due to collective effects (IBS, space charge), RF noise, and aperture limitations. Vacuum seems to play a minor role, since there is no blow-up and the losses stabilize when the RF is switched OFF.

It has also been observed that powering the vertical BGI dipoles leads to c.o. distortions and a reduced transmission along the FB. The transmission can be recovered if the corrector settings are re-optimized.

WP scans have been performed to explore the tune diagram

TRANSVERSE STUDIES WITH IONS AT SPS FLAT BOTTOM

and measure the excitation of the betatron resonances. So far no better WP has been found. However, a big amount of experimental data is still available for further analysis.

During the year 2017 no Pb beam runs are planned. Therefore, these measurements will only be continued in 2018. However, machine development runs with Xe beams in SPS could be of interest for exploring another region of the parameter space.

REFERENCES

- [1] H. Bartosik, *LIU Baseline for Ions*, presentation at LHC Performance Workshop 2017.
- [2] *LHC Injector Upgrade, Technical Design Report, Volume II: Ions*, EDMS 1626950 (2016).
- [3] A. Huschauer, H. Bartosik, and A. Saa Hernandez *Pb ion emittance evolution across the injector chain*, these proceedings.
- [4] H. Bartosik and T. Bohl, *Test of fixed harmonics in SPS*, these proceedings.

PB-IONS IN HARMONIC NUMBER 4653 AT SPS FLAT BOTTOM

H. Bartosik, T. Bohl*, A. Huschauer, CERN, Geneva, Switzerland

Abstract

Pb-ion beams suffer from strong beam degradation such as transverse emittance growth and losses on the long flat bottom of the SPS cycles used for LHC filling. A possible contribution to the losses could come from RF noise, especially due to the frequency and amplitude modulation during each revolution period of the fixed frequency acceleration mode required for the acceleration of these beams. A machine development session in 2016 was devoted to a direct comparison of a cycle with fixed harmonic number at flat bottom and a cycle with the usually used fixed frequency mode. The main results are reported here.

INTRODUCTION AND MOTIVATION

Pb-ion beams suffer from strong beam degradation (transverse emittance growth and losses) on the long flat bottom of the SPS cycles used for LHC filling. In fact, the SPS is presently *the* bottleneck for Pb-ion beams and this is in particular relevant for the performance reach in the context of the LHC injector upgrade project (LIU) [1]. To better understand the motivation for the machine development studies with harmonic number, h , of 4653, a short introduction about the RF low level needed to accelerate the heavy ion beams in the SPS should be made.

In a synchrotron the synchronism between the RF voltage for acceleration and the beam is established by choosing

$$f_{\text{RF}} = hf_{\text{rev}}.$$

In this case $h = \text{const}$ and $h \in \mathbb{N}$ (Fixed Harmonic Number Acceleration, FHA). For lead ions, $^{208}\text{Pb}^{82+}$, FHA is not possible in the SPS. The frequency swing of the revolution frequency, f_{rev} , between injection and flat top is such that with a constant value of h , the value of f_{RF} would be outside the bandwidth of RF system at a certain time during the acceleration cycle. The solution which was adopted consists of keeping $f_{\text{RF}} = \text{const}$ (Fixed Frequency Acceleration [2], FFA) and allowing a variable h

$$h = h(f_{\text{rev}}), h \in \mathbb{R}$$

This comes at a price of frequency modulation (FM) and amplitude modulation (AM) of f_{RF} at f_{rev} . At each SPS revolution period of about 23 μs the RF is switched on before bunches enter the Lon Straight Section (LSS) in BA3, and the RF is switched off when the beam has left LSS3 with a 50% duty cycle at the same time while it is modulated in frequency. At first sight it is expected that the RF noise in amplitude and phase would be larger with AM and FM. Therefore, in view of the future low level RF system (after

Long Shutdown 2), the question was whether FHA (no FM and no AM) at the flat bottom could improve the transmission of the ion beam in the SPS.

COMPARISON OF FFA AND FHA

Conditions

In 2016 it was the first time that a comparison of FFA with FHA was possible with the same optics and the same injected beam. To make the comparison it was required to i) make FFA and FHA ppm, ii) operate FFA with standard conditions for iLHC beam, FM, AM and iii) operate FHA with $h = 4653$, no FM, no AM.

Some limitations were encountered: The length of the flat bottom was only about 20 s (in the past it had been nearly twice as long) and no acceleration was possible due to software limitations related to the Coarse Frequency Program. Furthermore, the cavity phasing was not ppm: for $h = 4653$ $V_{\text{RF}} \approx 0.5V_{\text{RF,LSA}}$, nevertheless equal V_{RF} values could be achieved at flat bottom.

In detail, the conditions for the FFA/FHA comparison were that the Q20 optics was used in both cycles, LHC_ION_7Inj_Q20, ID: 10127 (LHCION2) and LHC_ION_7Inj_Q20_2016_MD, ID: 10877 (LHCION4). The Nominal Beam with 4 bunches spaced by 100 ns was injected with about $N_Q = 2.9 \times 10^{10}$ charges per bunch. All observations were made using the first batch and observing i) the bunch length, ii) the bunch peak amplitude and iii) the bunch position along the flat bottom.

Results

The bunch profiles at injection for the two cases of FFA and FHA are shown in Fig. 1. They confirm that the injected beam had been the same in the two cases. The bunch profiles at the end of the flat bottom are shown in Fig. 2. Also here, there is no difference between the bunch shapes for the two cases of FFA and FHA.

Comparing the bunch length versus time, in each case for the four bunches of the first batch, there is no visible difference, see Fig. 3. The same applies for the bunch peak amplitude versus time as can be seen in Fig. 4. Also with a higher vertical resolution, there is no difference between the two cases of FFA and FHA. This is true both for the bunch length and the bunch peak amplitude versus time, see Fig. 5 and Fig. 6. The numeric values of the bunch length reduction and the bunch peak amplitude reduction between $t_1 = 294$ ms and $t_2 = 20\,000$ ms are identical, see Table 1. Also the values of the standard deviation of the bunch positions, a measure of the RF noise, during the same period, do not show any difference.

* thomas.bohl@cern.ch

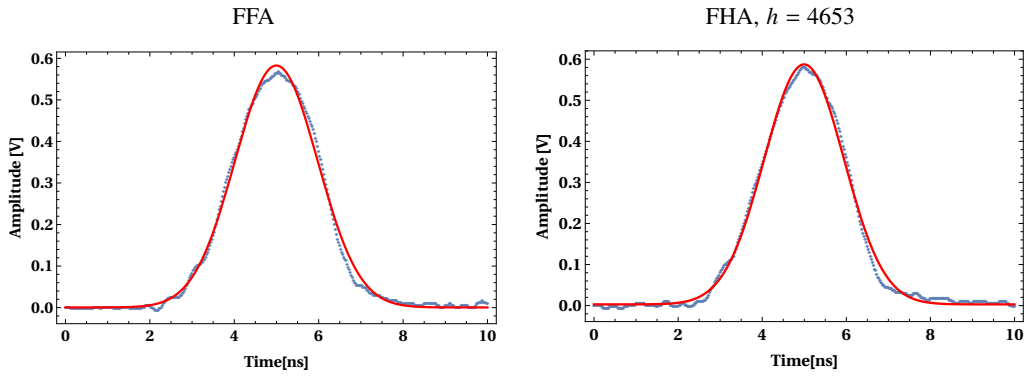


Figure 1: Typical bunch profile of the first injected bunch for the two cases of FFA and FHA.

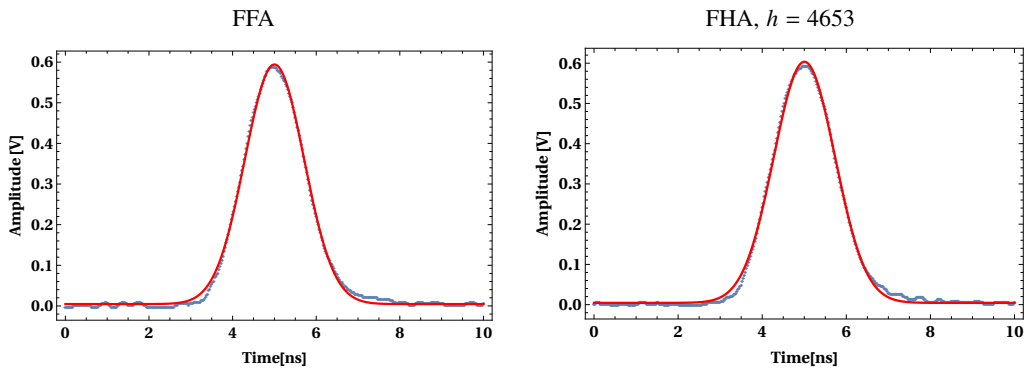


Figure 2: Typical bunch profile of the first bunch at the end of the flat bottom for the two cases of FFA and FHA.

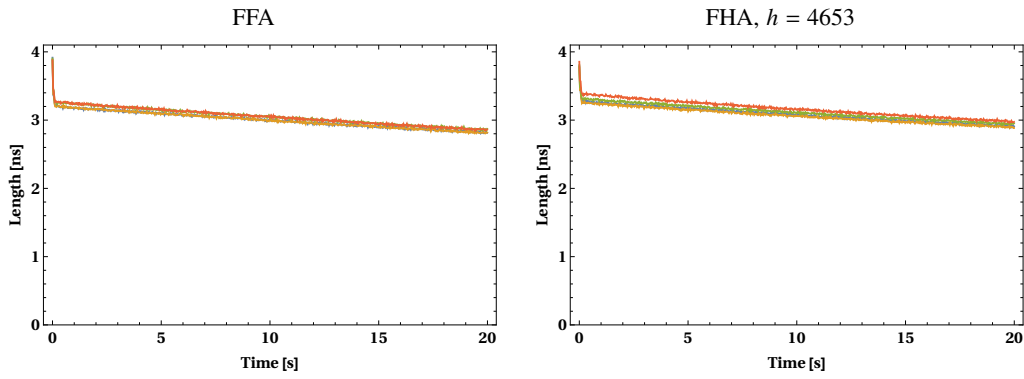


Figure 3: Bunch length of the four bunches versus time for the two cases of FFA and FHA.

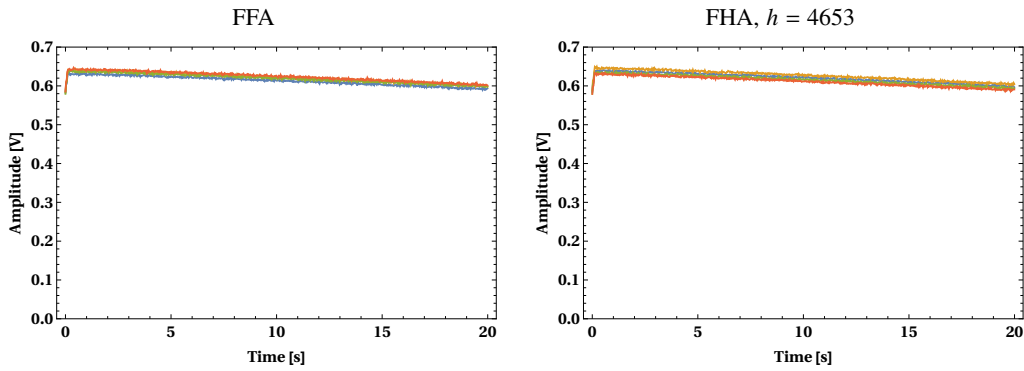


Figure 4: Bunch peak amplitude of the four bunches versus time for the two cases of FFA and FHA.

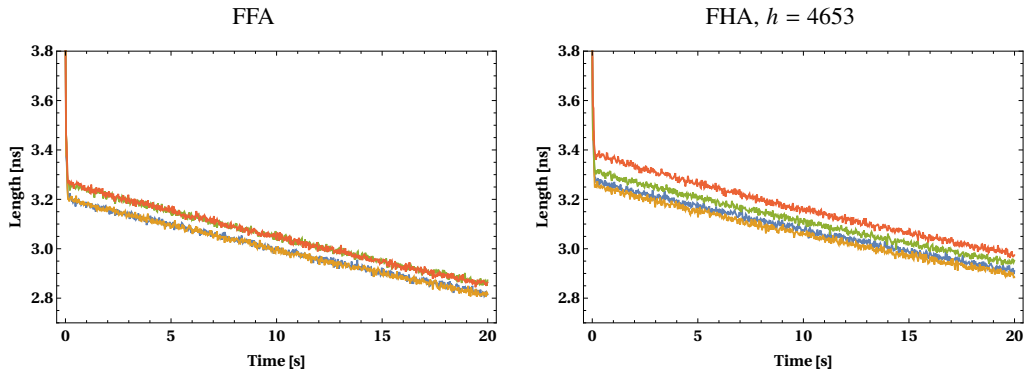


Figure 5: Bunch length of the four bunches versus time for the two cases of FFA and FHA.

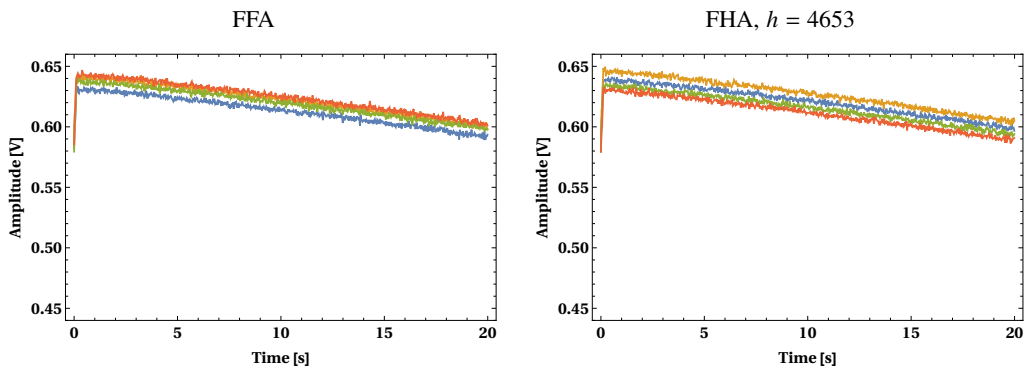


Figure 6: Bunch peak amplitude of the four bunches versus time for the two cases of FFA and FHA.

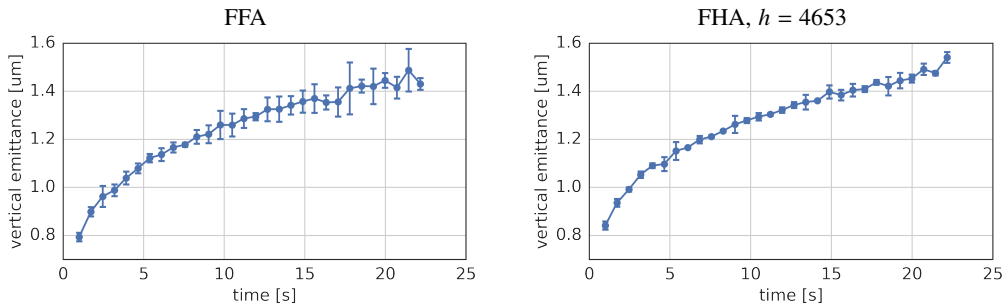


Figure 7: Vertical emittance measured with the BGI along the flat bottom with FFA and FHA.

Table 1: Comparison FFA and FHA

	FFA	FHA
bunch length reduction	-12%	-12%
bunch peak amplitude reduction	-6%	-6%

Another comparison was made in terms of transverse emittance blow-up. As reported in [3], relatively strong vertical emittance blow-up is observed along the flat bottom of the operationally used cycle with FFA. The same behaviour is observed in the cycle with FHA, as seen by the vertical emittance evolution measured with the Beam Gas Ionisation (BGI) monitor illustrated in Fig. 7. Unfortunately the horizontal BGI monitor could not be used during the MD.

BEAM LOSS ALONG FLAT BOTTOM

As discussed in the previous section, the beam behaviour in FHA compared to FFA is very similar both in terms of bunch length and bunch peak amplitude evolution along the flat bottom. Similarly, the evolution of the intensity along the flat bottom was the same on both cycles. In particular, important losses out of the RF bucket were observed. This is shown in Fig. 8 for the case of the FHA. The integrated longitudinal bunch profile measured with a wall current monitor clearly shows that some particles are not captured into the RF bucket at injection (about 2%), but they remain in the machine as observed by the DC beam current transformer (BCT) measurements. In addition, since the discrepancy between integrated bunch profiles and BCT signal grows along

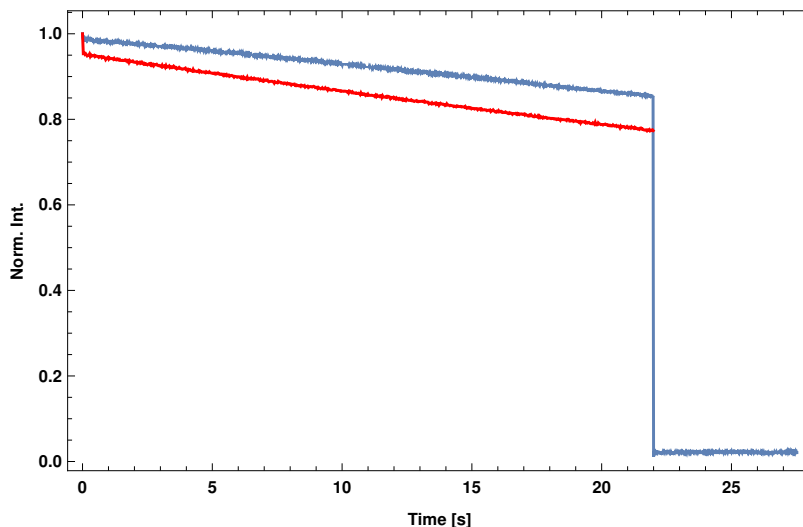


Figure 8: Intensity along the flat bottom of the FHA cycle as measured with the DC-BCT (blue) and as obtained from integrating the longitudinal profile measured with the wall current monitor (red).

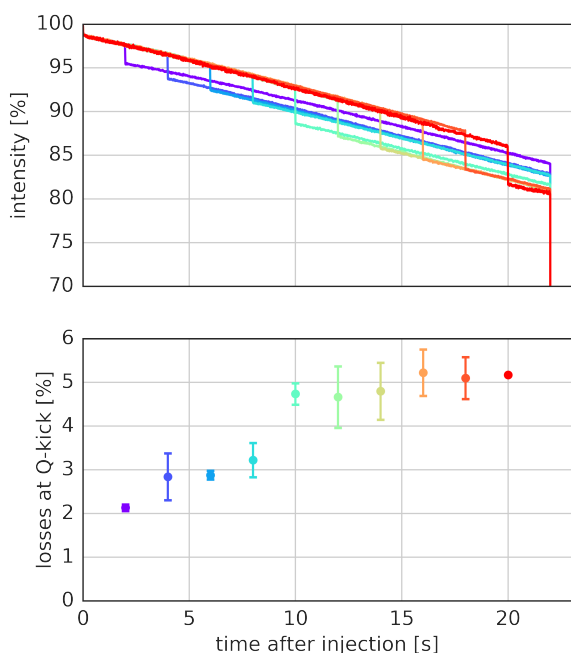


Figure 9: Evolution of intensity along the flat bottom of the FHA cycle as measured with the DC-BCT (top) and losses at the moment of the tune kick to eliminate uncaptured beam (bottom). The different colours correspond to different trigger times of the tune kicker. An average of about 3 cycles were used in each configuration and the errorbars indicate the standard deviation.

the flat bottom, some particles are continuously spilling out of the RF buckets. At the end of the flat bottom more than 5% of the particles are outside of the RF buckets. This was also verified with an independent measurement by pulsing the SPS vertical tune kicker at maximum voltage with a waveform adapted to cover only the empty RF buckets of the

SPS circumference. By adjusting the trigger time of the tune kicker the amount of uncaptured beam along the flat bottom can be obtained from the BCT measurement as shown in Fig. 9. Also this measurement shows that the amount of uncaptured beam increases along the flat bottom, from about 2% at injection to more than 5% at the end of 20 s storage time, which is consistent with the measurement above.

SUMMARY AND CONCLUSION

The comparison of the two Q20 cycles with a 20 s long flat bottom shows no significant differences between the operation with FFA and FHA at $h = 4653$, both in terms of bunch length and bunch peak amplitude evolution along the flat bottom. Also the losses and the vertical emittance evolution (horizontal could not be measured) are very similar. Measurements in the FHA cycle show that more than 5% of particles are spilled out of the RF bucket along the flat bottom, similar as with FFA. No improvement of the flat bottom transmission was observed with FHA compared to the operationally used FFA.

ACKNOWLEDGEMENT

The help of A. Pashnin, the SPS Operators and of U. Wehrle in the preparation of the cycle with $h = 4653$ is highly appreciated.

REFERENCES

- [1] “LHC Injectors Upgrade Technical Design Report, Volume 2: Ions”, EDMS 1626950, CERN, Geneva, Switzerland (2016).
- [2] D. Boussard, J. M. Brennan, T. P. R. Linnekar, “Fixed Frequency Acceleration in the SPS”, CERN SPS/89-49 (ARF), December 1989.
- [3] A. Saa Hernandez *et al.*, “Transverse studies with ions at SPS flat bottom”, these proceedings.

SMOOTH B-TRAIN

T. Bohl, A. Pashnin, CERN, Geneva, Switzerland

Abstract

The transmission of the $^{208}\text{Pb}^{82+}$ Early Beam between the time of Start Ramp up to transition of the LHCION cycles in the SPS has been improved in 2016 by optimising the transfer function of the Frequency Program Data used for the generation of the Master DDS output.

MOTIVATION

The transmission of the $^{208}\text{Pb}^{82+}$ between the time of Start Ramp up to transition had been unsatisfactory for any of the LHCION cycles in the SPS used in 2016. At the same time it had been observed that there was a large transient on the phase loop phase discriminator signal, $\Delta\Phi_{\text{PL}}$, shortly after a B^+/B^- pulse from the reference magnet arrived at the DSP Frequency Program of the beam control used for Fixed Frequency Acceleration. The signal $\Delta\Phi_{\text{PL}}$ and the B^+/B^- pulses are shown in Fig. 1.

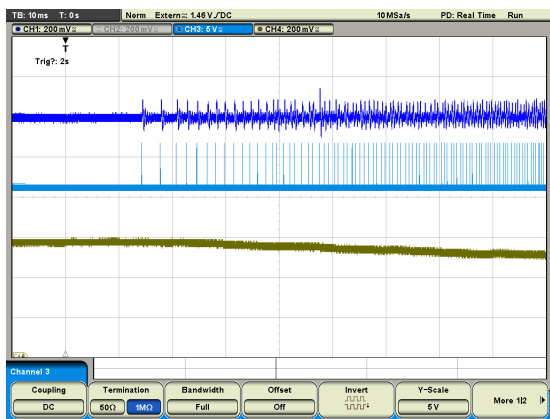


Figure 1: CH1 (top, blue): $\Delta\Phi_{\text{PL}}$, CH3 (centre, blue): B^+/B^- pulses, CH4 (bottom, green): AEW_{pk} (bunch peak amplitude), trigger: Start Ramp.

MECHANISM

The B^+/B^- pulses are treated in the DSP Frequency Program, where they lead to the calculation of new Frequency Program Data, see Fig. 2. These are then transmitted to the Master DDS. The Master DDS generates a frequency which is used to finally produce f_{LO} . The f_{LO} is up-converted to f_{RF} by mixing with a 10.7 MHz XTAL oscillator. This f_{RF} is then amplified by the RF power amplifiers and it is the RF seen by the beam in the travelling wave cavities.

REMEDY

To reduce the deleterious effect of the B^+/B^- pulses, the transfer function of the Frequency Program Data to the Master DDS was improved. The result can be seen in Fig. 3 by comparing the beam transmission for the two cycles without

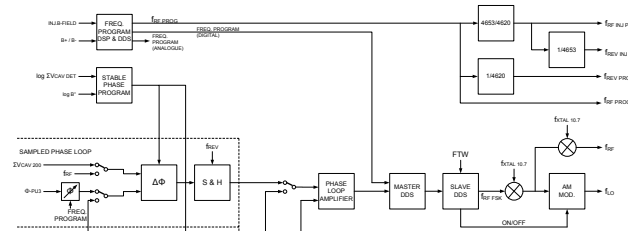


Figure 2: Part of the simplified block diagram of the low level used for FFA relevant for the discussion of the smooth B-train.

(blue trace) and with the improvement (black trace) in the case of the Early Beam. The capture loss at the beginning of the acceleration ramp starting at $t = 620$ ms is the same in both cases. However, the following losses up to transition at $t = 1465$ ms are completely removed (black trace).

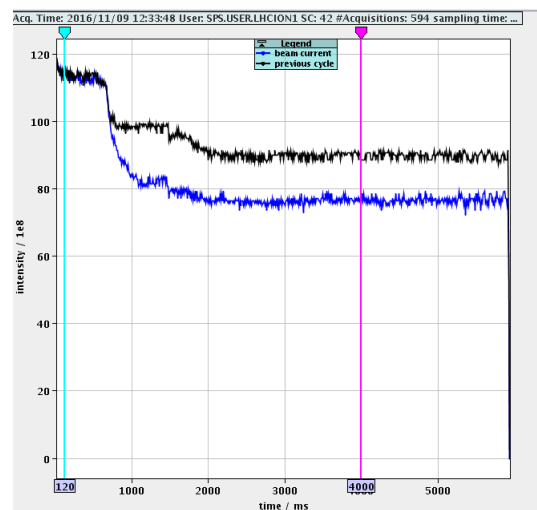


Figure 3: BCT screenshot. low level used for FFA relevant for the discussion of the smooth B-train.

OUTLOOK

The next step would be to apply this improvement and optimise it for the case of the Nominal Beam.

On a longer time scale, for the new beam control after Long Shutdown 2 (LIU SPS Upgrade), a better control of the effect of the B-train on the f_{RF} generation will be available as well as an improved control of the phase loop transfer function.

